Lecture Notes on Particle Physics

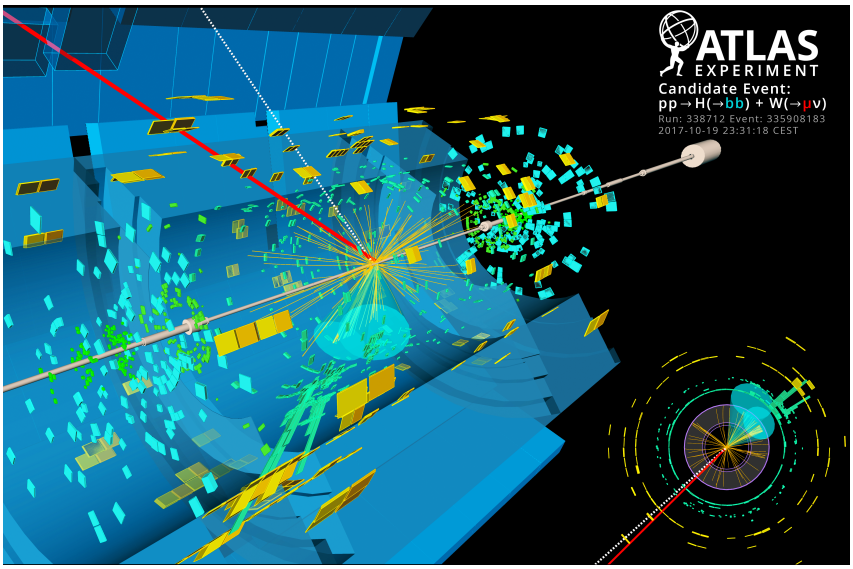

Glen D. Cowan and Veronique Boisvert

Physics Department
Royal Holloway, University of London

ROYAL HOLLOWAY UNIVERSITY OF LONDON

Last revised: November 2, 2023

Preface

These notes were written for the course on Elementary Particle Physics for third-year students at Royal Holloway, University of London. The goal of the course is to become acquainted with the basic ingredients and ideas of elementary particles and their interactions. We'll see that all matter can be described as consisting of a relatively small number of different types of particles, which interact in very specific ways. This description is well enough established that it's called the Standard Model. We'll spend most of the course talking about the Standard Model and how it was developed. This will lead into discussions of theory and experiment and the interplay between the two. The formal mathematical description of the Standard Model uses Quantum Field Theory (QFT), which is beyond the scope this course. A less formal approach is taken here, focusing on the physics concepts, in a way that should allow a smooth transition to more advanced treatments that include QFT.

We begin in Chapters 1 and 2 with an overview of the Standard Model and its theoretical framework. Chapters 3 and 4 then provide a basic description of experimental techniques, including an overview of particle accelerators and detectors. In Chapters 5 through 8, we take a step back and go through the discoveries that led to the various components of our current picture. We will describe these developments using the language of today's Standard Model, which was in most cases not possible at the time of the discoveries themselves. In Chapters 9 and 10 we continue our description of the electroweak and strong interaction with emphasis on recent experiments that have provided verification of the Standard Model to a high level of precision. Chapter 11 describes one of the predicted and possibly very recently observed pieces of the Standard Model, the Higgs boson. Finally, in Chapter 12 we discuss why we believe that the Standard Model is not complete, even though it is currently consistent with all experimental observations, and we introduce a possible extension to it called Supersymmetry.

For further information, the book best suited for this course is *Particle Physics* by Martin and Shaw [1]. The recent book by Thomson [2] is very good and modern, but is a bit too advanced. The books by Hughes [3] and Perkins [4] are also good but are also somewhat more advanced. The history of particle physics from the standpoint of experiment is covered in the book by Cahn and Goldhaber [5].

It would be appreciated if corrections, suggestions and comments on these notes could be communicated to `g.cowan@rhul.ac.uk` and `veronique.boisvert@rhul.ac.uk`.

GDC, VB
August, 2023

Contents

Chapter 1

Overview of particle physics and basic concepts

The purpose of this chapter is to present the cast of characters and to introduce some basic concepts of elementary particle physics. We will also discuss a number of open questions.

1.1 Particles of Nature

According to our current understanding of Nature, all matter is made up of a small number of different types of particles. Remarkably, this basic idea repeats itself on different distance or energy scales. To describe processes where the energies involved are typically around 1 eV, the fundamental building blocks are atoms, of which there are about 100 different kinds. A typical atomic distance scale is around 10^{-10} m. If we collide particles together with higher energies, we find out that atoms are not elementary but rather are made up of more fundamental objects, namely, negatively charged electrons surrounding a small positively charged nucleus. In processes involving energies around 1 MeV or more, one finds that the nucleus itself is not elementary but is made of neutrons and protons, with diameters of somewhat less than 10^{-15} m. In reactions at even higher energies we find out that protons and neutrons are not elementary but are made out of more fundamental objects called quarks and gluons (collectively called partons).

In our current picture, called the *Standard Model*, we have a relatively small number of fundamental particles whose interactions are governed by a set of abstract mathematical laws. It appears we can describe all processes that take place in the universe by a set of physical laws plus initial conditions. Our knowledge of the rules is not complete, however, and it is not clear, for example, whether the separation between physical laws and initial conditions will be part of a more final theory. The fact that the Standard Model works as well as it does is nevertheless remarkable, and we're therefore confident that we're on the right track.

1.2 The fundamental particles of the Standard Model

In the Standard Model, the fundamental particles of matter are spin-1/2 fermions, which interact by emitting and absorbing spin-1 particles called gauge bosons. The fermions come in two types:

quarks and *leptons*. There are six types or 'flavours' of quarks: up, down, strange, charm, bottom and top, usually referred to by their first letters: u, d, s, c, b, t. The u, c and t quarks have an electric charge $Q = 2/3$, while the d, s and b quarks have $Q = -1/3$. Here we are measuring the charge Q in units of the proton's charge, i.e.,

$$Q = q/e \, , \tag{1.1}$$

where q is the usual electric charge and e is that of the proton. The quarks, their charges, and approximate masses (strictly speaking, their rest mass energies mc^2) are listed in Table 1.1.

Table 1.1: Quarks and their properties [7].

name (symbol)	charge (Q)	mass ($\times c^2$)
up (u)	$2/3$	3 MeV
down (d)	$-1/3$	6 MeV
strange (s)	$-1/3$	100 MeV
charm (c)	$2/3$	1.2 GeV
bottom (b)	$-1/3$	4.2 GeV
top (t)	$2/3$	173 GeV

Free quarks have never been observed directly. They are always found bound together in groups of three, called *baryons*, or as a quark q and an antiquark $\overline{q}$, called a *meson*. Examples of baryons are the proton, composed of uud, and the neutron, which is udd. Examples of mesons are pions, which can be charged ($\pi^+ = u\overline{d}$, $\pi^- = d\overline{u}$) or neutral ($\pi^0 =$ mixture of $u\overline{u}$ and $d\overline{d}$, $\mathrm{K}^0 = d\overline{s}$). Mesons and baryons are collectively called *hadrons*.

There are also six leptons, three with charge -1 and three which are neutral, called neutrinos. These are listed in Table 1.2. The simplest version of the Standard Model treats the neutrinos as having zero rest mass. Therefore Table 1.2 only lists for them experimental upper limits [7]. In fact, indirect evidence for very small neutrino masses has recently been discovered in a phenomenon called *neutrino oscillations*. For these lectures we will usually treat the neutrinos as being massless, as this will be an excellent approximation for the reactions considered.

Table 1.2: Leptons and their properties.

name (symbol)	charge (Q)	mass ($\times c^2$)
electron (e^-)	-1	0.511 MeV
muon (μ^-)	-1	105.7 MeV
tau (τ^-)	-1	1.777 GeV
electron neutrino (ν_e)	0	< 2 eV
muon neutrino (ν_μ)	0	< 0.19 MeV
tau neutrino (ν_τ)	0	< 18.2 MeV

The fermions interact by exchanging spin-1 gauge bosons. The type of gauge boson exchanged determines the type of interaction: strong, electromagnetic or weak. In principle, the gravitational interaction should also be describable in terms of the exchange of a gauge

boson, the graviton, but gravity is extremely weak compared to the other interactions and we will neglect it in these lectures. At present there does not exist an accepted theory describing the gravitational interactions of particles at the quantum mechanical level, although a theoretical framework called *string theory* may eventually provide this.

The electromagnetic interaction is mediated by the exchange of a virtual photon (denoted by γ), and the weak interaction proceeds by exchange of a virtual Z (electrically neutral), or a $\mathrm{W}^{\pm}$ (charge $+1$ or -1). Both quarks and leptons participate in electromagnetic and weak interactions. In addition, quarks participate in the strong interactions, mediated by exchange of the *gluon*, whereas leptons do not. Some properties of the gauge bosons are listed in Table 1.3.

Table 1.3: Gauge bosons and their properties.

particle	charge (Q)	mass ($\times c^2$)	interaction
photon (γ)	0	0	electromagnetic
$\mathrm{W}^{\pm}$	± 1	80.4 GeV	weak
Z	0	91.2 GeV	weak
gluon (g)	0	0	strong

The particles γ, $\mathrm{W}^{\pm}$ and Z can be seen as mediating a unified 'electroweak' interaction. Those involving the $\mathrm{W}^{\pm}$ and Z are weak in the sense that the masses of these particles lead to a suppression of the interaction probability when the energy of the reaction is much less than the boson's mass.

In addition to the fundamental fermions and gauge bosons, the simplest version of the Standard Model predicts the existence of a neutral spin-0 particle known as the Higgs boson. This particle is related to the mechanism by which all particles of the Standard Model acquire mass. The mass of the Higgs boson itself is not predicted by the Standard Model. In July 2012 the ATLAS and CMS experiments reported that they had observed a new particle consistent with the Standard Model Higgs boson. We will discuss this in Chapter 11.

1.3 Families

From Tables 1.1 and 1.2 we see that there are three quarks with charge $2/3$, three with $-1/3$, three leptons with charge -1 and three types of neutrinos. We can group these particles into families, as shown in Table 1.4.

Table 1.4: The three families of quarks and leptons.

charge	family		
(Q)	1	2	3
$2/3$	u	c	t
$-1/3$	d	s	b
0	ν_{e}	ν_{μ}	ν_{τ}
-1	e^-	μ^-	τ^-

The three families are given in order of increasing mass. The families also group the particles according to the reactions in which they participate with the highest probability: u and d quarks interact in a sense as a pair, as does c with s, and t with b. Electron neutrinos are produced in association with electrons, muon neutrinos with muons, tau neutrinos with taus.

1.4 Antiparticles, baryon number, lepton number

For every particle there exists an antiparticle with the same mass but opposite charge. These are denoted either with a bar or with a superscript that indicates the opposite charge, i.e., the antiquarks are

$$\overline{u},\, \overline{d},\, \overline{s},\, \overline{c},\, \overline{b},\, \overline{t}\ ,$$

and the antileptons are

$$\mathrm{e}^+,\, \mu^+,\, \tau^+,\, \overline{\nu}_\mathrm{e},\, \overline{\nu}_\mu,\, \overline{\nu}_\tau\ .$$

The interactions of quarks and leptons are such that certain quantities or *quantum numbers* are conserved. The first example you are no doubt familiar with is the electric charge. In addition, we define the *baryon number* B to be $1/3$ for the quarks, $-1/3$ for antiquarks, and zero for all other fundamental particles. The baryon number of a system of particles is simply the sum of the individual baryon numbers. So, for example, the baryon number of a proton (uud) or neutron (udd) is 1. In all reactions that have been observed, the total baryon number is conserved, i.e., the baryon number of the initial state particles equals that of the final state. There are indirect hints that baryon number may not be perfectly conserved, and we will return to this point in Section 8.5.

In a similar way, one assigns a *lepton number* L of 1 to the leptons, -1 to the antileptons, and 0 to all the other particles. The lepton number is also conserved in all reactions that have been observed, but the indirect hints mentioned above about baryon number violation hold also for lepton number.

In addition to the total lepton number L, we can define a separate lepton number for each family: $L_\mathrm{e} = 1$ for e^- and ν_e, $L_\mu = 1$ for μ^- and ν_μ, $L_\tau = 1$ for τ^- and ν_τ, with -1 for the corresponding antiparticles, and otherwise they are zero. For any system of particles we have

$$L = L_\mathrm{e} + L_\mu + L_\tau\ . \tag{1.2}$$

In the simplest version of the Standard Model with massless neutrinos, these quantum numbers are conserved separately. The recent observation of neutrino oscillations, however, has indicated that this is not the case in Nature. For the reactions we will talk about in this course, however, L_e, L_μ and L_τ will all be separately conserved.

So, for example, in the beta decay of a neutron,

$$n \to p\, \mathrm{e}^-\, \overline{\nu}_\mathrm{e}\ , \tag{1.3}$$

the initial state has $B = 1$, $L = 0$, and the final state has the same. Note that L_e, L_μ and L_τ are also all conserved. The reaction

$$p \to \pi^0 e^+ \,, \tag{1.4}$$

however, violates both baryon and lepton number conservation and has never been observed, despite extensive attempts to see it experimentally.

1.5 Open questions

To date there exists no significant discrepancy between experimental observations and the predictions of the Standard Model. Nevertheless, it is widely believed that the Standard Model cannot be Nature's final answer to the structure of matter. Below we list some open questions and unsolved problems. We'll add more as we go along. For a readable discussion of how close we might be to solving these problems, see the book by Weinberg [8].

- The model itself contains around two dozen free parameters, whose values must be obtained by comparing experimentally measured quantities with the corresponding predictions and adjusting the parameters to give the best agreement. It is hard to believe that Nature at her most fundamental level would be described by so many arbitrary parameters. It is widely believed that the Standard Model represents a low energy 'effective theory', similar to the way that Newton's theory of gravity represents an effective approximation to General Relativity in the limit of weak, slowly varying gravitational fields. This more general particle physics theory, if and when we find it, should explain why the parameters (at least some of them) have the values that they do.

- The masses of particles are poorly understood. They are all free parameters, and no one has yet succeeded in finding any understandable pattern in their values. In order for particles to have mass in the Standard Model, the Higgs boson should exist, and although a particle consistent with the Higgs has been observed by ATLAS and CMS as reported in July 2012, it has not yet been established if it is the Standard Model Higgs, or one of several Higgs particles.

- Gravity is not yet included. A final 'Theory of Everything' should incorporate all of the four known interactions: gravitational, electromagnetic, weak and strong. Already, electromagnetic and weak interactions are understood to be different aspects of a unified 'electroweak' interaction. No one has succeeded, however, in describing electromagnetism and gravity as different manifestations of the same thing. This is a difficult task, especially when one considers that gravity is so weak. For example, the ratio of the forces of electrical repulsion to gravitational attraction between two electrons is more than 10^{42}.

  A promising candidate for such a unified description of all four interactions is called *superstring theory*, where the various elementary particles are described as different vibrational states of small loops of string. The loops have extremely small sizes, on the order of 10^{-33} cm, so in all experiments that we can carry out today they appear as point-like particles. Currently we do not know whether superstring theory is correct or even which of this class of theories should be taken to describe our universe. An introduction to the basic ideas of superstrings can be found in the book by Greene [9].

- Why are there three families of particles? Almost all phenomena of our usual world can be described with particles from the 1st family: nuclei are made of neutrons and protons, which are made of u and d quarks; the nuclei are surrounded by electrons; the nuclear reactions in stars involve electron neutrinos. Why Nature has given us three families of particles, the heavier two of which are almost completely decoupled from everyday life, is not understood.

- Why do the equations describing elementary particles possess the mathematical symmetries they do? For example, many processes we see are symmetric with respect to right and left (i.e., a mirror-image experiment would run the same way as the original) and with respect to matter and antimatter, but in the weak interaction these symmetries are violated. It is not clear why Nature should be this way. It is possible that the asymmetry between particles and antiparticles may be related to the presence of the 2nd and 3rd families, and this may have played an important role at times just after the Big Bang, when the temperature of the universe, i.e. the average energies of the particles, was much higher. This in turn could explain why the universe appears to be made almost exclusively of matter, rather than a mixture of matter and antimatter.

- Are our current 'elementary particles' truly elementary or do they possess some sort of substructure, which we could resolve in higher energy interactions? One possibility for this is the superstring theory mentioned above. Other theories have been proposed in which quarks and leptons are composed of particles called *preons*. No experimental evidence for this type of compositeness has been seen.

- From measurements of experiments like WMAP [10], we can estimate that the energy density of the Universe is approximately: 4% normal matter, 21% dark matter and 75% dark energy. The description of dark matter and dark energy is beyond the scope of this course, but we have good indirect experimental evidence for the existence of dark matter. We now need a direct observation of dark matter and a theoretical framework as to how this new particle fits into the current Standard Model.

1.6 Some basic concepts

In this section we introduce some basic tools and concepts that will be needed in the lectures to follow. We recall the system of units used in particle physics and review some important aspects of Special Relativity. Finally we'll discuss what it is that we usually measure in particle physics experiments, namely, cross sections and decay rates.

1.6.1 Units

The system of units used in particle physics is summarised in Table 1.5. Making the indicated replacements amounts to working in units where $\hbar = c = 1$. That is, whenever we write p for momentum, this really stands for the usual momentum (having units GeV/c) times c, so that the units of our 'particle physics' momentum are GeV.

For converting between the two systems, it's sufficient to know c and $\hbar c$:

Table 1.5: Units used in particle physics.

quantity	units	to convert back to normal units
energy E	GeV	–
momentum p	GeV	divide by c
mass m	GeV	divide by c^2
distance x	GeV^{-1}	multiply by $(\hbar c)$
time t	GeV^{-1}	multiply by $\hbar$
area a	GeV^{-2}	multiply by $(\hbar c)^2$

$$\begin{aligned} c &= 2.997 \times 10^8 \text{ m/s} = 2.997 \times 10^{23} \text{ fm/s} \\ \hbar c &= 0.1973 \text{ GeV fm.} \end{aligned}$$

To convert from particle physics units back to normal units, simply insert the factors of c and $\hbar c$ necessary to obtain the desired dimension. For example, cross sections in standard units having dimensions of length squared will have units GeV^{-2} in the particle physics system. To get back to normal units, i.e. fm^2, you have to multiply by $(\hbar c)^2$.

In addition we will usually give the electric charge of a particle as a multiple of the proton's charge e. In particle physics units, e is a dimensionless number with a value of 0.303. It's easier, however, to remember the fine structure constant α, given by

$$\alpha = \frac{e^2}{4\pi} \approx \frac{1}{137} \, . \tag{1.5}$$

1.6.2 Special relativity and invariant mass

For almost all of the particle reactions we will look at, the speeds involved will be significant fractions of the speed of light, and therefore we will need to use Special Relativity. The most important relations we will need are the relativistic equations relating a particle's energy E, momentum vector $\mathbf{p} = (p_x, p_y, p_z)$ and rest mass m (in the following, the term 'mass' will always mean rest mass):

$$E = \gamma m \, , \tag{1.6}$$

$$\mathbf{p} = \boldsymbol{\beta}\gamma m \, , \tag{1.7}$$

$$E^2 = p^2 + m^2 \, . \tag{1.8}$$

Here $\boldsymbol{\beta} = \mathbf{v}/c$ gives the speed of the particle, $\gamma = 1/\sqrt{1-\beta^2}$, and $p = |\mathbf{p}|$ is the magnitude of the momentum vector. Note that in these relations we have set $c = 1$ as discussed in Section 1.6.1. A handy consequence of (1.6) and (1.7) is the relation between the energy, momentum and $\boldsymbol{\beta}$ of a particle: $\boldsymbol{\beta} = \mathbf{p}/E$.

Now consider the case where a particle of mass M, energy E and momentum vector $\mathbf{P}$ decays into n daughter particles with masses m_i, energies E_i and momentum vectors $\mathbf{p}_i$, with $i = 1, \ldots, n$. From the relations above we know that for the original particle,

$$E^2 = P^2 + M^2 \; . \tag{1.9}$$

Furthermore, from conservation of energy and momentum we have

$$E = \sum_{i=1}^{n} E_i \; , \tag{1.10}$$

$$\mathbf{P} = \sum_{i=1}^{n} \mathbf{p}_i \; . \tag{1.11}$$

Substituting these into equation (1.9) and solving for M^2 gives

$$M^2 = \left(\sum_{i=1}^{n} E_i \right)^2 - \left(\sum_{i=1}^{n} \mathbf{p}_i \right)^2 \; . \tag{1.12}$$

Equation (1.12) defines the *invariant mass* (squared) of a system of particles, regardless of whether they originated as the decay products of a single more massive particle.[1] Notice that the second term on the right-hand-side of (1.12) says to construct the vector sum of the momenta and then to square it, i.e. to take the scalar product of it with itself.

Recall that the energy and momentum of a particle together form a *four-vector*, which we can write as

$$p^\mu = (E, \mathbf{p}) \; , \tag{1.13}$$

where $\mathbf{p} = (p_x, p_y, p_z)$ is the usual momentum vector and the index μ takes on the values 0, 1, 2, 3. Recall also that the 'square' of a four-vector means the energy component squared minus the sum of the squares of the momentum components. That is, the invariant mass squared of a particle (or system of particles) is simply the square (in the four-vector sense) of the total four-momentum.

In particle physics there is a widespread but unfortunate notational convention that you must be aware of. If we define p^μ to be a four-vector, then sometimes we write p^2 to mean $E^2 - |\mathbf{p}|^2$, i.e. the four-momentum squared. At other times we might define $\mathbf{p}$ to be a usual three-vector, and we write p^2 to mean $|\mathbf{p}|^2$. So if you see something like p^2 written in an equation, make sure you understand which possibility is meant.

An important property of the invariant mass is that, as the name implies, it is a Lorentz invariant. That is, if we were to observe the system of particles in a different reference frame moving at a speed β releative to the original one, then the energies and momenta would be

[1] We often speak of invariant mass but then write down the equation for the mass squared, since it's a bit easier to work with. You must determine from context which is actually meant.

different, but the invariant mass would be the same. We can see this by using a Lorentz transformation to obtain the energy E and momentum $\mathbf{P}$ in the boosted reference frame,

$$\begin{aligned} E' &= \gamma E - \beta\gamma P_{\parallel} \\ P'_{\parallel} &= -\beta\gamma E + \gamma P_{\parallel} \\ P'_{\perp} &= P_{\perp} \, . \end{aligned} \tag{1.14}$$

Here $P_{\parallel}$ and $P_{\perp}$ are the components of $\mathbf{P}$ parallel and perpendicular to the boost and the quantities in the boosted frame are written with primes. It is easy to show that the invariant mass squared in the boosted frame M'^2 is therefore equal to M^2 i.e., it is the same as in the original reference frame.

Suppose we consider a system of n particles for which the invariant mass squared is given by equation (1.12). If we go to a reference frame in which the total momentum is zero, then taking the square root of both sides of (1.12) gives

$$M = \sum_{i=1}^{n} E_i = E_{\rm cm} \, . \tag{1.15}$$

That is, the invariant mass is the total energy in the rest frame of the system of particles. This is usually called the *centre-of-mass* energy, written as $E_{\rm cm}$.

One use of the invariant mass is that it allows us to tell whether a particular set of particles originated as the decay products of a more massive particle, since then the invariant mass will be equal to the rest mass of the original particle. Suppose we consider a high energy reaction such as proton-proton collisions. These collisions lead to events with large numbers of particles being produced. The Higgs particle could also be produced, and if this happens, then it should decay a small fraction of the time into two photons. In a high energy collision, however, many other photons could be produced in addition to those from the Higgs. This is illustrated schematically in Fig. 1.1. In principle we can measure the energy and direction of all of the photons in such an event.

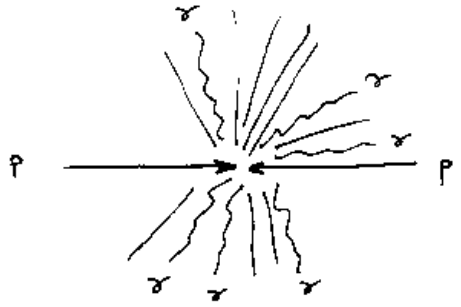

Figure 1.1: Proton-proton collisions at high energy result in the production of many particles.

How do we know if any of the pairs of photons came from a Higgs particle? We simply compute the invariant mass squared for *all pairs* of photons in the event. Using equation (1.12) for two photons i and j gives

$$\begin{aligned} m_{ij}^2 &= (E_i + E_j)^2 - (\mathbf{p}_i + \mathbf{p}_j)^2 \\ &= E_i^2 + 2E_iE_j + E_j^2 - (p_i^2 + 2\mathbf{p}_i \cdot \mathbf{p}_j + p_j^2) \\ &= 2E_iE_j(1 - \cos\theta_{ij}) \ , \end{aligned} \tag{1.16}$$

where we used the fact that for photons $E = p$ (i.e. they have zero rest mass). By computing this for all possible pairings of the photons and entering them into a histogram, we might get after including many events something like Fig. 1.2. The clustering of entries around a single invariant mass corresponds to those photon pairs which did in fact come from Higgs decays. The rest of the entries are from pairs of photons that did not originate from the same particle, and hence their invariant mass is simply some random value. The plot is from a simulation of Higgs boson production in proton-proton collisions with a hypothetical Higgs mass of 130 GeV, and the peak around 130 GeV is clearly visible.

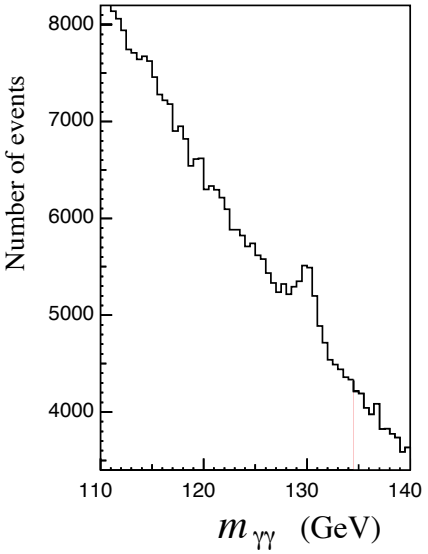

Figure 1.2: A histogram of the invariant mass of pairs of photons showing evidence for a particle with a mass of 130 GeV (from [6]).

So the invariant mass allows us to infer the existence of a new particle without seeing it directly. For this reason, invariant mass has played a role in many important particle discoveries, and we will use it repeatedly in these lectures.

1.6.3 Observables

There are basically two types of quantities that get measured in particle physics experiments: cross sections and decay rates (or functions thereof). These quantities are the interface between experiment and theory. Basically they represent probabilities for a specified reaction to occur, and hence they can be predicted by a quantum mechanical theory like the Standard Model. One measures these probabilities by in effect giving the reaction the opportunity to take place many times and determining the fraction of times it actually does. In this section we describe two important types of reactions: particle scattering and particle decays.

Cross sections

An important type of particle physics experiment is called *scattering*, where two particles are collided together and one measures what comes out. In *elastic* scattering, the outgoing particles are the same as the incoming, e.g. $e^+e^- \to e^+e^-$. In *inelastic* scattering, new particles are produced, and the incoming ones may be destroyed, e.g. $e^+e^- \to \mu^+\mu^-$. One of the initial state particles may be at rest (a *fixed-target experiment*), or two beams of particles may be collided together.

In any case, we want to measure how often a certain final state is produced, i.e. the number of events. Consider a beam of particles of cross sectional area A, hitting a broad target of thickness d. The beam flux J is the number of particles in the beam per unit area per unit time, so the number of incident particles per unit time is given by JA. The number of events N will be proportional to the number of times we let the particles collide, i.e., it is proportional to the number of incoming particles per unit time, JA, times the number of target particles they can hit. This is proportional to the thickness d times the number of target particles per unit volume n. The product of all of these factors is called the *luminosity* $\mathcal{L}$,

$$\mathcal{L} = JAdn \,, \tag{1.17}$$

which has units of $\mathrm{cm}^{-2}\mathrm{s}^{-1}$. The luminosity can depend on the time t, since, for example, the flux might vary in time. The total number of events produced is thus proportional to the integral of the luminosity over time. The proportionality constant σ is called the *cross section*,

$$N = \sigma \int \mathcal{L}\, dt \,. \tag{1.18}$$

The cross section is a measure of the probability for a given final state to be produced. It depends only on the nature of the particle interaction, and is independent of the details of the experimental set-up, namely, beam flux, target density and target thickness. So theorists can compute cross sections without knowing anything about how intense the beams are in a given accelerator. The experimentalist then combines this with the integrated luminosity to get the prediction for the expected number of events of a certain type.

In normal units the cross section has the dimension of area, which in particle physics units corresponds to GeV^{-2}. Usually one converts the prediction back to normal units before comparing with experiment. The unit of area used for cross sections is the *barn*, defined as 10^{-24} cm^2. Most cross sections of interest are significantly smaller than 1 barn, and one often sees, for example, nanobarns (1 nb = 10^{-33} cm^2), picobarns (1 pb = 10^{-36} cm^2) and femtobarns (1 fb = 10^{-39} cm^2).

The formula for the luminosity is a bit more complicated when the target is itself another beam of particles, e.g. in an e^+e^- collider. In any case, equation (1.18) always gives the relation between the number of events, integrated luminosity and cross section.

For example, at the PEP-II e^+e^-storage ring at the Stanford Linear Accelerator Center (SLAC) in California, the average luminosity is around $\mathcal{L} = 3 \times 10^{33}$ cm^{-2} s^{-1}. One year's nominal running gives around 10^7 s of useful time, i.e., given the practical constraints of running an accelerator and particle detector, one can take data a third of the time. The cross section for

the reaction $e^+e^- \to B^0\overline{B}^0$ is about 0.6 nb (the B^0 is a meson consisting of $d\bar{b}$), so in one year, the number of events of this type will be

$$\begin{aligned} N(e^+e^- \to B^0\overline{B}^0) &= \sigma\mathcal{L}t \\ &= 0.6 \text{ nb } \times 3 \times 10^{33} \text{ cm}^{-2} \text{ s}^{-1} \times 10^7 \text{ s } \times \frac{10^{-33} \text{ cm}^2}{1 \text{ nb}} \\ &\approx 2 \times 10^7 \text{ events} . \end{aligned} \tag{1.19}$$

Decay rates and lifetimes

Often the particles produced in high energy reactions are unstable. One of the quantities that we can both predict and measure is the mean lifetime, i.e., the average proper decay time. Remember that if the particle is moving, then because of time dilation its proper decay time is given by the observed decay time divided by γ.

One of the more general predictions of quantum mechanics is that the proper decay times of unstable particles will follow an exponential probability distribution. That is, the probability of observing a proper decay time t in the interval $[t, t + dt]$ is

$$p(t)\, dt = \frac{1}{\tau}\, e^{-t/\tau}\, dt . \tag{1.20}$$

The constant of proportionality $1/\tau$ comes from the requirement that the integral of $p(t)$ from 0 to ∞ be equal to unity. The parameter τ is in fact the mean lifetime, as can be seen by computing the expectation value of t:

$$\begin{aligned} \langle t \rangle &= \int_0^\infty t\, p(t)\, dt \\ &= \int_0^\infty t\, \frac{1}{\tau} e^{-t/\tau}\, dt \\ &= \tau . \end{aligned} \tag{1.21}$$

As an example, muons can be trapped in a detector and the time that it takes for them to decay can be measured. The time for each decay can be entered into a histogram as shown in Fig. 1.3. The curve shown along with the histogram has the exponential form of equation (1.20). The value of the mean lifetime τ has been adjusted (or 'fitted') to give the best agreement between the curve and the histogram, resulting in $\tau = 2.2$ μs.

The total decay rate Γ is defined by

$$\Gamma = \frac{1}{\tau} , \tag{1.22}$$

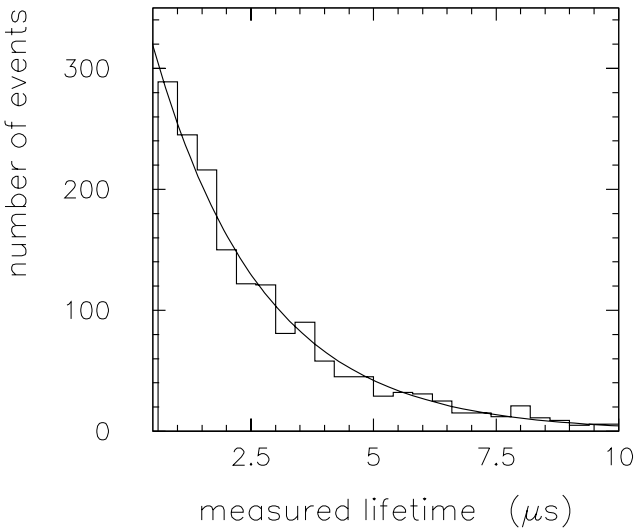

Figure 1.3: A histogram of decay times for muons.

and it therefore carries the same information as the mean lifetime. If a particle X can decay into a number of different states i, then the partial decay rate Γ_i is defined as the total decay rate times the probability for the decay to result in i, which is also called the *branching ratio* $\mathcal{B}$ for the state i,

$$\Gamma_i = \Gamma \times \mathcal{B}(X \to i) \; . \tag{1.23}$$

The branching ratio is often expressed as a percent, and the sum of all of the branching ratios for a particle must be unity. Equivalently, the sum of the partial decay rates is equal to the total decay rate,

$$\sum_i \Gamma_i = \Gamma \; . \tag{1.24}$$

For the K^0_S meson, for example, the main decay modes and branching ratios are shown in Table 1.6 [7].

For some types of particles, the decay time is too short to be experimentally resolved. We can still measure the mean lifetime, however, by exploiting the uncertainty relation between mass (i.e. energy) and time,

$$\Delta m \, \tau \sim 1 \; . \tag{1.25}$$

Table 1.6: Principal decay modes and branching ratios of the K^0_S meson.

mode	branching ratio
$\pi^+\pi^-$	68.43%
$\pi^0\pi^0$	31.39%
$\pi^+\pi^-\gamma$	0.0018

(Recall we are working in units where $\hbar = 1$.) If a type of particle decays with a mean lifetime τ, then its mass must be uncertain by an amount on the order of $1/\tau$. Therefore if we look at the invariant mass distribution of the decay products of the particle, the peak will have a certain width. Some of this will stem from imperfect measurement resolution (this is in fact the case in Fig. 1.2), but for sufficiently small lifetimes the so-called *natural width* will dominate. Thus by measuring the width of a peak in an invariant mass distributions one can indirectly determine the mean lifetime of a particle.

Chapter 2

Theoretical framework

In this chapter we give an overview of the theoretical framework of the Standard Model. You may ask why we don't simply state the assumptions of the model, calculate what these predict for the outcomes of various possible experiments, and show how well these agree with observations. The problem is that the Standard Model involves a complicated mathematical apparatus that cannot be digested so quickly. Just understanding how the theory is defined in a rigorous way goes beyond the scope of this course. Deriving the predictions for experiment is in some ways even more difficult. Nevertheless, in this chapter we'll try to sketch the outlines of the theory and give some flavour of how predictions for cross sections and decay rates are extracted.

2.1 Quantum field theory

In high energy particle interactions, particles are observed to be created and destroyed. For example, an electron and positron can collide and produce a pair of muons: $e^+e^- \to \mu^+\mu^-$. So the theory we develop must allow for creation and destruction of particles. In addition, it should be consistent with the laws of quantum mechanics and relativity. *Relativistic quantum field theory* is a mathematical framework that satisfies these requirements.

The Standard Model of particle physics is an example of such a quantum field theory. It contains the basic idea of quantum mechanics, which is that for every reaction such as a scattering or a decay, there exists a complex number called the *amplitude* $\mathcal{M}$. If the reaction can occur by means of more than one path or intermediate state, then the total amplitude is a sum of terms corresponding to each path (recall this is how we get quantum mechanical interference). The probability for the reaction to occur is proportional to the absolute square of the total amplitude $|\mathcal{M}|^2$. These probabilities are expressed as scattering cross sections, denoted by σ, or as decay rates, Γ.

The Standard Model is defined by specifying what fermions (quarks and leptons) we want to have in the theory and by writing down a mathematical function called the *Lagrangian density*, analogous to the Lagrangian of classical mechanics. As in classical mechanics, one requires a principle of least action, whereby the integral of the Lagrangian density over space and time is a minimum. This determines how the particles, or rather, their wave functions, evolve in time. It turns out that by requiring a certain mathematical symmetry of the Lagrangian called gauge symmetry (invariance of the Lagrangian under a specific group of transformations) one fixes

what gauge bosons must exist, namely, the photon, $W^{\pm}$, Z, and gluon. This in turn determines how the particles interact.

A large part of a more advanced course on particle physics would involve developing the formalism of quantum field theory and showing how to calculate the amplitudes for various processes, which in turn would allow us to compute cross sections and decay rates. Calculating the amplitudes is greatly simplified by using Feynman diagrams to represent the reaction. There exists a set of 'Feynman rules', which tell how to write down the amplitudes directly from the diagrams. The total amplitude for a reaction is obtained by summing all of the diagrams with the same initial and final states. Deriving the Feynman rules for a theory such as the Standard Model is beyond the scope of this course. We can, however, state a subset of the rules which will tell us some information about the amplitudes.

2.2 Feynman diagrams

Feynman diagrams are space-time diagrams in which the type of line indicates the type of particle, as shown in Fig. 2.1. In addition, arrows are usually drawn on fermion lines going forward in time for particles, and backwards in time for antiparticles. This won't be important in this course and we'll usually drop the arrows.

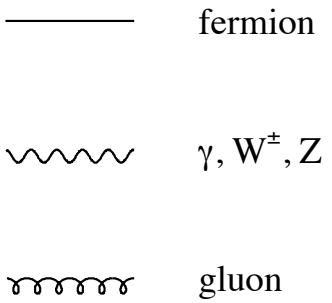

Figure 2.1: Lines used in Feynman diagrams to indicate different kinds of particles.

The lines for the different particles can be joined together to represent whatever reaction we would like to describe, e.g. Compton scattering, $e^-\gamma \to e^-\gamma$, shown in Fig. 2.2. The diagrams are usually drawn such that the vertical direction corresponds to particles' separation, and the horizontal direction denotes the flow of time. (The opposite convention is sometimes found as well.) In Fig. 2.2, for example, the electron absorbs the photon and then emits it.

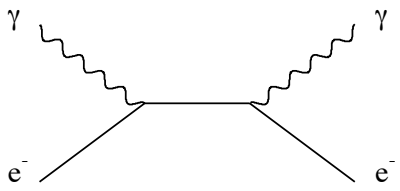

Figure 2.2: A Feynman diagram for the reaction $e^-\gamma \to e^-\gamma$ (Compton scattering).

The places where lines come together in the diagrams are called *vertices*. Only specific vertices are allowed in a given theory. Quantum numbers such as charge, baryon number and lepton number are conserved at every vertex. For example, in the first vertex of Fig. 2.2, an electron and a photon come in (total charge -1, lepton number 1, baryon number 0) and an electron goes out (also charge -1, lepton number 1, baryon number 0).

2.3 Electromagnetic interactions, coupling strength

The part of the Standard Model describing electromagnetic processes is called *quantum electrodynamics* or QED. Electromagnetic interactions always involve a vertex where a charged particle interacts with a photon. One of the general Feynman rules is that every vertex in a diagram is associated with a 'coupling' or charge, which characterizes the strength of the interaction. The amplitude contains a factor of the coupling for each vertex. For fermion–photon vertices, the coupling is simply the magnitude of the fermion's electric charge, i.e. e for the charged leptons, and $2e/3$ or $e/3$ for up- and down-type quarks. Recall that in particle physics units, $e = 0.303$, or equivalently, the fine structure constant is $\alpha = e^2/4\pi = 1/137$. The basic fermion–photon vertex is shown in Fig. 2.3. Note that since the neutrino is neutral the coupling strength is zero, and hence we would never even write down a Feynman diagram containing a neutrino–photon vertex. Note also that the charged fermions involved in the coupling are of the same family (no electron–muon–photon or up–charm–photon vertices allowed).

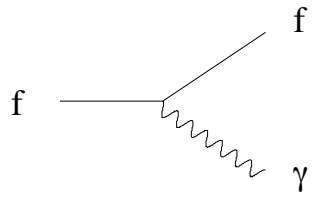

Figure 2.3: The basic coupling between a charged fermion f and a photon γ. The coupling strength is given by the charge of the fermion, i.e., e for electrons, $2e/3$ for up-type quarks, $e/3$ for down-type quarks.

One of the rules for manipulating Feynman diagrams is that you can move any of the external lines between initial and final states by replacing particle with antiparticle and vice versa. So the vertex for $f \to f\gamma$ can be twisted around to represent $\gamma \to f\overline{f}$, $f\gamma \to f$, etc., where $\overline{f}$ denotes the antiparticle partner of the fermion f. For all cases, the coupling would be given by the electric charge of f.

There are two electron–photon vertices in Fig. 2.2, so the corresponding amplitude is proportional to e^2. To get the cross section σ, we square the amplitude:

$$\mathcal{M} \propto e^2 , \tag{2.1}$$

$$\sigma \propto |\mathcal{M}|^2 \propto e^4 \propto \alpha^2 . \tag{2.2}$$

2.4 Weak interactions

Weak interactions involve exchange of $W^{\pm}$ or Z bosons. Some representative vertices with fermions coupling to $W^{\pm}$ and Z bosons are shown in Fig. 2.4. Note that for the W couplings, the two fermions are different, e.g., the charged electron is transformed into a neutrino by emission of a W^-, and the charge 2/3 up-quark is transformed into a charge $-1/3$ down quark. Similar diagrams can be drawn using quarks and leptons from the 2nd and 3rd families. Note that charge, baryon number and lepton number are conserved at every vertex.

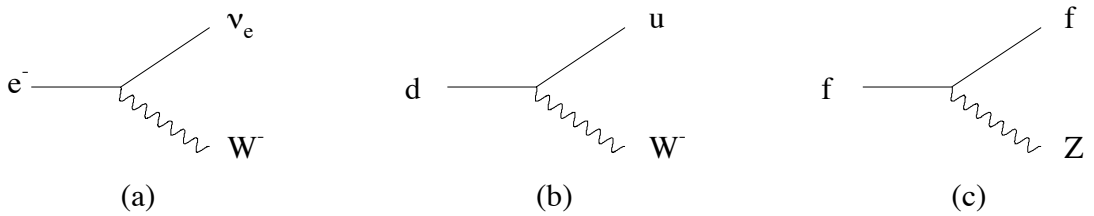

Figure 2.4: The basic coupling between a charged fermion f and a photon γ. Possible couplings between W bosons and (a) leptons and (b) quarks. (c) The coupling between a fermion f and a Z, where f represents any of the fermion types.

For the lepton–W vertices in the Standard Model, the charged lepton and the neutrino must be of the same family. In Fig. 2.4(a), for example, the electron is transformed into a W^- and an electron-type neutrino. If neutrinos have a non-zero mass, then processes are possible where the lepton family changes, and recent observations of neutrino oscillations show that this is, in fact, the case. For most of the reactions we will see in this course, however, the lepton family number is conserved.

For the vertices involving a W and quarks, one of the quarks is always charge 2/3 (up-type) and one is always charge 1/3 (down-type). In principle, such a vertex could contain any up-type quark (u, c or t) paired with any down-type (d, s or b). The coupling strength is greatest, however, when the two quarks are from the same family.

For the fermion–Z vertices, the two fermions are always of the same type. For example, $u \to uZ$ is allowed, but the vertex $u \to cZ$ is not present in the theory, even though it would conserve charge, baryon number and lepton number.

For every W–fermion vertex, the amplitude contains a factor of the weak coupling constant g, whose value is

$$g = 0.65 \; . \tag{2.3}$$

It turns out that the ratio of g to the mass of the W boson can be determined with greater precision than either of the two quantities separately. Therefore we more often use the *Fermi constant*, defined as

$$G_{\rm F} = \frac{\sqrt{2}g^2}{8M_{\rm W}^2} = 1.166 \times 10^{-5} \; {\rm GeV}^{-2} \; , \tag{2.4}$$

to express the coupling (the factors of $\sqrt{2}$ and 8 are present for historical reasons).

The coupling g is the same for lepton–W and quark–W vertices. For the quark–W vertices, however, the amplitude has an additional factor called the *CKM matrix element*. It is approximately equal to one when the two quarks are in the same family, e.g. for $d \to u\mathrm{W}^-$, and it is significantly smaller if they are not in the same family, e.g. $s \to u\mathrm{W}^-$. We will return to this point in Chapter 8.

The Z couples to all of the fermion types, as indicated in Fig. 2.4(c). The Z–fermion couplings are a bit more complicated and we won't give them here explicitly. They are functions of e and g which depend on the fermion type and on the spin state of the fermions. Simply keep in mind that the couplings are predicted by the Standard Model and that they are of the same order of magnitude as e or g. Note that in contrast to the photon, the Z does couple to neutrinos.

2.5 Strong interactions, hadrons

The part of the Standard Model responsible for the strong interaction is called *Quantum Chromodynamics* (QCD), which describes the interactions of quarks and gluons. Quarks and gluons possess an additional type of charge known as colour. Quarks come in one of three colours, and a gluon is characterized by a colour and an anticolour.

The possible quark and gluon interactions are shown in Fig. 2.5. The quark–gluon vertex (a) and triple gluon vertex (b) both have the coupling strength g_s, whereas the four-gluon vertex in (c) has a coupling of g_s^2. The quark–gluon coupling is independent of the flavour of the quark. As far as the strong interaction is concerned, u, d, s, c, b and t behave in the same way; the only differences in strong interaction processes arise from the differences in their masses. When discussing QCD processes, we often use q to denote a quark of any flavour.

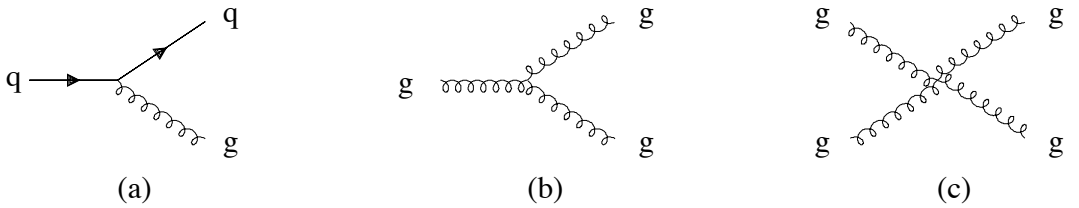

Figure 2.5: Possible couplings between quarks and gluons.

In the strong, electromagnetic and weak interactions, the coupling strengths all turn out to depend on the energy scale of the reaction. The presence of the triple-gluon vertex in QCD has profound implications for low-energy processes, since it causes g_s to become very large, hence the term 'strong interaction'. For high energy reactions, however, g_s is smaller, and at an energy scale close to the mass of the Z (91.2 GeV), we have

$$g_\mathrm{s} \approx 1.2, \tag{2.5}$$

i.e. not too much larger than e or g. In analogy with the fine structure constant α, one often uses the strong coupling constant α_s, defined as

$$\alpha_{\rm s} = \frac{g_{\rm s}^2}{4\pi} \approx 0.12 \; . \tag{2.6}$$

One of the consequences of the particular energy dependence of $g_{\rm s}$ is that free quarks or gluons are never observed. Rather, we only see the bound states $q\overline{q}$ (mesons) or qqq (baryons). In principle, it should be possible to form other combinations such as gg, but the evidence for these is far less direct. All of these bound states are 'colour neutral'. Sometimes we will draw Feynman diagrams showing the partons (quarks and gluons) inside hadrons (mesons or baryons). For example, we will draw a proton, which consists of uud, by three lines running parallel to each other as in Fig. 2.6(a).

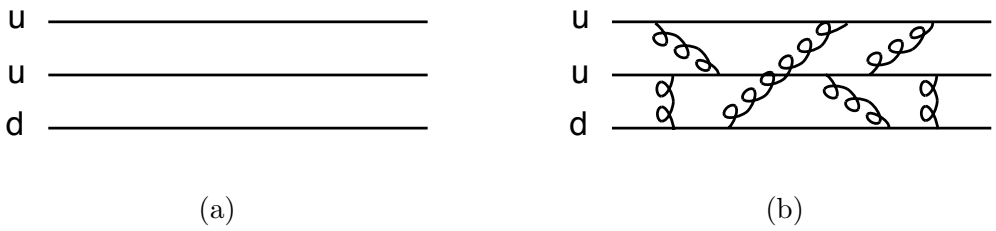

Figure 2.6: Representations of a proton in Feynman diagrams: (a) an ideal proton consisting of uud, (b) the quarks along with exchanged gluons.

It should be understood that this is a very idealized view of the proton, since the quarks are not free particles but rather are constantly exchanging gluons, as in Fig. 2.6(b). For many purposes, however, one can ignore the effects of gluon exchange and we will often represent hadrons with only the quark or antiquark lines.

2.6 Triple gauge boson couplings

In Fig. 2.5(b) we saw that QCD predicts a triple gluon vertex. The analogous vertex $\gamma\gamma\gamma$ is absent in QED; photons do not couple to themselves. In the electroweak part of the Standard Model, however, there exist 'triple gauge boson couplings' in which the photon, $\mathrm{W}^{\pm}$ and Z interact. These are shown in Fig. 2.7. The coupling strength for $\gamma\mathrm{W}^+\mathrm{W}^-$ is simply the charge of the W, namely, e. The coupling for $\mathrm{ZW}^+\mathrm{W}^-$ is $\sqrt{g^2 - e^2}$. Note that the Standard Model does not contain a ZZZ or a γZZ vertex.

Figure 2.7: Electroweak triple gauge boson couplings: (a) $\gamma\mathrm{W}^+\mathrm{W}^-$, (b) $\mathrm{ZW}^+\mathrm{W}^-$.

As in the case of the four-gluon vertex in QCD, there also exist vertices where four gauge bosons come together such as $\gamma\gamma W^+W^-$ and ZZW^+W^-. The coupling strengths for these are proportional to e^2. These vertices do not play an important role in the processes that we will encounter in this course and we will not deal with them further.

2.7 Virtual particles, propagators

Each particle represented in a Feynman diagram is characterized by a certain energy and momentum. This holds not only for the 'external lines', i.e. those representing initial and final state particles, but also for the internal lines. The rule is that four-momentum is conserved at every vertex. That is, the four-momentum q^μ of the intermediate state electron in Fig. 2.2 is given by

$$\begin{aligned} q^\mu &= p_e^\mu + p_\gamma^\mu \\ &= (E_e + E_\gamma, \mathbf{p}_e + \mathbf{p}_\gamma) \, . \end{aligned} \tag{2.7}$$

Remember that (2.7) is really four equations that represent energy and three components of momentum.

Recall earlier we said that the four-momentum squared of a particle is equal to its mass squared. This holds for initial or final state particles, but for internal lines in Feynman diagrams the situation is more complicated. If we consider the four-momentum squared of the intermediate electron, we obtain

$$\begin{aligned} q^2 &= (E_e + E_\gamma)^2 - (\mathbf{p}_e + \mathbf{p}_\gamma)^2 \\ &= E_e^2 - p_e^2 + E_\gamma^2 - p_\gamma^2 + 2(E_e E_\gamma - \mathbf{p}_e \cdot \mathbf{p}_\gamma) \\ &= m_e^2 + m_\gamma^2 + 2(E_e E_\gamma - p_e E_\gamma \cos\theta) \\ &= m_e^2 + 2E_\gamma \left(\sqrt{p_e^2 + m_e^2} - p_e \cos\theta \right) \, , \end{aligned} \tag{2.8}$$

where $p = |\mathbf{p}|$, θ is the angle between $\mathbf{p}_e$ and $\mathbf{p}_\gamma$, and we used the fact that $m_\gamma = 0$. So for the intermediate electron here, q^2 is different from m_e^2. Such a particle is said to be *virtual* or *off-shell* and the four-momentum squared is also called the *virtual mass* squared. The 'shell' refers to the idea that $E^2 = p^2 + m^2$ can be viewed as the equation of a circle. If the equation holds, the particle is said to be *real* or *on-shell*. The on-shell condition holds in for initial and final state particles, but not in general for particles in intermediate states.

To summarize, the *virtual* mass squared of a particle, often denoted by q^2, is

$$q^2 = E^2 - |\mathbf{p}|^2 \, , \tag{2.9}$$

where E and $\mathbf{p}$ are defined even for intermediate lines in Feynman diagrams by conserving energy and momentum at every vertex. The *real* mass squared of a particle is given by the same

formula (2.9) when applied to a free particle, e.g., one in an initial or final state of a scattering reaction.

We can state another Feynman rule for diagrams in which a particle appears in an intermediate state, i.e., as an internal line in a diagram. The rule is that for every internal line, the amplitude contains a factor called the *propagator*,

$$\frac{1}{q^2 - M^2} \ , \tag{2.10}$$

where M^2 is the particle's (real) rest mass squared and q^2 is its four-momentum squared, i.e., its virtual mass squared. For the case of the intermediate electron in Fig. 2.2, for example, we have $M = m_{\rm e} = 0.511$ MeV and q^2 is given by equation (2.8).

In some cases, the virtual mass squared q^2 will be much less than the real (on-shell) mass squared of the exchanged particle, and the propagator can be approximated by $-1/M^2$. We will also see cases where q^2 and M^2 are of comparable magnitudes, i.e., the intermediate state particle is almost on-shell. This leads to a large enhancement in the amplitude called a *resonance*.

If the intermediate state particle has spin 0, then the factor $1/(q^2 - M^2)$ contains in fact the entire dependence of the amplitude on M and the four-momentum q^μ. For particles of higher spin, however, the propagator is multiplied by other quantities that depend on M and q^μ, but these are always such that the same qualitative picture holds, i.e., the amplitude is large for q^2 close to M^2.

Roughly speaking, intermediate state particles are allowed to be off-shell for short times because of the uncertainty principle. Note that this does not mean, however, that energy and momentum aren't conserved at each vertex; for Feynman diagrams they are. But it means that for an intermediate state particle with four-momentum $q^\mu = (E, \mathbf{p})$, the virtual mass squared $q^2 = E^2 - p^2$ is unequal to the real mass squared M^2. It is in this sense that the classical relations between energy and momentum are temporarily violated. The denominator $q^2 - M^2$ in the propagator is a measure of how far off-shell the intermediate state particle is, suppressing the amplitude for increasing difference between real and virtual mass.

2.8 Space and time location of vertices

Before we go any further with Feynman diagrams we need to clarify two points concerning the location of vertices in space and time. Both of these issues are illustrated in the diagram for the reaction $\mathrm{e^+e^-} \to \gamma\gamma$, shown in Fig. 2.8.

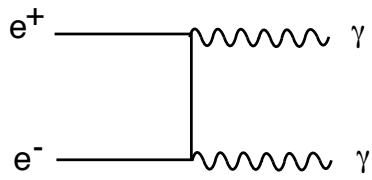

Figure 2.8: Feynman diagram for the reaction $\mathrm{e^+e^-} \to \gamma\gamma$.

The first point is that the lines representing the incoming and outgoing particles have been drawn parallel. Earlier, however, we said that the vertical axis in the diagram represents the

spatial separation, so strictly speaking we should have the two vertices closer together than the particles in the initial and final states. They are often drawn parallel simply because this is easier. One must know from context whether the incoming particles are supposed to be colliding together and the outgoing ones moving apart, as here, or whether the particles are part of a bound state, as for the three quarks in the proton of Fig. 2.6(a).

The second point concerns the time ordering of the two vertices and the nature of the intermediate particle in the diagram. In fact, the amplitude that one writes down according to the Feynman rules for Fig. 2.8 includes both time orderings shown in Fig. 2.9. In Fig. 2.9(a) the positron first emits a photon and at a later time it annihilates with the electron into the second photon. In Fig. 2.9(b), the electron first emits a photon and then annihilates with the positron.

Figure 2.9: Different time orderings of the vertices in $e^+e^- \to \gamma\gamma$.

So the intermediate particle in Fig. 2.8 represents both an e^+ and an e^-. We will therefore sometimes label it without the charge indicated. In other cases it can be useful to draw explicitly a particular time ordering of the vertices and to give the charge of the intermediate particle, but it should be understood that the amplitude that one writes down includes both time orderings.

The two issues about the space and time location of the vertices are in fact closely related. If we associate a space–time location to each vertex in Fig. 2.8, say, $(t_1, \mathbf{x}_1)$ and $(t_2, \mathbf{x}_2)$, then according to the rules of quantum mechanics, we must add together all amplitudes corresponding to the possible paths for the interaction. That is, we need to integrate over all possible values of $(t_1, \mathbf{x}_1)$ and $(t_2, \mathbf{x}_2)$. So in principle, the interaction takes place everywhere and it extends over an infinite period of time. This is consistent with the uncertainty principle where we are working with states of well-defined energy and momentum. In practice, of course, the interaction takes place in a space–time volume which is small by macroscopic standards but large compared to the wavelengths of the particles involved.

2.9 Perturbation theory

According to the rules of quantum mechanics, if a reaction can proceed by more than one path or intermediate state, then we must sum the amplitudes for each path to obtain the total amplitude. So, for example, to obtain the total amplitude for $e^+e^- \to \mu^+\mu^-$, we should sum the amplitudes corresponding to all possible graphs with this initial and final state, some of which are shown in Fig. 2.10.

In Fig. 2.10(b), for example, the virtual photon dissociates into an e^+e^- pair, which then recombines back into a photon. In Fig.2.10(c), the final state μ^+ emits a photon and then reabsorbs it at a later time. In Fig.2.10(d), two photons are exchanged. More loops and boxes

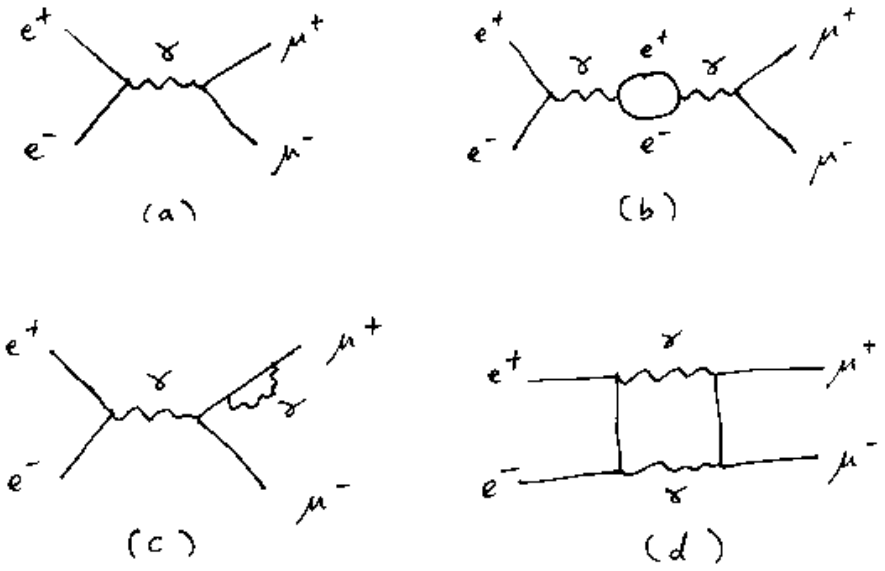

Figure 2.10: Some Feynman diagrams contributing to the reaction $e^+e^- \to \mu^+\mu^-$.

of these types are possible, and in principle we should sum the amplitudes for all of them, i.e. an infinite number of graphs.

In practice, matters are made simpler by the fact that the more complicated graphs all contain more vertices, and therefore more factors of the coupling, in this case e, or equivalently, $\alpha = e^2/4\pi$. In the graphs in Fig. 2.10, the amplitude (a) is proportional to α, and (b)–(d) are proportional to α^2. We could write down further graphs all proportional to some power of α.

So when we square the total amplitude to obtain the cross section, it will contain a term corresponding to the first graph squared, proportional to α^2, and there will also be terms corresponding to the product of graph (a) with (b)–(d) proportional to α^3. The terms from (b)–(d) squared are proportional to α^4, and so on. In general, the prediction for the cross section can be written as a power series in α,

$$\sigma = \sum_{n=0}^{\infty} C_n \alpha^n \ . \tag{2.11}$$

In the case of $e^+e^- \to \mu^+\mu^-$, the first nonzero term in the series has $n = 2$, i.e., something proportional to α^2 (the so-called *leading order*). The expansion coefficients C_n can be calculated by using the full set of Feynman rules to write down the amplitude $\mathcal{M}$, taking its absolute square, and then identifying the coefficients of the various powers of the expansion parameter α.

The important thing to note is that here the expansion parameter $\alpha = 1/137$ is a small number, so in this case the series converges rapidly. Even if we only include the first graph, the approximation is quite good, since the next-order corrections to this are suppressed by an additional factor of 1/137. Equation (2.11) is an example of a *perturbation series* and the mathematical technique used to compute cross sections in this way is called perturbation theory.

The graphs with more vertices and therefore more powers of α are regarded as higher order corrections.

The same mathematical technique can be used to obtain predictions for processes involving the weak and strong interactions. For the strong interactions at an energy scale around M_{Z}, however, recall that $\alpha_{\mathrm{s}} \approx 0.12$ is significantly larger than α, so that the higher order corrections tend to be more important. For strong interactions at even lower energies, α_{s} is so large that the series blows up and perturbation theory does not provide reliable predictions. Low-energy processes such as the binding of quarks into colour neutral hadrons are said to be *non-perturbative*. Here, tools other than perturbation theory must be applied which severely limits our ability to test QCD at low energies.

2.10 Examples of Feynman diagrams

We have now seen essentially all of the building blocks needed to construct Feynman diagrams for any Standard Model process, except for those involving the Higgs boson, which we will deal with later. Some diagrams for a number of reactions are shown in Fig. 2.11. You should easily be able to write down how the amplitudes and cross sections depend on the couplings e, g and g_{s}, or equivalently on α, G_{F} and α_{s}. For diagrams containing intermediate particles, you should be able to write down the corresponding propagators. Note that there are two amplitudes both at order e^2 for the reaction $\mathrm{e^+e^-} \to \mathrm{e^+e^-}$ shown in Fig. 2.11(e) and (f). The total amplitude to order e^2 requires both terms. Similarly, there are two amplitudes both to order g_{s}^2 for the reaction $q\overline{q} \to gg$ shown in Fig. 2.11(g) and (h), where q stands for a quark of any flavour.

Table 2.1 contains a recipe for building the Feynman diagrams associated with a given reaction.

Table 2.1: Recipe for building Feynman diagrams associated with a reaction.

1. Find out which interaction(s) is/are involved (e.g., neutrinos: weak, gluons: strong, photons: EM or weak).
2. For that interaction, remember the mediating particle and build allowed vertices such that the incoming and outgoing legs correspond to the initial and final particles in the reaction (remember that some diagrams are vertical).
3. Check that each vertex conserves electric charge.
4. Check that you don't include vertices forbidden in the SM (γZZ, ZZZ, $\gamma\gamma\gamma$, flavour-changing neutral currents, e.g., Zuc).
5. For strong interaction diagrams, it may help to check colour conservation at each vertex (see Chap. 10).

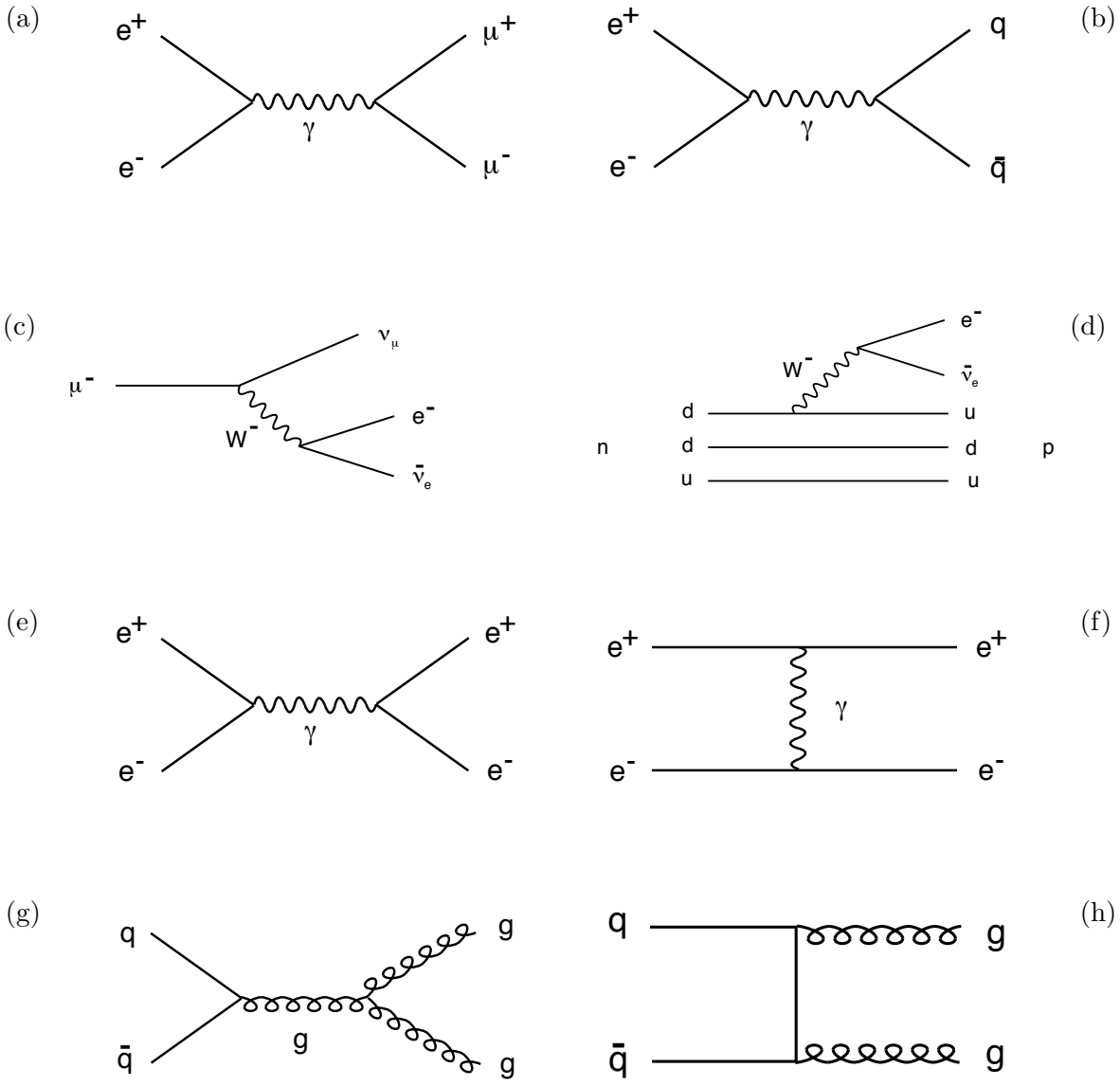

Figure 2.11: Some lowest order Feynman diagrams for several reactions: (a) $e^+e^- \to \mu^+\mu^-$, (b) $e^+e^- \to q\overline{q}$, (c) $\mu^- \to e^-\nu_\mu\overline{\nu}_e$, (d) $n \to pe^-\overline{\nu}_e$ (beta decay), (e,f) $e^+e^- \to e^+e^-$ (Bhabha scattering), (g,h) $q\overline{q} \to gg$.

Chapter 3

Particle accelerators

A large part of our knowledge about elementary particles comes from studying reactions where high energy particles collide into each other. In the early days of particle physics this was done with high energy cosmic rays, which are constantly bombarding the earth from outer space. Nature provides this particle source for free, but it is of uncertain composition, the incident energies of the particles can be difficult to determine, and the very high energy particles, which produce the most interesting reactions, are rare. It was therefore an important step forward to be able to produce beams of high energy particles under controlled conditions and to direct them at a target. In this chapter we take a look at the tool that makes this possible: the particle accelerator.

3.1 Why high energies?

There are two main reasons why we need to go to high energies in order to learn about elementary particles. First, high energies are needed to resolve small distances. Recall that the De Broglie wavelength λ of a particle is

$$\lambda \sim \frac{1}{p} \, . \tag{3.1}$$

(Strictly speaking, $\lambda = h/p$, but we in our units $\hbar = 1$ and we won't worry here about factors of 2π.) So if we want to resolve, say, the substructure of a composite particle, we need a high momentum probe. This is in fact how the substructure of the proton was discovered.

Second, we need high energies in order to produce particles that have high masses. For example, if one wants to study the reaction

$$\mathrm{e}^+\mathrm{e}^- \to \mathrm{W}^+\mathrm{W}^- \, .$$

the total centre-of-mass energy needs to satisfy

$$E_{\mathrm{cm}} \geq 2M_{\mathrm{W}} \, . \tag{3.2}$$

As the mass of the $W^{\pm}$ boson is 80.4 GeV, a centre-of-mass energy of at least about 161 GeV was needed, which was achieved at the LEP e^+e^- collider at CERN.

Many extensions to the Standard Model predict new particles which we may not see simply because they are too massive to be produced in today's accelerators. So one way – perhaps the only way – of finding out whether these theories are correct is to collide particles together with higher energies. For this reason, the name 'elementary particle physics' is in most cases synonymous with ' high energy physics' (HEP).

3.2 Accelerator principles

The basic idea behind an accelerator is to allow a charged particle to pass through an electric field or series of electric fields thereby gaining energy. With a potential difference V, a particle with charge q gains an energy

$$\Delta E = qV \ . \tag{3.3}$$

If $q = e$ and V is in volts, then the energy has units of electron-volts (eV). A television, for example, accelerates electrons up to around 30 keV. Using a single accelerating gap allows for energies up to several million eV. At potential differences higher than several million volts, the electrons are pulled directly out of the electrodes and a direct discharge occurs.

Accelerators can also be used to produce beams of high energy neutral particles, but this is always done in an indirect way. First, the accelerator produces a high energy beam of charged particles, and then these are converted in some reaction into neutrals. For example, we could accelerate deuterons, which are a bound state of a neutron and proton, in an electric field. These can then be sent through a thin foil which causes the neutron and proton to dissociate, and the protons can be bent out of the way with a magnetic field. The result is a beam of neutrons. Proton beams can be used to produce charged pions which then decay giving a neutrino beam. Laser light can be back-scattered off high energy electrons to provide a high energy photon beam.

3.3 Linear accelerators

In order to attain energies higher than several MeV, the accelerating structure must be repeated a number of times. This can be done with a linear accelerator or *linac* as illustrated in Fig. 3.1. A number of conducting drift tubes are arranged in a line. An RF voltage source with potential

$$V(t) = V_0 \sin \omega t \tag{3.4}$$

is applied to every other drift tube and the others are fixed at ground potential. At certain times, the voltage $V(t)$ will be such that there is an accelerating field for, say, protons from the source to the first tube. Note that at this point, the electric field in the gap between the first and second tubes is pointing in the opposite direction. The protons are accelerated from the source to the first tube and then coast in the field-free region to the gap between the first and second tubes. The frequency ω of the voltage source and the length must be set such that when

the particles arrive at the second gap, the direction of the field has reversed and the particles are accelerated into the second tube.

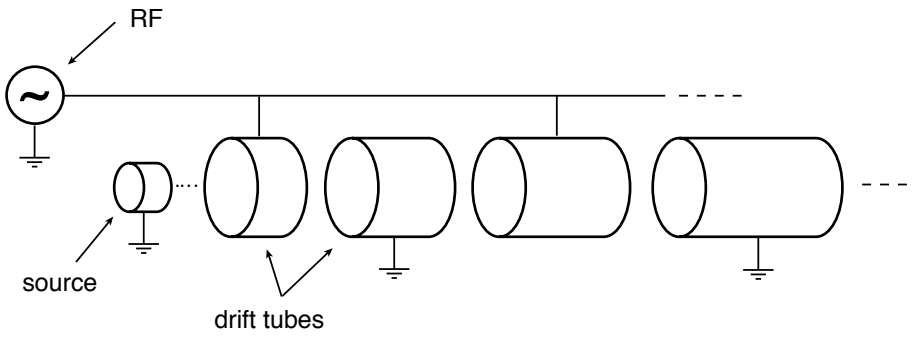

Figure 3.1: Schematic illustration of a linear accelerator.

This continues for a number of stages with the particles gaining energy at each accelerating gap. Notice that in the early stages while the particles have speeds $\beta \ll c$, the non-relativistic relations between energy and speed hold, and thus the particle increases in speed at each gap. Therefore the lengths of the drift tubes must also increase, since the traversal time decreases for increasing speed. One can easily show that the distances must increase as the square root of the energy attained. After the particles become relativistic, however, the speed saturates close to c and the drift tubes have constant length.

Accelerators of this type were developed in the 1920s through 1940s by Wideroe, Alvarez and others. In the 1960s, a 2 mile long electron linac was built at Stanford, shown in Fig. 3.2. Instead of drift tubes it has a radio frequency (RF) structure that provides an electromagnetic wave along which the electrons surf for the entire two miles. The linac forms the main research instrument of the Stanford Linear Accelerator Center (SLAC). It can reach a maximum energy of around 50 GeV and has been involved in 3 Nobel prizes, all of which we will discuss later in the course.

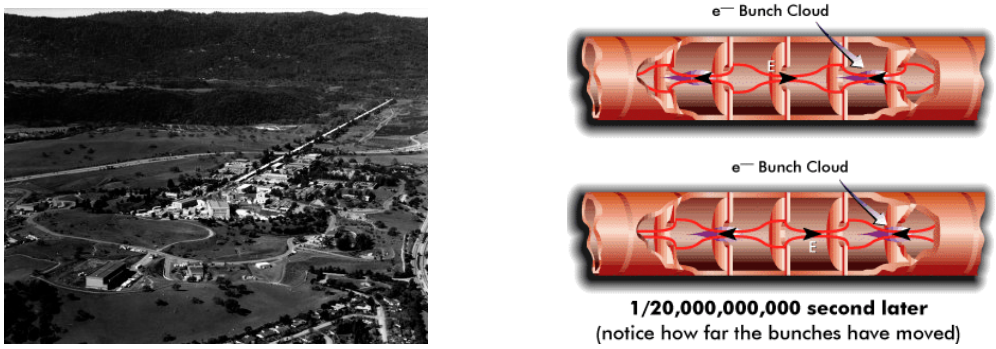

Figure 3.2: The SLAC linac (left) and its RF cavities (right) (from [11]).

The main disadvantage of a linac is that to achieve higher energies, it must be made longer. Roughly speaking, the cost is directly proportional to the energy. At two miles, SLAC is the longest linac ever built. Others currently being planned may have lengths up to 30 km.

3.4 Circular accelerators

At some point, the length and cost of a linear accelerator become limiting factors. Rather than placing the accelerating structures one after the next, however, it is possible by bending the particles in a magnetic field to run them through the same accelerating structure many times. This idea is the basis of the *cyclotron*, invented by E.O. Lawrence in 1930.

The basic set-up of a cyclotron is illustrated in Fig. 3.3. Two hollow, conducting 'D'-shaped structures (called *dees*) are placed next to each other and both are immersed in a magnetic field. Charged particles are first accelerated across the gap at a point near the middle of the dees. They then enter region inside one of the dees where they are bent around by the magnetic field and directed back to the other. In the time that it has taken this to happen, the electric field must have reversed so that the particles are accelerated across the gap in the opposite direction. This continues a number of times with the particles gaining energy each time. As the particles gain energy, the radius of their trajectory in the dees increases. When the particles reach the edge of the dees they are deflected out of the cyclotron and sent to a target.

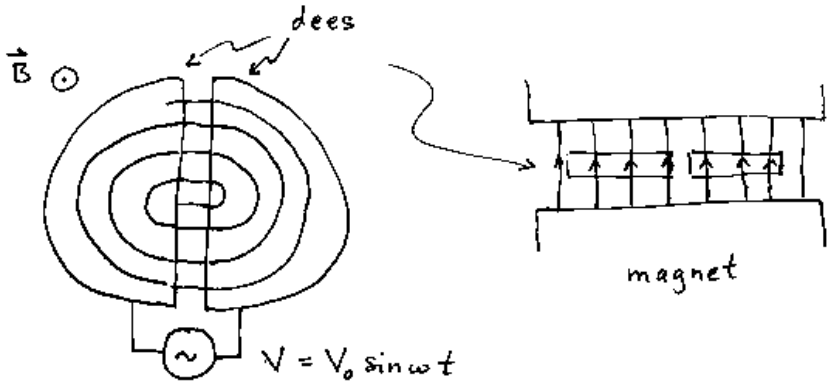

Figure 3.3: Schematic illustration of a cyclotron: (left) top view, (right) side view.

The momentum p of a particle of charge q in a magnetic field B is related to the radius of its orbit by $p = qBr$. The time that it takes to complete a half revolution inside the dee is the distance travelled divided by the speed,

$$T_{1/2 \text{ rev.}} = \frac{\pi r}{\beta c} = \frac{\pi p}{qB\beta c} \,. \tag{3.5}$$

In the non-relativistic limit, momentum can be approximated by $p \approx m\beta c$. If this holds, then the time to complete the half revolution turns out to be independent of β, which means that the voltage applied to the dees can have a fixed frequency. This is called the *cyclotron frequency*, ω, given by

$$\omega = \frac{2\pi}{2 \times T_{1/2 \text{ rev.}}} = \frac{qB}{m} \,. \tag{3.6}$$

When the particles become relativistic, however, we need to use $p = m\beta\gamma c$, which means the half-revolution time is proportional to γ. This means that the frequency of the applied

voltage must be decreased as the particles gain energy. A device with this capability is called a *synchrocyclotron*.

A disadvantage of a cyclotron or synchrocyclotron is that the entire device must be immersed in a magnetic field. One of the largest ever built is the 184-inch synchrocyclotron at Berkeley, which could accelerate protons to a kinetic energy of 350 MeV.

At some point the magnet size becomes the limiting factor in going to higher energies. The way forward is to inject particles pre-accelerated up to some minimum energy into an evacuated beam pipe that follows a circular path with some radius r. Above and below the beam pipe are magnets that provide a vertical magnetic field in the region of the pipe and essentially no field in the interior of the ring. The particles are accelerated in the electric field of RF cavities at one or possibly many locations around the ring. Since the radius r, beam momentum p and magnetic field B are related by $p = qBr$, one has to ramp up B as the energy increases in order to keep the beam on a path of constant r. A device of this type is called a *synchrotron*.

An example of a high-energy proton synchrotron is the Tevatron, at the Fermi National Accelerator Laboratory (Fermilab) near Chicago, shown in Fig. 3.4. The smaller ring in the lower left (the main injector) accelerates protons and antiprotons to energies of 150 GeV. From there they are injected into the main ring with a circumference of 4 miles, where they reach energies close to 1 TeV (10^{12} eV). Beams of particles extracted from the Tevatron can be directed towards the fixed-target area, visible in the upper part of the photo.

Figure 3.4: Aerial view of Fermilab. The larger of the two rings houses the Tevatron (from [12]).

At the Tevatron and other proton synchrotrons, the energy is limited by the magnetic field needed to keep the particles going around in a circular path. To increase the energy one must either increase the field strength or increase the radius of the ring, in accordance with the relation $p = qBr$. In the 27 km circumference Large Hadron Collider, for example, the proton beams will eventually have an energy of 7 TeV (currently they reach 6.5 TeV, giving a centre-of-mass energy of 13 TeV). To achieve this, a large effort was put into developing high field superconducting magnets. Using the relation for particles of unit charge $p[\text{GeV/c}] = 0.3B[\text{Tesla}] \times r[\text{meters}]$, the

average field needed to keep a 7 TeV proton in a 27 km ring is

$$B = \frac{p[\mathrm{GeV/c}]}{0.3r[\mathrm{m}]} = \frac{7000}{0.3 \times (27000/2\pi)} = 5.4\mathrm{Tesla}\ . \tag{3.7}$$

In fact, it isn't possible to cover the entire ring with magnets, and so the actual fields necessary is higher, around 8.4 T. This is almost five times higher than the field obtainable in iron magnets.

At synchrotrons that accelerate electrons or positrons such as the Large Electron Positron (LEP) Collider at CERN, an entirely different problem limits the energy that can be achieved. When the trajectory of a charged particle is bent in a magnetic field, it emits electromagnetic radiation called *synchrotron radiation*. For relativistic particles ($\beta \approx 1$), the radiated power P depends on γ and on the radius of curvature as

$$P \propto \frac{\gamma^4}{r} = \frac{(E/m)^4}{r}\ . \tag{3.8}$$

Thus for a fixed energy E, the radiated power is inversely proportional to the fourth power of the particle's mass. That is, if we consider electron and proton beams of equal energies in synchrotrons of equal size, then the ratio of emitted synchrotron radiation power $P_\mathrm{e}/P_\mathrm{p}$ is

$$\frac{P_\mathrm{e}}{P_\mathrm{p}} = \left(\frac{m_\mathrm{p}}{m_\mathrm{e}}\right)^4 = \left(\frac{0.938\ \mathrm{GeV}}{0.000511\ \mathrm{GeV}}\right)^4 \approx 10^{13}\ . \tag{3.9}$$

So the basic conclusion is that synchrotron radiation is very important for circular $\mathrm{e^+e^-}$ accelerators, and is usually negligible at proton accelerators. The cost of operating LEP with a maximum beam energy 104 GeV, for example, was dominated by the electrical power that had to be put back into the beams because of synchrotron radiation losses (3.6 GeV energy loss per particle per turn). For the LHC with proton beam energies 70 times higher, the energy loss per particle per turn is only 7 keV.

In order to reduce synchrotron radiation losses of an electron synchrotron, one can increase the diameter of the ring. From equation (3.8), however, we see that the radiated power is inversely proportional to only the first power of the radius. So to double the energy for a given amount of radiated synchrotron power, one would have to increase the radius by a factor of $2^4 = 16$. The LEP collider with a circumference of 27 km (Fig. 3.5) is therefore essentially at the practical limit.

The limit of infinitely large radius, however, is of course a linear accelerator. That is, the SLAC linac has essentially no losses from synchrotron radiation; that was in fact the main reason for making it straight. Future linear accelerators are planned that will allow beam energies of perhaps 0.5 TeV or more.

3.5 Fixed target vs. colliding beams

Early accelerator experiments used beams of particles directed at a fixed target. Suppose we have a beam particle of mass m_1 and fire it against a stationary target particle with mass m_2. The centre-of-mass energy is found by computing the invariant mass of the two-particle system.

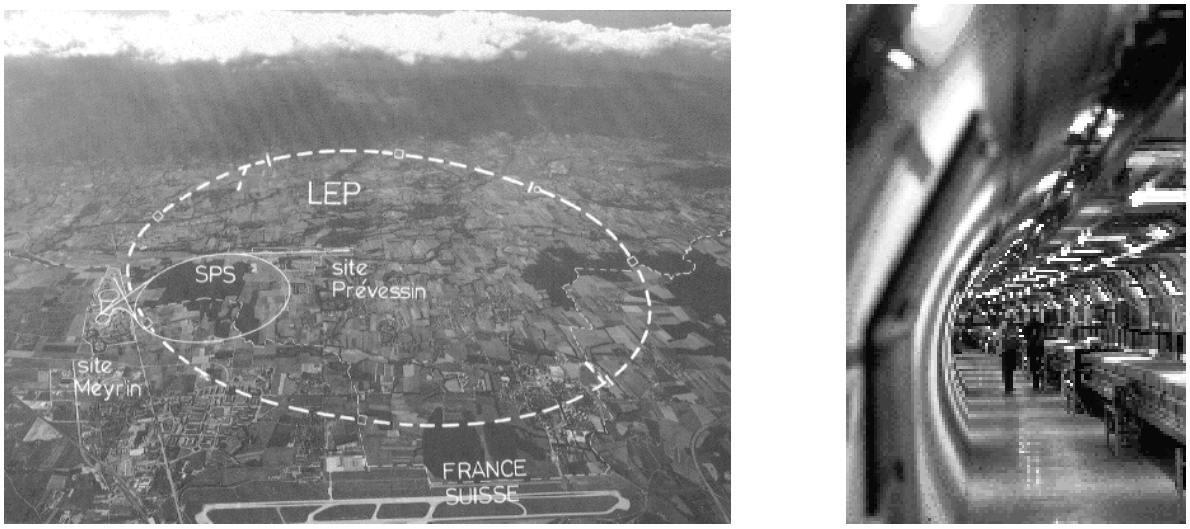

Figure 3.5: The LEP collider at CERN: (left) aerial view; (right) inside the tunnel (from [13]). The LEP tunnel now houses the LHC.

Suppose the beam particle has an energy E_1 and momentum $\mathbf{p}_1$ and the target has an energy m_2 and a momentum of zero. Then the centre-of-mass energy $E_{\rm cm}$ is

$$\begin{aligned} E_{\rm cm} &= \sqrt{(E_1 + m_2)^2 - (\mathbf{p}_1 + 0)^2} \\ &= \sqrt{E_1^2 + 2E_1 m_2 + m_2^2 - p_1^2} \\ &= \sqrt{m_1^2 + m_2^2 + 2E_1 m_2} \\ &\approx \sqrt{2E_1 m_2} \qquad (\text{for } E_1 \gg m_1, m_2)\ . \end{aligned} \tag{3.10}$$

So for sufficiently high energies, the centre-of-mass energy in a fixed-target experiment only grows as the square root of the beam energy. The centre-of-mass energy is what limits our ability to produce new particles and so it is what we want to maximize. The rest of the energy in a fixed-target experiment goes into boosting the entire system of reaction products in the direction of the beam.

If, however, two beams of particles are collided together head on, then the centre-of-mass energy is

$$\begin{aligned} E_{\rm cm} &= \sqrt{(E_1 + E_2)^2 - (\mathbf{p}_1 + \mathbf{p}_2)^2} \\ &= \sqrt{m_1^2 + m_2^2 + 2E_1 E_2 - 2\mathbf{p}_1 \cdot \mathbf{p}_2} \\ &\approx \sqrt{2E_1 E_2 (1 - \cos\theta)} \qquad (\text{for } E_1, E_2 \gg m_1, m_2) \\ &= 2\sqrt{E_1 E_2} \qquad (\text{for } \cos\theta = -1)\ . \end{aligned} \tag{3.11}$$

If, for example, we take $E_1 = E_2 \equiv E_{\rm beam}$, then (3.11) becomes $E_{\rm cm} = 2E_{\rm beam}$. In cases where the two beam energies are unequal, however, one must go back to equation (3.11) to find $E_{\rm cm}$.

In any case, equation (3.11) shows that there is a tremendous increase in the centre-of-mass energy that can be achieved with a collider relative to a fixed-target machine. For the LEP collider with $E_1 = E_2 = 100$ GeV, the centre-of-mass energy is $E_{\rm cm} = 200$ GeV. Just for comparison, suppose one wanted to achieve the same centre-of-mass energy with a an e^+ beam hitting a stationary e^- target. Solving equation (3.10) for E_1 and requiring $E_{\rm cm} = 200$ GeV gives

$$E_1 = \frac{E_{\rm cm}^2}{2m_2} = \frac{(200\ {\rm GeV})^2}{2 \times 0.000511\ {\rm GeV}} = 7.8 \times 10^7\ {\rm GeV}\ . \tag{3.12}$$

Any reasonable calculation based on present-day technology shows that beam energies this high are out of the question. For this reason, most of the high energy accelerator projects currently in operation or proposed for the foreseeable future involve colliding beams.

The technological difficulty that must be overcome with a collider is of course that the two beams of particles must be forced to collide and they must be tightly focussed in order to provide a sufficiently high luminosity. The particles are typically clustered together in bunches with lengths on the order of 1 cm and with transverse dimensions usually measured in microns. For a collider the luminosity $\mathcal{L}$ is given by

$$\mathcal{L} = \frac{f n_1 n_2}{4\pi\sigma_x\sigma_y}\ , \tag{3.13}$$

where f is the collision frequency of the bunches of particles, n_1 and n_2 are the number of particles per bunch in the two beams, and σ_x and σ_y are the horizontal and vertical dimensions of the bunch transverse to its direction of motion.

For the LEP collider, for example, there were 4 bunches of $e^+$and e^- and a circumference of 27 km. This results in a collision frequency of $f = 1/22\,\mu$s. The numbers of particles per bunch are approximately given by $n_1 \approx n_2 \approx 10^{11}$. The transverse dimensions of the bunches were around $\sigma_x \approx 100\,\mu$m (horizontal) and $\sigma_y \approx 10\,\mu$m (vertical). Plugging in the numbers gives $\mathcal{L} \approx 4 \times 10^{30}\ {\rm cm}^{-2}{\rm s}^{-1}$. This was a typical luminosity for the early operation of LEP (starting 1989). By increasing the number of bunches in the machine and reducing the bunch size, LEP eventually reached luminosities almost an order of magnitude higher than this. At the LHC, the design luminosity was $\mathcal{L} \approx 1 \times 10^{34}\ {\rm cm}^{-2}{\rm s}^{-1}$ and this value has been surpassed during the 13 TeV operation ($\mathcal{L} \approx 2.1 \times 10^{34}\ {\rm cm}^{-2}{\rm s}^{-1}$).

3.6 Some existing and planned accelerators

Most of the accelerators in existence today are used not for particle physics research but rather for medical purposes. Beams of charged particles are used in treatment of cancer and other diseases. Table 3.1 summarizes some of the larger existing and planned accelerators used in particle physics.

Table 3.1: Some major particle accelerators [7, 14].

accelerator (location), start year	particles	type	energy
SLAC (California), 1966	e^-	linac	$E_{\text{beam}} = 50$ GeV
SPEAR (SLAC), 1972	e^+e^-	linac & storage ring	$E_{\text{cm}} = 8$ GeV
PETRA (DESY, Hamburg), 1978	e^+e^-	circular collider	$E_{\text{cm}} = 44$ GeV
PEP (SLAC), 1980	e^+e^-	linac & storage ring	$E_{\text{cm}} = 29$ GeV
CESR (Cornell University), 1980	e^+e^-	synchrotron & storage ring	$E_{\text{cm}} = 10.6$ GeV
Sp$\overline{\text{p}}$S (CERN, Geneva), 1981	p$\overline{\text{p}}$	circular collider	$E_{\text{cm}} = 540$ GeV
Tevatron (Fermilab, Chicago), 1986	p$\overline{\text{p}}$	circular collider	$E_{\text{cm}} = 2$ TeV
TRISTAN (KEK, Japan), 1987	e^+e^-	circular collider	$E_{\text{cm}} = 64$ GeV
SLC (SLAC), 1989	e^+e^-	linear collider	$E_{\text{cm}} = 91$ GeV
LEP (CERN), 1989	e^+e^-	circular collider	$E_{\text{cm}} = 208$ GeV
HERA (DESY), 1992	ep	circular collider	$E_{\text{e}} = 30$ GeV $E_{\text{p}} = 820$ GeV
PEP-II (SLAC), 1999	e^+e^-	linac & storage rings	$E_{+} = 3.1$ GeV, $E_{-} = 9.0$ GeV
LHC (CERN), 2009	pp	circular collider	$E_{\text{cm}} = 7, 8, 13$ 14 (design) TeV
ILC (Japan), >2025	e^+e^-	linear collider	$E_{\text{cm}} = 250, 500,$ 1000 GeV
CLIC (CERN), >2030	e^+e^-	linear collider	$E_{\text{cm}} = 380, 1500,$ 3000 GeV
CEPC (China), >2025	e^+e^-	circular collider	$E_{\text{cm}} = 250$ GeV
FCC-ee (CERN), ?	e^+e^-	circular collider	$E_{\text{cm}} = 365$ GeV
SPPC (China), ??	pp	circular collider	$E_{\text{cm}} = 50 - 80$ TeV
FCChh (CERN), ??	pp	circular collider	$E_{\text{cm}} = 100$ TeV
High-E LHC (CERN), ??	pp	circular collider	$E_{\text{cm}} = 27$ TeV
Muon Collider (FNAL?), ???	$\mu^+\mu^-$	circular collider	$E_{\text{cm}} = 2$ TeV

Chapter 4

Particle detectors

In the previous chapter we saw how to produce high energy particle collisions with various types of accelerators. The products of whatever reactions take place must then be detected, the particle types identified and momenta determined. In this chapter we look at the various ways that particles can interact with matter to produce a detectable signal and we'll see how these properties can been exploited in actual detector systems. The books by Martin and Shaw [1], Hughes [3] and Perkins [4] all contain material on particle detectors. More detailed information can be found in the books on detectors by Kleinknecht [14], Grupen [15] and Leo [16].

4.1 The particles we can detect

Before we begin talking about detectors, we need to have a rough idea of the types of particles we can observe. Table 4.1 summarizes the particles that are detected directly (or almost directly) and some of their properties. The table includes the mean lifetime τ and the equivalent distance $c\tau$. This is a useful quantity for knowing whether the particle will live long enough to enter the detector. Recall that the mean flight length of a particle is $\beta\gamma c\tau$, so for highly relativistic particles ($\beta \approx 1$), the mean flight length is approximately $\gamma c\tau = (E/m)c\tau$.

Consider first the leptons. We can detect the electron, which is stable, and the muon, which has $c\tau = 660$ m and for most cases can be treated as stable. The tau-lepton decays with a mean lifetime of only 290 fs ($c\tau = 87\,\mu$m), and so in most detectors it doesn't fly far enough to be observed directly. Rather, we see only its decay products. The neutrinos interact so weakly that we almost never detect them directly.

We never see free quarks and gluons; they are always bound together in hadrons, namely, baryons (three quarks) or mesons (quark and an antiquark). The mesons with long enough lifetimes to make it into a detector are the charged pion $\pi^{\pm}$, charged kaon $\mathrm{K}^{\pm}$, and the neutral kaons $\mathrm{K}^0_{\mathrm{S}}$ and $\mathrm{K}^0_{\mathrm{L}}$. The baryons we can directly see are the proton p, the neutron n, and some of the baryons containing one or more strange quarks. We can of course also observe the corresponding antiparticles.

In addition to these leptons and hadrons, we can also detect photons. A common source of these is the neutral pion, which decays very quickly 98.8% of the time as $\pi^0 \to \gamma\gamma$. So although we don't see the π^0 directly, we can reconstruct it by measuring the invariant mass of the two photons.

Many hadrons (called resonances) that we will encounter in Chapter 6 have lifetimes that are so short that they are never registered directly. This is also true for the W and Z bosons; only their decay products are seen in a detector.

Table 4.1: Some directly (or almost directly) measurable particles and their properties [7].

particle	type	mass (MeV)	τ (s)	$c\tau$
e^+, e^-	lepton	0.511	–	–
μ^+, μ^-	lepton	105.7	2.20×10^{-6}	660 m
π^+, π^-	meson ($u\overline{d}$, $d\overline{u}$)	139.6	2.60×10^{-8}	7.80 m
π^0	meson ($u\overline{u}$, $d\overline{d}$)	135.0	8.4×10^{-17}	25.1 nm
K^+, K^-	meson ($u\overline{s}$, $s\overline{u}$)	493.7	1.24×10^{-8}	3.71 m
K^0_S	meson ($d\overline{s}$, $s\overline{d}$)	497.7	0.893×10^{-10}	2.68 cm
K^0_L	meson ($d\overline{s}$, $s\overline{d}$)	497.7	5.17×10^{-8}	15.5 m
p, $\overline{p}$	baryon (uud)	938.3	–	–
n, $\overline{n}$	baryon (udd)	939.6	887	2.68×10^8 km
γ	gauge boson	0	–	–

4.2 Ionization energy loss, tracking detectors

When particles pass through matter, they interact in a number of different ways depending on their energy and type, and in particular on their charge and mass. In this section we'll discuss the interactions of charged particles.

The most important process that takes place when a charged particle passes through matter is that it knocks electrons out of the atoms of the material leaving a trail of electrons and positive ions (ionization). The basic goal of all charged-particle tracking detectors is to figure out where the ionization trail was located and thus to determine the trajectory of the particle.

Often the detector is immersed in a magnetic field $\mathbf{B}$, pointing, say, along the z axis. This causes a particle of charge q and momentum $\mathbf{p} = (p_x, p_y, p_z)$ to follow a helical trajectory with radius r. The radius, momentum and field strength are related by

$$p_\perp = qBr \tag{4.1}$$

where $p_\perp = \sqrt{p_x^2 + p_y^2}$ is the momentum component perpendicular to $\mathbf{B}$ and the axis of the helix is parallel to $\mathbf{B}$. The ratios of $p_\perp$ to p_z and p_y to p_x can be determined from the direction of the track. Thus by reconstructing the trajectory of the particle, all three components of the momentum at its point of production can be found. This supposes that the charge q is known. In fact, all of the charged elementary particles produced in high energy reactions are found to have charge $\pm e$; we will justify this assumption later. Using SI units on the right-hand side of equation (4.1) and 'particle physics' units ($c = 1$) on the left for a particle of unit charge gives

$$p_\perp[\text{GeV}] = 0.3\, B[\text{Tesla}]\, r[\text{m}]\ . \tag{4.2}$$

If we consider a very high energy (and hence high momentum) particle, then the radius of curvature will be large, i.e., the track becomes almost straight. Since the trajectory of the track is only determined with a limited precision, we will be unable to measure accurately momenta that are very high. One can show that under reasonably general conditions and for sufficiently high p, the relative accuracy σ_p/p of the momentum measurement in a tracking detector depends on the momentum as

$$\frac{\sigma_p}{p} \propto p \, . \tag{4.3}$$

In addition to giving us the particle's trajectory, the amount of ionization produced can provide information on its speed. Since the momentum, speed and mass are related by $p = \beta\gamma m$, measurements of the momentum and speed are sufficient to determine the mass.

The amount of energy lost in matter by ionization per unit path length l is proportional to the density ρ. We usually define

$$x = \int \rho \, dl \, , \tag{4.4}$$

i.e., $x = \rho l$ if the density is constant. In German this is called the *Massenbelegung* (there does not appear to exist a corresponding English word). If we say 'length', you must infer from the units whether this means length l (in cm) or length times density x (in g/cm^2). The energy loss per path length x, dE/dx, is then independent of the density and has units of MeV cm^2/g. It is given by the Bethe–Bloch formula [17, 18], which can be approximated by

$$-\frac{dE}{dx} = \frac{4\pi N_0 q^2 \alpha^2 (\hbar c)^2}{m_\mathrm{e}\beta^2} \frac{Z}{A} \left[\ln\left(\frac{2m_\mathrm{e}\gamma^2\beta^2}{I} \right) - \beta^2 \right] \, . \tag{4.5}$$

Here m_e is the electron mass in MeV, q is the incident particle's charge in units of e, $\beta = v/c$ is its speed, $N_0 = 6.0 \times 10^{23}\mathrm{g}^{-1}$ is Avagadro's number, Z and A are the atomic number and mass number of the medium, and I is an effective ionization potential with a magnitude of approximately $I = 10Z$ eV. For this formula, $m_\mathrm{e} = 0.511$ MeV has 'particle physics' units and the factor $\hbar c = 0.197 \times 10^{-10}$ MeV cm has been inserted to get back to normal units. Numerical results can thus be obtained by using

$$\frac{4\pi N_0 \alpha^2}{m_\mathrm{e}} (\hbar c)^2 = 0.307 \text{ MeV cm}^2\mathrm{g}^{-1} \, . \tag{4.6}$$

Note that the ionization energy loss is defined to be negative in (4.5), since the energy of the particle is decreasing. Usually we don't worry about the sign and we simply quote the dE/dx as a positive number.

From equation (4.5) we see that dE/dx depends on the square of the incident particle's charge q. Furthermore it depends only on the speed of the incident particle; it is independent of its mass.

The dependence of the ionization rate on the speed is shown in Fig. 4.1. Note that the horizontal axis is actually $\beta\gamma$ with a logarithmic scale. The speed can only go up to c, but $\beta\gamma$ continues to increase with energy. The dE/dx goes approximately as $1/\beta^2$ for non-relativistic

particles; this is because a slower particle has more time to interact with the surrounding atoms. It has a minimum at around $\beta \approx 0.96$ ($\beta\gamma \approx 3.5$), since for higher energies, the speed does not increase much. For higher $\beta\gamma$, dE/dx increases as $\ln\gamma$. This rise is due to the relativistic flattening of the particle's electric field resulting in higher transverse fields and thus higher ionizing power. Polarization effects in the medium not included in (4.5) lead to a saturation of the relativistic rise at very high $\beta\gamma$. This region is known as the *Fermi plateau*.

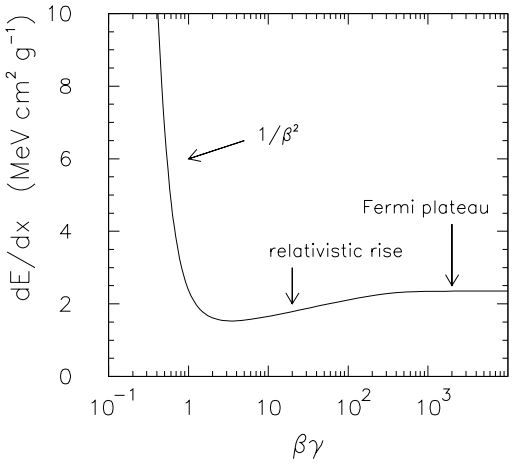

Figure 4.1: The mean ionization energy loss dE/dx as a function of $\beta\gamma$.

Particles with dE/dx at or near the minimum are called *minimum ionizing*. Almost all substances have a mean dE/dx in the range of 1–2 MeV cm^2 g^{-1} for a minimum ionizing particle. The main variation between different materials in the actual amount of ionization produced comes from the differences in mass density and in the mean energy W required to produce an electron–ion pair. For argon gas at atmospheric pressure and 20° C, for example, the mean dE/dx for a minimum ionizing particle is 1.5 MeV cm^2 g^{-1}, and the density is $\rho = 1.4 \times 10^{-3}$ g/cm^3. The amount of energy loss required to produce an electron–ion pair is approximately $W = 26$ eV for argon, which gives

$$\begin{aligned} \text{e}^-\text{–ion pairs / length} &= \frac{\rho\, dE/dx}{W} \\ &= 1.4 \times 10^{-3}\ \text{g/cm}^3 \times 1.5 \times 10^6\ \text{eV cm}^2\ \text{g}^{-1} / 26\ \text{eV} \\ &\approx 80\ /\ \text{cm}\ . \end{aligned} \tag{4.7}$$

Electron–ion production rates for a minimum ionizing particle of the order of 10^2/cm are typical for gases under these conditions. In the following sections, we discuss several types of detectors that exploit ionization to reconstruct charged particle tracks: Cloud and bubble chambers, wire chambers and solid state detectors.

4.2.1 Cloud chambers and bubble chambers

Cloud chambers and bubble chambers are no longer used in particle physics research, but they both played an important role in many major discoveries. The cloud chamber, invented by

C.T.R. Wilson in 1911, consists of a volume of air containing a vapour such as water or alcohol. The basic set-up is illustrated in Fig. 4.2. The temperature and pressure are adjusted so that the vapour is just above the condensation point. By rapidly extracting a piston and thus expanding the volume, the temperature drops causing supersaturation. Alternatively, a thermal gradient in the chamber can be used to form a stable layer of supersaturation. If a charged particle leaves a trail of ionization in the supersaturated vapour, droplets will form around the ions, leading to a visible track. The droplet density can be used to estimate the ionization rate.

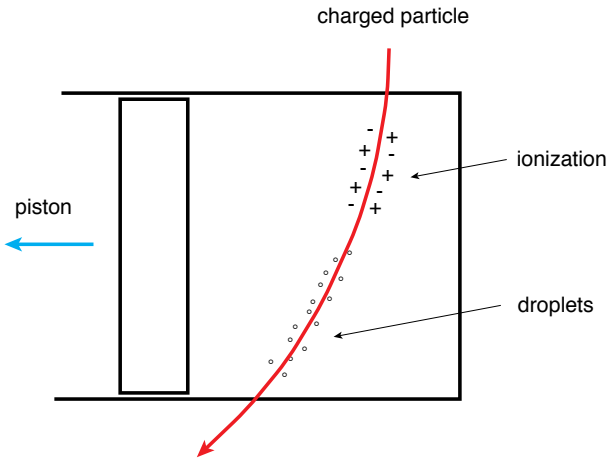

Figure 4.2: Schematic illustration of an expansion cloud chamber.

The bubble chamber, invented by D. Glaser in 1952, works on a similar principle. A chamber containing a liquid such as liquid hydrogen is kept just below the boiling point. A sudden expansion leads to a super-heated state. If a charged particle leaves a trail of ionization, the ions will nucleate the formation of bubbles leading to a visible track. A photograph from the Berkeley 72-inch liquid hydrogen bubble chamber is shown in Fig. 4.3 [19]. The curvature of the tracks in the magnetic field is clearly visible. In addition, the density of bubbles provides an estimate of the ionization rate.

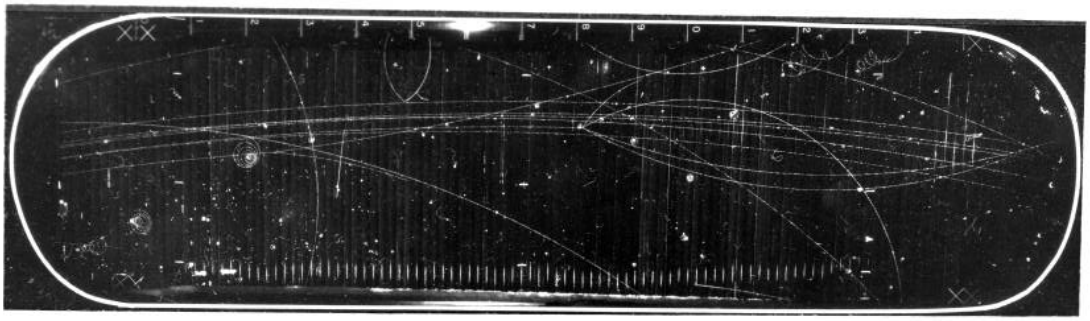

Figure 4.3: The Berkeley 72-inch bubble chamber [19]. A beam of particles enter from the left; an interaction can be seen near the middle of the chamber.

Both cloud and bubble chambers offer excellent position resolution and a complete view of all charged particles in an event. Their disadvantage is that the events must be photographed and scanned by eye. After each event the chamber must be reset to its initial temperature and pressure. Both of these factors severely limit the rate at which rare processes can be studied.

4.2.2 Multiwire proportional chambers

Wire chambers detect the passage of a particle by collecting the ionization produced in a gas with a wire electrode and converting it into an electrical pulse. The signal can be read out by an electronic circuit and fed into a computer. This allows for a software-based reconstruction of the particle tracks, which can proceed at a much higher rate than with cloud or bubble chamber photographs.

Wire chambers are in fact among the oldest instruments in particle physics, with early versions being developed by Geiger and Mueller in the 1920s. Until the advent of miniaturized electronics and computers, however, it was not possible to process the signals from a large set of wires. Chambers of this type were developed in the late 1960s by Georges Charpak, who received for this the Nobel Prize in 1992 [20].

A typical layout of a *multiwire proportional chamber* (MWPC) is shown in Fig. 4.4. The chamber is filled with a gas in which a charged particle will produce ionization. Argon is often used since the energy required to produce an electron–ion pair is relatively low ($W \approx 26$ eV). Higher Z noble gases such as krypton or xenon give more ionization, but are much more expensive. A plane of anode wires is held at a high positive potential (typically 1–5 kV) with respect to the cathode planes.

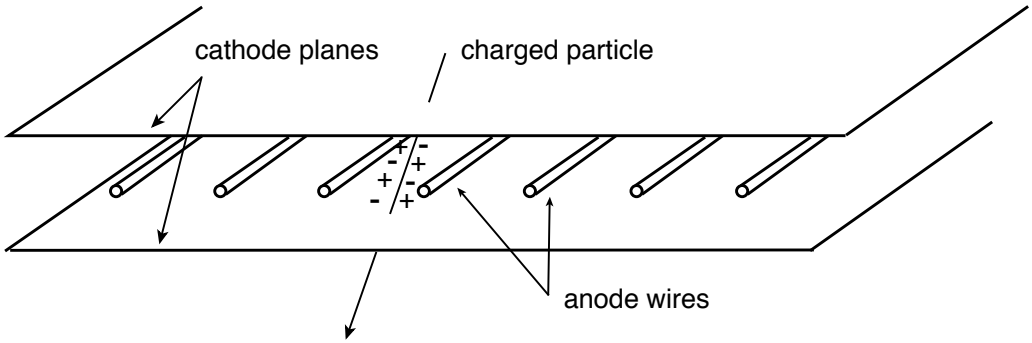

Figure 4.4: Schematic illustration of a single wire plane of a multiwire proportional chamber.

The anode wires typically have diameters in the range 10–30 μm so the electric field becomes very high close to the wire. As the electrons liberated in the gas are pulled towards the wires, they gain energy and produce additional electron–ion pairs. The voltage is set so that in the immediate vicinity of the anode wire an avalanche takes place, producing typically 10^4 to 10^5 electron–ion pairs for every incoming electron. As the positive ions released in the avalanche are pushed away from the anode wire, a voltage signal is induced on the wire which can be measured. For an appropriately chosen voltage and gas mixture, the output signal is proportional to the amount of ionization initially deposited, hence the name 'proportional chamber'. This means that the signal magnitude can be used to measure the ionization rate dE/dx.

In the set-up shown in Fig. 4.4, if a given wire 'fires' (produces a signal) then we only know that the particle traversed the wire plane closer to this wire than to its neighbours. By measuring the time when the avalanche takes place relative to the initial traversal time, the position where the particle crossed the wire plane can be more accurately localized. Used in this mode, an MWPC is called a *drift chamber*, the first working version of which was built by Walenta [21].

The initial traversal time must be determined by other means, and the position for a single wire plane is only determined up to a right–left ambiguity. Both of these problems can be overcome by using many wire planes or by combining the drift chamber's information with that from other detector components. Drift chamber wires are often arranged in concentric rings about the collision axis in colliding beam experiments.

By an arrangement of two or more perpendicular wire planes, both coordinates of a particle's passage through the detector can be determined. Often the cathode planes are segmented into electrically isolated *pads*. An avalanche on the wire will induce a measurable signal on the neighbouring pads, which provides still more information on the position where the particle passed through.

A particularly elegant type of drift chamber is the *time projection chamber* (TPC), invented by D. Nygren [22]. A schematic view of the first large volume TPC used in the TPC/2γ experiment at the PEP e^+e^- storage ring at SLAC is shown in Fig. 4.5. It consists of a large gas volume in which there are parallel magnetic and electric fields. The electric field causes the electrons liberated by the passage of a charged particle to drift to the end planes. There they are detected by MWPCs with many thousands of anode wires and cathode pads. The measured positions from the wires and pads plus the drift time allow one to reconstruct a three-dimensional image of the trajectories of many tracks. Spectacular events from the TPC used in the ALEPH experiment at LEP can be seen on posters, tee-shirts, wrist-watches and were under consideration for a Frank Zappa album cover. An example is shown in Fig. 4.2.2. Tracks of charged particles can be seen in the 18 individual MWPCs on each end of the TPC.

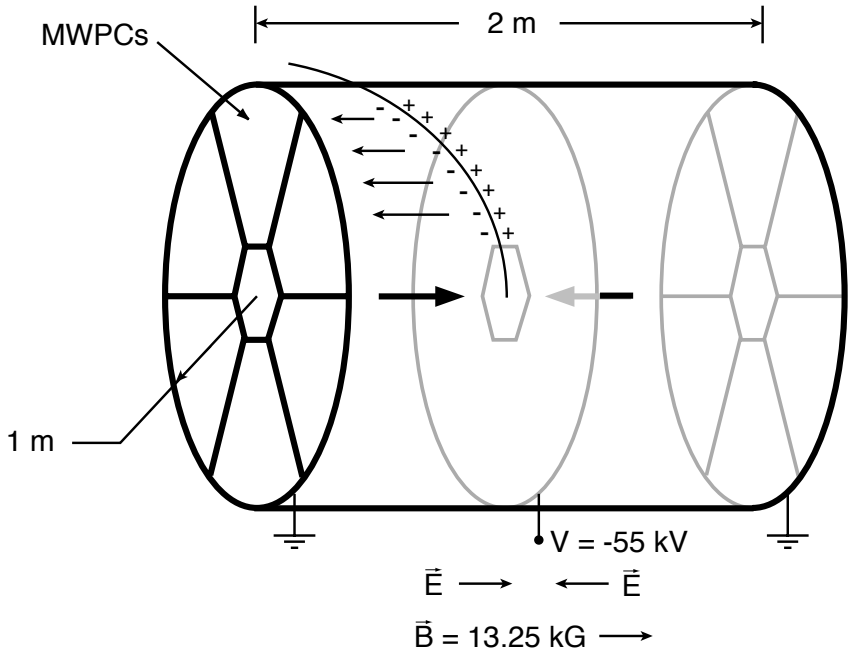

Figure 4.5: Schematic illustration of the TPC used in the TPC/2γ experiment at PEP (SLAC).

A valuable feature of tracking chambers is that one can combine measurements of momentum and ionization energy loss to estimate the mass of the ionizing particle, and hence to identify it. If we measure p and dE/dx for many tracks, we find that the values fall on well defined bands.

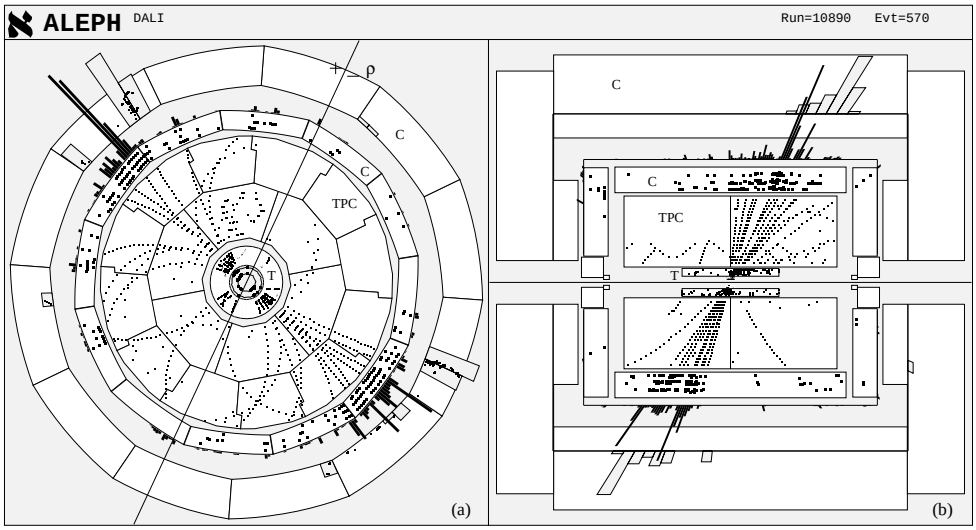

Figure 4.6: A multiparticle event seen in the ALEPH detector at LEP, viewed along (left) and perpendicular (right) to the beam axis [23].

This can be seen in Fig. 4.7, which shows data from the TPC/2γ detector [24]. No entries are found with ionization rates lower than the minimum ionizing value, here, around 12 keV/cm. This demonstrates that there are no particles produced with fractional charges, as would be expected, for example, if free quarks would have produced tracks. If any particles with charges other than $\pm e$ were produced, they would show up as a separate band on this plot.

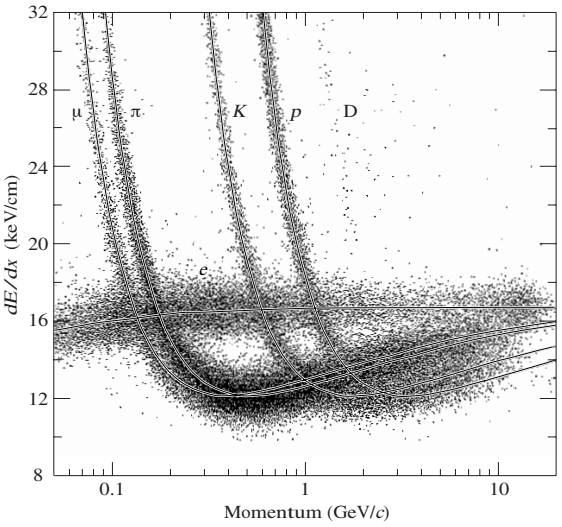

Figure 4.7: The ionization energy loss dE/dx as a function of momentum for particles produced in e^+e^- collisions [24].

4.2.3 Solid state detectors

The spatial resolution of MWPCs is at best 100–200 μm. Many unstable particles, however, have mean lifetimes in the picosecond range which, for typical momenta at which they are produced ($\sim$ GeV), result in flight lengths of 100 μm or less. In order to be able to accurately measure such distances, we need a chamber with very high position resolution that can be placed close

to the interaction point. Since the late 1980s, this task has been performed by semiconductor detectors consisting of silicon wafers with closely spaced strips, which are each connected to an amplifier and electronic read-out circuit. The strips thus play the role of the wires of an MWPC. The wafers typically have a thickness of 300 μm and a spacing between strips of 50 μm. The wafer itself usually consists of an n-type substrate with p-type strips implanted in one or both sides, as illustrated in Fig. 4.8.

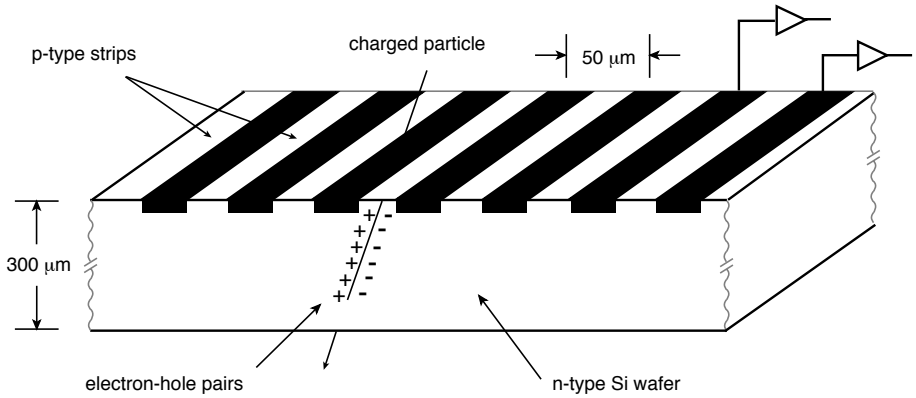

Figure 4.8: A silicon detector consisting of an n-type substrate with p-type strips.

A voltage is applied to the pn-junctions so as to deplete the silicon of charge carriers and establish an electric field inside the wafer. An ionizing particle produces electron–hole pairs causing a current to flow between the substrate and several of the nearby strips. By finding the centre-of-gravity of the strips giving signals, a position resolution of around 5–10 μm can be achieved, considerably smaller than the spacing between strips.

Figure 4.2.3 shows another multiparticle event from an e^+e^- collision seen in the ALEPH detector. The upper right-hand plot shows an expanded view of the silicon *vertex detector* (11 cm radius), so named because of its ability to resolve the decay vertices of short-lived particles. The wafers are shown edge-on. They have strips running parallel to the beam on the outside and perpendicular to it on the inside faces. The lower part of the plot shows a further expanded view in which several secondary vertices can be seen. By measuring the average flight lengths of particles in this way, their mean lifetimes can be determined.

4.3 Scintillators and photomultipliers

When a charged particle passes through matter creating ionization, it leaves the atoms or molecules of the substance in excited states. When these return to their ground states they emit photons, which is called *scintillation* light. Most substances are opaque to their own scintillation light, but for certain materials (aptly called *scintillators*) at least some of the photons can travel through the material and be detected.

There are two basic kinds of scintillators: organic and inorganic. Organic scintillators are often commonly produced as large plastic sheets from 1 mm to several cm thick with areas up to several square meters. The light production mechanism is basically the radiative decay of the excited molecules, which takes place typically within several ns. Organic scintillators are therefore useful for determining accurately the time when a particle passed through the detector.

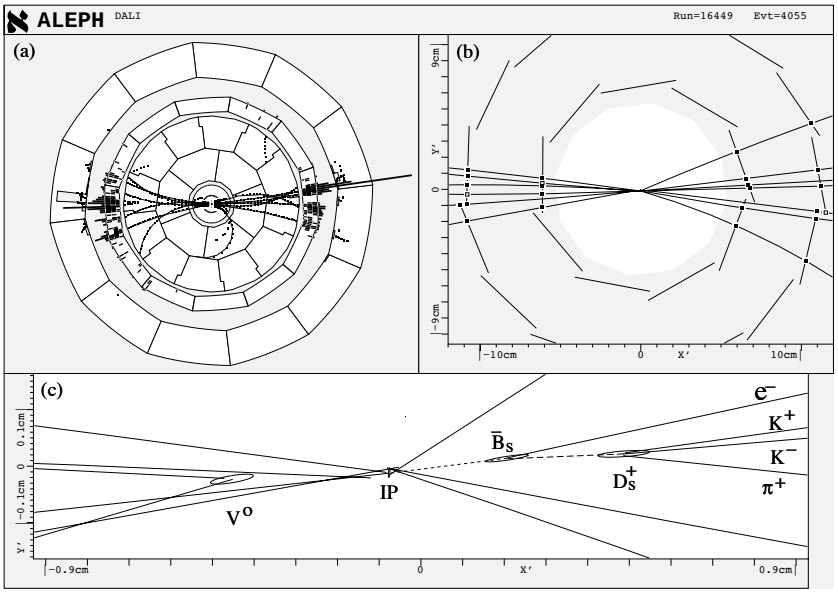

Figure 4.9: A multiparticle event seen in the ALEPH detector showing (a) the full detector, (b) an expanded view of the vertex detector and (c) a further expanded view of the interaction region [23].

The photons are emitted mostly in the UV range, which in most substances would quickly be absorbed. Organic scintillators, however, are doped with compounds such as polysterene that act as a *wavelength shifter*, i.e., they absorb the UV light and re-emit photons in the visible part of the spectrum.

Inorganic scintillators are crystals such as sodium iodide (NaI), caesium iodide (CsI) or bismuth germanate ($Bi_4Ge_3O_{12}$, usually called BGO). The amount of scintillation light produced in inorganic scintillators depends on the nature of the crystal lattice and the resulting allowed energy levels. The number of photons produced is usually higher than what can be obtained in organics, e.g., around 2×10^5 photons per cm for a minimum ionizing particle in NaI, compared to around 2×10^4 photons per cm in a plastic scintillator. The light emission times are typically on the order of 1 μs, i.e., much longer than in organic scintillators.

The light from a scintillator must somehow be collected and detected. This is usually achieved by connecting the scintillator to a *photomultiplier tube* (PMT) by means of a *light guide*. The light guide is simply a transparent piece of plastic formed so that one end fits onto the scintillator, often the rectangular end of a crystal or plastic sheet, and the other end fits onto the photomultiplier, which is usually round. A typical set-up is shown in Fig. 4.10. Some fraction of the photons will be internally reflected along the surface of the scintillator and light guide and enter through the window of the photomultiplier.

On the inside surface of the photomultiplier's window is a thin metal coating called the *photocathode*. This is a substance with a certain probability, typically around 25%, of emitting electrons through the photoelectric effect. The electrons are accelerated towards an electrode called a *dynode*. By striking the dynode with sufficient energy they cause the emission of several more electrons, which are accelerated to the next dynode. This processes continues for typically 10 to 15 stages, at the end of which a large number of electrons, perhaps on the order of 10^8, are produced. These electrons are collected at the anode and result in a measurable electrical

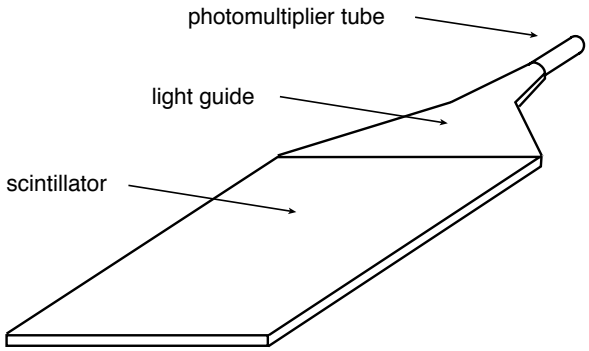

Figure 4.10: Schematic drawing of a scintillator, light guide and photomultiplier tube.

signal. A schematic illustration of a photomultiplier tube is shown in Fig. 4.11.

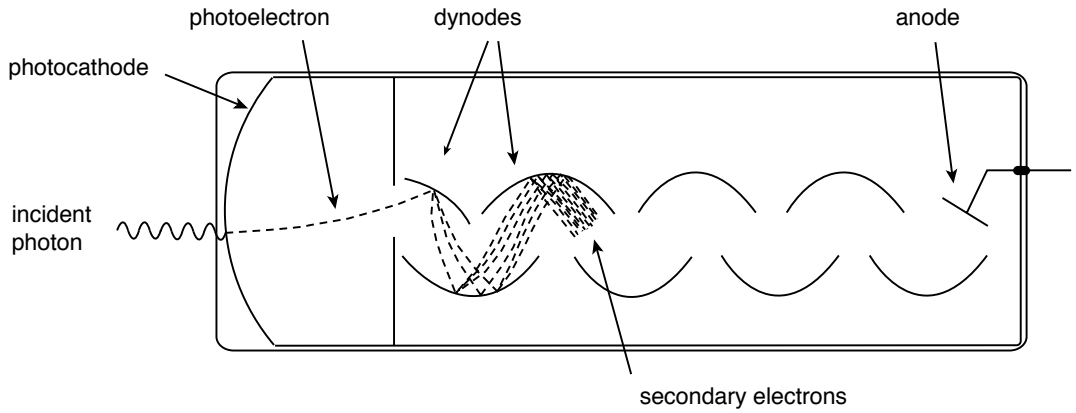

Figure 4.11: Schematic drawing of a photomultiplier tube.

Combinations of scintillators and photomultipliers are useful for determining the time at which ionizing particles traversed the detector. Their spatial resolution is limited to the statement that the particle passed somewhere through the detector that gave the signal. This can be improved by segmenting the scintillator into smaller sections with individual photomultipliers, which may be adequate for many applications. Scintillators are also used in electromagnetic calorimeters as described in the following section.

4.4 Electromagnetic showers, calorimeters

Many of the particles produced in high energy collisions are electrically neutral, and so they create no ionization trail and hence no track in a tracking detector. The most important example is the photon, and in this section we describe how another type of detector called an *electromagnetic calorimeter* that can be used to measure the energy and direction of high energy photons. In addition, the same device can help to distinguish between different types of charged particles, namely, between electrons and heavier particles such as muons or pions. The calorimeter works by causing the incident photon to initiate a shower of electrons, positrons and photons. The number of particles in the shower allows one to estimate the energy of the incident

particle. Before describing an actual calorimeter we'll first take a closer look at two important physical processes involved: pair production and bremsstrahlung.

When a high energy photon passes through matter, it can undergo e^+e^- *pair production*, schematically illustrated by the Feynman diagram in Fig. 4.12(a). Note that a free photon cannot dissociate into an e^+e^- pair by itself, since this would not conserve energy and momentum. Pair production is only possible if an additional particle, namely a nucleus N indicated in the diagram, participates in the interaction. Since the nucleus is much more massive than the electron or positron, however, it absorbs very little energy and momentum; these are transferred almost completely to the e^+e^- pair.

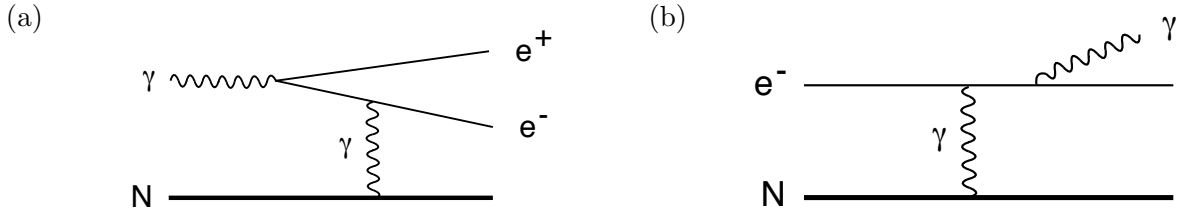

Figure 4.12: Electromagnetic processes: (a) pair production, (b) bremsstrahlung.

In a similar way, if a charged particle such as an electron comes close to a nucleus it can radiate a photon, as shown in Fig. 4.12(b). This process is called *bremsstrahlung* (German for 'braking radiation')[1]. As in the case of pair production, the nucleus absorbs very little energy. To a good approximation, a part of the charged particle's energy is simply transferred to the photon.

One can show that the energy loss due to bremsstrahlung of a charged particle depends on its energy E and mass m as

$$-\left(\frac{dE}{dx}\right)_{\text{brem}} \propto \frac{E}{m^2}$$

$$\equiv \frac{E}{X_0}\,, \tag{4.8}$$

$$E = E_0 e^{-x/X_0}\,, \tag{4.9}$$

where the inverse of the proportionality constant, X_0, is called the *radiation length*. It is the characteristic length scale for the occurrence of an electromagnetic process such as bremsstrahlung or pair production. Note that here the dependence on E is quite different from that of dE/dx from ionization, which is given by the Bethe–Bloch formula.

The dependence of $(dE/dx)_{\text{brem}}$ on the mass of the incident particle m in (4.8) enters through the fermion propagator for the Feynman diagram in Fig. 4.12(b). This means that since electrons are 207 times lighter than muons, they lose much more energy from bremsstrahlung, i.e.,

[1]Note that this radiation has the same physical origin as the synchrotron radiation seen in Eq. 3.8; in the case of *bremsstrahlung* the source of the change of direction of the incoming charged particle is given by the electric field of the nucleus and surrounding electrons of the material. However, notice the very different mass dependence between Eq. 3.8 and Eq. 4.8.

$$\frac{(dE/dx)_{\text{brem for e}^-}}{(dE/dx)_{\text{brem for }\mu^-}} = \frac{m_\mu^2}{m_\text{e}^2} = \left(\frac{105.7\text{ MeV}}{0.511\text{ MeV}}\right)^2 \approx 4\times 10^4\ . \tag{4.10}$$

The basic conclusion is that bremsstrahlung for muons is usually negligible, but for electrons it is very important.

From the Feynman diagram in Fig. 4.12(b), we see that the bremsstrahlung amplitude is proportional to Ze^3 or $Z\alpha^{3/2}$, so that the cross section, and thus also the energy loss are proportional to $Z^2\alpha^3$. Consequently, X_0 is inversely proportional to $Z^2\alpha^3$, and therefore is small for high Z materials like lead ($Z = 92$, $X_0 = 0.56$ cm) and large for low Z materials like beryllium ($Z = 4$, $X_0 = 35.3$ cm). These X_0 values assume that the incident particle is an electron; for muons, the corresponding numbers are larger by a factor of $(m_\mu/m_\text{e})^2$.

So when a photon of sufficiently high energy passes through matter, it will at some point undergo pair production. The distance traversed before the interaction is random, but will typically be on the order of X_0. The resulting e^+ and e^- will continue through the material and after a length of typically 1 X_0 will emit bremsstrahlung photons. If these have sufficiently high energy, they can give rise to more e^+e^- pairs. The result is an *electromagnetic shower*, as illustrated in Fig. 4.13(a).

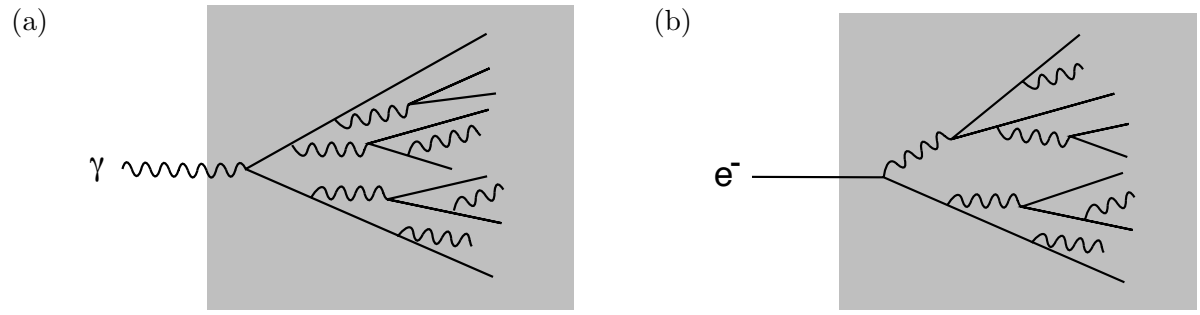

Figure 4.13: Electromagnetic showers initiated (a) by a photon and (b) by an electron.

If the incident particle is an electron, the electromagnetic shower looks almost the same, as shown in Fig. 4.13(b). The only difference is that the first interaction is bremsstrahlung rather than pair production. A heavier particle such as a muon or pion, however, will not initiate an electromagnetic shower.

Recall that in the processes of pair production and bremsstrahlung, energy is not dissipated but rather is transferred from the incident particle to the outgoing ones. Along the paths of the e^+ and e^- in the shower, however, energy is dissipated mainly by creation of ionization. The shower stops when the photons no longer have sufficient energy to produce e^+e^- pairs, after which they can lose their energy by Compton scattering or the photo-electric effect. The total energy of the incident particle is eventually absorbed in the material, which can be estimated by measuring the amount of ionization produced.

A device that measures the energies of electrons and photons in this way is called an *electromagnetic calorimeter*. The amount of ionization can be measured by interleaving layers of lead with planes of sense wires as in an MWPC. An example is the electromagnetic calorimeter of the ALEPH detector, which contains 45 sheets of lead, each 2 to 4 mm in thickness, i.e., 0.36

to 0.72 of a radiation length, interspersed with wire planes. The signals from the wires and segmented cathode pads tell not only how large the shower was, and thus the energy, but also the location of the shower, and therefore the direction of the incoming photon or electron.

Calorimeters can also be made out of scintillating crystals such as NaI or CsI. These substances have relatively short radiation lengths, e.g. $X_0 = 1.86$ cm for CsI, and so a calorimeter with 30 cm CsI crystals would represent 16 radiation lengths, enough to fully absorb an electromagnetic shower of up to 5–10 GeV. The number of shower particles is determined by measuring the number of scintillation photons produced using photomultipliers or similar devices. The electromagnetic calorimeter of the BaBar detector at SLAC contains 6580 CsI crystals each around 30 cm long.

The total number of shower particles produced for a fixed incident energy is subject to statistical fluctuations. That is, even if we repeatedly shot 10 GeV photons into a calorimeter, the measured energies would differ. One can show that under fairly general circumstances, the average amount of fluctuation in the production of n shower particles (more precisely, the standard deviation of n) is proportional to $\sqrt{n}$. Furthermore, the energy E is proportional to n, so the energy resolution of the calorimeter σ_E is proportional to $\sqrt{E}$, or equivalently, the relative energy resolution scales as

$$\frac{\sigma_E}{E} \propto \frac{1}{\sqrt{E}} \,. \tag{4.11}$$

The electromagnetic calorimeter of the ALEPH detector, for example, has an energy resolution of around $18\%/\sqrt{E}$ with E measured in GeV. Scintillating crystals provide significantly better resolution, e.g., around 1.5% for the BaBar CsI calorimeter for a photon energy of 1 GeV.

We can contrast the energy resolution of calorimeters with that of tracking detectors. There, we had $\sigma_p/p \propto p$, i.e., the momentum measurement becomes less precise as the energy increases. For calorimeters the opposite is true: the relative energy resolution improves with increasing energy.

4.5 Hadron calorimeters

Particles such as neutrons or K^0_L mesons leave no ionization in a tracking chamber and will not initiate an electromagnetic shower. Being hadrons, however, they will undergo strong interactions with nuclei as they pass through the material of the detector. A high energy collision between a hadron and a nucleus can lead to the production of a number of secondary particles, mainly consisting of pions and nuclear fragments. These particles can then collide with other nuclei, resulting in a *hadronic shower*. This continues until the energy of the incident particle has been dissipated.

The average amount of matter traversed before a hadron undergoes a nuclear interaction is characterized by the *nuclear interaction length* λ_I. This is longer than the radiation length for most substances. A commonly used substance for hadron calorimeters is iron, which has $\lambda_\mathrm{I} = 17$ cm. It therefore takes typically a meter or more of iron to contain a hadronic shower.

As in the case of an electromagnetic shower, the number of shower particles provides a measure of the energy of the incident particle. A *hadron calorimeter* estimates hadron energies

in this way. The hadron calorimeter of the ALEPH experiment, for example, consists of 23 layers of iron each 5 cm thick, interspersed with wire chambers to measure the presence of shower particles.

Owing to the larger statistical fluctuations inherent in the hadronic collisions, the energy resolution of such devices is typically worse than electromagnetic calorimeters, e.g. $\sigma_E/E \approx 84\%/\sqrt{E}$ (E in GeV) for ALEPH. Note that as in the case of electromagentic calorimeters, the resolution improves for increasing energies.

Hadron calorimeters are also useful for distinguishing between charged pions and muons. Both leave tracks in tracking chambers, and since their masses are similar, it is difficult to distinguish between them by using their momenta and ionization rates. A pion will also create a hadronic shower in a hadron calorimeter. A muon, however, does not interact strongly and will pass through a hadron calorimeter leaving only a single trail of ionization. Often a set of wire chambers is placed outside the hadron calorimeter to assist in muon identification.

4.6 Multicomponent detector systems

In most large particle physics experiments, the detector consists of a number of components, e.g., a vertex detector, tracking chamber, electromagnetic and hadronic calorimeters, etc. An example is the ALEPH detector, shown in Fig. 4.6. More information on the ALEPH detector can be found on the ALEPH web site [23].

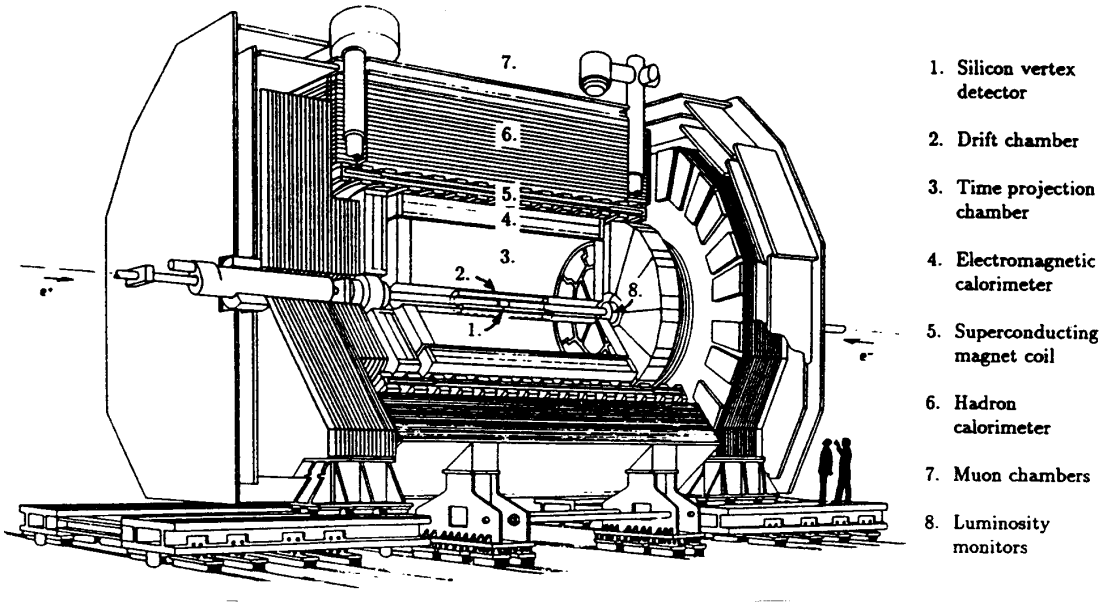

Figure 4.14: A view of the ALEPH detector showing its components [23].

The advantage of such a multicomponent detector is that different types of particles will leave different signals in each layer, allowing for an almost unambiguous identification for the particles produced. Some examples are shown in Fig. 4.15.

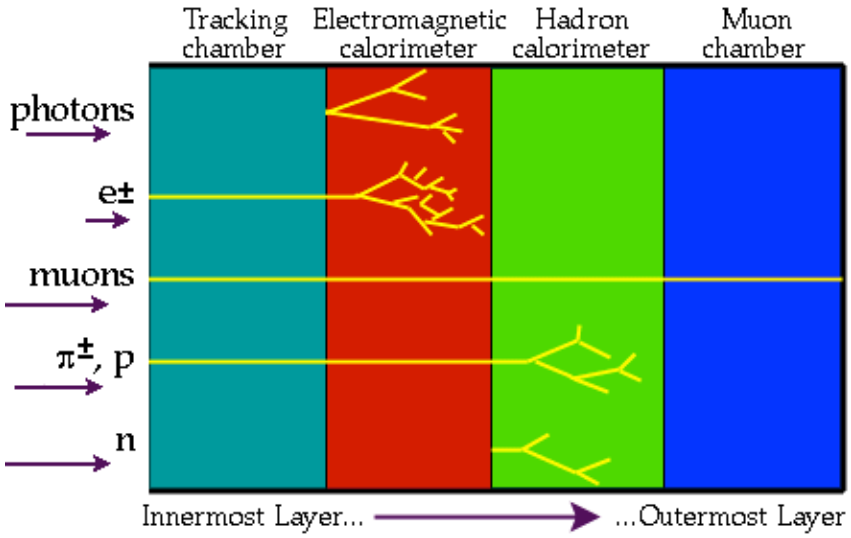

Figure 4.15: Schematic of the signatures left by various particles in different parts of a modern detector. A solenoid magnet could be placed for example between the tracker and the electromagnetic calorimeter as in the case of ATLAS. Note that this schematic does not represent the typical geometry of a detector.

Chapter 5

Leptons

We've now seen the basic components of the Standard Model and have briefly gone over how particle physics experiments can be done. Starting with this chapter we'll go back and look at how the various particles were discovered and how the ingredients of the model were put together. In this chapter we examine the discoveries and basic properties of the leptons. We include the positron, since it is a lepton, but it is also of more fundamental importance being the first example of antimatter to be discovered.

5.1 The electron

We won't cover the electron here since you have probably have heard about its discovery elsewhere. The web site of the Cavendish Laboratory at Cambridge has links to a number of interesting items on J.J. Thomson's 1897 discovery: `http://www.phy.cam.ac.uk/cavendish/history/electron/`.

5.2 The positron

The existence of the positron, the antiparticle of the electron, was predicted by Dirac in 1929 [25]. His relativistic theory of quantum mechanics contains solutions corresponding to particles with the same masses as the known particles, but with opposite values of the electric charge.

The positron was discovered by Carl Anderson at Caltech in 1932 [26]. Using a cloud chamber, Anderson was able to observe tracks of charged particles from cosmic rays. At the time, not much was known about cosmic ray particles other than that the primary radiation originated from outside the earth's atmosphere. The particles observed at sea level were understood to be created when the primaries interacted with nuclei in the air. In any event, it was clear that if they came from outer space, they must be headed downwards.

By measuring the radius of curvature r of the tracks in a magnetic field B and assuming an electric charge q equal in magnitude to that of the electron, he could measure their momentum p. By measuring the density of droplets of the tracks, he could determine the speed. By combining these two pieces of information, the mass of the particle could be estimated.

By selecting thin tracks with sufficient curvature in the magnetic field, Anderson was able to obtain a sample of particles with masses consistent with that of the electron and definitely much less than that of the proton. These tracks were observed to curve in both directions in the magnetic field, which led one to suspect that some were negative and others positive. This is what one would conclude if it were known that all particles came from above, as was expected for cosmic rays.

In order to be certain of the incident direction of the particles, Anderson installed a horizontal lead plate in the middle of the chamber. Since the particle loses some energy when traversing the plate, the radius of curvature must be larger on the incoming side than on the outgoing side. After a short time, the track shown in Fig. 5.1 was found. The ionization and curvature allowed him to conclude that the charge was positive, and that its mass was much less than that of the proton, being consistent with the electron's mass. Surprisingly, the first identified positron was actually moving upwards, presumably having been scattered from below. If one were to assume the proton mass, then the expected ionization rate given the measured momentum would be so high that the particle would not even be able to penetrate through the lead plate.

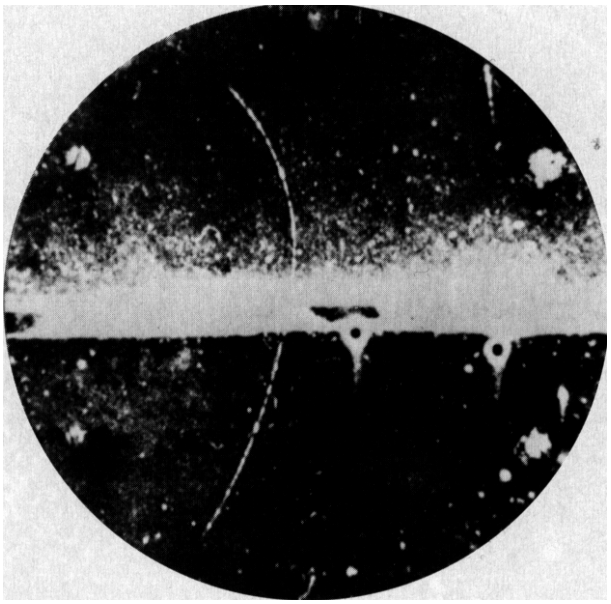

Figure 5.1: The first identified positron [26].

The concept of antimatter has been extended to include all of the known particles. The antiparticle has the same mass as its corresponding particle but opposite charge.

5.3 The muon

The muon is a charged lepton about 200 times more massive than the electron. It was discovered by Anderson and Neddermeyer, who had continued studying cosmic rays using a cloud chamber in a magnetic field with a 1 cm platinum plate in the middle. The first evidence for a new type of particle came by selecting tracks for which the momentum and speed corresponded to masses considerably less than that of the proton. For some of the tracks, the particle had lost most of

its energy in the platinum plate. This was what one in fact expected for electrons. For other tracks, very little energy loss was observed; these turned out to be muons.

More specifically, by measuring the track's radius of curvature on both sides of the plate, the momenta above $p_{\rm a}$ and below $p_{\rm b}$ could be determined. Highly relativistic particles could be selected by looking for tracks with low droplet densities. For these one has $E \approx p$, and thus the difference in energies above and below the plate is

$$\Delta E \approx p_{\rm a} - p_{\rm b} \ . \tag{5.1}$$

Tracks were selected with incident momenta in the range $100 - 500$ MeV. This requirement excludes protons, since for this momentum range, a proton would have $\beta\gamma = p/m$ around $0.1 - 0.5$, i.e. it would not be highly relativistic, and according to the Bethe–Bloch theory of ionization energy loss it would produce a much higher droplet density.

Thus for each selected track, the energy above the plate $E = p_{\rm a}$ and the energy difference ΔE were measured. A histogram of $\Delta E/E$ is shown in Fig. 5.2 [27]. The right-hand side of the histogram has tracks with less momentum below the plate than above. There is a clearly separated component where the particles lose almost all of their energy. These are mostly 'showering particles' (the hatched area), which are accompanied by other tracks in the chamber. The left-hand side (positive $\Delta E/E$) corresponds to particles with higher measured momenta below than above. For the region centred about zero, the values are consistent with zero energy loss to within the estimated measurement accuracy. (The single entry at $\Delta E/E = 1$ at the far left is only observed below the plate, and is almost certainly a particle coming from below.)

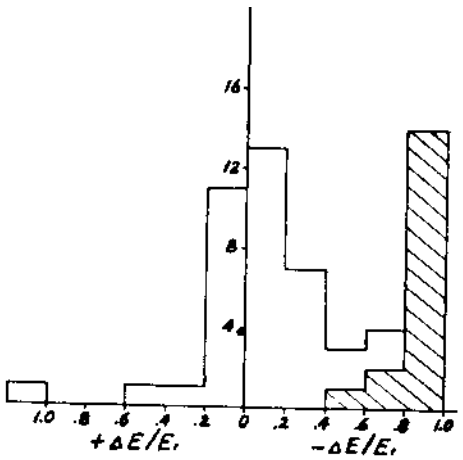

FIG. 2. Distribution of fractional losses in 1 cm of platinum.

Figure 5.2: Histogram of $\Delta E/E$ showing two distinct components: showering particles with $-\Delta E/E \approx 1$, and penetrating particles with $\Delta E/E$ centred about zero [27].

The showering particles are in fact what one would expect for electrons. They will lose energy through bremsstrahlung (photon emission), and subsequent production by the photons of electron-positron pairs. The component in the histogram centred about zero is not consistent with what would be expected with electrons.

Those particles with $\Delta E/E \approx 0$ were thus much less massive than a proton but lost much less energy when traversing matter than an electron. They were therefore a new highly penetrating particle, which was first called the mesotron, then renamed the mu-meson. Today the word

meson is reserved for a different type of particle, one consisting of a quark and an antiquark. The former mu-meson is now classified as a lepton and is simply called the muon (μ).

The first accurate measurement of the muon's mass was obtained by Anderson and Neddermeyer a few years later [28] with the cloud chamber photograph shown in Fig. 5.3. The particle enters from above, traverses a glass Geiger tube (used to trigger the chamber) and comes to rest below. Notice that the particle is much more highly ionizing after its energy is reduced by passing through the glass tube.

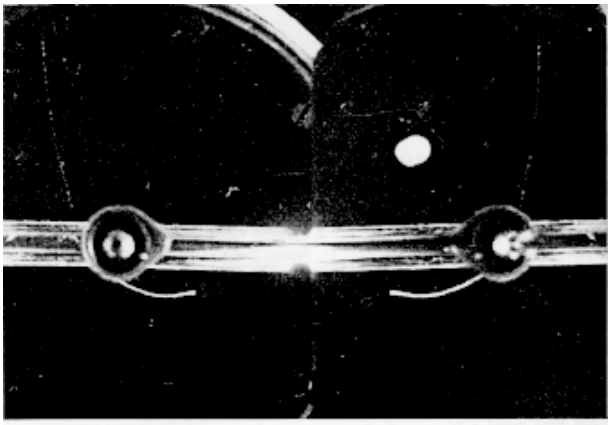

Figure 5.3: The stereoscopic cloud chamber photograph that provided the first accurate determination of the muon mass [28].

The initial momentum p can be determined from the radius of curvature above the Geiger tube. The incoming energy E can be estimated from the total range of the particle before coming to rest. If both E and p are measured, the mass can be determined by

$$m = \sqrt{E^2 - p^2} \; . \tag{5.2}$$

In this way, the muon's mass was estimated to be 220 ± 35 times that of the electron, or 112 ± 18 MeV. The current best measurement of the muon mass is 105.658389 ± 0.000034 MeV.

The muon appears to be just like an electron except that it is around 207 times heavier. Recall that the energy loss of a particle due to bremsstrahlung is inversely proportional to the mass squared, and thus bremsstrahlung for muons is suppressed by a factor of around 4×10^4 relative to electrons. So the greater penetrating power of the muon is exactly what would be expected for a particle of its mass, as long as it does not participate in any additional interactions. We have already mentioned that the charged pion has a mass even slightly greater than the muon's (140 MeV), but it is not nearly as penetrating. This is because the pion is a hadron and undergoes strong interactions with atomic nuclei. The muon, however, does not participate in the strong interaction.

An additional aspect of the muon's behaviour that is different from that of the electron is that it is unstable; this is also a consequence of its greater mass. There is basically only one decay mode available, namely,

$$\mu^- \rightarrow \mathrm{e}^- \overline{\nu}_\mathrm{e} \nu_\mu \; .$$

The μ^+ decays in the corresponding way with all particles replaced by their antiparticle partners.

We have not yet learned all the theoretical machinery needed to derive the Standard Model's prediction for the muon lifetime, but we can use dimensional arguments to make a rough estimate. Muon decay proceeds via the Feynman diagram shown in Fig. 5.4.

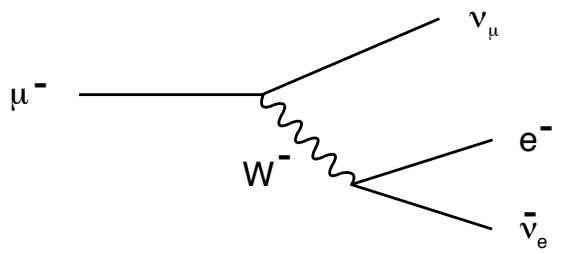

Figure 5.4: Feynman diagram for muon decay.

From the Feynman rules we know that the amplitude for this process will contain two factors of the weak coupling g and a propagator $1/(q^2 - m_{\rm W}^2)$, where q^2 is the four-momentum squared of the W boson and $m_{\rm W} = 80.4$ GeV. The value of q^2, which is equal to the invariant mass squared of the $\mathrm{e}^-\overline{\nu}_{\rm e}$ system, will depend therefore on the way that the energy is shared among the outgoing particles. The largest possible value for q^2 occurs if the ν_μ gets zero energy and the e^- and $\overline{\nu}_{\rm e}$ come out back to back, in which case we have by energy conservation

$$q^2 = m_\mu^2 \, . \tag{5.3}$$

So even the maximum possible value of q^2 is much less than the W mass ($M_{\rm W} = 80.4$ GeV), and therefore the W propagator can be approximated as $-1/M_{\rm W}^2$. So we know the amplitude will follow $\mathcal{M} \propto g^2/M_{\rm W}^2 \propto G_{\rm F}$, where $G_{\rm F}$ is the Fermi constant which we introduced in Chapter 2,

$$G_{\rm F} = \frac{\sqrt{2}g^2}{8M_{\rm W}^2} = 1.166 \times 10^{-5} \ \mathrm{GeV}^{-2} \, . \tag{5.4}$$

The decay rate $\Gamma(\mu^- \to \mathrm{e}^-\overline{\nu}_{\rm e}\nu_\mu)$ is proportional to the square of the amplitude, so it will be proportional to $G_{\rm F}^2$, which has units of GeV^{-4}. In normal units, a decay rate has dimension of inverse time, so in particle physics units this is GeV (see Table 1.5). Therefore we need to multiply the $G_{\rm F}^2$ by something with dimension GeV^5 to obtain the correct units. We don't expect the masses of final state particles to have an influence on the decay rate as long as they are small compared to the centre-of-mass energy of the system, i.e., the muon's mass. (This fact is perhaps not obvious but nevertheless true, and we will employ it in several cases in this course.) Therefore the only quantity available is m_μ and the decay rate must be given by approximately

$$\Gamma(\mu^- \to \mathrm{e}^-\overline{\nu}_{\rm e}\nu_\mu) \sim G_{\rm F}^2 m_\mu^5 \, . \tag{5.5}$$

The proportionality constant will contain various numerical factors which we could naively expect to be of order unity. In fact, they are not so close to unity in this case and a full calculation gives

$$\Gamma(\mu^- \to \mathrm{e}^-\overline{\nu}_{\rm e}\nu_\mu) = \frac{G_{\rm F}^2 m_\mu^5}{192\pi^3} \, . \tag{5.6}$$

Since the muon has essentially only one allowed decay mode (there is a small probability that we can neglect of emitting an additional photon), the decay rate $\Gamma(\mu^- \to e^- \overline{\nu}_e \nu_\mu)$ we have computed above is the total decay rate Γ_μ. Its inverse is therefore the muon's mean lifetime,

$$\tau_\mu = \frac{1}{\Gamma_\mu} \, . \tag{5.7}$$

The two numbers are thus equivalent, and it is in fact the mean lifetime which is usually quoted. For the muon it has been measured to be $\tau_\mu = 2.20$ microseconds (see Fig. 1.3). It is in fact this measurement which allows us to determine the value of the Fermi constant, so we cannot use the muon lifetime to test the theory. But once we have determined G_F we can use its value to predict the rates of other weak decays; we will do so for the τ lepton in Section 5.5.

5.4 The neutrino

The neutrino ν is a weakly interacting neutral lepton. It was predicted to exist by Pauli in 1930 in order to explain the apparent violation of conservation of energy observed in nuclear beta decay. [1] In the beta decay of ^{60}Co, for example, it was understood that the cobalt nucleus turns into ^{60}Ni and an electron is emitted. We now understand this to be the transformation of a neutron inside the nucleus into a proton, accompanied by emission of an electron. If we try to interpret this as the following decay of a cobalt nucleus at rest,

$$^{60}\mathrm{Co} \to ^{60}\mathrm{Ni} + e^- \, ,$$

then by energy conservation the electron should always have the same kinetic energy, T_e. Since the recoiling nucleus absorbs very little energy, this would be

$$T_e = m_{\mathrm{Co}} - m_{\mathrm{Ni}} - m_e \, . \tag{5.8}$$

But this was observed not to be the case. The electron kinetic energies varied continuously from zero up to a maximum amount $T_{\max}$, which depended on the nucleus in question. The measured values of $T_{\max}$ were in fact consistent with the amount one would expect for the two-body decay, i.e. the value predicted by equation (5.8).

Pauli's solution to the problem was to propose that an additional particle was being emitted in the decay. It must be electrically neutral in order to satisfy conservation of charge, and it must be weakly interacting, i.e. much more weakly interacting than a photon, or else it would have been detected. It was therefore called the neutrino ('little neutral one'), ν.

In 1934, Fermi proposed a theory of beta decay which incorporated Pauli's neutrino [30]. The neutrino was assumed to be a massless neutral particle, and the beta decay of the neutron was described as

[1] The prediction was (famously) never published but communicated to the participants of the Tübingen conference on radioactivity in a letter dated 4 December 1930, which began 'Liebe Radioaktive Damen und Herren,' – 'Dear radioactive ladies and gentlemen'. The letter can be viewed online from the Pauli Archive at CERN [29].

$$n \to p + \mathrm{e}^- + \overline{\nu} \,,$$

i.e. the proton and electron are accompanied by an antineutrino $\overline{\nu}$. Since the neutron, proton and electron were all understood to be spin 1/2 particles, conservation of angular momentum requires that the neutrino also be a fermion; in Fermi's theory it is assigned spin 1/2. Note that without the neutrino, beta decay cannot satisfy conservation of angular momentum, so that by proposing the new particle, Pauli actually rescued two conservation laws.

The neutrino was not observed experimentally until the 1950s. The experiment was carried out by Frederick Reines and Clyde Cowan, who used a nuclear reactor as an intense source of neutrinos (in fact antineutrinos), with a flux of 10^{13} cm^{-2}s^{-1}. A schematic illustration of the set-up is shown in Fig. 5.5.

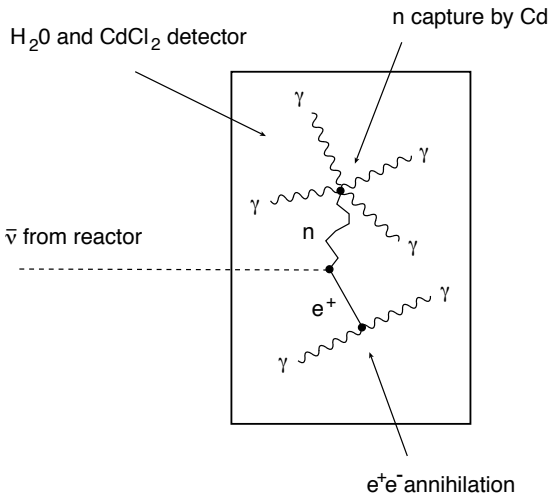

Figure 5.5: Schematic illustration of the experiment of Reines and Cowan to detect neutrinos.

The antineutrinos were directed at a large vat of water containing cadmium chloride ($CdCl_2$). An antineutrino can be absorbed by a proton in the water according to the inverse reaction of beta decay, i.e.

$$\overline{\nu} + p \to n + \mathrm{e}^+ \,.$$

The positron loses most of its energy and eventually annihilates with an electron, resulting in two photons,

$$\mathrm{e}^+\mathrm{e}^- \to \gamma\gamma \,.$$

The two photons emerge back-to-back each having energies approximately equal to the electron mass. They are registered in liquid scintillation detectors situated on both sides of the H_20 and $CdCl_2$ target. The neutron also wanders around in the target before finally being captured by a cadmium nucleus. The neutron capture occurs typically several microseconds after the positron annihilation, and is accompanied by emission of several gamma-ray photons; these are

also detected in the scintillation counters. Thus the observation of two simultaneous back-to-back photons each with energies of m_e followed several microseconds later by detection of several gamma-ray photons was a convincing indication that a neutrino interaction had taken place.

Even with an incident antineutrino flux of 10^{13} cm^{-2}s^{-1}, the observed event rate was only about 36 per hour, and out of these, approximately 80% were estimated to be due to background processes. To demonstrate convincingly that neutrinos were being observed, Reines and Cowan showed that the event rate was significantly higher with the nuclear reactor on than when it was off. Definitive results were published in 1959 [31].

In the 1960s it was further demonstrated that there are different types of neutrinos, each associated with a charged lepton [32]. Neutrinos produced in conjunction with muons, e.g. in the decay $\pi^+ \to \mu^+\nu$, were observed to participate in interactions in which a μ was again produced, and were therefore called ν_μ. Similarly, each charged lepton has its own neutrino type: ν_e, ν_μ and ν_τ. Although the indirect evidence for the tau neutrino has always been very strong, its direct observation was reported only in July 2000 [33].

Ever since Pauli proposed the neutrino, it was understood that it must be very light, since the maximum electron energies observed in beta decay did not leave any room for energy to be taken up by a neutrino rest mass. The most stringent limits on the mass of the electron type neutrino come from studies of beta decay of tritium (^{3}H), from which one obtained upper limits of around 3 eV.

In 1998, evidence for a non-zero neutrino mass was reported by the Super-Kamiokande experiment in Japan [34]. The experiment involved observation of electron- and muon-type neutrinos produced in secondary interactions of cosmic rays. It was found that the numbers of muon-type neutrinos created at large distances from the detector, namely, those coming from the opposite side of the earth, were significantly less than expected. The result was interpreted as evidence for 'neutrino oscillations', whereby muon-type neutrinos change into another type, such as ν_τ. The theoretical treatment of neutrino oscillations is beyond the scope of these lectures, but the important point is that in order for two neutrino species to oscillate, they cannot have the same mass. The difference of the masses squared of the two species participating in the oscillation was estimated to be in the range $5 \times 10^{-4} < \Delta m^2 < 6 \times 10^{-3}$ eV^2. Thus at least one species of neutrino must have a non-zero mass.

5.5 The tau lepton

The τ lepton was discovered in 1975 by M. Perl *et al.* in an experiment at the SPEAR electron-positron storage ring [35]. This experiment was investigating electron-positron interactions that produced various combinations of final-state particles. Out of approximately 350000 events, they observed 24 of the type

$$e^+e^- \to e^+\mu^- + \text{ missing energy },$$

i.e., the measured energy of the particles in the final state was significantly less than the energy of the e^+ and e^- from the initial state. Furthermore, by taking into account conservation of energy and momentum, one could show that the missing energy could not be accounted for by a single light particle such as a neutrino; it must have been carried away by at least two particles.

These events were interpreted as the production of a pair of new charged leptons, called the tau:

$$e^+e^- \to \tau^+\tau^- \ .$$

The lowest order Feynman diagram for this process is shown in Fig. 5.6. The τ was assumed to have the same electromagnetic and weak interactions as the other charged leptons, the electron and muon. The Feynman diagram for $\tau^+\tau^-$ production is thus the same as for $e^+e^- \to \mu^+\mu^-$ shown in Fig. 2.11(a), except with τ leptons in the final state instead of muons. In addition, the τ lepton was assumed to have its own neutrino partner, ν_τ.

The mass of the τ lepton is 1.777 GeV, i.e., around 3500 times more massive than the electron and 17 times more than the muon. Because of its greater mass, it can decay into combinations of particles that are forbidden in muon decay by energy conservation.

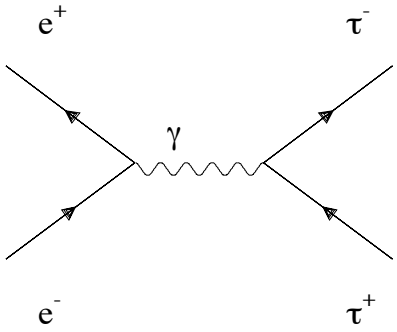

Figure 5.6: A Feynman diagram for the reaction $e^+e^- \to \tau^+\tau^-$.

In the 24 observed events, the τ leptons were interpreted as decaying according to $\tau^+ \to e^+\nu_e\overline{\nu}_\tau$ and $\tau^- \to \mu^-\overline{\nu}_\mu\nu_\tau$. The Feynman diagrams for these decays are shown in Fig. 5.7. In fact, many more than 24 $\tau^+\tau^-$ events were produced, but most were not recognized as such. Many decayed into hadrons (pions, kaons, etc.) which could not be distinguished from other events where hadron production results from a similar diagram where the virtual photon decays into a quark-antiquark pair.

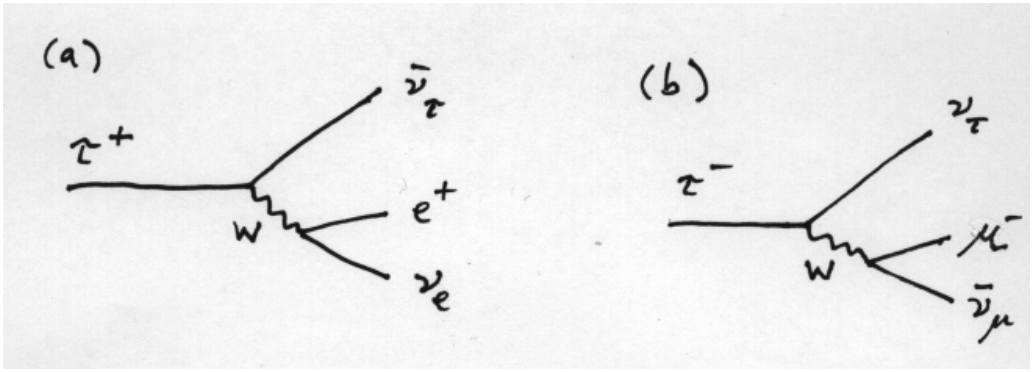

Figure 5.7: Feynman diagrams for the decays (a) $\tau^+ \to e^+\nu_e\overline{\nu}_\tau$ and (b) $\tau^- \to \mu^-\overline{\nu}_\mu\nu_\tau$.

Having determined the value of the Fermi constant from muon decay in Section 5.3, we can now use this to predict the decay rate of the τ. Because the weak and electromagnetic couplings

are assumed to be the same for all of the lepton types, the decay rate for $\tau^- \to e^- \nu_\tau \overline{\nu}_e$ should be the same as for the corresponding decay of the muon, $\mu^- \to e^- \nu_\mu \overline{\nu}_e$. By comparing with equation (5.6), we see that the decay rate $\Gamma(\tau^- \to e^- \nu_\tau \overline{\nu}_e)$ should be

$$\Gamma(\tau^- \to e^- \nu_\tau \overline{\nu}_e) = \frac{G_F^2 m_\tau^5}{192\pi^3} = \Gamma(\mu^- \to e^- \nu_\mu \overline{\nu}_e) \left(\frac{m_\tau}{m_\mu}\right)^5 . \tag{5.9}$$

In order to obtain the mean lifetime τ_τ, we cannot simply take the reciprocal of equation (5.9). This is because $\Gamma(\tau \to e^- \nu_\tau \overline{\nu}_e)$ is not the total decay rate Γ_τ, but rather only the partial rate for the particular decay mode $\tau \to e^- \nu_\tau \overline{\nu}_e$. The mean lifetime τ_τ is the reciprocal of the total decay rate Γ_τ, which itself is the sum of the decay rates for each of the possible decay modes (see equations (1.22) to (1.24)). The mean lifetime is thus

$$\tau_\tau = \frac{1}{\Gamma_\tau} = \frac{1}{\Gamma(\tau^- \to e^- \nu_\tau \overline{\nu}_e)} \times \frac{\Gamma(\tau^- \to e^- \nu_\tau \overline{\nu}_e)}{\Gamma_\tau} . \tag{5.10}$$

So to predict the mean τ lifetime, we still need the ratio of the partial to total decay rates, i.e. the branching ratio $\mathcal{B}(\tau^- \to e^- \nu_\tau \overline{\nu}_e)$,

$$\mathcal{B}(\tau^- \to e^- \nu_\tau \overline{\nu}_e) = \frac{\Gamma(\tau^- \to e^- \nu_\tau \overline{\nu}_e)}{\Gamma_\tau} . \tag{5.11}$$

This is simply the fraction of times that a τ^- decays into $e^- \nu_\tau \overline{\nu}_e$. To obtain it we need to compute Γ_τ, which we do by adding up all of the contributions from the possible decay modes.

In addition to the two decay modes shown in Fig. 5.7, the τ can decay into a ν_τ plus a quark and an antiquark. In the Standard Model the relevant couplings for the quarks are essentially the same as for the leptons, but the quarks can come in three different types or 'colours'. Furthermore, only one 'family' of quarks is light enough to participate in tau decay, so that in all there are five possible decay modes for the τ^-: $e^- \nu_\tau \overline{\nu}_e$, $\mu^- \nu_\tau \overline{\nu}_\mu$ and three times $\nu_\tau \overline{u} d'$, where the u is an up quark, the d' is to a good approximation the same as a d quark state (in fact it is a combination of down and strange quark states), and the factor of three comes from the three possible colours. So finally the result for the branching ratio is

$$\mathcal{B}(\tau^- \to e^- \nu_\tau \overline{\nu}_e) = \frac{1}{5} . \tag{5.12}$$

Combining the ingredients above, we can predict that the total decay rate of the τ to be

$$\Gamma_\tau = \Gamma(\tau^- \to e^- \nu_\tau \overline{\nu}_e) \times \frac{1}{\mathcal{B}(\tau^- \to e^- \nu_\tau \overline{\nu}_e)} = \Gamma(\mu^- \to e^- \nu_\mu \overline{\nu}_e) \left(\frac{m_\tau}{m_\mu}\right)^5 \times 5 . \tag{5.13}$$

We can therefore relate the mean lifetime of the τ to that of the μ by

$$\tau_\tau = \frac{1}{\Gamma_\tau} = \frac{1}{5} \tau_\mu \left(\frac{m_\mu}{m_\tau}\right)^5 . \tag{5.14}$$

Using the measured muon lifetime $\tau_\mu = 2.20$ microseconds and the masses $m_\mu = 0.1057$ GeV, $m_\tau = 1.777$ GeV, we finally obtain the prediction

$$\tau_\tau = 0.33 \text{ ps} . \tag{5.15}$$

A more refined calculation that takes into account the finite masses of final state particles and strong interaction effects gives a somewhat lower prediction of 0.290 ps for the mean lifetime and 17.8% for the branching ratio $\mathcal{B}(\tau^- \to \mathrm{e}^- \nu_\tau \overline{\nu}_\mathrm{e})$. The measurement uncertainties on the lifetime and on the branching ratios of the τ into lighter leptons are better than 1% and at this level they agree well with the Standard Model predictions. This constitutes an important test of the Standard Model, and in particular, it confirms that different families of leptons all have the same interactions; the only difference in their behaviour appears to stem from their different masses. This aspect of the Standard Model is called *lepton universality*.

Chapter 6

Hadrons

In this chapter we take a look at the discoveries and basic properties of some of the *hadrons*, i.e., particles that participate in the strong interaction.

6.1 Nuclear forces, the pion

According to the picture that emerged in the 1930s, the atomic nucleus consists of protons and neutrons bound together by a nuclear force with a range of around 1 fm. In 1935, Hideki Yukawa proposed a theory of the nuclear interaction based on an analogy with the then new theory of quantum electrodynamics. Whereas charged particles interact by exchanging photons, Yukawa proposed that nucleons interact by exchanging a particle that we now identify as the pion. To account for pp, np and nn interactions, the pion should come in three charge states: π^+, π^- and π^0. Some Feynman diagrams for nucleon–nucleon interaction by pion exchange are shown in Fig. 6.1.

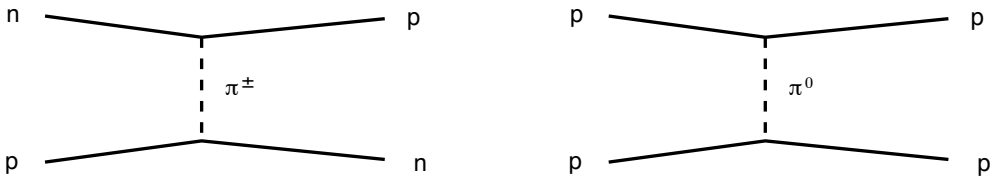

Figure 6.1: Feynman diagrams illustrating interaction of nucleons by pion exchange.

In theories of this type, one can show that the range r of the interaction is given by the inverse of the mass of the particle exchanged, i.e.,

$$r \sim \frac{1}{m} \, (\times \hbar c) \, , \tag{6.1}$$

where, using mass in MeV, the factor $\hbar c = 200$ MeV fm converts the range from units of inverse energy to length. Since the range was known to be around 1 fm, the mass of the exchanged particle was postulated to be of the order of 200 MeV.

In 1936, Anderson discovered the muon with a mass of around 100 MeV. This was close enough to Yukawa's prediction that one immediately tried to identify the muon with the particle

responsible for the nuclear force. Anderson's muon was highly penetrating, however, whereas Yukawa's particle was predicted to interact strongly with matter. Experiments by Conversi *et al.* in 1947 showed that negative muons often come to rest in matter and decay [36]. For Yukawa's, particle, however, this should not be possible, since it would quickly be absorbed by a nucleus before having the chance to decay.

Nevertheless, the particle corresponding to Yukawa's prediction was soon discovered using fine grain photographic emulsions. Charged particles from cosmic rays create ionization in the emulsion producing visible tracks. The tracks can be reconstructed by assembling a series of photographs taken through a microscope with the focal plane adjusted to different depths. Emulsions were used for a number of important discoveries, but then fell out of favour for many years because of the painstaking work required to analyze them. Recently, however, computerized pattern recognition programs have been developed that allow for automatic scanning of emulsions, and they are currently enjoying a limited comeback (see e.g. [15]).

Photographs of cosmic ray tracks in photographic emulsions made by D. Perkins [37] in 1947 showed a particle of intermediate mass that did in fact interact strongly, producing a number of secondary particles emanating from a nuclear disintegration. The nature of the intermediate mass particle thus seemed unclear.

The mystery was solved by Lattes *et al.*, who found pictures of cosmic ray interactions in emulsions that showed the decay of one intermediate mass particle into another, i.e., $\pi \to \mu$ [38]. The muons in the observed events all came to rest after travelling about 600 μm. That is, they all had about the same kinetic energy. Furthermore, the ionization rates indicated that the particles were moving at speeds significantly less than c. The events could be explained by the decay of a particle almost at rest into two other particles, one of which escapes unseen. This is now understood to be one of the decays

$$\begin{aligned} \pi^+ &\to \mu^+ \nu_\mu \\ \pi^- &\to \mu^- \overline{\nu}_\mu \, . \end{aligned}$$

The mass of the charged pion is 139.6 MeV, i.e. about a third heavier than the muon. Therefore the muons from the decay are not highly relativistic, and are thus sufficiently highly ionizing to produce tracks. The muons in these events presumably also decayed into an electron and neutrinos, but the electron would have been highly relativistic and therefore minimum ionizing, and did not produce a visible track. Later pictures with more sensitive emulsions were able to capture the entire decay chain $\pi \to \mu \to$ e. Some examples are shown in Fig. 6.2 [39].

In our modern view, the pion is the lightest example of a meson, a bound state of a quark and an antiquark. The π^+ is $u\overline{d}$ and its antiparticle the π^- is $d\overline{u}$. Pion decay can be represented by the Feynman diagram in Fig. 6.3(a). The virtual mass of the W is equal to the pion mass, which is much less than the W rest mass, i.e., in the propagator $1/(q^2 - M_{\rm W}^2)$ one has $q^2 = m_\pi^2 \ll M_{\rm W}^2$. Therefore the propagator is approximately $-1/M_{\rm W}^2$. This factor is responsible for the suppression of the decay amplitude and results in the comparatively long lifetime for the charged pion: $\tau = 2.60 \times 10^{-8}$ s or $c\tau = 7.80$ m.

Experiments with the 184-inch synchrocyclotron at Berkeley succeeded in producing neutral pions [40]. These decay very quickly into two photons according to the Feynman diagram in

Figure 6.2: Emulsion photographs showing the decay chain $\pi \to \mu \to$ e [39].

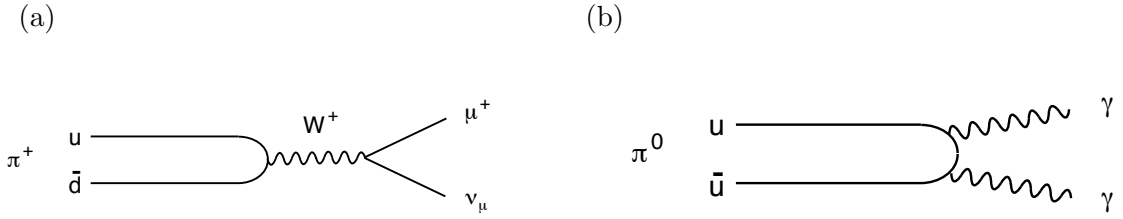

Figure 6.3: Feynman diagrams for the decay of (a) a charged pion, (b) a neutral pion.

Fig. 6.3(b). In the quark model, the π^0 is a superposition of $u\overline{u}$ and $d\overline{d}$ states. In contrast to the charged pion, the π^0 decay is purely electromagnetic and is not suppressed by a W propagator. Its mean lifetime is therefore much shorter: $\tau = 8.4 \times 10^{-17}$ s or $c\tau = 25.1$ nm. Thus the only thing we observe in a detector are the two photons. We can determine that they came from a π^0 by finding the invariant mass of the two photon system, which will be equal to the π^0's mass of 135.0 MeV.

6.2 Strange particles

In 1947, Rochester and Butler, working in Manchester, published the cloud chamber photograph shown in Fig. 6.4 [41]. Below the plate on the right is an inverted 'V'. This appears to be the decay of a neutral particle, which itself was produced inside the plate. This was the first example

of a V^0 particle, i.e., a neutral particle leading to a V-shaped pair of tracks. Over the next decade a number of different types of V^0s were found, all distinguished by a lifetime sufficiently long to lead to a visibly displaced decay vertex.

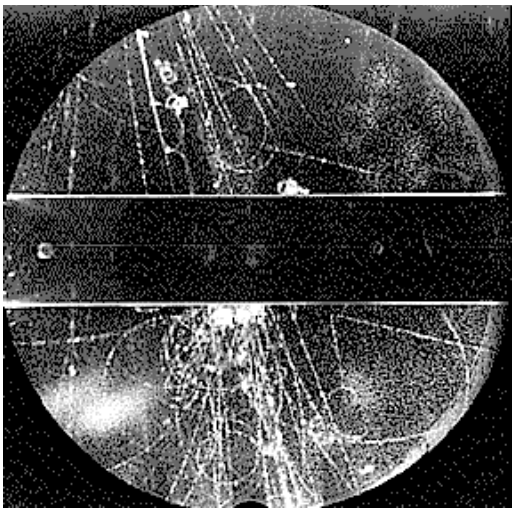

Figure 6.4: Cloud chamber photograph by Rochester and Butler showing a V^0 particle [41].

The first thing we would like to know about the V^0 in Fig. 6.4 is its mass. This can be obtained by computing the invariant mass of the two particles of the V. Their momenta are measured to be $p_1 = 340\,\mathrm{MeV}$, $p_2 = 350\,\mathrm{MeV}$, and their opening angle is 66.6°. The invariant mass squared is

$$\begin{aligned} m_{\mathrm{V}}^2 &= (E_1 + E_2)^2 - (\mathbf{p}_1 + \mathbf{p}_2)^2 \\ &= E_1^2 - p_1^2 + E_2^2 - p_2^2 + 2E_1E_2 - 2\mathbf{p}_1 \cdot \mathbf{p}_2 \\ &= m_1^2 + m_2^2 + 2\sqrt{p_1^2 + m_1^2}\sqrt{p_2^2 + m_2^2} - 2p_1p_2\cos\theta\ . \end{aligned} \tag{6.2}$$

To evaluate this, we need to know the rest masses of the two daughter particles. From their momenta and ionization rates, they are consistent with being pions. Using $m_1 = m_2 = m_\pi = 139.6$ MeV gives $m_{\mathrm{V}} = 470$ MeV, with an uncertainty due to the limited momentum resolution of around 25%.

The unseen particle in Fig. 6.4 is now known as the neutral kaon, which has a mass of 497.7 MeV. In fact it comes in two varieties with different lifetimes, known as 'short' and 'long'; the one in the figure is a 'K-short' or $\mathrm{K}^0_{\mathrm{S}}$, which has a mean lifetime of $\tau = 0.893 \times 10^{-10}$ s or equivalently $c\tau = 2.68$ cm.

In the quark model, the $\mathrm{K}^0_{\mathrm{S}}$ and $\mathrm{K}^0_{\mathrm{L}}$ are superpositions of $d\bar{s}$ and $s\bar{d}$ states. The combination $d\bar{s}$ is called a K^0 and $s\bar{d}$ is its antiparticle, the $\overline{\mathrm{K}}^0$. The states produced in the strong interaction are K^0 and or $\overline{\mathrm{K}}^0$, but for reasons we will not enter into now, the particles of well-defined mass, lifetime and decay modes are the superpositions $\mathrm{K}^0_{\mathrm{S}}$ and $\mathrm{K}^0_{\mathrm{L}}$. The point to emphasize here is that these are the first particles we've encountered that contain a strange quark or antiquark. The fact that their masses are greater than that of the pion reflects the higher mass of the s quark relative to u or d. The $\mathrm{K}^0_{\mathrm{S}}$ decays about 2/3 of the time as $\mathrm{K}^0_{\mathrm{S}} \to \pi^+\pi^-$ and the remainder mostly

to $\pi^0\pi^0$. Feynman diagrams representing the decays are shown in Fig. 6.5. In the diagrams we have only drawn the K^0 (i.e. $d\bar{s}$) state, so this only represents part of the amplitude for the K^0_S decay.

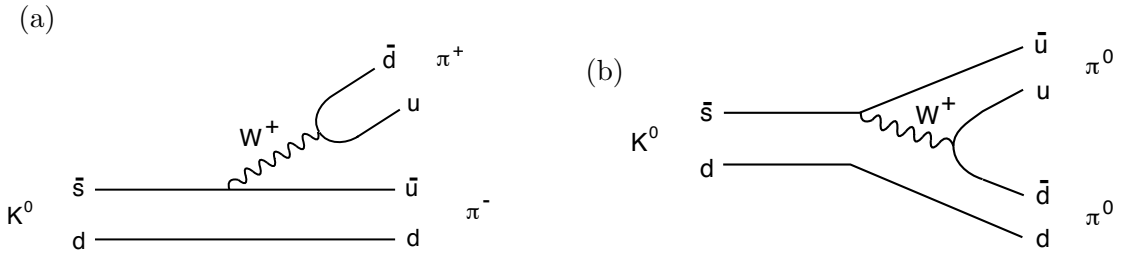

Figure 6.5: Feynman diagrams illustrating the decays (a) $K^0 \to \pi^+\pi^-$ and (b) $K^0 \to \pi^0\pi^0$.

Cloud chamber photographs soon revealed charged kaons K^+ ($u\bar{s}$), K^- ($s\bar{u}$) and the lambda baryon Λ (uds). The Λ also gives a V^0 type appearance when it decays into a proton and a charged pion: $\Lambda \to p\pi^-$.

The reason that particles such as the K^0 and Λ are said to be 'strange' is that they can be produced in pairs easily, with a production cross section that corresponds to a typical strong interaction process. Their decay rates, however, are comparatively long, indicating a weak decay. A typical example could be seen by shooting a π^- beam at a liquid hydrogen bubble chamber, giving events of the type shown in Fig. 6.6.

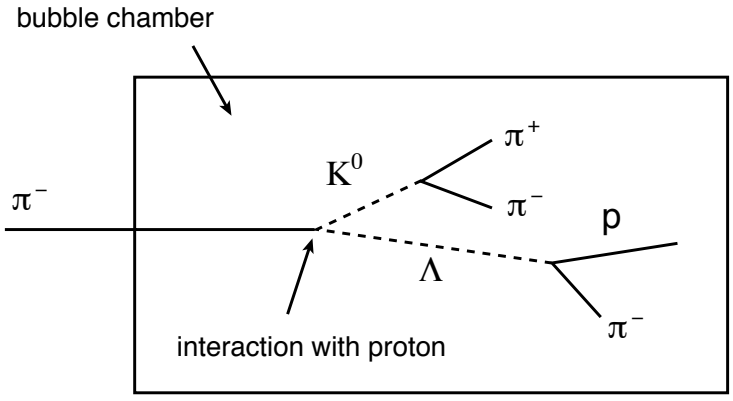

Figure 6.6: The Berkeley 72-inch bubble chamber [19]. Schematic illustration of a bubble chamber event showing the reaction $\pi^- p \to \Lambda K^0$ followed by the decays $\Lambda \to p\pi^-$ and $K^0 \to \pi^+\pi^-$.

The production reaction $\pi^- p \to \Lambda K^0$ can be represented by the Feynman diagram in Fig. 6.7. A u quark from the proton annihilates with the $\overline{u}$ from the π^- into a gluon. Recall that in the $q\bar{q}g$ vertex, the quarks are always of the same flavour. The gluon then splits into an $s\bar{s}$ pair. The d and $\overline{s}$ group together to form a neutral kaon and the u, d and s form the Λ baryon. This is really a highly simplified view of the production reaction, since this diagram only contains a single gluon and by itself would represent a poor approximation for the total amplitude. Additional diagrams with more gluons being exchanged will make significant contributions and in fact the perturbative predictions for hadronic reactions such as these are only reliable in restricted cases. But more importantly, the diagram shows that $\pi^- p \to \Lambda K^0$ proceeds entirely through the strong interaction and that the s and $\overline{s}$ are produced together as a pair.

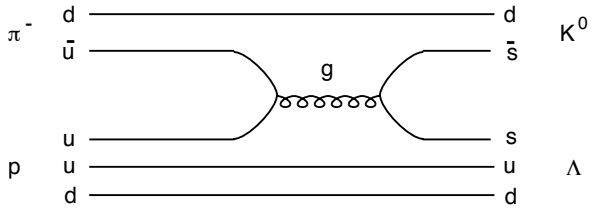

Figure 6.7: Feynman diagram for the reaction $\pi^- \mathrm{p} \to \Lambda \mathrm{K}^0$.

The s and $\bar{s}$ cannot decay by the strong interaction, and once they have separated they cannot annihilate with each other. So the only decay is through the weak interaction. We've already seen a Feynman diagram for the K^0 decay in Fig. 6.5. The Λ decay has a similar diagram, shown in Fig. 6.8.

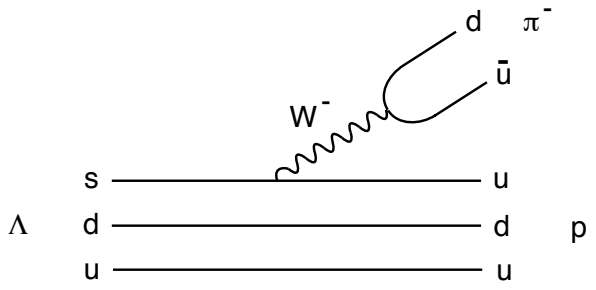

Figure 6.8: Feynman diagram for the decay $\Lambda \to \mathrm{p}\pi^-$.

These types of events were discovered in the 1940s and 50s, well before the quark picture of hadrons, which was not proposed until 1964. Before then one associated a new quantum number called *strangeness* S with each of the new hadrons. Using the quark picture, the strangeness S is simply the number of $\bar{s}$ antiquarks minus the number of s quarks in the hadron. So for example, the Λ baryon (uds) has a strangeness of $S = -1$. It was postulated that strangeness was conserved in the strong interaction, but was not conserved in weak decays. We now understand this to mean that a gluon can split into an $s\bar{s}$ pair, but this has a net strangeness of zero. In a weak decay, however, the s quark decays to a u quark and a virtual W^-, which then itself decays into leptons or quarks. Thus the net strangeness changes.

Shortly after the observation of the kaon and Λ baryon, cloud chamber events were found with a long-lived charged particle decaying into a light charged particle plus a V^0 [42, 43]. These events contained what is now called the Ξ^-, which is a baryon containing dss and thus has strangeness $S = -2$. It is also sometimes referred to as the cascade particle, since one first sees the decay $\Xi^- \to \Lambda\pi^-$, in which one s quark decays and the other is passed on to the Λ, followed by the decay $\Lambda \to \mathrm{p}\pi^-$, in which the remaining s quark decays. A cloud chamber photograph in which both decays can be seen is shown in Fig. 6.9 [43].

The existence of a baryon with $S = -3$ was predicted theoretically before its discovery in a spectacular event obtained with the Brookhaven 80-inch hydrogen bubble chamber. This is called the Ω^- baryon, which consists of three s quarks. The photograph and a line drawing showing the entire decay chain are shown in Fig. 6.10 [44].

The masses and mean lifetimes of the mesons and baryons containing at least one strange quark combined with u or d quarks are shown in Table 6.1. Notice in particular that the baryons with more strange quarks have higher masses, since the strange quark itself has a higher mass than u or d. The lifetimes are mostly of the order 10^{-10} s except for the Σ^0, which decays

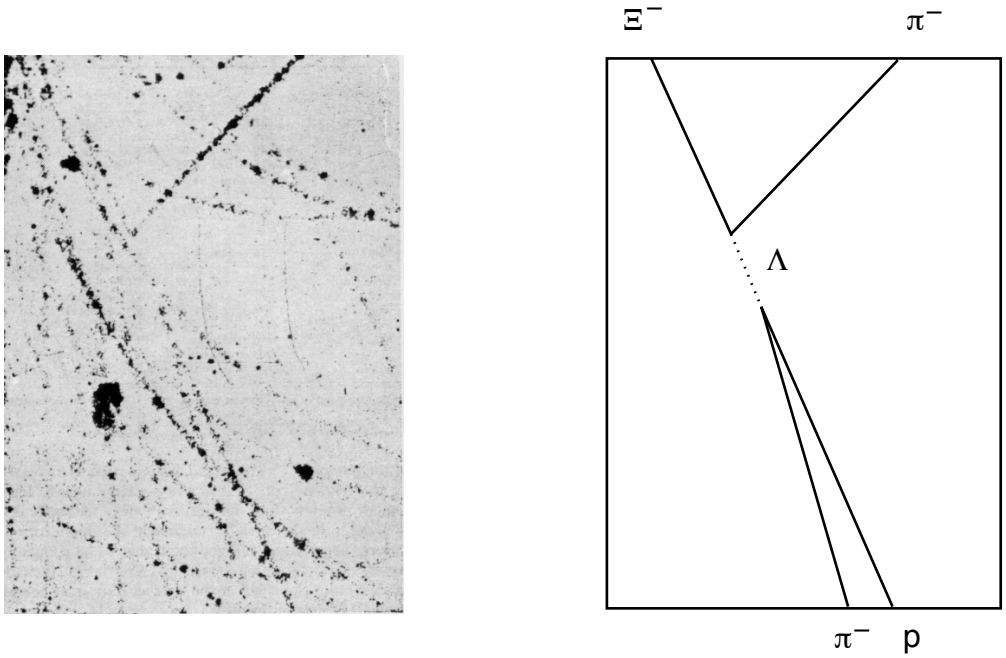

Figure 6.9: Cloud chamber photograph (left) and its interpretation (right) showing the decay $\Xi^- \to \Lambda\pi^-$ followed by $\Lambda \to \mathrm{p}\pi^-$ [43].

electromagnetically, and thus much more quickly, into $\Lambda\gamma$.

6.3 Hadron resonances

The development of synchrotrons in the 1940s allowed one to produce pions by bombarding a nuclear target with an incident proton beam. The pions produced in this way can be sent through a magnet and a particular momentum range selected. They can then be directed at a target where they participate in another scattering reaction. This allowed one to study processes such as

$$\begin{aligned} \pi^-\mathrm{p} &\to \pi^-\mathrm{p}\,, \\ \pi^+\mathrm{p} &\to \pi^+\mathrm{p}\,. \end{aligned}$$

Measured cross sections for $\pi^-\mathrm{p} \to \pi^-\mathrm{p}$ are shown in Fig. 6.11 as a function of the centre-of-mass energy [7]. One sees a series of peaks with widths on the order of 100 MeV.

We have already see in Chapter 2 that when computing the amplitude for a reaction, the Feynman rules tell us to include a propagator of the form

$$\frac{1}{q^2 - M^2} \tag{6.3}$$

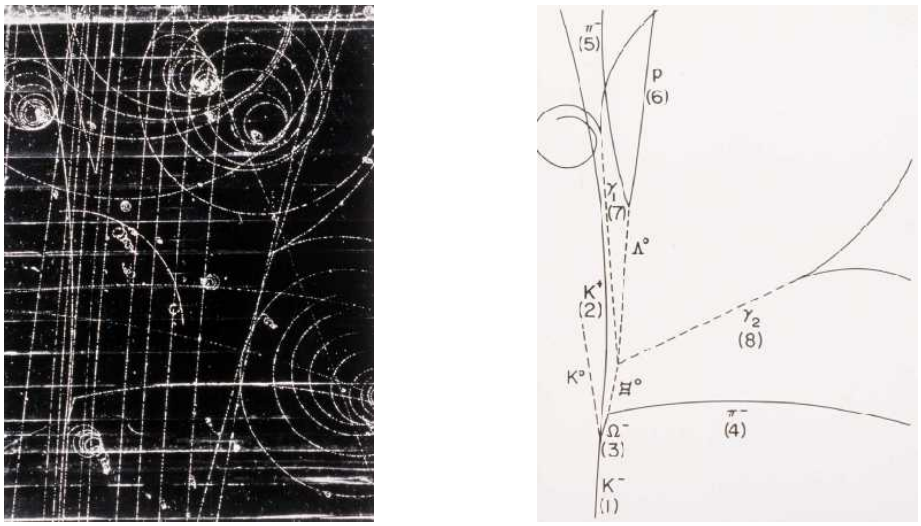

Figure 6.10: The bubble chamber photograph (left) and its interpretation (right) showing the first identified Ω^- baryon [44].

for an intermediate state particle of virtual mass q^2 and real mass M^2. This will lead to a large enhancement of the amplitude called a resonance when q^2 is close to M^2.

This is indeed how the peaks in the cross section are explained. For the first peak in the cross section of $\pi^-\mathrm{p} \to \pi^-\mathrm{p}$, for example, one postulates the existence of a neutral particle called the Δ^0 that appears as an intermediate state as indicated in the Feynman diagram in Fig. 6.12. Note that here, q^2 is the invariant mass squared of the incoming pion–proton system, which is simply the centre-of-mass energy squared. The position of the peak gives the mass of the Δ^0, around 1.23 GeV. Additional particles with higher masses are postulated to account for all of the observed peaks.

If the amplitude for the reaction contains a factor $1/(q^2 - M^2)$, one might expect a predicted cross section of infinity for $E_{\mathrm{cm}} = M$, which clearly cannot be correct. This is a sign that not enough terms have been included in the perturbation series. A better prediction can be obtained by using a different formula for the propagator which effectively takes into account a particular subset of higher order diagrams. How the diagrams themselves are evaluated is beyond the scope of this course, but the recipe for the improved propagator is quite simple. One makes the replacement

$$M \to M - \frac{i}{2}\Gamma \,, \tag{6.4}$$

where Γ is the total decay rate (inverse mean lifetime) of the intermediate state particle. The amplitude $\mathcal{M}$ therefore contains the factor

Table 6.1: Hadrons containing at least one s quark combined with u or d quarks [7].

particle	quarks	mass (MeV)	τ (s)	$c\tau$
K^0_S	$d\bar{s}$, $s\bar{d}$	497.7	0.893×10^{-10}	2.68 cm
K^0_L	$d\bar{s}$, $s\bar{d}$	497.7	5.17×10^{-8}	15.5 m
K^+, K^-	$u\bar{s}$, $s\bar{u}$	493.7	1.24×10^{-8}	3.71 m
Λ	uds	1115.7	2.63×10^{-10}	7.89 cm
Σ^+	uus	1189.4	0.799×10^{-10}	2.40 cm
Σ^0	uds	1192.6	7.4×10^{-20}	2.22×10^{-11} m
Σ^-	dds	1197.4	1.48×10^{-10}	4.43 cm
Ξ^0	uss	1314.9	2.90×10^{-10}	8.71 cm
Ξ^-	dss	1321.3	1.64×10^{-10}	4.91 cm
Ω^-	sss	1672.5	0.822×10^{-10}	2.46 cm

$$\begin{aligned} \mathcal{M} &\propto \frac{1}{q^2 - (M - \frac{i}{2}\Gamma)^2} \\ &= \frac{1}{q^2 - M^2 + iM\Gamma + \Gamma^2/4} \\ &\approx \frac{1}{q^2 - M^2 + iM\Gamma} \,, \end{aligned} \tag{6.5}$$

where the approximation is valid for $\Gamma \ll M$. The cross section is proportional to the absolute square of the amplitude, which means that near the resonance peak, we have

$$\sigma \propto |\mathcal{M}|^2 \propto \frac{1}{(q^2 - M^2)^2 + M^2\Gamma^2} \,. \tag{6.6}$$

This functional form is a particular version of a *Breit–Wigner* curve, and it describes the $E_{\rm cm}$ dependence of the resonance peaks in Fig. 6.11 where $E^2_{\rm cm} = q^2$ and M is the mass of the resonance particle. Often a somewhat different version is seen, namely,

$$\sigma(E_{\rm cm}) = \frac{\Gamma^2}{4} \frac{\sigma_0}{(E_{\rm cm} - M)^2 + \Gamma^2/4} \,, \tag{6.7}$$

where σ_0 is the cross section at $E_{\rm cm} = M$. You can easily verify that in the region of the peak, i.e., $E_{\rm cm} \approx M$, the two curves (6.6) and (6.7) are equivalent. It is often easier to work with this second form. A sketch of a resonance cross section vs. $E_{\rm cm}$ as predicted by (6.7) is shown in Fig. 6.13.

Note that at the points $E_{\rm cm} = M \pm \Gamma/2$, the cross section is equal to half its peak value. That is, Γ is the full width at half maximum of the peak, and often we call Γ the 'width' of the resonance.

We mentioned that the parameter Γ is the decay rate of the intermediate state particle. We can see this by considering the energy dependence of the wave function of a particle at rest,

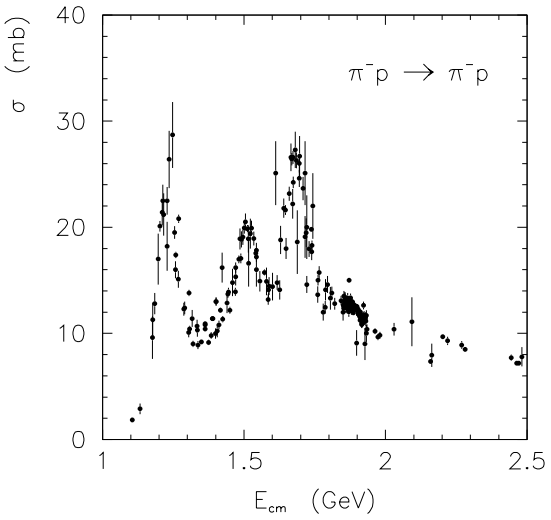

Figure 6.11: Measured cross section as a function of centre-of-mass energy for the reaction $\pi^- \mathrm{p} \to \pi^- \mathrm{p}$ [7].

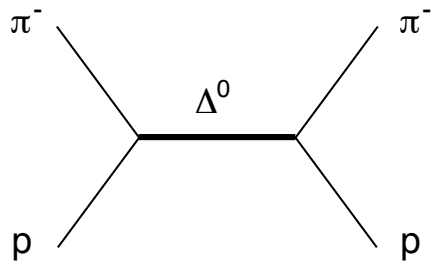

Figure 6.12: Feynman diagram for the reaction $\pi^- \mathrm{p} \to \pi^- \mathrm{p}$ showing the Δ^0 in the intermediate state.

$$\psi(t) \sim e^{-iEt} = e^{-iMt} \,, \tag{6.8}$$

where recall we are working in units where $\hbar = 1$ and $E = M$ for a particle at rest. Making the replacement $M \to M - \frac{i}{2}\Gamma$ gives

$$\psi(t) \sim e^{-i(M - \frac{i}{2}\Gamma)t} \,. \tag{6.9}$$

The probability of finding the particle anywhere at a time t is proportional to $|\psi(t)|^2$,

$$|\psi(t)|^2 \sim |e^{-i(M - \frac{i}{2}\Gamma)t}|^2 = e^{-\Gamma t} \,. \tag{6.10}$$

That is, the particle will decay at a random time t whose probability is given by an exponential distribution, which we have already encountered in equation (1.20), i.e.,

$$p(t) = \frac{1}{\tau}\, e^{-t/\tau} \,. \tag{6.11}$$

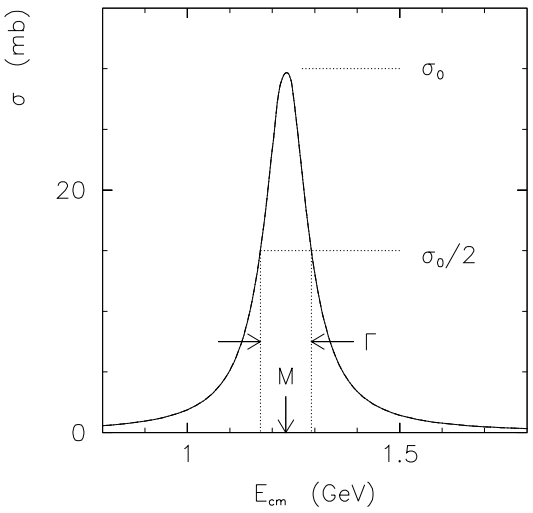

Figure 6.13: Prediction based on the Breit–Wigner curve for the shape of a resonance cross section.

Comparing (6.10) with (6.11) shows that $\Gamma = 1/\tau$ is the inverse mean lifetime or decay rate of the resonance particle.

Most of the resonances observed in hadron reactions as in Fig. 6.11 have widths of $\Gamma \approx 100$ MeV. The mean lifetimes of the intermediate state particles are therefore approximately

$$\tau = \frac{1}{\Gamma} = \frac{1}{100 \text{ MeV}} \times \frac{\hbar c}{c} = \frac{1}{100 \text{ MeV}} \times \frac{200 \text{ MeV fm}}{3.0 \times 10^{23} \text{ fm/s}} \approx 10^{-23} \text{ s} . \tag{6.12}$$

This is so short that particles such as the Δ^0 never live long enough to be observed directly. The mean lifetime corresponds approximately to the time it takes for light to travel the diameter of a proton.

Since $\Gamma = 1/\tau$, a shorter lifetime results in broader resonance curves. This is an illustration of the uncertainty principle, which says that the uncertainty ΔM in the mass of a particle and its lifetime τ must satisfy

$$\Delta M \, \tau \sim 1 . \tag{6.13}$$

That is, the width of the resonance Γ represents the uncertainty ΔM in the mass of the intermediate state.

Resonance particles are copiously produced in high energy collisions. At centre-of-mass energies near the Z mass, which is where much of the LEP collider's data was taken, the reaction $e^+e^- \to$ hadrons results in around 20 long-lived charged particles, most of which are pions. We have seen pictures of events of this type from the ALEPH detector in Figs. 4.2.2 and 4.2.3. If some of these particles are the decay products of short-lived resonances, then we can determine which ones these are by measuring their invariant mass.

For example, we can consider all possible pairs of a positive pion with a negative pion, i.e., if there are ten of each in an event, then there are 100 possible $\pi^+\pi^-$ pairs. For each pair, we can compute the invariant mass and enter the value in a histogram, an example of which is shown in Fig. 6.14 (here in fact only $\pi^+\pi^-$ combinations having a total momentum of at least

25 GeV are shown). There is a peak at around 770 MeV with a width of $\Gamma \approx 150$ MeV. This is a short-lived particle called the ρ^0 having a mass equal to the position of the peak, 770 MeV. Of course most of the pairs of π^+ and π^- are not the decay products of a ρ^0; their invariant mass is some random value that contributes to the smooth background (often called *combinatorial* background). By subtracting the background and measuring the area under the remaining peak, we can estimate the number of ρ^0 mesons produced. Measurements by ALEPH determined an average of around 1.5 ρ^0 mesons produced per event [45].

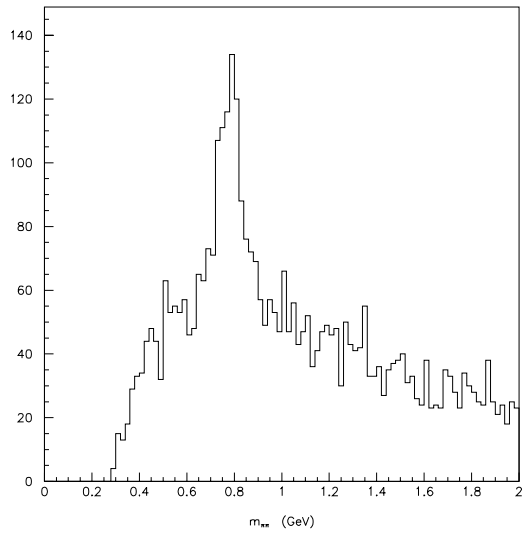

Figure 6.14: Invariant mass distribution for pairs of oppositely charged pions from the reaction $e^+e^- \to$ hadrons.

6.4 The quark model of hadrons

By the early 1960s, over 100 different resonances had been discovered, having widths ranging from several MeV to several hundred MeV. This proliferation of particles was a clear sign that hadrons were not truly elementary, but rather must be composed of smaller constituents. In 1964, Gell-Mann and Zweig independently proposed that baryons and mesons are composed of fractionally charged, spin-1/2 particles, called quarks by Gell-Mann and aces by Zweig. The name 'quark', inspired by the line 'Three quarks for Muster Mark' from James Joyce's *Finnigen's Wake*, won out. To describe the particles known at the time, only the u, d and s quarks were needed. All the known baryons could be classified as a combination of three quarks, and all the mesons as a quark and an antiquark.

The long-lived hadrons such as the proton, neutron, pion and kaon were interpreted as the lowest energy (i.e. lowest mass) bound states of the quarks. For the baryons, this is a state of relative angular momentum $L = 0$ and total angular momentum $J = 1/2$. For the mesons, the lowest energy states are likewise $L = 0$ and the spins are aligned antiparallel, resulting in $J = 0$.

The parity of the lightest mesons is negative. This results from the fact that the intrinsic parity of a fermion is opposite to that of the antifermion, which itself follows from the Dirac equation. The parity of the quark-antiquark system $P_{q\bar{q}}$ is therefore the product of the quark and antiquark intrinsic parities times the factor $(-1)^L$, which accounts for the behaviour of the spatial part of the wave function under the parity operation. Thus we have

$$P_{q\bar{q}} = P_q P_{\bar{q}} (-1)^L = (-1)^{L+1} \ , \tag{6.14}$$

which gives $P_{q\bar{q}} = -1$ for the $L = 0$ mesons. Particles with $J = 0$ and negative parity are called *pseudoscalars*, usually written with the notation $J^P = 0^-$. The term *scalar* means spin 0, since there is only one possible spin state. The prefix 'pseudo' refers to the negative parity. The pseudoscalar mesons include the various charge states of the pion and the kaon as well as two other particles called the η (eta) and the η' (eta prime). In similar way, one can show that the lowest energy wave function for a three quark system has positive parity, i.e. the proton is a $\frac{1}{2}^+$ baryon.

The short-lived resonances are interpreted as excited states. For example, the Δ^0 consists of udd in a $J = 3/2$ state with positive parity. It is basically an excited state of a neutron. The ρ^0 meson has the same quark content as the π^0, namely, a superposition of $u\bar{u}$ and $d\bar{d}$. In the ρ^0, however, the spins are aligned parallel giving an $L = 0$, $J = 1$ state. The parity is $1 \times -1 \times (-1)^L = -1$. Particles with $J^P = 1^-$ are called *vector* particles. These include vector mesons such as the ρ^0 as well as vector gauge bosons like the photon, $\mathrm{W}^\pm$ and Z.

These spin and parity assignments have consequences for the predicted angular distributions in scattering and in decays. A large effort in the 1950s and 60s was put into determining the spin and parity of the observed hadrons by means of such experiments. Higher angular momentum states have even higher masses and larger widths. A complete list of resonances and their properties is compiled yearly by the Particle Data Group [7] [1]. Some of the more important ones are listed in Table 6.2.

Table 6.2: Some hadron resonances and their properties [7].

particle	quarks	J^P	mass (MeV)	Γ (MeV)
ρ^0	$u\bar{u}$, $d\bar{d}$	1^-	770	150
$\rho^\pm$	$u\bar{d}$, $d\bar{u}$	1^-	770	150
ω	$u\bar{u}$, $d\bar{d}$	1^-	782	8.4
$\mathrm{K}^{*\pm}$	$s\bar{u}$, $u\bar{s}$	1^-	892	51
K^{*0}	$d\bar{s}$	1^-	896	50
ϕ	$s\bar{s}$	1^-	1020	4.4
Δ^{++}	uuu	$3/2^+$	1230	120
Δ^+	uud	$3/2^+$	1230	120
Δ^0	udd	$3/2^+$	1230	120
Δ^-	ddd	$3/2^+$	1230	120
Σ^{*+}	uus	$3/2^+$	1383	36
Σ^{*0}	uds	$3/2^+$	1384	36
Σ^{*-}	dds	$3/2^+$	1387	39

If hadrons consist of quarks, then it seemed natural that one should be able to break apart a proton in high energy collisions and see fractionally charged particles, similar to the way in which atoms can be ionized into their constituent electrons and nuclei. Searches for free quarks

[1] For more information on the quantum numbers used in the PDG, see PDG's Chapter 15: Quark Model

can exploit the fact that the ionization rate of a particle passing through matter is proportional to the square of its charge. Therefore charge 2/3 quarks should have an ionization rate equal to 4/9 that of a π^+, and they would show up as a separate band in a plot of dE/dx vs. momentum such as Fig. 4.7. Many searches of this type have been carried out and no evidence for free quarks has been found.

Thus despite the success of the quark model at classifying the large number of observed hadrons, it was not clear to what extent quarks should be considered as 'real particles', rather than perhaps just a clever bookkeeping trick. Convincing confirmation of the quark picture came in the late 1960s in electron–proton scattering experiments, which we consider in the next chapter.

Chapter 7

Inside hadrons

In this chapter we look at electron–proton scattering experiments and examine what they tell us about the internal structure of hadrons. First we consider elastic e^-p scattering, i.e., an electron and proton collide and the same two particles come out. By looking at the probability for scattering as a function of the angle of the outgoing electron, we will determine that the proton is not a point particle but rather has a size of around 1 fm. More details on this topic can be found in Martin and Shaw, Section 7.3, and in Perkins Sections 6.2–6.5.

Next, we look at inelastic e^-p scattering. That is, an electron and proton collide, and an electron plus a number of other particles, e.g., a proton plus several pions, come out. By looking at the probability of this reaction as a function of the energy and angle of the scattered electron, we will see evidence that the charge of the proton is not uniformly spread out but rather is concentrated in point-like scattering centres called *partons*. These are identified with the quarks, which we introduced in the previous chapter as a means of classifying the large number of observed hadrons. More material on this can be found in Martin and Shaw Section 7.4. Inelastic electron–proton scattering and the parton model are discussed at length, and at a more advanced level, in Perkins Chapter 8 and Halzen and Martin Chapter 8.

7.1 Elastic electron–proton scattering

7.1.1 The basic set-up, differential cross sections

Experiments in the 1950s on elastic electron–proton scattering provided the first evidence for the finite size of the proton. At that time, electron beams of several hundred MeV energy could be produced. The distance scale that can be resolved by an electron of momentum p is given by the (reduced) de Broglie wavelength,

$$\frac{\lambda}{2\pi} = \frac{\hbar}{p} = \frac{\hbar c}{pc} = \frac{197.3\,\text{MeV-fm}}{pc} \,. \tag{7.1}$$

So a 200 MeV electron beam will be able to resolve structure at a distance scale of about 1 fm.

The basic experimental set-up of e^-p scattering is sketched in Fig. 7.1. Electrons are incident on a hydrogen target and are scattered by an angle θ. The azimuthal angle of the scattered particle about the incident direction is denoted by ϕ.

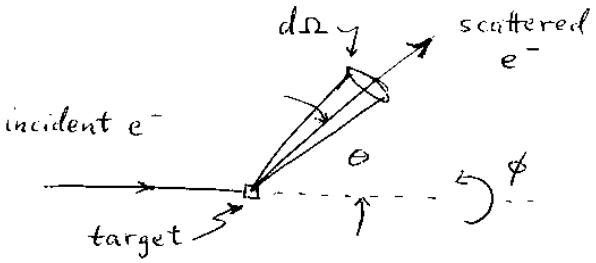

Figure 7.1: The experimental set-up for elastic ep scattering.

In Chapter 1.6 we saw that the probability for a scattering event to occur can be expressed by the cross section. We now define the event to mean that the outgoing particle has a scattering angle θ and azimuthal angle ϕ, and is contained within a cone of solid angle $d\Omega$ centered about the direction defined by θ and ϕ. In this case the number of scattering events will be proportional to $d\Omega$, and so the equation relating the number of scattering events into $d\Omega$ to the luminosity $\mathcal{L}$ can be written

$$\left(\begin{array}{c} \text{number scattered} \\ \text{into } d\Omega(\theta,\phi) \end{array} \right) = \frac{d\sigma}{d\Omega}(\theta,\phi)\, d\Omega \times \int \mathcal{L}\, dt \; . \tag{7.2}$$

The quantity $d\sigma/d\Omega$ is called the *differential cross section*, which in general is a function of the angles θ and ϕ. If we want the number of events scattered at any angle, then we integrate (7.2) over θ and ϕ,

$$\left(\begin{array}{c} \text{number scattered} \\ \text{at any angle} \end{array} \right) = \int_0^{2\pi} d\phi \int_{-1}^{1} d\cos\theta \, \frac{d\sigma}{d\Omega}(\theta,\phi) \times \int \mathcal{L}\, dt \; , \tag{7.3}$$

where have expressed the solid angle element as

$$d\Omega = \sin\theta \, d\theta \, d\phi = d\cos\theta \, d\phi \; . \tag{7.4}$$

Comparison with equation (1.18) shows that the integral of the differential cross section over all angles is simply the total cross section σ.

7.1.2 Predictions for $d\sigma/d\Omega$

We now want to see what the theoretically predicted differential cross section is for electron-proton scattering, first in the case where both particles are treated as point-like, i.e., having no internal structure. A Feynman diagram for *ep* scattering is shown in Fig. 7.2. The incoming electron has a four-momentum $p_1^\mu = (E_1, \mathbf{p}_1)$ and the outgoing electron has $p_2^\mu = (E_2, \mathbf{p}_2)$, where the Lorentz index $\mu = 0, 1, 2, 3$ is a convenient way of referring to the energy ($\mu = 0$) or momentum ($\mu = 1, 2, 3$ for x, y, z) components. The proton has incoming and outgoing four-momentum vectors k_1^μ and k_2^μ, respectively.

In the diagram, the electron emits a photon, which is at a later time absorbed by the proton. Keep in mind that the amplitude that we will write down according to the Feynman rules includes

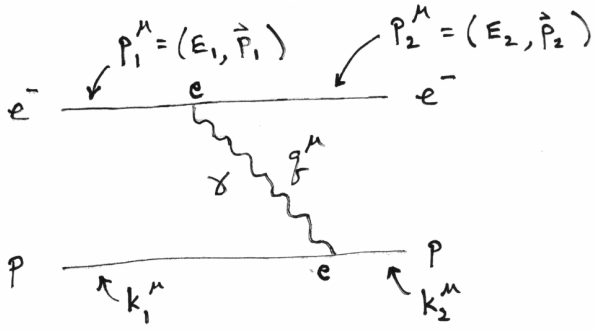

Figure 7.2: A Feynman diagram for elastic, point-like electron-proton scattering.

both this time ordering as well as the opposite one. For the order shown, the four-momentum of the exchanged photon is

$$q^\mu = p_1^\mu - p_2^\mu \ . \tag{7.5}$$

Recall this is a short-hand way of writing four equations (i.e., for $\mu = 0, 1, 2, 3$) that express conservation of energy and momentum at the vertex where the photon is emitted. The invariant mass squared of the exchanged photon is

$$\begin{aligned} q^2 &= (E_1 - E_2)^2 - (\mathbf{p}_1 - \mathbf{p}_2)^2 \\ &= E_1^2 - 2E_1E_2 + E_2^2 - |\mathbf{p}_1|^2 + 2\mathbf{p}_1 \cdot \mathbf{p}_2 - |\mathbf{p}_2|^2 \\ &= 2m_e^2 - 2E_1E_2 + 2\,|\mathbf{p}_1|\,|\mathbf{p}_2| \cos\theta \ , \end{aligned} \tag{7.6}$$

where θ is the angle between the momentum vectors $\mathbf{p}_1$ and $\mathbf{p}_2$, and we used the fact that both the incoming and outgoing electrons are real, and therefore $E_1^2 - \mathbf{p}_1^2$ and $E_2^2 - \mathbf{p}_2^2$ are both equal to m_e^2. You should check that if the opposite time ordering for the emission and absorption vertices had been chosen, the value of q^2 would be the same.

Now consider the reaction in the centre-of-mass frame, as shown in Fig. 7.3, so here θ refers to the c.m. scattering angle. In this frame, by definition the magnitudes of the incoming are the same, and because of energy conservation and the fact that the scattering is elastic, the incoming and outgoing momentum magnitudes and energies are also the same, i.e.,

$$E_1' = E_2' \equiv E' \ , \tag{7.7}$$

$$|\mathbf{p}_1'| = |\mathbf{p}_2'| \equiv p' \ . \tag{7.8}$$

Using Eq. (7.7) in Eq. (7.6) for the q^2 of the exchanged photon gives

$$q^2 = 2\left(m_e^2 - E'^2 + p'^2 \cos\theta\right) \tag{7.9}$$

$$= -2p'^2(1 - \cos\theta) \tag{7.10}$$

$$= -4p'^2 \sin^2\frac{\theta}{2} \ , \tag{7.11}$$

where to obtain the second line above we used $E^2 - p^2 = m_e^2$, and for the third line we applied the trigonometric identity $\sin^2(\theta/2) = (1 - \cos\theta)/2$.

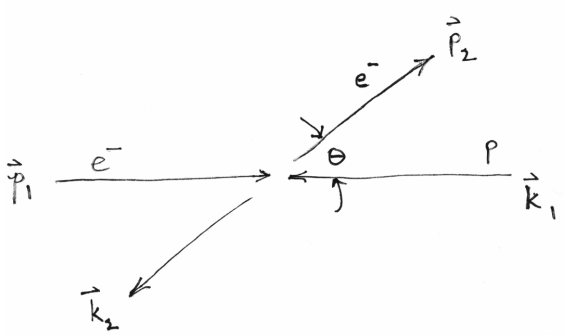

Figure 7.3: Definition of incoming and outgoing momenta for elastic ep scattering (see text).

Notice that in this reaction, the invariant mass squared of the exchanged photon is zero only if $\theta = 0$, and otherwise is negative with a magnitude increasing with scattering angle. Such a virtual photon is said to be *space-like*, and one can understand the terminology by writing down the q^2 in terms of its components,

$$q^2 = (q^0)^2 - \left((q^1)^2 + (q^2)^2 + (q^3)^2\right) \ . \tag{7.12}$$

Here the term $(q^0)^2$ is the square of the time (energy) component of the four-vector, and $(q^1)^2$, $(q^2)^2$ and $(q^3)^2$ represent the space (momentum) components. So if the space components are large compared to the time component, the square (in the four-vector sense) of the invariant mass is negative. The opposite case, $q^2 > 0$ is called a time-like four vector, and this would occur in other types of Feynman diagrams, such as annihilation of a particle and antiparticle into a photon.

We now have the ingredients to write down the amplitude for ep scattering using the basic Feynman rules. Taking q^2 from Eq. (7.9) together with the coupling strengths for photon emission and absorption (e in both cases) gives

$$\mathcal{M} \propto \frac{e^2}{q^2 - m_\gamma^2} \propto \frac{e^2}{p^2 \sin^2 \frac{\theta}{2}} \ , \tag{7.13}$$

where we used the fact that the photon is massless and thus set $m_\gamma = 0$.

The differential cross section $d\sigma/d\Omega$ gives the probability for scattering an electron into a cone of solid angle $d\Omega$, pointing in the direction of θ (and also at some azimuthal angle ϕ). This is proportional to the square of the amplitude, and therefore we can write

$$\frac{d\sigma}{d\Omega} \propto |\mathcal{M}|^2 \propto \frac{\alpha^2}{p^4 \sin^4 \frac{\theta}{2}} \ , \tag{7.14}$$

where the final expression is written in terms of the fine structure constant $\alpha = e^2/4\pi$ instead of the electric charge e.

Here we have only derived the expression as a proportionality. A full calculation for the point-like case gives what is called the Rutherford cross section,

$$\left(\frac{d\sigma}{d\Omega}\right)_{\text{Rutherford}} = \frac{m_e^2\alpha^2}{4p^4\sin^4\frac{\theta}{2}} \ . \tag{7.15}$$

Because the mass of the proton (the target) is much greater than that of the projectile (the electron), the proton does not recoil much and our result above for the c.m. frame is in fact a good approximation for the distribution of the lab-frame scattering angle. A number of refinements can be made to this formula, including taking into account the proton's recoil, spin and relativistic effects. This leads to a more complicated formula for $d\sigma/d\Omega$ called the *Rosenbluth* cross section, the details of which are not important here. We emphasize simply that the assumption of a point-like proton leads to a specific prediction for the form of $d\sigma/d\Omega$.

7.1.3 Comparison with experiment – the size of the proton

Figure 7.4 shows the set-up of the electron–proton scattering experiment carried out by McAllister and Hofstadter at Stanford in 1956 [46]. Electrons with an energy of 188 MeV are incident on a hydrogen target. The detector only covered a small solid angle element $\Delta\Omega$, and could be rotated around to different scattering angles θ.

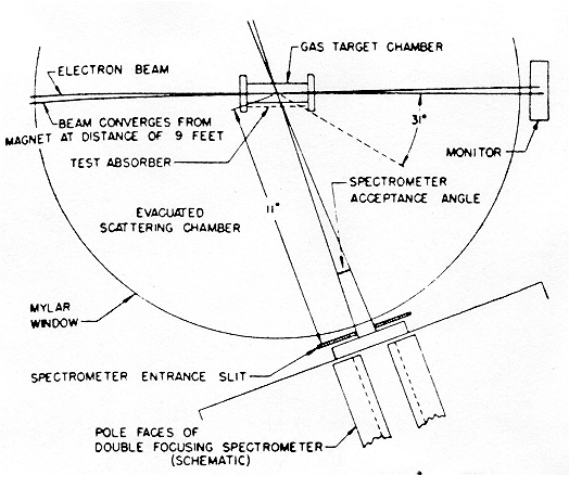

Figure 7.4: The experimental set-up of McAllister and Hofstadter for elastic e^-p scattering (from [46]).

Figure 7.5 shows the results of the experiment along with several theoretical predictions. The prediction for a point-like proton is the upper solid curve. At large scattering angles (greater than about 90 degrees), the data points lie significantly below the prediction. If we still believe that the Coulomb potential is valid at these energies, then our assumption that the charge is concentrated at a point is not correct. We will therefore make a different assumption for how the charge is distributed and see what this implies for the scattering cross section.

If the charge distribution of the proton is assumed to follow a density in space $\rho(\mathbf{x})$ (normalized such that $\int \rho(\mathbf{x})d^3x = 1$), then one can show that the differential cross section $d\sigma/d\Omega$ predicted by Eq. (7.15) is modified to become

$$\frac{d\sigma}{d\Omega} = \left(\frac{d\sigma}{d\Omega}\right)_{\text{Rutherford}} |G_{\text{E}}(\mathbf{q})|^2 \ , \tag{7.16}$$

where

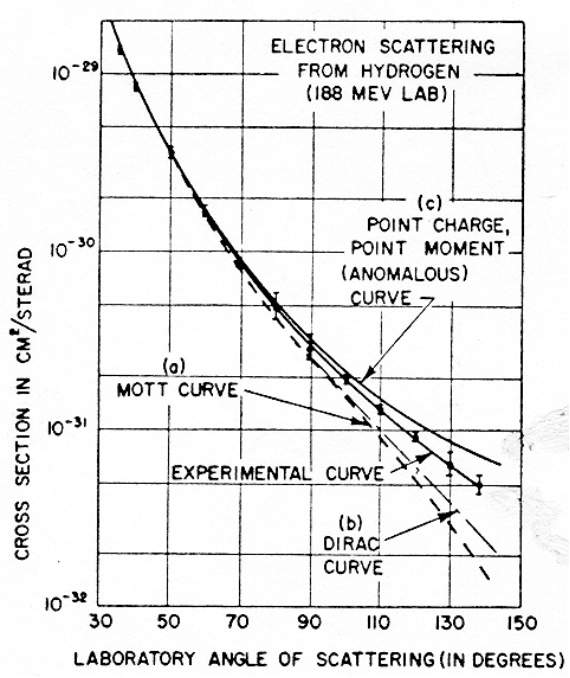

Figure 7.5: The differential cross section for ep scattering as a function of scattering angle measured by McAllister and Hofstadter. The upper solid curve is the prediction for a point-like proton (from [46]).

$$G_{\rm E}(\mathbf{q}) = \int \rho(\mathbf{x}') e^{i\mathbf{q}\cdot\mathbf{x}'}\, d^3x' \tag{7.17}$$

is called the *electric form factor* of the proton. It is essentially the Fourier transform of the charge density.

In order to compute $G_{\rm E}(\mathbf{q})$, we need to make an assumption about the form of the charge distribution $\rho(\mathbf{x})$. A reasonable Ansatz is that it falls off exponentially with radius r,

$$\rho(\mathbf{x}) = \rho_0 e^{-\mu r}\ , \tag{7.18}$$

where requiring $\int \rho(\mathbf{x}) d^3x = 1$ implies $\rho_0 = \mu^3/8\pi$. Substituting the density (7.18) into equation (7.17) for the electric form factor and evaluating the integral gives

$$G_{\rm E}(\mathbf{q}) = \int \frac{\mu^3}{8\pi} e^{-\mu r}\, e^{i\mathbf{q}\cdot\mathbf{x}}\, d^3x = \frac{1}{\left(1+\frac{q^2}{\mu^2}\right)^2} = \frac{1}{\left(1+\frac{4p^2\sin^2\frac{\theta}{2}}{\mu^2}\right)^2}\ . \tag{7.19}$$

From the form of $G_{\rm E}(\mathbf{q})$ we can see that its effect is to suppress the probability for large angle scattering relative to what is predicted by the point-like formula. The same basic picture holds when proton recoil and spin effects are included. A reduction in the predicted rate of large angle scattering is just what is needed to bring the theoretical curve in line with the measured cross section. The parameter μ controls the spatial extent of the charge distribution, i.e. at $r = 1/\mu$, the density has fallen to $1/e$ of its value at $r = 0$. Adjusting μ to give the best fit with the data gives

$$\mu = 0.92 \pm 0.30 \text{ GeV}\ . \tag{7.20}$$

Equivalent to this is the root mean square (rms) radius of the density. This is the square root of the mean of r^2, which is defined as

$$\langle r^2 \rangle = \int r^2 \rho(\mathbf{x})\, d^3x \,. \tag{7.21}$$

For the exponential density (7.18) we obtain

$$\langle r^2 \rangle^{1/2} = \frac{\sqrt{12}}{\mu} = 3.7 \pm 1.2 \text{ GeV}^{-1} \,. \tag{7.22}$$

Multiplying this by $\hbar c = 0.1973$ GeV-fm to get back to normal distance units, this becomes

$$\langle r^2 \rangle^{1/2} = 0.74 \pm 0.24 \text{ fm} \,. \tag{7.23}$$

This was the first experimental evidence that the proton has a finite size. Note that the 'radius' of the proton is not the same thing as the radius of a billiard ball, but rather a parameter which characterizes the spatial extent of a particular hypothesized charge distribution. Subsequent measurements have verified the exponential form of the charge distribution at the several percent level. Martin and Shaw quote a more recent value of the rms radius of 0.85 ± 0.02 fm.

Determining the size of the proton provides a nice example of what it means to measure something in particle physics. We propose a theory or model that contains certain free parameters, in this case a parameter μ. We then derive from it a prediction for the outcome of an experiment, i.e. we predict how may events we should see in a certain angular range for a given integrated luminosity. The predicted number will depend on the value of the free parameter. We then *fit* the prediction to the data, i.e. we find the value of the parameter for which the best agreement with experiment is obtained.

It's not obvious that we can ever exclude a theory with this approach. If the theory doesn't agree with the data, maybe it means that we simply haven't adjusted the parameters in the right way. Roughly speaking, we can test a theory meaningfully as long as it doesn't have too many parameters and we have enough different measurements. We will return to this point later on in the course when we discuss tests of the Standard Model.

7.2 Deep inelastic electron–nucleon scattering

From elastic electron–proton scattering we've seen evidence that the proton has a finite size. For incident electron energies of several hundred MeV, the proton's charge is consistent with being smeared out according to the exponential density (7.18). As the energy in electron–proton scattering increases, however, the probability for elastic collisions decreases. Instead, events are observed in which additional particles, mostly pions, are produced (inelastic scattering). Experiments on inelastic scattering provided the first evidence for point-like constituents (partons) inside the proton.

Inelastic electron–proton scattering can be described by the Feynman diagram shown in Fig. 7.6.

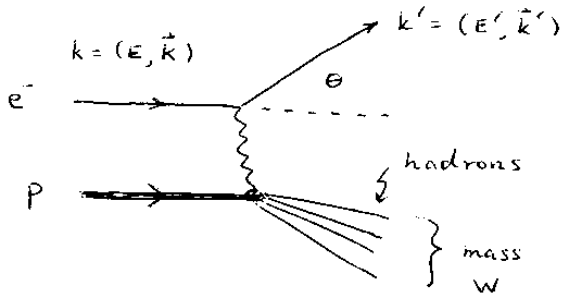

Figure 7.6: Feynman diagram for inelastic electron–proton scattering.

The incident electron (mass m) has a four-momentum $k = (E, \mathbf{k})$. The electron is scattered at an angle θ. Since the collision is inelastic, there is no longer the constraint from energy and momentum conservation that the electron's energy remain unchanged. Instead, the scattered electron has a four-momentum $k' = (E', \mathbf{k}')$ where in general $E' \leq E$. It will be convenient to use the four-momentum transfer

$$q = k - k' \tag{7.24}$$

and in particular its (four-vector) square,

$$\begin{aligned} q^2 &= (k - k')^2 \\ &= k^2 + k'^2 - 2k \cdot k' \\ &= 2m^2 - 2(EE' - \mathbf{k} \cdot \mathbf{k}') \,, \end{aligned} \tag{7.25}$$

where we used $k^2 = k'^2 = m^2$. Since we will be considering highly relativistic electrons ($E \gg m$), we can neglect the term $2m^2$, and furthermore we have $E \approx |\mathbf{k}|$ and $E' \approx |\mathbf{k}'|$. Equation (7.25) therefore becomes

$$q^2 = -2EE'(1 - \cos\theta) = -4EE' \sin^2 \frac{\theta}{2} \equiv -Q^2 \,. \tag{7.26}$$

One usually uses $Q^2 = -q^2$ since it is more convenient to deal with a positive quantity. It is largest for low energy loss ($E' \approx E$) and large angle scatters. By 'deep' inelastic scattering (often abbreviated DIS), one means inelastic collisions with high Q^2.

A very high-Q^2 event from the H1 detector at the HERA collider at DESY (Hamburg) is shown in Fig. 7.7 [47]. The event is actually a positron–proton collision, where the incident positron with an energy of 27.5 GeV enters from the left and scatters off an 820 GeV proton entering from the right. (From a standpoint of investigating the proton's structure, e^-p and e^+p collisions provide essentially the same information.) The positron is scattered back to the lower left, and a large number of hadrons from the collision can be seen to the upper left.

The basic idea of deep inelastic scattering is to measure for every event the scattering angle of the electron θ and its final energy E'. That is, one measures the differential cross section

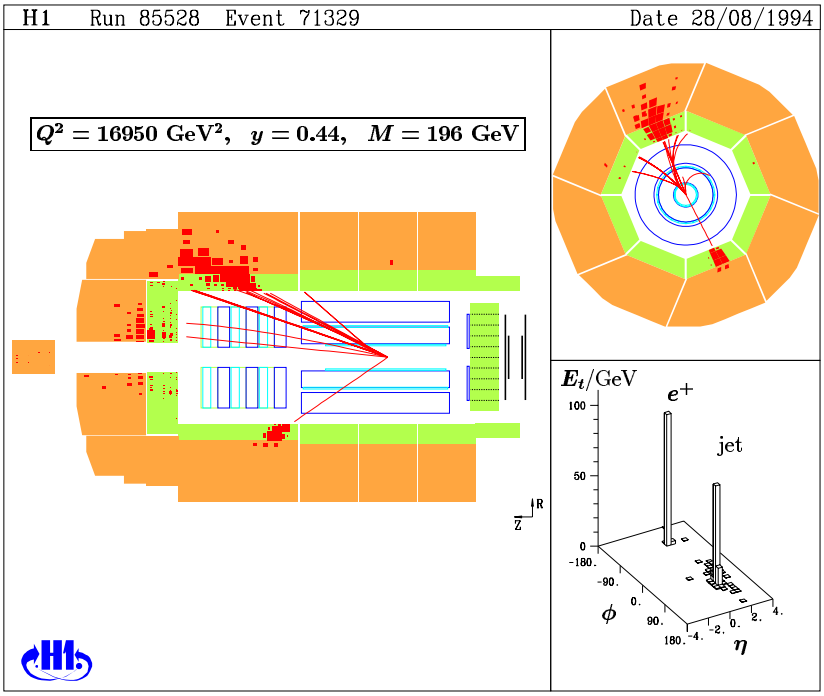

Figure 7.7: A very high-Q^2 positron–proton collision from the H1 detector at the HERA collider (from [47]).

$$\frac{d\sigma}{dE'd\Omega} \tag{7.27}$$

and compares this with the predictions of theories which describe the internal structure of the proton.

In addition to Q^2 it is useful to define another variable used in deep inelastic scattering: the Bjorken x variable is a Lorentz invariant and it is defined as

$$x = \frac{Q^2}{2p \cdot q} \,, \tag{7.28}$$

where p is the initial four-momentum of the proton and q is the four-momentum transferred. From energy and momentum conservation one can show that x is also equal to

$$x = \frac{Q^2}{Q^2 + W^2 - M^2} \,, \tag{7.29}$$

where M is the mass of the proton and W^2 is the invariant mass squared of the final state hadrons (i.e. everything in the final state except the scattered electron). For elastic scattering one has $W^2 = M^2$ and hence $x = 1$. Small x then means that one has $W^2 - M^2 \gg Q^2$; this corresponds to a broad jet of hadrons in the final state. In general one has $0 < x \leq 1$.

So instead of measuring $\frac{d\sigma}{dE'd\Omega}$, one can transform variables to x and Q^2 and measure $\frac{d\sigma}{dxdQ^2}$. The two quantities are equivalent and one can transform from one to the other. Figure 7.8 shows

a scatter plot of x and Q^2 from the Zeus experiment, also at the HERA collider [48]. The basic idea is thus to measure how many points are found in various regions of this plane and to use this to infer something about the internal structure of the proton.

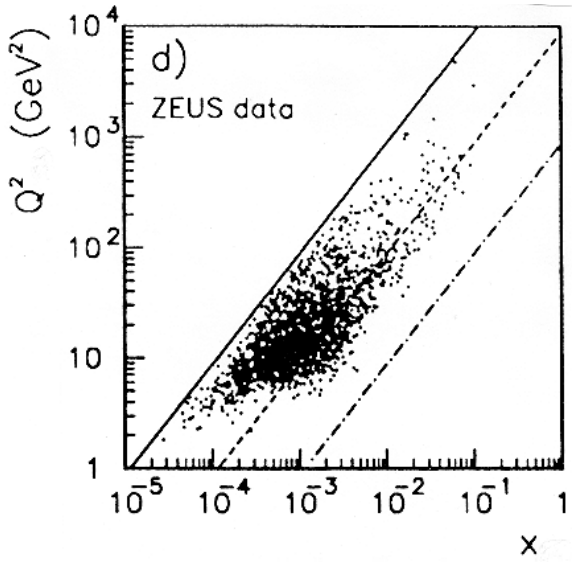

Figure 7.8: A scatter plot of Q^2 vs. x measured by the Zeus detector (from [48]).

7.2.1 Structure functions and scaling

We can write down a general expression for the inelastic differential cross section as

$$\frac{d\sigma}{dxdQ^2} = \frac{4\pi\alpha^2}{Q^4}\left[\frac{(1-y)}{x}F_2(x,Q^2) + y^2F_1(x,Q^2)\right] , \tag{7.30}$$

where $y = \nu/E$. The functions F_1 and F_2 are called *structure functions*. We have not yet made any prediction as to what they should look like; they are general functions of x and Q^2, and thus (7.30) does not represent a prediction for the cross section, but rather is a general expression.

For small angle scattering, one can show that $y \ll 1$ and thus the cross section is approximately proportional to F_2. This was in fact a good approximation in the experiments carried out at the Stanford Linear Accelerator Center (SLAC) in the late 1960s, and thus the measurements of the cross section gave directly F_2. What these experiments showed was that for a fixed value of x, F_2 is almost independent of Q^2 (see Fig. 7.9, from [49]). That is, F_2 is only a function of x. This property is called *scaling*.

Having observed scaling of structure functions, one must then figure out what theory for the structure of the proton predicts such behaviour. This was done by Feynman, who showed that scaling is predicted by a model in which the proton consists of point-like constituents which he called *partons*. Feynman's partons did not have to be the same objects as the quarks introduced by Gell-Mann and Zweig several years earlier, but in fact this identification was made and has been subsequently confirmed.

We can roughly understand why point-like scattering leads to this behaviour by considering the form factors introduced to describe elastic scattering. There we saw that the effect of

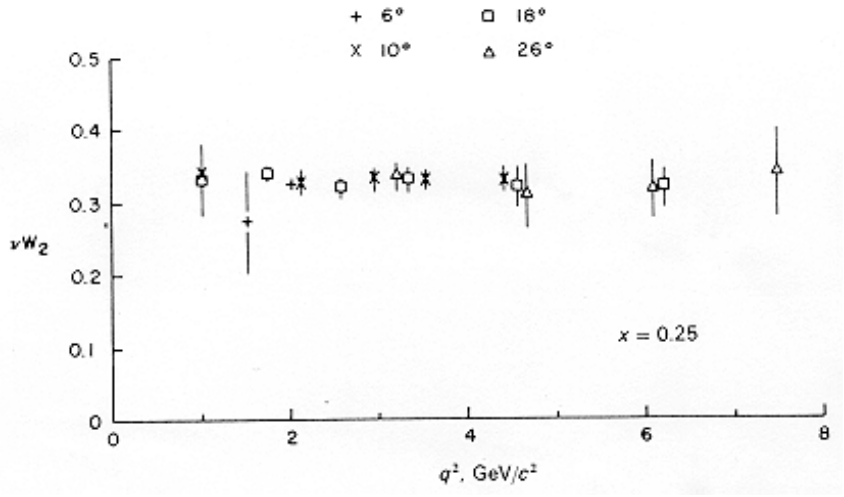

Figure 7.9: Measurements of $F_2 = \nu W_2$ at fixed x as a function of Q^2 (from [49]).

a distributed charge was to decrease the cross section at large scattering angles (i.e. at high Q^2) relative to the point-like cross section. The fact that the inelastic cross section does not fall off faster for increasing Q^2, i.e. that F_2 remains constant, means that the electron is not interacting directly with a smeared out charge distribution but rather with a point-like charge. This is essentially the same argument which led Rutherford to conclude that the high probability observed for large angle scattering of alpha-particles on gold meant that the atom consisted of a small nucleus surrounded by a swarm of electrons.

Experiments on structure functions can also give information on the spin hypothesis of the partons inside the protons. By measuring ratios of structure functions it was possible to infer that partons are spin-1/2 particles.

7.2.2 The parton model and parton density functions

In the parton model, the proton is modelled as a collection of charged point-like objects. The electron exchanges a virtual photon with one of the partons and knocks it out of the proton. Partons are not, however, directly observed. The hadronic final state consists of jets of 'usual' hadrons (mostly pions). The details of the transformation of partons into hadrons (called *hadronization*) are not clear, but provisionally we assume it occurs with a probability of unity.

The partons within the proton are assumed not to be all standing still, but rather buzzing around with a sort of random thermal motion. If we consider a boosted reference frame in which the proton is moving very fast (the 'infinite momentum' frame), then each parton will carry some fraction z of the momentum of the proton. In this frame we can neglect the momentum components of the partons perpendicular to the direction of the proton's motion and thus we have

$$z = \frac{E_{\text{parton}}}{E_{\text{proton}}} \approx \frac{p_{\text{parton}}}{p_{\text{proton}}} \,. \tag{7.31}$$

One might naively think that if we have a proton consisting of, say, three partons and if it is travelling very fast, then each parton would simply have one third of the proton's momentum.

In fact, the momentum fraction can take on any value between 0 and 1. This is a consequence of the fact that the intrinsic motion of the partons inside the proton is relativistic, i.e., the 'thermal' kinetic energy of a parton is large compared to its rest mass.

Inelastic scattering in the parton model is described by the Feynman diagram shown in Fig. 7.10. The electron interacts by exchanging a virtual photon with only one of the partons, which has a momentum fraction z.

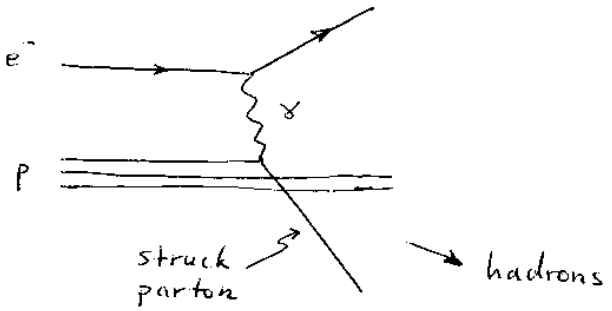

Figure 7.10: Feynman diagram for inelastic electron–proton scattering in the parton model.

If one assumes that the parton behaves as a free particle inside the proton, i.e. that it is only interacting very weakly with its neighbours, and that the quark and proton masses are small compared to their kinetic energies, then one can show from energy and momentum conservation that the momentum fraction z is related to the scattered electron's energy and angle by

$$z = \frac{2EE' \sin^2 \frac{\theta}{2}}{M(E - E')} = x \; . \tag{7.32}$$

That is, the momentum fraction z turns out to be equal to the variable x defined in equation (7.28), which is something we measure for each event. In fact, one usually denotes both quantities by x, and from now on we will do so and drop the variable z.

The cross section for electron scattering with a point-like charged parton can be computed using the usual tools of relativistic quantum mechanics. The prediction will depend on what we assume for the parton's spin and charge, and it will depend on the parton's initial momentum $p_{\text{parton}} = x p_{\text{proton}}$, that is, it will depend on x. Furthermore, we will assume that there are different types of partons (e.g. the u and d quarks), which have different electric charges. So to get the cross section for electron–proton collisions, we have to consider first the electron–parton cross section of a given parton type and x value, and then sum over parton types and integrate over x. Symbolically we have

$$\left(\begin{array}{c} \text{e–proton} \\ \text{cross section} \end{array} \right) = \sum_{i=u,d,s,\ldots} \int_0^1 \left(\begin{array}{c} \text{e–parton} \\ \text{cross section for} \\ \text{parton at } x \end{array} \right) f_i(x)\, dx \; , \tag{7.33}$$

where, $f_i(x)dx$ is the number of partons of type i having a momentum fraction in the interval $[x, x + dx]$. The functions $f_i(x)$ are called *parton density functions* (PDF).

These parton density functions are especially important for LHC physics since the processes produced in the proton-proton collisions actually come from the interactions of the partons

inside the colliding protons. It is not feasible to obtain the PDFs from first principles since the coupling of the strong interaction (α_s) is large and these calculations are then non-perturbative. In practice, the proton PDFs are extracted from a global fit to a all of the available experimental data, within the constraints of QCD.

If we think of the proton in terms of three quarks (uud) it turns out that the momentum fraction of each one is about 0.18, which gives a total of 0.5, highlighting the fact that about half of the proton momentum appears to be unaccounted for. The rest comes from the gluons inside the proton. Looking at Fig. 7.11 one can start to understand the shape of the PDF given various models for the partons inside the proton.

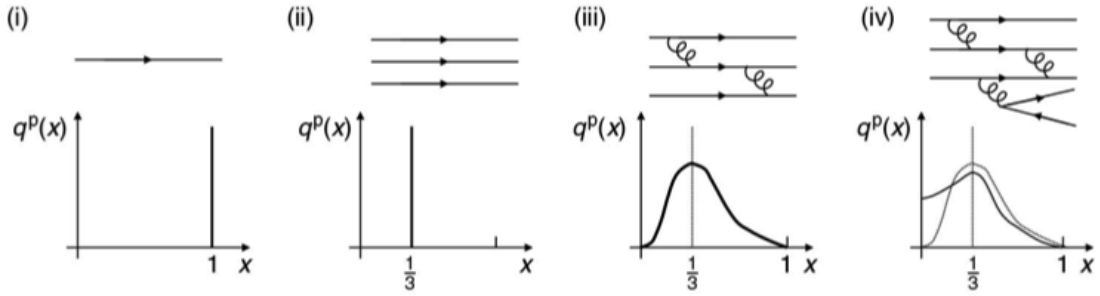

Figure 7.11: Possible shapes of the quark PDFs within the proton [2].

Figure 7.11(i) represents the proton consisting of a single point-like particle which carries all of the momentum of the proton, so that in this case the PDF is a delta-function at $x = 1$; (ii) represents the proton as consisting of three quarks each of which carries 1/3 of the momentum of the proton, so that in this case the PDF is a delta-function at $x = 1/3$ with a normalisation of 3; (iii) shows the proton as consisting of three quarks interacting with each other, and so in that case the delta function at $x = 1/3$ is smeared out as the quarks exchange momentum; finally in (iv) higher-order processes are included, such as virtual quarks being produced from gluons inside the proton, so in that case there is an enhancement of the PDF at low x.

The virtual quarks being produced from gluon are called the *sea* of quarks, while the uud quarks of the proton are called the *valence* quarks. At the LHC, the centre-of-mass energy is high enough that the momentum fractions typically involved in the collisions are low. At low x the dominant contribution comes from the gluons inside the protons, hence at the LHC the most likely partons to interact are actually the gluons rather than the valence or sea quarks. One can write the PDF of the up and down quarks as a sum of PDFs from the valence and sea quarks as

$$u(x) = u_V(x) + u_S(x) , \tag{7.34}$$

$$d(x) = d_V(x) + d_S(x) . \tag{7.35}$$

Note that the antiquark PDFs for the proton can only come from sea quarks:

$$\bar{u}(x) = \bar{u}_S(x) , \tag{7.36}$$

$$\bar{d}(x) = \bar{d}_S(x) . \tag{7.37}$$

Some reasonable assumptions can be made for sea quarks. First, since they come from gluons splitting into a quark and an anti-quark, one can assume that the sea part of the quark PDF will be the same for quarks and anti-quarks. Second, since the mass of the up and down quarks are similar, their sea quark PDFs will also be very similar. One could expect that the sea quarks would dominate at low x regime of the proton and indeed this is supported by the data. One could also expect that valence quarks would dominate at high x, which is also indicated by the data although an interesting observation has also emerged, which indicates that the ratio

$$d_{\rm V}(x)/u_{\rm V}(x) \to 0 \text{ as } x \to 1 \; . \tag{7.38}$$

One could try to explain this observation by making use of the exclusion principle: the configuration where the d quark carries a large fraction of the proton momentum and the two up quarks carry a very small fraction is disfavoured since this would imply that the two up quarks are in the same state.

Chapter 8

Heavy quarks

The term *heavy quark* is usually taken to mean the flavours charm, bottom or top. In this chapter we take a look at how these quarks were discovered and how they fit into the Standard Model.

8.1 The Cabibbo angle

When the quark model was introduced in 1964, only the flavours u, d and s were needed to describe all of the known particles. From the rates of weak decays involving (u,d) transitions, one could determine that the coupling strength for a udW vertex was approximately equal to the value of the coupling g obtained from purely leptonic vertices such as $e^-\nu_e W$ or $\mu^-\nu_\mu W$. An example is the decay $\pi^- \to \mu^-\overline{\nu}_\mu$, shown in Fig. 8.1(a).

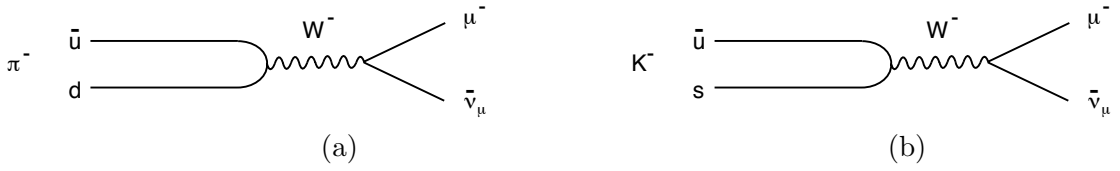

Figure 8.1: Feynman diagrams for the decays (a) $\pi^- \to \mu^-\overline{\nu}_\mu$ and (b) $K^- \to \mu^-\overline{\nu}_\mu$.

If in Fig. 8.1(a) we replace the d quark in the pion by an s quark, we get the decay $K^- \to \mu^-\overline{\nu}_\mu$ shown in Fig. 8.1(b). After taking into account differences in the pion and kaon masses, one determined that the coupling strength for the vertex joining the $\overline{u}$, s and W^- was four to five times less than the coupling for $\overline{u}$, d and W^-.

In 1963, Cabibbo [50] proposed that this state of affairs could be explained by assuming that the coupling strength g applied not to the $\overline{u}Wd$ vertex but rather to when the $\overline{u}$ and W couple to a superposition of d and s states, namely,

$$d' = d\,\cos\theta_C + s\,\sin\theta_C\ . \tag{8.1}$$

The superposition is parametrized by the mixing angle θ_C, now called the Cabibbo angle, such that the normalization of the state vectors is preserved. The state orthogonal to d' is

$$s' = -d \sin\theta_C + s \cos\theta_C \ . \tag{8.2}$$

The coupling of s' to the u quark is hypothesized to be zero. The amplitudes for pion and kaon decay, however, involve the d and s states. These can be expressed in terms of d' and s' simply by inverting equations (8.1) and (8.2):

$$d = d' \cos\theta_C - s' \sin\theta_C \ , \tag{8.3}$$

$$s = d' \sin\theta_C + s' \cos\theta_C \ . \tag{8.4}$$

This means that the coupling of $\overline{u}$, d and W^- in Fig. 8.1(a) is not g but rather $g\cos\theta_C$, and the coupling of $\overline{u}$, s and W^- in Fig. 8.1(b) is $g\sin\theta_C$. By comparing the measured decay rates and accounting for the differences between the pion and kaon masses, one obtains for the Cabibbo angle $\theta_C = 12.8°$, or equivalently

$$\cos\theta_C = 0.975 \ , \tag{8.5}$$

$$\sin\theta_C = 0.221 \ . \tag{8.6}$$

8.2 The GIM hypothesis

The Cabibbo mechanism describes the observed pion and kaon decay rates, but the s' state seems to play no role since it does not couple to the W boson. The situation with the leptons, on the other hand, appeared to be more symmetric. The $e^-$and ν_e interact with the W as a pair, as do $\mu^-$and ν_μ. Already in 1964, the possibility of a fourth quark, which Glashow called the *charmed* quark, was discussed. This was motivated mainly by the idea that the quark and lepton parts of the theory of weak interactions should have the same form.

Beyond the aesthetic objections to having only three quarks when at the time there were four known leptons, Cabibbo's model with only u, d and s quarks makes an incorrect prediction for the decay of a neutral kaon into a $\mu^+\mu^-$ pair. A Feynman diagram for this decay is shown in Fig. 8.2. The d couples to a W^- boson and u quark with the strength $g\cos\theta_C$, and the u couples to the W^+ and $\overline{s}$ with the strength $g\sin\theta_C$. (Recall that the line representing the u quark also represents $\overline{u}$ upon a reversal of the time ordering of the vertices where it is produced and absorbed; here we will refer to it simply as u.)

The couplings for the W bosons to the muons and intermediate neutrino are g, so the amplitude $\mathcal{M}_u$ for this graph follows

$$\mathcal{M}_u \propto g^4 \sin\theta_C \cos\theta_C \ , \tag{8.7}$$

where the subscript u refers to the fact that the graph includes a u quark in the intermediate state. We don't know enough of the Feynman rules to work out the amplitude in this case,

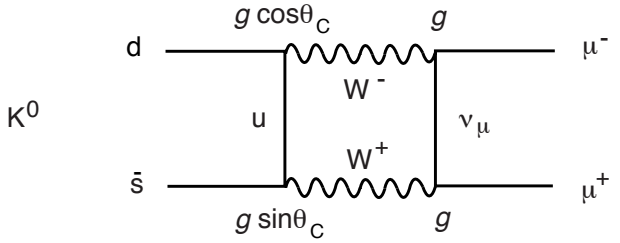

Figure 8.2: Feynman diagram for the decay $K^0 \to \mu^+\mu^-$ with an intermediate u quark.

but the result is large; from this graph one would expect that $K^0 \to \mu^+\mu^-$ should make up a significant fraction of the total number of neutral kaon decays. The measured branching ratio for this decay mode is, however, a minuscule 10^{-8}.

In 1970, Glashow, Iliopoulos and Maiani pointed out that the discrepancies between theory and experiment for reaction rates such as $K^0 \to \mu^+\mu^-$ could be explained by the existence of the charmed quark [51]. They assumed that the c couples to the s' with strength g and that its coupling to d' is zero, thus creating a symmetric picture. That is, the interaction of the W boson with the quark pairs

$$\begin{pmatrix} u \\ d' \end{pmatrix} \qquad \text{and} \qquad \begin{pmatrix} c \\ s' \end{pmatrix}$$

is the same as for the lepton pairs

$$\begin{pmatrix} \nu_e \\ e^- \end{pmatrix} \qquad \text{and} \qquad \begin{pmatrix} \nu_\mu \\ \mu^- \end{pmatrix},$$

i.e. they all have the coupling strength g. This scheme was named after its authors the *GIM hypothesis*.

In this picture, the decay $K^0 \to \mu^+\mu^-$ can proceed by means of an additional intermediate state with the u quark replaced by c, as shown in Fig. 8.3.

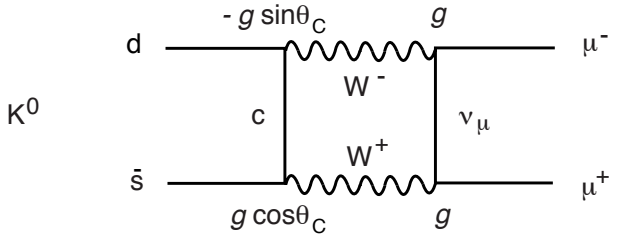

Figure 8.3: Feynman diagram for the decay $K^0 \to \mu^+\mu^-$ with an intermediate c quark.

The amplitude $\mathcal{M}_c$ for this graph is the same as $\mathcal{M}_u$ except that now the c quark couples only to the component of the d state proportional to s', which according to equation (8.3) gives the amplitude a factor $-g\sin\theta_C$. Similarly the $c\mathrm{W}s$ vertex gives a factor $g\cos\theta_C$. If the u and c quarks had the same mass, then the crucial minus sign would be the only difference between the amplitudes $\mathcal{M}_u$ and $\mathcal{M}_c$, and the two would cancel, resulting in a predicted branching ratio for $K^0 \to \mu^+\mu^-$ of zero. In fact, the branching ratio is measured to be around 10^{-8}, and from this one can estimate the mass of the c quark. Using similar arguments applied to a different

observable, namely, the mass difference between the K^0_S and K^0_L mesons, Gaillard and Lee were able to predict the mass of the c quark to be around 1.5 GeV, before the actual 'discovery' of charm in 1974 [52].

The decay $K^0 \to \mu^+\mu^-$ provides a classic example of quantum mechanical interference. The diagram of Fig. 8.2 provides one possible path for the decay to proceed and by itself would give a certain prediction for the probability. We then allow for a second possible path with a c quark instead of a u in the intermediate state. In a non-quantum world, one might naively think that the predicted probability could only increase. But in quantum mechanics we add amplitudes, not probabilities. In this case, the cancellation of $\mathcal{M}_u$ and $\mathcal{M}_c$ is almost complete. This results in an almost vanishing rate for the decay, which is in good agreement with experiment.

8.3 The charmed quark

In November 1974, direct evidence for the charmed quark was discovered almost simultaneously in two independent experiments. Accounts of the 'November Revolution' are given in the book by Cahn and Goldhaber [5] and in the paper by Goldhaber in [53].

The first of the two experiments was being carried out by Samuel Ting and co-workers at the Brookhaven National Laboratory in New York. Protons with an energy of 30 GeV hit a beryllium target and events of the type $pBe \to e^+e^-X$ were selected, where X represents any system of hadrons. By measuring the energies of the e^+ and e^- as well as the opening angle of the pair, the invariant mass m_{ee} of the e^+e^- system could be determined. By October 1974 Ting *et al.* found the distribution of m_{ee} to fall in a smooth way except for a peak at 3.1 GeV. This appeared to be a new resonance, which they named the J particle. Given, however, that their experiment was new and the detector not yet fully understood, the finding was not reported until additional checks could be carried out.

At the same time at SLAC (Stanford, California), a group led by Burton Richter was investigating electron–positron collisions using the SPEAR e^+e^- storage ring, shown in Fig. 8.4.[1] At the time, one was interested in measuring the cross section for e^+e^- collisions to result in hadrons, e.g., several or more pions. The SPEAR group measured $\sigma(e^+e^- \to \text{ hadrons})$ as a function of the centre-of-mass energy in steps of $\Delta E_{\rm cm} = 200$ MeV. At $E_{\rm cm} = 3.2$ GeV, the measured cross section came out around 30% higher than expected, and before the measurement could be published it was felt that a remeasurement of the questionable region was necessary.

At $E_{\rm cm} = 3.1$ GeV, the cross section for $e^+e^- \to$ hadrons suddenly appeared to be a factor of two higher than expected. Proceeding in even smaller steps of $E_{\rm cm}$ revealed the resonance shown in the left-hand plot of Fig. 8.5 [19], with a maximum cross section two orders of magnitude higher than the value away from the peak. They first named the resonance SP (for SPEAR), but then considered that a two letter name was unacceptable and decided upon ψ.

Within two days, Ting found out about Richter's discovery and *vice versa*, and both groups rushed to publish their results [54, 55]. Neither group backed down on the name and it is now

[1] One can almost make out in the photo that the ring doesn't have properly built walls but rather consists of concrete blocks stacked together. This is because the funding for SPEAR was never actually approved and the SLAC management was forbidden from spending money on its construction. By a technicality in the rules, stacking together concrete blocks didn't constitute 'construction', and the project went ahead and eventually yielded two Nobel prizes.

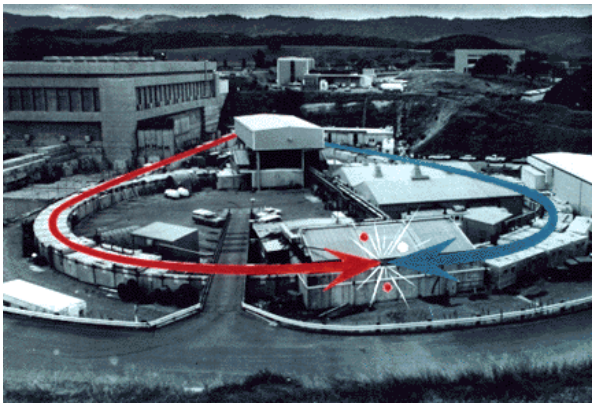

Figure 8.4: The SPEAR e^+e^- storage ring at SLAC. The arrows indicate the collision point of the e^+ and e^- beams (from [11]).

known as the J/ψ. So it wound up with two letters after all – the only particle to have this distinction.

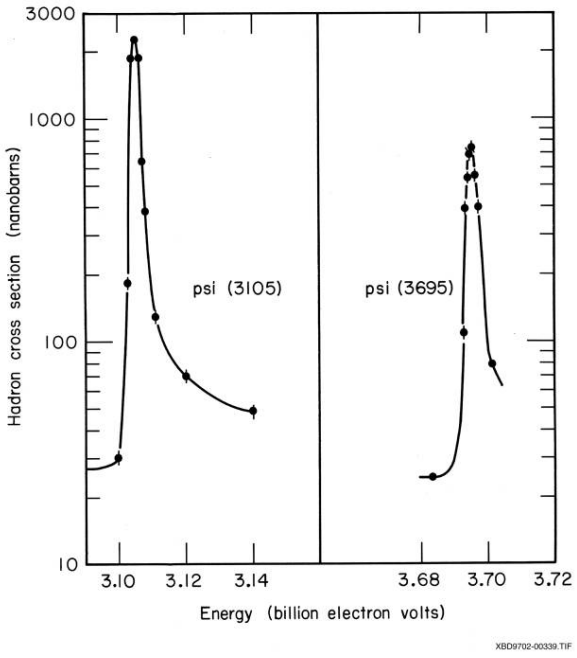

Figure 8.5: The cross section $\sigma(e^+e^- \to$ hadrons) measured by the SLAC-LBL experiment at SPEAR showing (left) the ψ and (right) the ψ' resonances (from [19]).

As in the case of the hadronic resonances discussed in Chapter 6, the peak in the cross section $\sigma(e^+e^- \to$ hadrons) and the peak in the e^+e^- invariant mass distribution seen by Ting *et al.* are explained by assuming the existence of a new particle, namely, the J/ψ. For $e^+e^- \to$ hadrons, for example, one would then have the Feynman diagram shown in Fig. 8.6. The amplitude for this reaction therefore contains a propagator

$$\frac{1}{q^2 - {M_{\mathrm{J}/\psi}}^2} \,, \tag{8.8}$$

where $M_{\mathrm{J}/\psi} = 3.1$ GeV is the mass of the resonance and q^2 is its virtual mass squared, which here is equal to the centre-of-mass energy squared.

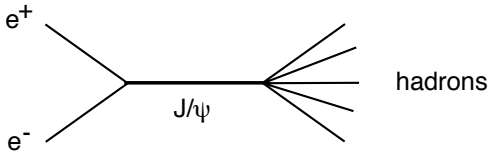

Figure 8.6: Feynman diagram for $e^+e^- \to$ hadrons showing the intermediate J/ψ.

The cross section should therefore have the Breit–Wigner form of equation (6.7), namely,

$$\sigma(E_{\rm cm}) = \frac{\Gamma^2}{4} \, \frac{\sigma_0}{(E_{\rm cm} - M_{{\rm J}/\psi})^2 + \Gamma^2/4} \; . \tag{8.9}$$

In fact, one can see from Fig. 8.5 that $\sigma(E_{\rm cm})$ does not quite have this form, but rather has a tail extending towards higher energies. This is because if $E_{\rm cm}$ is higher than $M_{{\rm J}/\psi}$, a photon can be emitted from either the electron or positron such that the virtual J/ψ becomes almost on-shell (i.e. $q^2 \approx {M_{{\rm J}/\psi}}^2$), resulting in a large amplitude. Events of this type are sometimes called *radiative returns*, i.e., by emitting a photon the e^+e^- system 'returns' back to the mass of the resonance.

Furthermore, the actual width of the peak measured in Fig. 8.5 (around 2 MeV) is not the total decay rate of the resonance, because the energies of the e^+ and e^- beams themselves had a finite energy spread; this accounts for almost all of the observed width. Nevertheless, by combining the cross section measurements with measurements of the branching ratio of J/$\psi \to e^+e^-$ (around 6%), one can infer a total decay rate of 87 keV, i.e., some three orders of magnitude smaller than a typical hadronic resonance such as the ρ^0 or K^*.

A connection was immediately made between the new resonances and the charmed quark. The J/ψ is interpreted as a meson consisting of c and $\bar{c}$. The Feynman diagram from Fig. 8.6 can therefore be interpreted as the annihilation of the e^+ and e^- into a virtual photon which couples directly to the $c\bar{c}$ state. The J/ψ must therefore have the same quantum numbers as the photon, namely, $J^P = 1^-$. The J/ψ then decays into hadrons by first decaying to three gluons, as shown in Fig. 8.7. (There is a rule of quantum mechanics called *Yang's theorem*, according to which a spin-1 particle cannot decay into two identical bosons. The J/ψ can therefore decay into three gluons, but not two.) The process by which the gluons, which carry colour charge, transform into colour neutral hadrons such as pions and kaons cannot in practice be computed directly from QCD, but it is assumed to occur with a probability of unity.

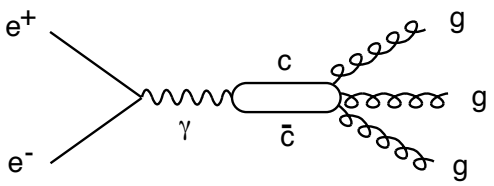

Figure 8.7: Feynman diagram for $e^+e^- \to ggg$ showing the intermediate photon and $c\bar{c}$ states.

Encouraged by their success at 3.1 GeV, the SLAC group continued to measure the cross section in small steps of $E_{\rm cm}$. Within 10 days they found a second resonance at 3.7 GeV which they called the ψ', shown in the right-hand plot of Fig. 8.5. This is interpreted as a radial excitation of $c\bar{c}$ having principal quantum number $n = 2$. Over the next several years an entire

system of $c\bar{c}$ states, often called *charmonium states*, was discovered. The names and properties of some of the more important ones are listed in Table 8.1.

Table 8.1: Some $c\bar{c}$ states, their quantum numbers, masses and decay widths [7].

particle	J^P	mass (GeV)	Γ
η_c	0^-	2.980	13 keV
J/ψ(1S)	1^-	3.097	87 keV
ψ(2S)	1^-	3.686	277 keV
χ_{c0}(1P)	0^+	3.415	15 MeV
χ_{c1}(1P)	1^+	3.510	0.9 MeV
χ_{c2}(1P)	2^+	3.556	2.0 MeV

Charmonium studies have provided important information for understanding the strong force which is responsible for the binding of the c and $\bar{c}$. Because of the relatively large mass of the charmed quark, the $c\bar{c}$ system can be treated to reasonable accuracy with non-relativistic quantum mechanics. Recall that the energy levels of a hydrogen atom or of an e^+e^- bound state (positronium) can be predicted by solving the Schrödinger equation with a Coulomb potential,

$$V_{\rm C}(r) = -\frac{\alpha}{r} \ , \tag{8.10}$$

where $\alpha = e^2/4\pi$. In the same way, the masses of charmonium states can be predicted by using the corresponding potential for the strong force. A functional form for such a potential which can be motivated by but not rigorously derived from QCD is

$$V_{\rm QCD}(r) = -\frac{4}{3}\frac{\alpha_{\rm s}}{r} + kr \ , \tag{8.11}$$

where $\alpha_{\rm s}$ is the strong coupling constant and the factor of 4/3 comes from summing over all the possible colour states for the $c\bar{c}$ system. We will discuss this strong potential in more details in Chapter 10. The second term in (8.11) contains a parameter k called the *string tension*. The observed charmonium masses can be described taking $\alpha_{\rm s} \approx 0.3$ and $k \approx 1$ GeV/fm.

Note that the $\alpha_{\rm s}$ here is considerably larger than the value mentioned in Chapter 2 of 0.12. This is because the latter value pertained to processes at an energy scale of $M_{\rm Z} = 91$ GeV, whereas the relevant energy scale for the charmonium system is given by the masses of the $c\bar{c}$ states, i.e. around 3 GeV. We will return to the question of the energy dependence of $\alpha_{\rm s}$ in Chapter 10.

The derivative of the potential corresponds to the force, and so the linear term kr says in effect that the force between a quark and antiquark at large distances becomes a constant, rather than dying off as $1/r^2$ as in the case of the electric force. So if QCD predicts a linear potential, then this explains why we can never see isolated quarks. Numerical QCD calculations based on a discretized set of points in space and time (called *lattice* calculations), indicate in fact the presence of such a linear term.

If the J/ψ and ψ' in fact consist of $c\bar{c}$, it should be possible to produce mesons consisting of c and a light (u, d or s) antiquark. Such a meson would possess 'open charm', in the same

sense that a kaon possesses a non-zero (i.e. 'open') strangeness. It was expected that by going to sufficiently high energies, one should see e.g.

$$e^+e^- \to D^+D^- \ ,$$

where the D^+ is $c\overline{d}$ and its antiparticle D^- is $\overline{c}d$. Similarly one should see neutral D mesons consisting of c and $\overline{u}$. This should be possible via the Feynman diagram of Fig. 8.8, but only if the mass of the $c\overline{c}$ state is greater than twice the mass of the D meson.

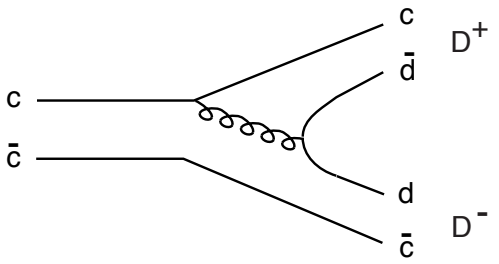

Figure 8.8: Feynman diagram for a $c\overline{c}$ system decaying into a pair of D mesons.

The search for such particles proved more difficult than some expected, but by 1976 running at centre-of-mass energies between 3.9 and 4.6 GeV, the SPEAR team found evidence [57] for the decays

$$D^0 \to K^-\pi^+$$
$$D^0 \to K^-\pi^-\pi^+\pi^+$$
$$D^+ \to K^-\pi^+\pi^- \ .$$

This evidence consisted (of course) of peaks in invariant mass distributions of the various combinations of pions and kaons. A recent measurement of the $K^-\pi^+$ mass distribution from the ALEPH experiment is shown in Fig. 8.9 [58].

The peak corresponds to $K^-\pi^+$ pairs from D^0 decays; from the peak position one determines that the D^0 mass is 1.864 GeV. The charged charmed meson $D^\pm$ has a similar mass of 1.869 GeV. These values are both more than half the masses of the J/ψ and ψ' (3.1 and 3.7 GeV, respectively), so these particles cannot decay into pairs of D mesons. Rather, the c and $\overline{c}$ have to annihilate each other. This explains why the resonances are so narrow. The total widths of the $c\overline{c}$ resonances having masses above the threshold to decay into pairs of D mesons are indeed much larger. The properties of some mesons and baryons containing c quarks are shown in Table 8.2.

8.4 The bottom quark

With the discovery of the c quark in 1974, there were four known quarks and four leptons. The symmetry was short-lived, however, since the τ lepton was discovered in 1975. One could then ask whether there was also a third family of quarks, and sure enough, in 1977, evidence for the bottom quark was found by Lederman *et al.* at an experiment at Fermilab [59].

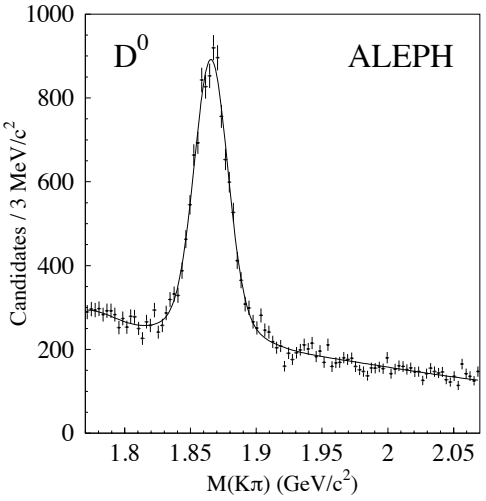

Figure 8.9: The invariant mass distribution for $K^-\pi^+$. The peak at 1865 MeV corresponds to the D^0 meson. The width of the peak is almost entirely due to the experimental resolution for the invariant mass [58].

Table 8.2: Some hadrons containing c quarks and their properties [7].

particle	quarks	J^P	mass (GeV)	τ (s)	$c\tau$ (μm)
$D^\pm$	$d\bar{c}$, $c\bar{d}$	0^-	1.869	1.05×10^{-12}	315
D^0	$c\bar{u}$	0^-	1.864	0.413×10^{-12}	124
$D_s^\pm$	$s\bar{c}$, $c\bar{s}$	0^-	1.969	0.496×10^{-12}	149
Λ_c^+	udc	$\frac{1}{2}^+$	2.285	0.21×10^{-12}	62

Lederman's experiment was in many ways similar to that used by Ting and co-workers to discover the J. Protons with energies of 400 GeV hit a nuclear target and events with a $\mu^+\mu^-$ pair (plus hadrons) were selected. The invariant mass distribution of the $\mu^+\mu^-$ pairs showed two peaks at 9.4 and 10.2 GeV. These were named the Υ (upsilon) and Υ' (upsilon prime) resonances, and interpreted as bound states of b and $\bar{b}$.

The SPEAR e^+e^- ring could only reach a maximum centre-of-mass energy of 8 GeV, so the Υ resonances were out of reach. By 1978, the PLUTO [60] and DASP [61] groups at the DORIS e^+e^- ring at DESY (Hamburg) observed the Υ, and since that time, e^+e^- production of $b\bar{b}$ resonances at several accelerators has revealed a system of states analogous to charmonium. Four of these states can be seen from the cross section measurements by the CUSB collaboration in Fig. 8.10.

Since the upsilon resonances couple directly to the photon (as do the J/ψ and ψ', see Fig. 8.7), they must have the same spin and parity as the photon, namely, $J^P = 1^-$. As they are the lowest mass states with this spin and parity, they are assumed to have orbital angular momentum $L = 0$. In the spectroscopic notation inherited from atomic physics, the states with $L = 0, 1, 2, 3$ are labelled S, P, D, F, and thus the Υ states are now usually called $\Upsilon(1S)$, $\Upsilon(2S)$, ..., rather than the original names Υ, Υ', etc. The number in front of the S indicates the principal quantum number $n = 1, 2, \ldots$, so the upsilon states with higher n are radial excitations of the same L and J^P. The naming conventions for the other $b\bar{b}$ states is similar to that for the charmonium

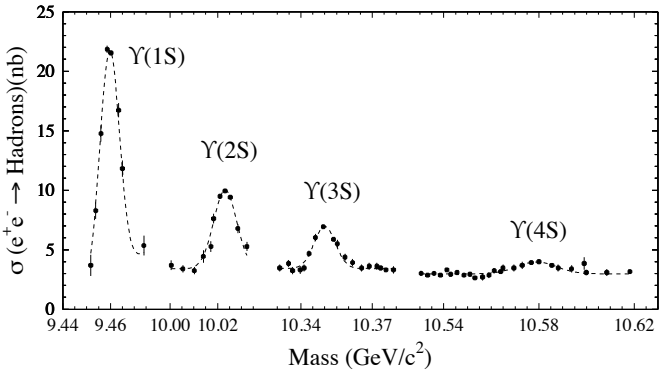

Figure 8.10: The cross section $\sigma(e^+e^- \to \text{hadrons})$ showing the first four Υ resonances (from [62]).

system with the subscript c replaced by b. That is, $L = 1$ states are called χ_b, and the $J^P = 0^-$ state, which presumably exists but has not yet been seen experimentally, is called the η_b. Some of the more important $b\bar{b}$ states and their properties are listed in Table 8.3.

Table 8.3: Some $b\bar{b}$ states, their quantum numbers, masses and decay widths. The widths of the χ_b states have not yet been measured [7].

particle	J^P	mass (GeV)	Γ
$\Upsilon(1S)$	1^-	9.46	52 keV
$\Upsilon(2S)$	1^-	10.02	44 keV
$\Upsilon(3S)$	1^-	10.35	26 keV
$\Upsilon(4S)$	1^-	10.58	14 MeV
$\Upsilon(5S)$	1^-	10.86	110 MeV
$\Upsilon(6S)$	1^-	11.02	79 MeV
$\chi_{b0}(1P)$	0^+	9.86	—
$\chi_{b1}(1P)$	1^+	9.89	—
$\chi_{b2}(1P)$	2^+	9.91	—

The *spectroscopy* of $b\bar{b}$ states, i.e. the study of their masses, quantum numbers, and allowed transitions, provides information on the strong interaction that binds the quarks, similar to the situation with charmonium states. In fact, because of the b quark's higher mass, the information about the strong interaction from $b\bar{b}$ spectroscopy is more reliable and can be more easily compared with theoretical predictions.

Similar to the D mesons which consist of a c quark and a lighter antiquark, there are mesons consisting of a b quark combined with an antiquark of another flavour. These are called B mesons, and if needed they are written with a subscript to indicate the flavour of the other quark and with a superscript to indicate the charge. Note that by convention, the B^0 meson consists of $d\bar{b}$ and its antiparticle, the $\overline{B}^0$, is $b\bar{d}$. If no subscript is given, the paired quark is understood to be u or d, i.e. $B^\pm$ is $b\bar{u}$ or $u\bar{b}$. The names and properties of some important hadrons containing b quarks are given in Table 8.4.

The first three upsilon resonances are too light to decay into pairs of B mesons. Starting with

Table 8.4: Some hadrons containing b quarks and their properties [7].

particle	quarks	J^P	mass (GeV)	τ (s)	$c\tau$ (μm)
$B^{\pm}$	$u\bar{b}$, $b\bar{u}$	0^-	5.28	1.65×10^{-12}	496
B^0	$d\bar{b}$	0^-	5.28	1.55×10^{-12}	464
B_s^0	$s\bar{b}$	0^-	5.37	1.49×10^{-12}	448
$B_c^{\pm}$	$c\bar{b}$, $b\bar{c}$	0^-	6.4	0.5×10^{-12}	150
Λ_b	udb	$\frac{1}{2}^+$	5.62	1.2×10^{-12}	368

the $\Upsilon(4S)$, however, these decays do take place, and in fact the $\Upsilon(4S)$ decays approximately 50% of the time to B^+B^- and 50% to $B^0\overline{B}^0$. The accessibility of these decay channels which do not require annihilation of the b and $\bar{b}$ explains why the decay width for the Υ(4S) is so much larger than that of the lighter Υ resonances. The $\Upsilon(4S)$ cannot, however, decay into pairs of B_s^0 mesons, since these are somewhat heavier than the $B^{\pm}$ and B^0 (see Table 8.4). Starting with the $\Upsilon(5S)$, however, the decay into $B_s^0\overline{B}_s^0$ is possible.

For e^+e^- annihilation at even higher energies, one can produce pairs of B mesons in different combinations along with other hadrons. The amplitude for this reaction is given by the Feynman diagram shown in Fig. 8.11. The conversion of the quarks into hadrons is not computable using perturbation theory but is simply assumed to occur with unit probability. The amplitude is proportional to the charge of the b quark, and thus the cross section is proportional to its charge squared. The measured hadronic cross sections indicate that the b quark has charge of magnitude $1/3\,e$. In keeping with the convention for the other charge 1/3 quarks, the b quark is assigned charge $-1/3$ and the $\bar{b}$ is $+1/3$.

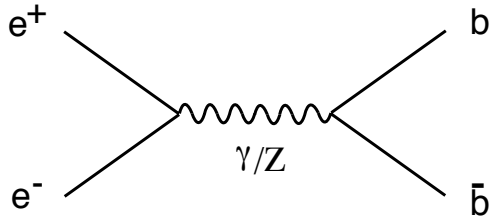

Figure 8.11: Feynman diagram for the reaction $e^+e^- \to b\bar{b}$. There are two separate amplitudes in which the intermediate boson is either a γ or a Z.

8.5 The CKM matrix and CP violation

We saw in Section 8.1 that the coupling strength g applied not to the vertices joining a W with ud or cs but rather with ud' and cs', where d' and s' are superpositions of d and s states. Since d and s were orthonormal states, and we wanted d' and s' also to be orthonormal, the transformation relating them was unitary. For two quark families this is equivalent to a rotation in 'ds' space by the angle θ_C (the Cabibbo angle),

$$\begin{pmatrix} d' \\ s' \end{pmatrix} = \begin{pmatrix} \cos\theta_C & \sin\theta_C \\ -\sin\theta_C & \cos\theta_C \end{pmatrix} \begin{pmatrix} d \\ s \end{pmatrix} . \tag{8.12}$$

With the discovery of the third family in the mid 1970s, this picture had to be generalized. In doing so the existence of the t quark was assumed, although it was not observed directly until the mid 1990s. One defines the states d', s' and b' to be the ones that couple to u, c and t, respectively, with the coupling strength g. The new states are related to the old ones, d, s and b, by a unitary transformation which can be represented by a 3×3 matrix V, called the *Cabibbo–Kobayashi–Maskawa (CKM) matrix*,

$$\begin{pmatrix} d' \\ s' \\ b' \end{pmatrix} = \begin{pmatrix} V_{ud} & V_{us} & V_{ub} \\ V_{cd} & V_{cs} & V_{cb} \\ V_{td} & V_{ts} & V_{tb} \end{pmatrix} \begin{pmatrix} d \\ s \\ b \end{pmatrix} . \tag{8.13}$$

The row of the matrix (i.e. the first index) always refers to a charge $2/3$ quark, u, c, or t, and the column (second index) refers to d, s, or b. At a vertex containing a W boson, a charge $2/3$ quark of type $i = u, c, t$ and a charge $-1/3$ quark of type $j = d, s, b$, the coupling strength is therefore not g but rather gV_{ij}.

The magnitudes of the CKM matrix elements $|V_{ij}|$ have approximately the following values:

$$|V_{ij}| \approx \begin{pmatrix} 0.975 & 0.220 & 0.003 \\ 0.220 & 0.975 & 0.04 \\ 0.008 & 0.04 & 0.999 \end{pmatrix} . \tag{8.14}$$

Note that the diagonal elements are close to unity. That is, the coupling strength for vertices containing a W and ud, cs, or tb is close to g. The coupling strength for us and cd vertices is reduced by a factor of 0.22 (in the two-family model this was $\sin\theta_{\rm C}$). Naively one expected the suppression of the couplings for c with b to be of a similar magnitude, but in fact it turned out to be significantly smaller, namely, $|V_{cb}| \approx 0.04$. Transitions between the 1st and 3rd families are suppressed even further, with $|V_{ub}| \approx 0.003$ and $|V_{td}| \approx 0.008$.

In order for d', s' and b' to form an orthonormal set of states, the CKM matrix V must be unitary. That is, we require

$$VV^\dagger = I \, , \tag{8.15}$$

where $V^\dagger$ is the adjoint of V (complex conjugate of the transposed matrix), and I is the 3×3 unit matrix. An arbitrary complex 3×3 matrix contains 18 numbers, but equation (8.15) represents 9 constraints. Furthermore one can show that 5 more constraints can be obtained from the freedom to redefine the phases of the quark states. Therefore the most general form of V consistent with unitarity can be represented by 4 real parameters. A commonly used parametrization of the CKM matrix due to Wolfenstein [63] is

$$V = \begin{pmatrix} 1 - \lambda^2/2 & \lambda & A\lambda^3(\rho - i\eta) \\ -\lambda & 1 - \lambda^2/2 & A\lambda^2 \\ A\lambda^3(1 - \rho - i\eta) & -A\lambda^2 & 1 \end{pmatrix} . \tag{8.16}$$

One can show that this form of V is not exactly unitary, but that $VV^\dagger \approx I$ plus corrections of order λ^4. To the extent that λ is small, this is a good enough approximation. The parameters are measured to be:

$$\lambda = 0.22535 \pm 0.00065 \,, \tag{8.17}$$

$$A = 0.811^{+0.022}_{-0.012} \,, \tag{8.18}$$

$$\rho = 0.131 \pm 0.026 \,, \tag{8.19}$$

$$\eta = 0.345 \pm 0.013 \,. \tag{8.20}$$

Kobayashi and Maskawa actually proposed the 3×3 generalization of Cabibbo's transformation in 1973 [64], even before the discovery of charm (but after charm's predicted existence through the GIM hypothesis). An important reason was that one can show that with a three-family model, particles and antiparticles behave in slightly different ways. This is a violation of what is called CP symmetry, where C stands for charge conjugation (replacement of particles by antiparticles) and P stands for parity (equivalent to a mirror reflection of the system). Violation of CP symmetry had been discovered in neutral kaon decays in 1964. Kobayashi and Maskawa realized that a three-family model could account for this, hence their extension of Cabibbo's idea.

The reason why CP violation does not occur in a two-family version of the Standard Model but does with three families is not at all trivial. It is related to the fact that the most general 2×2 transformation matrix can be taken to be real, i.e., the rotation matrix of equation (8.12). In the three-family model, however, at least some of the CKM matrix elements will in general be complex. In the Wolfenstein parametrization, this occurs if η is nonzero. This leads to coupling strengths which are complex, and this in turn leads to effects in which CP is not conserved, i.e., to differences in the predicted behaviour of matter and antimatter.

The universe appears to be predominantly made up of matter. If other parts of the universe were made of antimatter, then collisions between matter and antimatter dominated regions would lead to easily observable signals, and this is not seen. In the most plausible scenarios for the Big Bang, however, one starts with equal amounts of matter and antimatter, and the imbalance develops over time. This can only happen if the reaction rates which result in production of matter are unequal to those which result in antimatter, and this means one needs a violation of CP symmetry. (In addition one needs baryon-number violating processes and a departure from thermal equilibrium.) So although the 3rd family of quarks does not play an important role in the low-energy processes we see in our everyday lives, it appears to play a crucial role in CP violation and thus in the explanation for why we live in a matter-dominated universe.

A large amount of experimental effort has gone into the study of CP violation in B mesons decays. Experiments such as BaBar at SLAC and BELLE at KEK (Japan), used the reaction $e^+e^- \to \Upsilon(4S)$ to obtain pairs of B and $\overline{B}$ mesons from the $\Upsilon(4S)$ decay. Information on CP violation can obtained by measuring the decay rates of B mesons to various final states as a function of the decay time and comparing these to the corresponding results for the charge conjugate decays, i.e., with all particles replaced by their antiparticle partners. So far, all of their results have shown consistency with the predictions.

8.6 Lifetimes of charmed and bottom hadrons

Most of the important decays of D and B mesons can be modelled by assuming that the c or b quark decays without any influence from the partner antiquark; this is called the *spectator model*. For example, the decay $D^0 \to K^-\pi^+$, can be described by the Feynman diagram in Fig. 8.12.

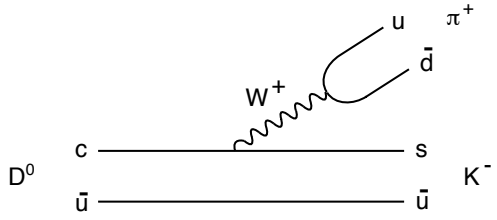

Figure 8.12: Feynman diagram for the decay $D^0 \to K^-\pi^+$.

The mean lifetime of the D hadrons is thus determined to a good approximation by the mean lifetime of the c quark, regardless of its surroundings. A Feynman diagram for the decay $c \to se^+\nu_e$ is shown in Fig. 8.13. One has similar diagrams for $c \to s\mu^+\nu_\mu$ and $c \to su\overline{d}'$

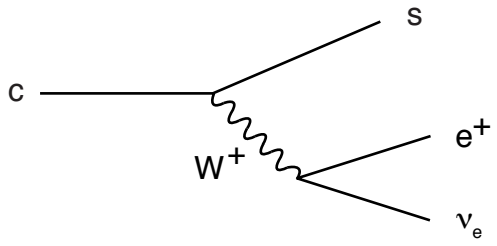

Figure 8.13: A Feynman diagram for the decay $c \to se^+\nu_e$. The coupling strength at the Wcs vertex is gV_{cs}.

The decay rate can be written down by comparing with the corresponding formula for muon decay, equation (5.6),

$$\Gamma(c \to se^+\nu_e) = \frac{G_F^2 m_c^5}{192\pi^3}|V_{cs}|^2 \,. \tag{8.21}$$

The only differences with the corresponding formula for the muon are that here we have the c quark's mass to the 5th power and in addition the factor $|V_{cs}|^2$. We can guess that $|V_{cs}|$ should be close to unity, however, since the c and s quarks are in the same family. If we take 1.2 GeV for the c quark's mass, include all of the kinematically allowed final states to compute the total decay rate, and correct for the influence of the finite masses of final state particles, one obtains a predicted mean lifetime for the c quark of around 1 ps. The various D meson states have in fact lifetimes in this range, as seen in Table 8.2.

We can carry out a similar calculation to estimate the b quark's lifetime. The decay rate $\Gamma(b \to ce^-\overline{\nu}_e)$ will be

$$\Gamma(b \to ce^-\overline{\nu}_e) = \frac{G_F^2 m_b^5}{192\pi^3}|V_{cb}|^2 \,. \tag{8.22}$$

Here we have no simple way of knowing what V_{cb} will be, and this is needed in order to predict the b quark's lifetime. In fact one uses the measured B meson lifetime of around 1.5 ps to

determine $|V_{cb}| \approx 0.04$. This surprisingly small value means that B mesons actually live longer than D mesons, despite the fact that the decay rate goes as the 5th power of the quark's mass.

8.7 The top quark

After the discovery of the bottom quark, the τ lepton, and the indirect but compelling evidence for its associated neutrino, one was back to a situation similar to before the discovery of charm in 1974. That is, there were three full families of leptons but only two and one half families of quarks. It was immediately supposed that an additional quark called *top* should exist[2].

Every e^+e^- collider since SPEAR has listed the search for the top quark among its aims. The reaction $e^+e^- \to t\bar{t}$ should proceed through the same Feynman diagram as that for $e^+e^- \to b\bar{b}$. For a correctly chosen centre-of-mass energy, namely, around twice the mass of the t quark, a system of resonances similar to the Υ system was expected. For $E_{\rm cm} \geq 2m_t$, $e^+e^- \to t\bar{t}$ becomes kinematically possible and this channel should contribute to the total hadronic cross section.

By looking at the masses of the first five quarks and naively guessing where Nature would put the sixth, it seemed reasonably certain that it should be found by the PETRA e^+e^- ring at DESY (Hamburg), which eventually achieved $E_{\rm cm} = 44$ GeV. It was not. Nor was it found by the Japanese at the e^+e^- ring TRISTAN, which reached $E_{\rm cm} = 64$ GeV, nor by the LEP e^+e^- collider, which began running in 1989 at $E_{\rm cm}$ near 91 GeV.

In an indirect sense, however, the top quark was in fact first seen at LEP. Just as the GIM hypothesis had used the then hypothetical c quark to predict reaction rates based on its presence as a virtual particle in intermediate states, Feynman diagrams containing virtual top quarks have an influence on predicted reaction rates even if the t quark is not produced in the final state. An example is the graph in Fig. 8.14, which contains an intermediate loop consisting of W boson and the t quark. This is a higher order correction to the diagram for $e^+e^- \to b\bar{b}$ shown in Fig. 8.11, and its influence on the cross section $\sigma(e^+e^- \to b\bar{b})$ depends on the top quark's mass. By measuring this and other cross sections, by the early 1990s the top quark's mass had been estimated to be around 170 GeV with an uncertainty of 20 to 30 GeV.

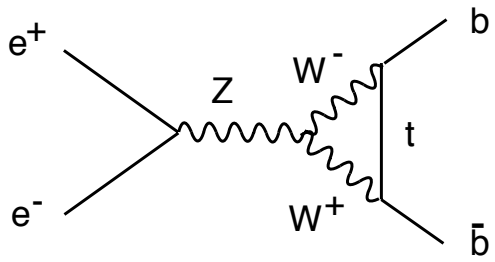

Figure 8.14: A higher order correction to the amplitude for $e^+e^- \to b\bar{b}$ that is sensitive to the mass of the top quark.

Real (i.e. on-shell) top quarks were finally observed in 1995 in proton–antiproton collisions by the CDF and D0 detector at Fermilab, and this is generally recognized as the 'discovery' of top [65]. The most important amplitude for the production of a $t\bar{t}$ pair is shown in Fig. 8.15(a). A quark from the proton annihilates with an antiquark of the same flavour in the antiproton into a gluon, which then dissociates into the $t\bar{t}$ pair. The t quark has a mass of around 175 GeV,

[2]Instead of top and bottom, the names *truth* and *beauty* were sometimes used.

i.e. much more massive even than the W boson, which has a mass of around 80 GeV. Therefore its dominant decay mode is into a b quark and an on-shell W boson, according to the Feynman diagram in Fig. 8.15(b).

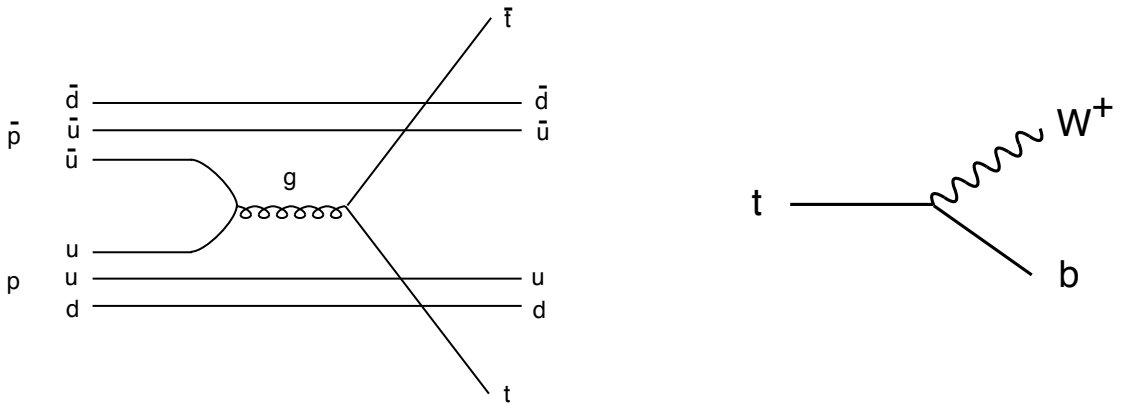

(a) (b)

Figure 8.15: Feynman diagrams for (a) the production of a $t\bar{t}$ pair in proton–antiproton collisions and (b) the decay $t \to \mathrm{W}^+ b$.

The b quark produces a jet of hadrons which will contain a B hadron, and this can be identified by the fact that it lives long enough for its decay vertex to be displaced several mm from the $t\bar{t}$ production point. As we have seen, the W boson can decay either into a lepton–neutrino pair or into a quark and antiquark. The top's discovery exploited those events where one of the Ws decayed into an electron or muon plus the associated neutrino. This is because electrons and muons are both relatively easy to identify in multiparticle events. Furthermore, the neutrinos escape detection and lead to an overall imbalance in the momentum of the final state particles, and this can also be used as a 'signature' of $t\bar{t}$ events. A classic top event from the CDF detector is shown in Fig. 8.16 (from [66]). The initial discovery was made from 12 candidate events sifted out of over 10^{12} proton–antiproton collisions.

When both W bosons decay into leptons, we call this type of $t\bar{t}$ events "dileptonic". Although the branching ratio for this type of event is small, the backgrounds are also quite small, making it a good experimental signature for top-quark pair events. When one of the Ws decays into leptons while the other to quarks, we call this the "Lepton+jets" channel. This channel is also quite good experimentally since even though the backgrounds are higher than in the dilepton channel, the branching ratio is also higher, providing more signal events for the same amount of integrated luminosity. Finally, when both Ws decay into quarks, there are no lepton in the event and although this has the highest branching ratio, the backgrounds are very large. We call this the "all-hadronic" channel.

From the energies and momenta of the top's decay products, the top quark's mass has been determined to be [7]

$$m_t = 173.5 \pm 1.0 \text{ GeV} . \tag{8.23}$$

This is in good agreement with the current best determined value of m_t from higher order corrections involving virtual top quarks, namely, 168 ± 8 GeV [7].

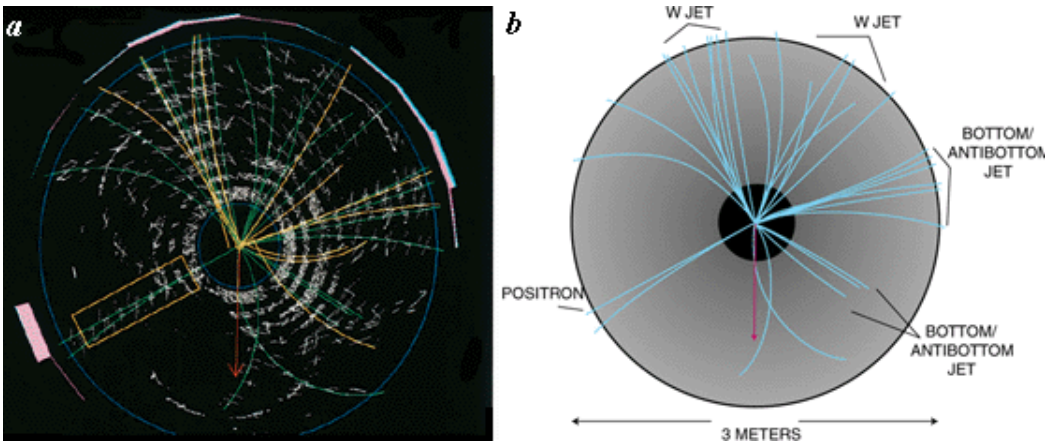

Figure 8.16: An event from the CDF detector showing the production and decay of a $t\bar{t}$ pair. The arrow pointing downwards in the right-hand diagram shows the missing momentum due to the neutrino from the decay $\mathrm{W}^+ \to \mathrm{e}^+\nu_\mathrm{e}$ [66].

For all of the other weakly decaying quarks, the decay rate is proportional to the 5th power of the quark's mass. The top quark is different, however, because it is more massive than the W. In this case, we don't write down a propagator for the W because we regard it as a 'final state' particle. Of course it decays as well, but as far as the decay rate of the t quark is concerned, this is not important.

The amplitude in Fig. 8.15(b) for $t \to b\mathrm{W}^+$ is therefore proportional to the weak coupling g, and by dimensional grounds one might naively expect the decay rate to go as $g^2 m_t$. The Feynman rules are a bit more complicated, however, when we have a massive vector boson such as the W in the final state, and in fact the decay rate is given by [67]

$$\Gamma(t \to bW) = \frac{G_\mathrm{F} m_t^3}{8\pi\sqrt{2}} |V_{tb}|^2 \approx 1.74 \text{ GeV} , \tag{8.24}$$

where $|V_{tb}| \approx 1$ is the CKM matrix element discussed in Section 8.5. As $t \to b\mathrm{W}$ is expected to be the dominant decay mode, the decay rate (8.24) is to a good approximation the total decay rate, and thus its inverse gives the mean lifetime of the top quark. Inserting the factors of c and $\hbar c$ to get back to normal units one obtains

$$\tau_t = \frac{1}{\Gamma_t} = \frac{1}{1.74 \text{ GeV}} \times 0.197 \text{ GeV-fm} \times \frac{1}{3.0 \times 10^{23} \text{ fm/s}} = 3.8 \times 10^{-25} \text{ s} . \tag{8.25}$$

In this time, a particle moving at the speed of light can travel a distance $d = \tau_t c$, which is

$$d = 3.8 \times 10^{-25} \text{ s} \times 3.0 \times 10^{23} \text{ fm/s} \approx 0.1 \text{ fm} . \tag{8.26}$$

Recall from Chapter 7, however, that the size of a hadron is around 1 fm. Roughly speaking, this represents the size of the orbit of a quark–antiquark system. We see that the top's lifetime is so short that it decays long before a meson can be formed, i.e. before it can complete a single orbit.

The consequence of this is profound: there are no mesons or hadrons containing top quarks and the information from the top quark (like its spin, etc.) is passed to its decay products. Top-quark studies offer a way of studying a "naked" quark. Moreover, because it is the heaviest particle, it is intimately linked to the Higgs boson. For example, by combining information on the mass of the W boson and the mass of the top quark one can constrain the mass of the Higgs. If the measured mass of the Higgs were to disagree with this indirect constraint, this would be a sign that there is something missing in the Standard Model or in the Higgs mechanism.

The LHC is sometimes referred to as a "top quark factory" because it produces some many events containing top quarks, allowing very precise measurements to be made about the top quark. At the LHC, the most common production of top quarks is via the strong interaction involving gluons buried inside the colliding protons as shown in Fig. 8.17.

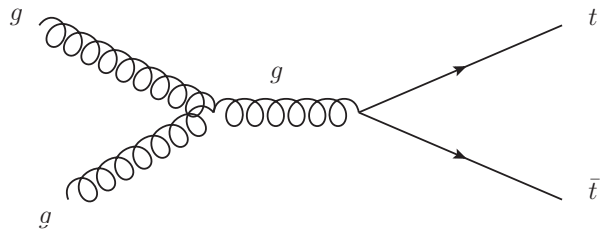

Figure 8.17: Production of top quark pair events at the LHC from gluons inside the colliding protons.

Chapter 9

The electroweak standard model

In this chapter we put together many of the ingredients we have seen into a unified theory that forms the core of the Standard Model. First, in Section 9.1 we take a look at Fermi's original theory of weak interactions and show why people did not believe that this was entirely correct. The guiding principle for constructing a better theory is *gauge invariance*, which we introduce in Section 9.2. In putting together such a theory we have to take into account that weak interactions, for reasons that are not well understood, distinguish between right and left. This is reflected in the non-conservation of parity, and is discussed in Section 9.3. In Section 9.4 we describe how all this is put together into what we call the GWS model of *electroweak* interactions, which gives a unified description of electromagnetic and weak phenomena. In Sections 9.5 through 9.8 we take a look at the experimental evidence that both determines the free parameters of this theory and provides stringent tests of its predictions.

9.1 Theoretical need for the intermediate vector boson

In 1934 Fermi proposed a theory of weak interactions to describe processes such as nuclear beta decay [30]. Some modifications of the theory were made in the following decades, most notably concerning the dependence of the interaction on the spin states of the particles involved; these changes were settled by 1957. In this theory, amplitudes for processes such as the decay $\mu^- \to \mathrm{e}^-\nu_\mu\overline{\nu}_\mathrm{e}$ are described by a *four-fermion vertex* as shown in Fig. 9.1(a). The coupling strength for the vertex is the Fermi constant, $G_\mathrm{F} = 1.166 \times 10^{-5}$ GeV^{-2}.

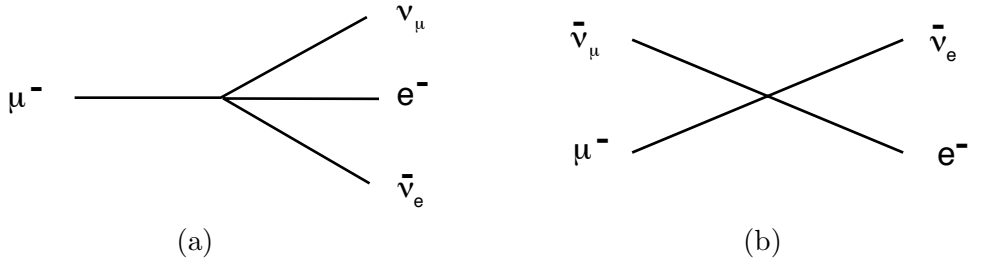

Figure 9.1: Feynman diagrams in Fermi's theory for (a) muon decay, $\mu^- \to \mathrm{e}^-\nu_\mu\overline{\nu}_\mathrm{e}$, and (b) $\mu^-\overline{\nu}_\mu \to \mathrm{e}^-\overline{\nu}_\mathrm{e}$.

Fermi's theory could also describe other processes that should be possible in principle but which for technological reasons have not been investigated experimentally. An example is the scattering reaction $\mu^-\overline{\nu}_\mu \to \mathrm{e}^-\overline{\nu}_\mathrm{e}$, which would be described by the diagram in Fig. 9.1(b). For those processes that could be measured such as beta decay, muon decay, etc., predictions based on lowest order diagrams were in good agreement with experiment. Nevertheless, it was clear from an early stage that the theory couldn't be completely correct.

The reason for this was that the predictions for very high energy reactions didn't make sense. Consider, for example, the scattering reaction $\mu^-\overline{\nu}_\mu \to \mathrm{e}^-\overline{\nu}_\mathrm{e}$ in Fig. 9.1(b). The coupling strength for the vertex is G_F, and so the cross section is proportional to G_F^2, which has dimension of energy^{-4}. In particle physics units, a cross section has dimension energy^{-2}, so to obtain this, we need to multiply G_F^2 by something with units of energy squared. For high energies, we expect the rest masses of initial and final state particles not to have an influence on the cross section, so the only available quantity is the centre-of-mass energy. Thus we expect

$$\sigma(\mu^-\overline{\nu}_\mu \to \mathrm{e}^-\overline{\nu}_\mathrm{e}) \sim G_\mathrm{F}^2 E_\mathrm{cm}^2 \,, \tag{9.1}$$

where the constant of proportionality turns out to be of order unity.

The problem with the cross section (9.1) is that it becomes arbitrarily large for increasing energy. Recall, however, that a cross section is a way of quantifying the probability that a process will take place, and a probability is bounded to lie between zero and one. We can determine the maximum allowed cross section, called the *unitarity limit*, which corresponds to the reaction taking place with unit probability. For $\mu^-\overline{\nu}_\mu \to \mathrm{e}^-\overline{\nu}_\mathrm{e}$, this is at an energy of around 300 GeV. While it was not actually possible to do experiments at such high energies (in fact, it is not technologically possible to do $\mu^-\overline{\nu}_\mu$ scattering at all), it was nevertheless clear that Fermi's theory could at best represent a sort of low-energy approximation.

One could try to argue that the apparent violation of unitarity might result from using only the lowest order diagram for the prediction. By systematically applying the rules of perturbation theory, one should include higher order corrections from diagrams such as the one shown in 9.2. Rather than being small corrections, however, the amplitudes corresponding to diagrams of this type contain divergent integrals, i.e., they are infinite.

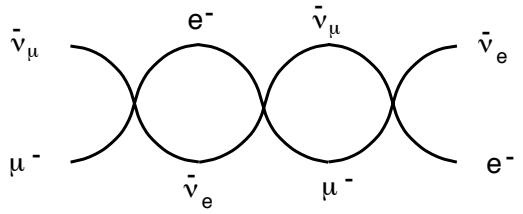

Figure 9.2: A higher order correction in Fermi's theory for $\mu^-\overline{\nu}_\mu \to \mathrm{e}^-\overline{\nu}_\mathrm{e}$.

The problem with infinite corrections plagued not only Fermi's theory but also quantum electrodynamics. By the late 1940s, Feynman, Schwinger and Tomonaga developed a set of techniques called *renormalization*, by which the infinities are eliminated from predictions for observable quantities. This procedure worked well with QED, but it could not be applied to Fermi's theory of weak interactions.

It was realized early on that the problem with cross sections exceeding the unitarity limit could be solved if the weak interaction involved the exchange of a virtual particle, much in

the way that the electromagnetic interaction between charged particles involves the exchange of photons. In analogy with QED, theories were proposed involving the exchange of a spin-1 (i.e. a vector) particle, called therefore an *intermediate vector boson* or IVB.

In order to explain the slowness of weak decays, the IVB would have to be massive. Amplitudes involving the exchange of an IVB contain a propagator that goes as $1/(q^2 - M^2)$, and thus with a sufficiently high mass one could explain the 'weakness' of the weak interaction. This IVB is basically what we now identify as the W boson. The amplitudes for muon decay and for $\mu^-\nu_\mu \to \mathrm{e}^-\overline{\nu}_\mathrm{e}$ in the IVB theory are shown in Figs. 9.3.

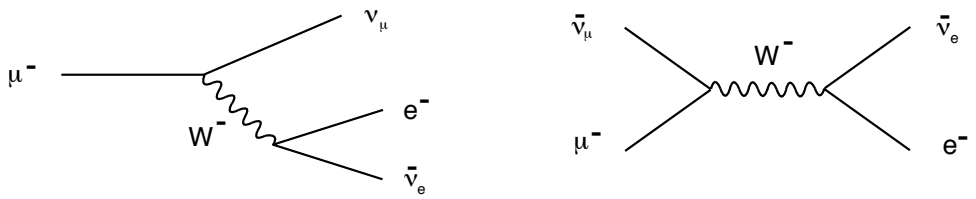

Figure 9.3: Feynman diagrams in the IVB theory for (a) muon decay and (b) $\mu^-\overline{\nu}_\mu \to \mathrm{e}^-\overline{\nu}_\mathrm{e}$.

As we have already seen in Chapter 5, the amplitude for muon decay follows

$$\mathcal{M} \propto \frac{g^2}{q^2 - M_\mathrm{W}^2} \approx \frac{-g^2}{M_\mathrm{W}^2} \,, \tag{9.2}$$

where the approximation holds since q^2, the virtual mass squared of the W, must be on the order of the muon–electron mass difference, and this is small compared to what we will eventually find for M_W (around 80 GeV). Recall that in Fermi's theory, the corresponding amplitude is proportional to G_F. For historical reasons, the exact relation between G_F and g^2/M_W^2 contains some additional numerical factors, being

$$G_\mathrm{F} = \frac{\sqrt{2}g^2}{8M_\mathrm{W}^2} \,. \tag{9.3}$$

In a similar way, the amplitude for neutrino–muon scattering follows

$$\mathcal{M} \propto \frac{g^2}{q^2 - M_\mathrm{W}^2} = \frac{g^2}{E_\mathrm{cm}^2 - M_\mathrm{W}^2} \,, \tag{9.4}$$

where in this diagram the virtual mass of the W is equal to the centre-of-mass energy. For $E_\mathrm{cm} \gg M_\mathrm{W}$, we can neglect M_W in the propagator. This means that at very high energies, the cross section does not increase as $G_\mathrm{F}^2 E_\mathrm{cm}^2$, but rather it falls as

$$\sigma(\mu^-\overline{\nu}_\mu \to \mathrm{e}^-\overline{\nu}_\mathrm{e}) \propto |\mathcal{M}|^2 \sim \frac{g^4}{E_\mathrm{cm}^2} \,, \tag{9.5}$$

where an extra factor of E_cm^2 in the numerator came from the phase-space part of the amplitude, which is needed for a scattering process.

In this way, the cross section does not exceed the unitarity limit and predicted probabilities for scattering reactions remain below unity.

Experimental searches for intermediate vector bosons through the 1970s excluded their existence for masses up to around 20 GeV. And although they appeared to solve the unitarity problem, there was no compelling criterion by which the detailed properties of the IVB theory could be determined. Furthermore, the problem with the infinities in higher order corrections remained.

9.2 Gauge symmetry

In 1954 Yang and Mills proposed a general framework for theories involving the exchange of intermediate vector bosons [68]. This class of theory is based on what is called *local gauge symmetry*, i.e., an invariance of the Lagrangian of the theory under a local gauge transformation.

Quantum electrodynamics is a particular example of such a theory. We can gain some insight into how gauge symmetry works without the full machinery of QED simply by considering the electromagnetic interaction as described in non-relativistic quantum mechanics. First recall the Schrödinger equation (with $\hbar = 1$) for a free particle of mass m,

$$-\frac{1}{2m}\nabla^2\psi = i\frac{\partial}{\partial t}\psi \ . \tag{9.6}$$

We can find a solution $\psi(t, \mathbf{x})$, normalize it in some volume, and we will see that it is not unique. For example, if $\psi(t, \mathbf{x})$ is a solution, then the function

$$\psi'(t, \mathbf{x}) = \psi(t, \mathbf{x})e^{i\alpha} \ , \tag{9.7}$$

where α is an arbitrary constant, is also a solution. Equation (9.7) is called a *global gauge transformation*, i.e., global in the sense that the phase change for ψ is the same for all values of space and time.

In a similar way, if $\psi(t, \mathbf{x})$ is a solution to the Schrödinger equation we can ask if the function

$$\psi'(t, \mathbf{x}) = \psi(t, \mathbf{x})e^{i\alpha(t,\mathbf{x})} \tag{9.8}$$

is also a solution, where now α is taken to be an arbitrary function of space and time. This is called a *local* gauge transformation, i.e., the change in phase is allowed to be different in space and time. Substituting into (9.6) shows that this ψ' will not in general be a solution.

If, however, the particle has charge q and is in an electromagnetic field described by a vector potential $\mathbf{A}$ and scalar potential φ, the Schrödinger equation becomes

$$\left\{\frac{1}{2m}(-i\nabla - q\mathbf{A})^2 + q\varphi\right\}\psi = i\frac{\partial}{\partial t}\psi \ . \tag{9.9}$$

We can then show that if $\psi(t, \mathbf{x})$ is a solution, then the function

$$\psi'(t, \mathbf{x}) = \psi(t, \mathbf{x})e^{i\alpha(t,\mathbf{x})} \tag{9.10}$$

will also be a solution as long we replace the potentials by

$$\mathbf{A}' = \mathbf{A} + \frac{1}{q}\nabla\alpha \,, \tag{9.11}$$

$$\varphi' = \varphi - \frac{1}{q}\frac{\partial\alpha}{\partial t} \,. \tag{9.12}$$

That is, the equations describing a particle in an electromagnetic field are invariant under a local gauge transformation. It can easily be verified that the transformations of $\mathbf{A}$ and φ do not change the electric or magnetic fields.

Suppose now that we knew about some particle that obeyed the Schrödinger equation, but that we didn't yet know about the electromagnetic field, i.e., we hadn't yet discovered the photon. If we wanted to insist that the solution to the Schrödinger equation be symmetric under a local gauge transformation, then we can show that this would only be possible if the terms in the equation corresponding to $\mathbf{A}$ and φ also exist and that transformations of both the wave function and the potentials are carried out. That is, if for some reason we had wanted to require this sort of local gauge symmetry, we could have predicted the existence of the photon.

Historically, one discovered the laws of electromagnetism and quantum mechanics and then observed that the equations possessed local gauge symmetry. Once we see that electromagnetism has this property, however, we can guess that other interactions might also have a similar type of symmetry. We then find that local gauge symmetry is only possible if other particles are introduced into the theory, in the same way that it only worked for a particle of charge q if we have $\mathbf{A}$ and φ, i.e., if the photon exists. These additional particles are called *gauge bosons*. Local gauge symmetry turns out to be the fundamental guiding principle of the Standard Model, and one predicts in this way not only the photon but also the $\mathrm{W}^{\pm}$, the Z and the gluon.

9.3 Non-conservation of parity

In Section 9.1 we mentioned that certain modifications to Fermi's theory were introduced to account for the dependence of the weak interaction on the spin state of the particles involved. These modifications were necessary because the observed angular distribution of electrons emitted in beta decay of polarized nuclei indicated that parity is not conserved in the weak interaction.

We can roughly understand conservation of parity as meaning that a system behaves the same as its mirror image. Suppose we build some device such as a clock. Now build another one which is the exact mirror image of the first, including all of its internal screws and springs and so on. We can then ask whether the two clocks will run in the same way. If only the electromagnetic interaction, gravity or the strong interaction are involved, it appears that Nature's answer is yes. If, however, the weak interaction comes into play, then the two clocks will not keep the same time.

Now consider a nucleus with nonzero magnetic moment such as ^{60}Co, which undergoes the beta decay

$$^{60}\mathrm{Co} \rightarrow ^{60}\mathrm{Ni} + \mathrm{e}^- + \overline{\nu}_\mathrm{e} \,.$$

Suppose we produce a magnetic field by running a current through a coil of wire as shown in Fig. 9.4(a). The spins of the nuclei will then line up with the magnetic field, and we can measure the number of electrons emitted as a function of the angle θ as shown in the figure.

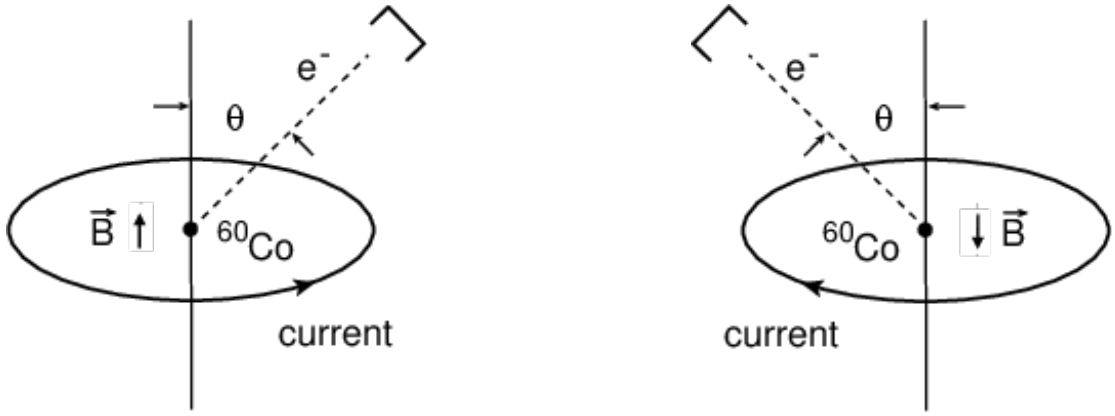

(a) (b)

Figure 9.4: (a) An experiment in which nuclear spins are aligned parallel to a magnetic field created by a current loop, and the number of beta electrons is measured at the angle θ. (b) The mirror image experiment.

The mirror image experiment is shown in Fig. 9.4(b). If parity is conserved, we should expect the same numbers of electrons to be found in the two detectors. Note however, that in constructing the mirror image experiment, the current in the coil runs in the opposite direction. This means that the magnetic field in this experiment will point downwards, and the nuclear spins therefore also point down. In the mirror image experiment, the angle between the detector and the magnetic field is therefore not θ but rather $\pi - \theta$. That is, the mirror image experiment at $\pi - \theta$ is identical to the original experiment at θ, but with the entire apparatus rotated top for bottom.

In practice we don't literally build the mirror image experiment. We are happy to assume that a rotation by 180° shouldn't matter, and we simply measure the number of electrons $N(\theta)$ as a function of θ. If parity is conserved, we should find

$$N(\theta) = N(\pi - \theta) \; . \tag{9.13}$$

This was measured by Wu in 1957 [69], after it had been pointed out by Lee and Yang [70] that parity non-conservation could be a real possibility. She found that equation (9.13) did *not* hold, and therefore that parity was not conserved.

What she found, in fact, was an angular distribution of the electrons emitted from polarized nuclei that could be explained if one assumed that the antineutrino always comes out with its spin parallel to its direction of motion. For a massless particle, which for the neutrino is a good approximation for now, the state with the spin parallel to the momentum is said to be *right-handed*. The Dirac equation then says that if only right-handed antineutrinos exist, then neutrinos are always left-handed, i.e., their spin is always aligned antiparallel to their direction of motion.

We have no explanation for why Nature chooses to be right–left symmetric for electromagnetism, strong interactions and gravity, and then is completely asymmetric in this regard for the weak interactions. But this has been measured to a high level of precision in many weak interaction processes, and we must therefore include it in any theory of weak interactions we try to construct. We should emphasize that it does not emerge as a prediction or a consequence of the theory that we will eventually call the Standard Model; for now, parity violation has to be put in 'by hand'.

9.4 Electroweak unification

Having seen that quantum electrodynamics obeys a local gauge symmetry, the hope was that by requiring the equations describing quarks and leptons to obey a similar symmetry one would find a theory containing the W boson. Unfortunately, this appeared to work only for massless exchange particles, whereas we have seen that the theory of weak interactions requires a massive IVB.

In the mid 1960s, Peter Higgs and others showed that by suitable modification of the theory, gauge symmetry to could work even for massive particles [71]. This modification is called the *Higgs mechanism*, and leads to the prediction of the recently discovered *Higgs boson*. By the late 1960s, Glashow [72], Weinberg [73] and Salam [74] had independently constructed a theory based on this mechanism and on a particular gauge transformation which in the arcane language of group theory can be labelled as $\mathrm{SU(2)_L} \otimes \mathrm{U(1)}$.

Initially, it was not clear whether the Glashow–Weinberg–Salam (GWS) theory would be renormalizable, i.e., whether the infinities that crop up in the higher order corrections could be eliminated. In 1971 it was shown by 't Hooft that the GWS theory was renormalizable, and in fact it was shown that *all* renormalizable theories must be gauge theories of the Yang–Mills type [75]. We'll now take a closer look at how the $\mathrm{SU(2)_L} \otimes \mathrm{U(1)}$ gauge transformation works and how this results in the theory that we want.

First, the wave functions describing the quarks and leptons are split into what are called right- and left-handed components; for relativistic particles, these correspond to the states with orientation of the spin parallel and antiparallel to the direction of motion. The local gauge transformation for the right-handed parts is similar to that discussed above for electromagnetism. One allows for a change of the wave function's phase which can be different at different places and times. This is called a U(1) (one-dimensional unitary) transformation.

The left-handed components of the leptons and quarks are then grouped into pairs called *doublets*:

$$\begin{pmatrix} \nu_\mathrm{e} \\ \mathrm{e}^- \end{pmatrix} \qquad \begin{pmatrix} \nu_\mu \\ \mu^- \end{pmatrix} \qquad \begin{pmatrix} \nu_\tau \\ \tau^- \end{pmatrix} \tag{9.14}$$

and

$$\begin{pmatrix} u \\ d' \end{pmatrix} \qquad \begin{pmatrix} c \\ s' \end{pmatrix} \qquad \begin{pmatrix} t \\ b' \end{pmatrix}, \tag{9.15}$$

where d', s' and b' are the CKM rotated mixtures of d, s and b as seen in Chapter 8. For the left-handed doublets, in addition to the change of phase one allows for a mixing of the upper and lower components, corresponding to multiplication of the doublet by a 2×2 unitary matrix with determinant equal to unity. This is called an $\mathrm{SU(2)_L}$ transformation, where S stands for 'special', i.e., determinant equal to one, and L stands for 'left'. The different transformations for right- and left-handed components are necessary in order to obtain a theory that contains the parity violation seen in beta decay.

Requiring invariance of the Lagrangian density under the combined $\mathrm{SU(2)_L} \otimes \mathrm{U(1)}$ gauge transformation predicts four gauge bosons whose wave functions are denoted W_1, W_2, W_3 and B. Two orthogonal superpositions of W_1 and W_2,

$$W^{\pm} = \frac{1}{\sqrt{2}}(W_1 \mp iW_2) \; , \tag{9.16}$$

can be identified with the charged $\mathrm{W}^{\pm}$ bosons.

A particular superposition of the W_3 and B states will form the photon, whose wave function is denoted by A, and the state orthogonal to this will be a massive neutral boson which Weinberg called the Z. A general orthogonal mixture of the W_3 and B can be expressed as a rotation by an angle θ_{W}, called the *weak mixing angle*:

$$\begin{pmatrix} A \\ Z \end{pmatrix} = \begin{pmatrix} \cos\theta_{\mathrm{W}} & \sin\theta_{\mathrm{W}} \\ -\sin\theta_{\mathrm{W}} & \cos\theta_{\mathrm{W}} \end{pmatrix} \begin{pmatrix} B \\ W_3 \end{pmatrix} \; . \tag{9.17}$$

As a result of this superposition, the coupling strengths of the quarks and leptons to the A and Z states will be functions of their couplings to B and W_3. The value of θ_{W} is determined by the requirement that state A, i.e. the photon, should not couple to the neutrino, since this is electrically neutral. One can show that this implies a relation between $\sin\theta_{\mathrm{W}}$ and the coupling strengths e and g,

$$\sin\theta_{\mathrm{W}} = \frac{e}{g}. \tag{9.18}$$

Usually one quotes a value for $\sin^2\theta_{\mathrm{W}}$, since this is what appears in the predictions for a number of important observables. Using $e = 0.303$ and $g = 0.65$ gives $\sin^2\theta_{\mathrm{W}} = 0.22$.

Recall that the GWS theory employed the Higgs mechanism to have local gauge symmetry for a theory with massive particles. One can show that this implies a relation between $\sin\theta_{\mathrm{W}}$ and the masses of the W and Z bosons, namely,

$$\sin^2\theta_{\mathrm{W}} = 1 - \frac{M_{\mathrm{W}}^2}{M_{\mathrm{Z}}^2} \; . \tag{9.19}$$

Once the W and Z bosons were finally discovered, as we will describe in Section 9.6, one could use their measured masses $M_{\mathrm{W}} = 80.4$ GeV and $M_{\mathrm{Z}} = 91.2$ GeV to predict $\sin^2\theta_{\mathrm{W}} = 0.222$, in good agreement with the value based on the coupling strengths e and g.

So in the end, the GWS theory describes not only the weak interaction but electromagnetism as well. It is therefore said to describe a unified *electroweak* interaction. At the time the theory

was proposed, however, no direct evidence for the charged W existed, and indeed there was no evidence at all for the neutral Z. In fact there was still no experimental result contradicting Fermi's theory. Nevertheless, for theoretical reasons people's interest shifted to gauge theories, and in particular to the GWS theory of electroweak interactions.

9.5 Discovery of weak neutral currents

The first evidence of weak interactions mediated by a massive neutral boson (what are called *weak neutral current processes*), was found in a neutrino scattering experiment with the Gargamelle bubble chamber at CERN in 1973 [76]. A beam of muon-type neutrinos was produced by first creating beams of π^+ and π^-, which then decay as $\pi^- \to \mu^- \overline{\nu}_\mu$ and $\pi^+ \to \mu^+ \nu_\mu$. The muons and any remaining hadrons are then absorbed in a thick earth absorber and only the ν_μ or $\overline{\nu}_\mu$ make it as far as the bubble chamber.

The Gargamelle bubble chamber was filled with freon, a dense liquid, in which hadrons either interact or are absorbed. Only muons are sufficiently penetrating to leave a long track in the chamber. In the event shown in Fig. 9.5, for example, one sees a neutrino interaction producing a number of hadrons and in addition a muon which exits the chamber to the right. The Gargamelle group also observed events where hadrons were produced but without muons, as shown in Fig. 9.6.

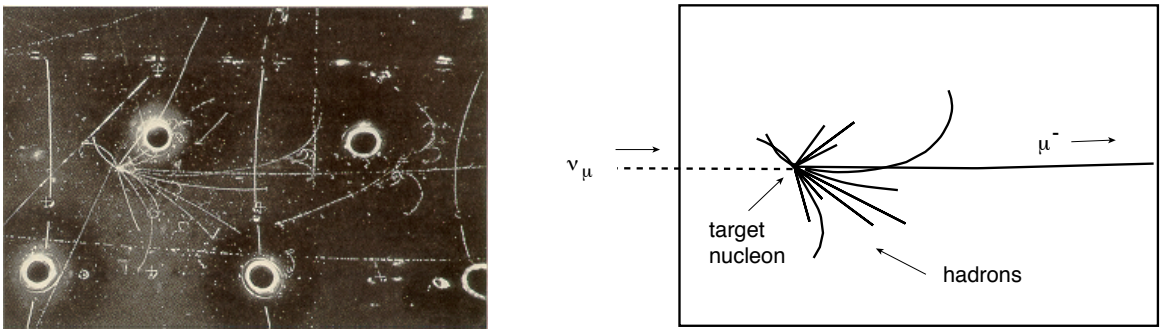

(a) (b)

Figure 9.5: Bubble chamber photograph (left) and its interpretation (right) showing the reaction $\nu_\mu \mathrm{N} \to \mu^- +$ hadrons, where N is a nucleon (from D. Perkins in [53], p. 428). The neutrino enters from the left and the muon exits to the right.

These two kinds of events can be interpreted with Feynman diagrams such as the ones shown in Fig. 9.7. In Fig. 9.7(a), the neutrino emits a charged W boson and is converted into a muon. The W is absorbed by a d quark in the nucleon and changes into a u quark, which is kicked out at a large angle. The quarks produce a system of hadrons consisting of at least one nucleon (to conserve baryon number) and a number of mesons. Since the charge of the lepton is changed, these are called a *charged current* (CC) events. In Fig. 9.7(b), the neutrino exchanges a neutral Z with the nucleon, and as a result it stays a neutrino; no muon is produced. The only thing one sees in the bubble chamber are the hadrons. These are *neutral current* (NC) events.

The cross sections for charged current and neutral current events depend on the coupling strengths of the W and Z to the quarks and leptons involved. In the GWS electroweak theory,

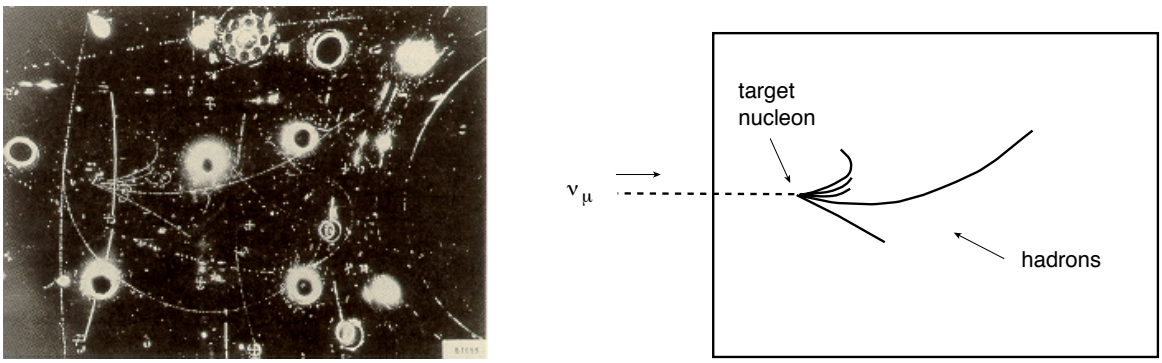

(a) (b)

Figure 9.6: Bubble chamber photograph (left) and its interpretation (right) showing the reaction $\nu_\mu \mathrm{N} \to \nu_\mu +$ hadrons (from D. Perkins in [53], p. 428). The neutrino enters from the left. All of the final state particles are identified as hadrons.

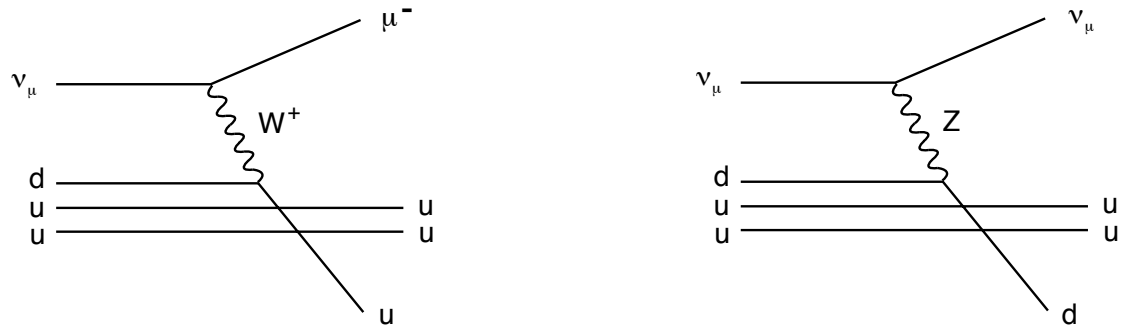

(a) (b)

Figure 9.7: Feynman diagrams for (a) a charged current and (b) a neutral current neutrino scattering event.

these couplings depend on the value of the weak mixing angle θ_W. From the observed ratio of charged current to neutral current events, the Gargamelle group was able to conclude that $\sin^2\theta_\mathrm{W}$ was around 0.3 to 0.4. More recent measurements give $\sin^2\theta_\mathrm{W} = 0.23$. Much more important than the measured values of the couplings was simply the observation of weak neutral current events, which indicated that something like the Z boson must exist.

9.6 The discovery of the W and Z bosons

Once neutral current processes had been well established and a promising candidate theory of electroweak interactions existed, it became clear that the next step was to produce real (i.e. on-shell) W and Z bosons and to study their properties. This was accomplished by converting CERN's Super Proton Synchroton (the SPS) into a proton–antiproton collider, called the Sp$\overline{\mathrm{p}}$S. The p and $\overline{\mathrm{p}}$ beams collided head-on with a centre-of-mass energy of 540 GeV. Two detectors, called UA1 and UA2, were built to observe the collisions and to look for evidence of W and Z

production.

W and Z bosons can be created by processes such as those shown in Fig. 9.8. In both Feynman diagrams, the bosons are shown to decay into leptons, since these are particularly easy to identify experimentally. The hadronic decay channels are in fact more frequent but also more difficult to distinguish from background events. In the case of $W^- \to e^- \overline{\nu}_e$, the presence of the neutrino can be inferred from the large imbalance in the momenta of the final state particles transverse to the beam line. For $Z \to e^+e^-$ or $Z \to \mu^+\mu^-$, the invariant mass of the lepton pair is equal to the mass of the Z boson.

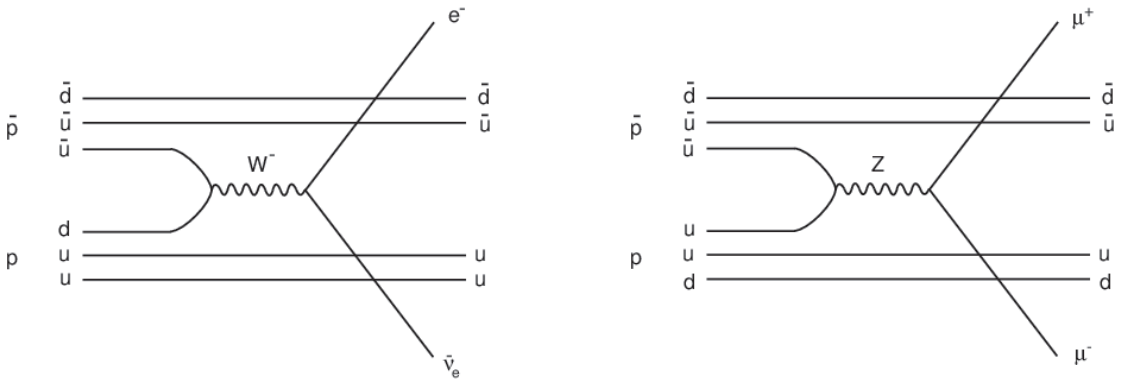

(a) (b)

Figure 9.8: Feynman diagrams for (a) production of a W boson and (b) production of a Z boson in proton–antiproton collisions.

In an intense competition between the two collaborations, the UA1 team succeeded first in finding evidence for the W and Z in early 1983 [77, 78]. If the W were to be produced at rest, then the electron energy in the decay $W^- \to e^- \overline{\nu}_e$ would be $M_W/2$. In fact, the W is not moving very fast because it is so massive. By looking at as many events as possible and taking into account the W's motion, one can infer its mass indirectly from the distribution of the lepton's momentum and from the missing momentum component transverse to the beam line; the UA1 collaboration found $M_W = 81 \pm 5$ GeV. A distribution of the invariant mass of e^+e^- pairs from the UA1 detector is shown in Fig. 9.9; the peak around 90 GeV corresponding to the decay $Z \to e^+e^-$ is clearly visible.

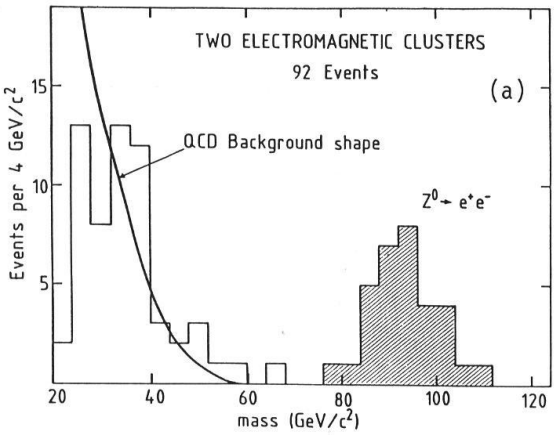

Figure 9.9: The invariant mass distribution of e^+e^- pairs produced in proton–antiproton collisions measured by the UA1 detector, showing evidence for production of the Z boson (from [5]).

So much indirect evidence for the GWS theory had accumulated since the early 1970s that pretty much everyone felt that the W and Z had to be there. In fact, Glashow, Salam and

Weinberg had already been awarded the Nobel Prize in 1979. The experimental 'discovery' of the W and Z was nevertheless a major triumph and the 1984 Nobel prize went to the UA1 collaboration leader, Carlo Rubbia, and to Simon van der Meer, who led the effort to convert the SPS into a proton–antiproton collider.

9.7 Z physics: SLC and LEP I

The UA1 and UA2 teams continued to study W and Z production through most of the 1980s. In 1986 the Tevatron $p\overline{p}$ collider began operation with a much higher energy, $E_{\rm cm} = 1.8$ TeV, which greatly increases the W and Z production rate. In proton–antiproton collisions, however, the measurements are limited by the fact that the energies of the colliding partons are not known, since these carry only a fraction of the hadron's momentum. Furthermore the interesting events are masked by a much larger number of 'boring' inelastic $p\overline{p}$ collisions that produce large numbers of hadrons in the detector.

In electron–positron collisions, however, all of the centre-of-mass energy can be used to produce a Z, and these events can be easily distinguished from background processes. The Feynman diagram for Z production in e^+e^- collisions is shown in Fig. 9.10. The Z is shown to decay into a fermion–antifermion pair, which can be a neutrino, charged lepton or a quark of flavour u, d, s, c or b. Decay of an on-shell Z into a $t\bar{t}$ pair is not possible since the mass of the top quark is more than half the mass of the Z.

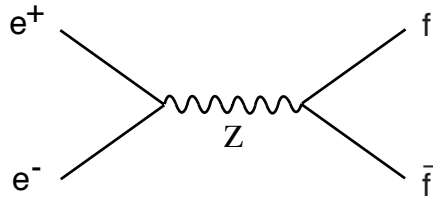

Figure 9.10: A Feynman diagram for Z production in e^+e^- collisions.

As soon as the Z's existence was established in proton–antiproton collisions, two projects were begun to produce Zs in e^+e^- annihilation. At SLAC, the Stanford Linear Collider (SLC) was built to accelerate electrons and positrons to energies equal to half of $M_{\rm Z}$ in the existing linac and then to bend these around in two arcs so that they collide head on with $E_{\rm cm} = M_{\rm Z}$. The e^+ and e^- bunches only cross once, and so to produce a high enough luminosity the beams had to be very tightly focussed. The SLC succeeded in producing several hundred Zs by the summer of 1989.

The second project – the Large Electron–Positron (LEP) collider – was built at CERN and began operation in August 1989. LEP is a 27 km circumference ring in which bunches of electrons and counter-rotating bunches of positrons collide at four points. Complex detectors built by large collaborations – ALEPH, DELPHI, L3 and OPAL – were located at each collision point.

Although SLC had the honour of being first, LEP produced within the first several months of operation a hundred thousand – and by the mid 1990s, around 20 million – Zs. The cross sections for several reactions from LEP and lower-energy experiments are shown in Fig. 9.11. The large data samples from LEP (and eventually a medium-sized sample from SLC) allowed

for many precision measurements related to the GWS theory and QCD, which by this time were called collectively 'the Standard Model'.

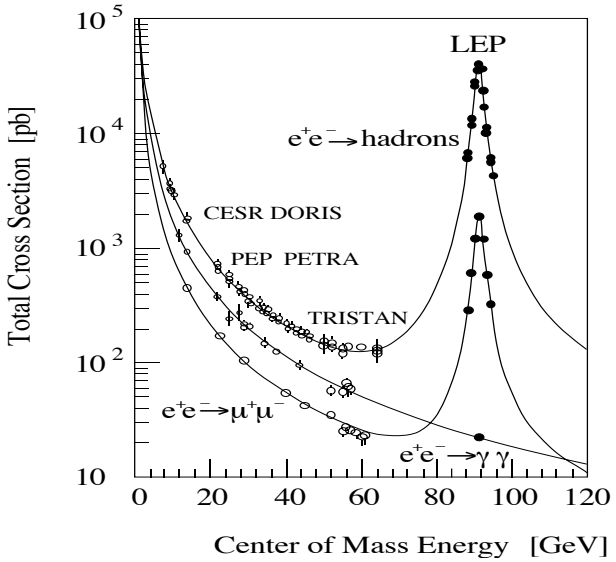

Figure 9.11: The cross section for several e^+e^- reactions as a function of the centre-of-mass energy (from [23]).

For the reaction $e^+e^- \to f\overline{f}$, where f is any charged fermion except the electron, two main Feynman diagrams contribute to the total amplitude. One is given by the annihilation of the e^+ and e^- into a Z as shown in Fig. 9.10, and the other is the same except with an intermediate photon. The reaction $e^+e^- \to e^+e^-$, i.e., Bhabha scattering, is different because for it one must also include graphs where a virtual photon or Z is exchanged; see Fig. 2.11(f). For $e^+e^- \to \nu\overline{\nu}$, the diagram with the virtual photon is absent, since the neutrino is electrically neutral and therefore does not couple to the photon.

Since the photon has zero rest mass, the propagator in that part of the amplitude goes as

$$\frac{1}{E_{\rm cm}^2} \ , \tag{9.20}$$

since the virtual mass squared of the photon is equal to the centre-of-mass energy squared. Similarly, the amplitude with the intermediate Z goes as

$$\frac{1}{E_{\rm cm}^2 - M_{\rm Z}^2} \ . \tag{9.21}$$

For $E_{\rm cm} \ll M_{\rm Z}$ we can ignore the diagram with the Z. The amplitude squared then goes as $1/E_{\rm cm}^4$, but to get a quantity with the correct dimension for a cross section we need to multiply this by $E_{\rm cm}^2$ and one finds that in this limit the cross section falls as $1/E_{\rm cm}^2$. This behaviour can be seen in Fig. 9.11 for energies below around 30 GeV.

For $E_{\rm cm}$ close to the $M_{\rm Z}$, the Z propagator becomes very large and we can neglect the graph with the intermediate photon. As we have seen in Chapter 6, squaring the amplitude leads to a Breit–Wigner curve for the cross section, namely (see equation 6.6),

$$\sigma(e^+e^- \to f\overline{f}) = M_{\rm Z}^2\Gamma_{\rm Z}^2 \, \frac{\sigma_{f\overline{f}}}{(E_{\rm cm}^2 - M_{\rm Z}^2)^2 + M_{\rm Z}^2\Gamma_{\rm Z}^2} \ , \tag{9.22}$$

where $M_{\rm Z}$ and $\Gamma_{\rm Z}$ are the mass and total decay rate of the Z and $\sigma_{f\overline{f}}$ is the value of the cross section at the peak.

The parameters $M_{\rm Z}$ and $\Gamma_{\rm Z}$ can be determined from the energy and width of the cross section peak. The combined result from all of the LEP experiments [79] yielded

$$M_{\rm Z} = 91.1872 \pm 0.0021 \text{ GeV} \tag{9.23}$$

$$\Gamma_{\rm Z} = 2.4944 \pm 0.0024 \text{ GeV} . \tag{9.24}$$

From the total decay rate of the Z, we can determine the total number of neutrino generations into which the Z can decay. This may seem surprising, as we do not actually need to observe the events $\mathrm{e^+e^-} \to \nu\overline{\nu}$ to do this; all we need is the measurement of $\Gamma_{\rm Z}$, which we obtain from the resonance curve. The point is that the total decay rate, i.e., the width of the cross section peak from any of the reactions $\mathrm{e^+e^-} \to f\overline{f}$, is equal to the sum of all of the partial decay rates,

$$\Gamma_{\rm Z} = \sum_{q=u,d,s,c,b} \Gamma(\mathrm{Z} \to q\overline{q}) + \sum_{l=e,\mu,\tau} \Gamma(\mathrm{Z} \to l^+l^-) + \sum_{i=1}^{N_\nu} \Gamma(\mathrm{Z} \to \nu\overline{\nu}) . \tag{9.25}$$

Once the fundamental parameters of the Standard Model have been measured (basically the coupling strengths and $M_{\rm Z}$), then all of the terms in this sum are predicted. One can show that the partial decay widths are

$$\Gamma(\mathrm{Z} \to f\overline{f}) = \frac{G_{\rm F} M_{\rm Z}^3}{6\pi\sqrt{2}} (v_f^2 + a_f^2)\, N_{\rm c} , \tag{9.26}$$

where $N_{\rm c}$ is the number of colours for the fermion species f ($N_{\rm c} = 3$ for quarks, 1 for leptons), and v_f and a_f, called the *vector* and *axial vector* couplings, are specific combinations of the coupling strengths that can be expressed as functions of the weak mixing angle, $\sin^2\theta_{\rm W} = e^2/g^2 \approx 0.23$. They are given in Table 9.1 for the different fermion types along with the resulting partial decay widths.

Table 9.1: The vector and axial vector couplings and decay widths for $\mathrm{Z} \to f\overline{f}$ (the widths are given for $\sin^2\theta_{\rm W} = 0.23$).

fermion pair	v_f	a_f	$\Gamma(\mathrm{Z} \to f\overline{f})$
$u\overline{u}$	$\frac{1}{2} - \frac{4}{3}\sin^2\theta_{\rm W}$	$\frac{1}{2}$	287 MeV
$d\overline{d}$	$\frac{1}{2} - \frac{2}{3}\sin^2\theta_{\rm W}$	$\frac{1}{2}$	370 MeV
l^+l^-	$\frac{1}{2} - 2\sin^2\theta_{\rm W}$	$\frac{1}{2}$	84 MeV
$\nu\overline{\nu}$	$\frac{1}{2}$	$\frac{1}{2}$	167 MeV

The values of v_f and a_f for $u\overline{u}$ above are the same for $c\overline{c}$ and $t\overline{t}$ (the charge-2/3 quarks) and the values for $d\overline{d}$ are the same as for $s\overline{s}$ and $b\overline{b}$. Because the top quark's mass is greater than $M_{\mathrm{Z}}/2$ and therefore the decay $\mathrm{Z} \to t\overline{t}$ is kinematically forbidden, $t\overline{t}$ does not contribute to the width of the Z. Similarly, the partial widths are the same for all charged leptons and for all neutrino species assuming they are much lighter than $M_{\mathrm{Z}}/2$. The total decay width of the Z is therefore given by

$$\Gamma_{\mathrm{Z}} = 2\Gamma(\mathrm{Z} \to u\overline{u}) + 3\Gamma(\mathrm{Z} \to d\overline{d}) + 3\Gamma(\mathrm{Z} \to l^+l^-) + N_\nu\Gamma(\mathrm{Z} \to \nu\overline{\nu}) \; . \tag{9.27}$$

Normally we take $N_\nu = 3$, i.e., we assume there is one neutrino species for each charged lepton. One can always ask, however, whether there exist additional heavier families of quarks or leptons. If these would be heavier than $M_{\mathrm{Z}}/2$, then the Z could not decay into them and they would not contribute to Γ_{Z}. We do not observe any additional charged quarks or leptons lighter than $M_{\mathrm{Z}}/2$. If, however, there were to exist an additional lepton family with the charged partner heavier than $M_{\mathrm{Z}}/2$, but for which the neutrino was lighter, then the decay into the neutrino–antineutrino pair would contribute to Γ_{Z}.

If we take $N_\nu = 3$, equation (9.27) predicts $\Gamma_{\mathrm{Z}} = 2.44$ GeV. By including a number of higher order corrections, the prediction increases to close to 2.5 GeV. We have seen that the measured value of Γ_{Z} is close to 2.5 GeV, and any additional neutrino family would increase the predicted Γ_{Z} by 167 MeV. We can therefore exclude a fourth neutrino family. If one treats N_ν not as representing literally the number of neutrino families but as a sort of effective parameter, then the best fitted value [79] is

$$N_\nu = 2.9835 \pm 0.0083 \; . \tag{9.28}$$

Although this is 1.7 times the quoted error bar below 3, it is clear that $N_\nu = 3$ fits reasonably well and that any other value is excluded.

The fact that $N_\nu = 3$ fits the data well can be seen directly from the measured cross sections $\sigma(\mathrm{e}^+\mathrm{e}^- \to f\overline{f})$ for any of the fermions. An example measured by the ALEPH experiment is shown in Fig. 9.12 for $\mathrm{e}^+\mathrm{e}^- \to$ hadrons, which corresponds to the sum of the cross sections for all kinematically accessible quark species (i.e., all but top).

During the first six years of LEP's operation at centre-of-mass energies near the Z mass (called the LEP I programme), many measurements related to the electroweak part of the Standard Model were carried out. As we have seen, the cross sections for electron–positron annihilation into quark–antiquark and lepton–antilepton pairs as functions of E_{cm} provide measurements of the mass and width of the Z. An additional important class of measurements was the distribution of the scattering angle in the reaction $\mathrm{e}^+\mathrm{e}^- \to f\overline{f}$ for the various fermion–antifermion pairs. Here the scattering angle is defined as the angle between the outgoing fermion and the incoming electron, as shown in Fig. 9.13.

Once the free parameters of the Standard Model are known, the probability distribution functions of θ or equivalently the differential cross sections $d\sigma/d\cos\theta$, for all of the fermion pairs are determined. To a good approximation, these are fixed by the parameters α, G_{F} and M_{Z}. The fine structure constant α is determined to high precision from the Quantum Hall Effect, and the Fermi constant G_{F} is well measured from the mean lifetime of the muon. As we have seen, the position of the Z resonance determines M_{Z} to high accuracy. The angular

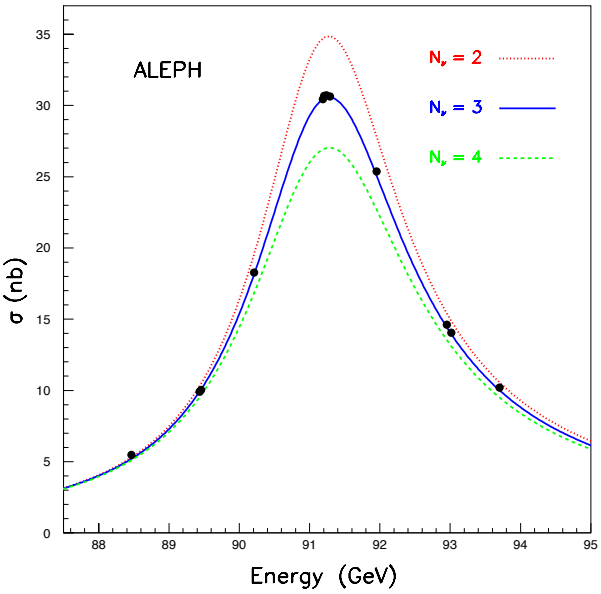

Figure 9.12: The cross section $\sigma(\mathrm{e^+e^-} \to \text{hadrons})$ measured by ALEPH shown with the predictions for $N_\nu = 2, 3, 4$ (from [23]).

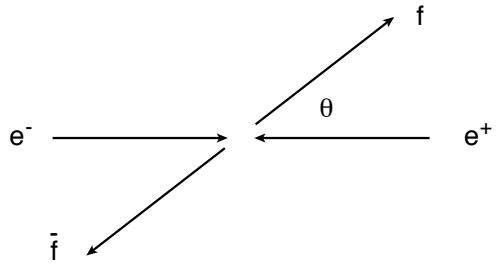

Figure 9.13: The reaction $\mathrm{e^+e^-} \to f\overline{f}$ showing the definition of the scattering angle θ.

distributions are less sensitive to the other parameters of the Standard Model, namely, fermion masses, CKM matrix elements, and the Higgs mass. So here it is fair to say that by comparing the measured angular distributions with the Standard Model predictions we are truly testing the theory, and not just determining its free parameters.

One finds that the differential cross section $d\sigma/d\cos\theta$ can be expressed as

$$\frac{d\sigma}{d\cos\theta}(\mathrm{e^+e^-} \to f\overline{f}) = \sigma_{\mathrm{tot}}\, \tfrac{3}{8}\,(1 + \tfrac{8}{3}A_{\mathrm{FB}}\cos\theta + \cos^2\theta)\ , \tag{9.29}$$

where σ_{tot} is the total cross section for the reaction and A_{FB} is called the *forwards–backwards asymmetry*, both of which depend on the fermion–antifermion pair in question and on the centre-of-mass energy. We have already seen that the total cross section follows a Breit–Wigner function. The asymmetry A_{FB} is also a specific function of the centre-of-mass energy whose form is determined by the Standard Model, being negative at energies below M_{Z}, crossing through zero at the resonance peak and then going positive for $E_{\mathrm{cm}} > M_{\mathrm{Z}}$.

Figure 9.14 shows measurements by the ALEPH experiment of the differential cross sections for $\mathrm{e^+e^-} \to l^+l^-$ for all of the lepton types combined at different centre-of-mass energies (on the plots E_{cm} is called $\sqrt{s}$) [80]. Here even $\mathrm{e^+e^-} \to \mathrm{e^+e^-}$ has been included, but its angular distribution modified by subtracting off the contribution that is expected to come from

the photon-exchange amplitude shown in Fig. 2.11(f). Having done this, the e^+e^- angular distribution should be the same as for $\mu^+\mu^-$ and $\tau^+\tau^-$. The curves are the Standard Model predictions, which are seen to be in good agreement with the data. Notice that for energies below M_Z, the outgoing negative lepton is more likely to go backwards, i.e., to have $\cos\theta < 0$, and for $M_Z > E_{cm}$ it is more likely to go forwards. At $E_{cm} = M_Z = 91.2$ GeV, the differential cross section is forwards–backwards symmetric, i.e., A_{FB} is zero.

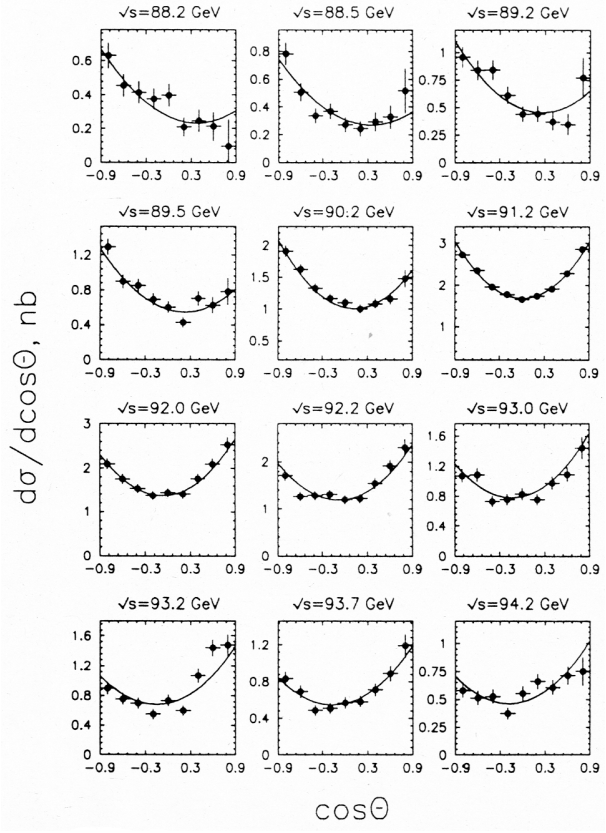

Figure 9.14: Differential cross sections $d\sigma/d\cos\theta$ for $e^+e^- \to l^+l^-$ for all charged leptons combined (from [80]).

The predicted form of $d\sigma/d\cos\theta$ for electron–positron annihilation into $\mu^+\mu^-$, $q\overline{q}$, etc., depends on our assumption that the quarks and leptons are spin-$\frac{1}{2}$ particles. If, for example, we had described the quarks and leptons as spin-0 particles, we would have found $d\sigma/d\cos\theta \propto \sin^2\theta$. From the plots, we can see that the spin-$\frac{1}{2}$ assignment agrees well with the data.

9.8 $e^+e^- \to W^+W^-$: the LEP II programme

Starting at the end of 1995 the energy of the LEP collider was increased in several steps, eventually reaching $E_{cm} = 209$ GeV. During this period of operation, called LEP II, one of the main physics goals was the study of the reaction $e^+e^- \to W^+W^-$. At leading order there are three Feynman diagrams for this reaction, which are shown in Fig. 9.15. In Fig. 9.15(a), the e^+ and e^- exchange an electron-type neutrino, emitting the two Ws. In diagrams (b) and (c), the W^+W^- pair couples to a γ or a Z; these are triple gauge-boson couplings.

The W bosons decay very quickly into either lepton–neutrino or quark–antiquark pairs. All of the lepton pairs, i.e., $\nu_e e^+$, $\nu_\mu \mu^+$ and $\nu_\tau \tau^+$ are possible final states and all have the same

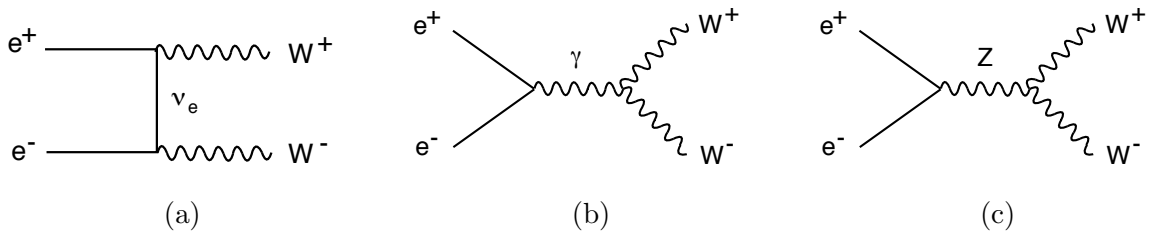

Figure 9.15: Feynman diagrams for $e^+e^- \to W^+W^-$.

coupling strength, namely, g. For the quark–antiquark pairs, to first approximation only $u\overline{d}$ and $c\overline{s}$ contribute as the top quark is too heavy to be produced. The combinations $u\overline{s}$, $u\overline{b}$, $c\overline{d}$ and $c\overline{b}$ are also possible but are CKM suppressed. Neglecting these we have three possible lepton–antilepton pairs and $2 \times 3 = 6$ possible quark–antiquark pairs, where the factor of three comes from the fact that the quarks can be produced in three different colour states. All of these final states have the same probability, so the probability of any one of them is 1/9. The Standard Model prediction for the branching ratios of the W^+ are thus

$$\mathcal{B}(W^+ \to \nu_l l^+) = 1/9 \ ,$$
$$\mathcal{B}(W^+ \to \ \text{hadrons}) = 2/3 \ ,$$

where l^+ means any one of e^+, μ^+ or τ^+ and 'hadrons' refers to any of the final states involving a quark–antiquark pair. The corresponding branching ratios for the W^- are of course the same.

This means in $2/3 \times 2/3 = 4/9$ of the W^+W^- events, both Ws will decay to quark–antiquark pairs resulting in four jets of hadrons. An example is shown in Fig. 9.16. For this event, the centre-of-mass energy was just above the kinematic threshold, namely, $E_{\rm cm} = 161$ GeV, so both Ws were produced almost at rest. The quark and antiquark from each W come out back-to-back.

Figure 9.17 shows an event where the W^- decayed into $e^-\overline{\nu}_e$ and the W^+ decayed into a quark–antiquark pair. The electron is identified by the shower left in the electromagnetic calorimeter, and the ray towards the top of the plot shows the direction of the missing momentum carried away by the $\overline{\nu}_e$. Here the centre-of-mass energy was 172 GeV so that the Ws were produced not at rest but rather receding away from each other. This can be seen from the fact that the hadronic jets are no longer back-to-back, nor are the electron and the antineutrino.

The first goal in studying $e^+e^- \to W^+W^-$ was a determination of the W boson's mass. Two main methods can be used to measure M_W with this reaction.. The first is simply to measure the cross section $\sigma(e^+e^- \to W^+W^-)$ as a function of $E_{\rm cm}$. For energies below the kinematic threshold, $E_{\rm cm} < 2M_W$, the reaction should not be possible. For energies higher than this, the cross section climbs and then eventually drops back down according to a function predicted by the Standard Model. By measuring the threshold where the reaction first becomes possible, we can determine the W's mass.

In practice things are not quite so simple, since the Ws themselves are not final state particles but rather they decay very quickly into lepton–neutrino or quark–antiquark pairs. Therefore they are allowed to be off-shell, i.e., their virtual mass does not have to be equal to M_W. These effects can be taken into account, however, and the measurement still works on the principle that the threshold energy for the reaction is basically $2M_W$. This can be seen from the cross

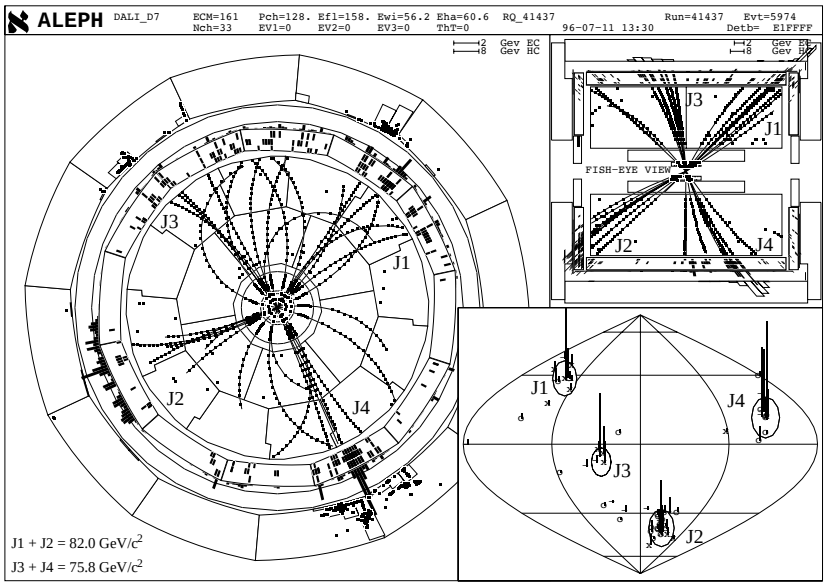

Figure 9.16: An event of the type $e^+e^- \to W^+W^-$ from the ALEPH experiment, where both W bosons decay into quark–antiquark pairs resulting in jets of hadrons (from [23]).

section $\sigma(e^+e^- \to W^+W^-)$ measured as a function of the centre-of-mass energy in Fig. 9.18 [82]. The measurements are shown as points with error bars at energies starting at $E_{\rm cm} = 161$ GeV. The solid curve represents the Standard Model's prediction evaluated at $M_{\rm W} = 80.4$ GeV.

Also shown in Fig. 9.18 are the predicted cross sections if one omits the amplitude with the ZWW vertex or if one takes only the ν_e exchange graph (see Figs. 9.15). These curves are both far too high, providing convincing evidence for the presence of the of the triple-gauge boson vertices, which are required by the electroweak theory. In theories beyond the Standard Model the triple gauge boson couplings could be different, and an important part of the cross section measurements was to constrain the extent to which this could be the case. No evidence for so-called *anomalous couplings* has been found.

The other method of determining $M_{\rm W}$, which is in fact more accurate than using the threshold energy, is to measure the invariant mass of the W's decay products. This is particularly straightforward in events where one of the Ws decays into hadrons and the other into lepton–neutrino. In such events we can easily tell which particles came from which W and therefore the invariant mass for each can be determined. It can even be determined for the one that decayed into lepton–neutrino, since we know the total energy of the system, $E_{\rm cm}$, and the total momentum, namely, zero. By energy and momentum conservation we can therefore determine the energy and direction of the neutrino, provided we assume that it was the only particle that escaped undetected.

The invariant-mass method also works for events where both Ws decay into hadrons, but here one must guess which hadrons came from which W. To do this one selects events with four jets like the one in Fig. 9.16. There are three possible ways of forming two pairs out of the four jets. For the right combination, the invariant mass of each pair will be close to the W mass; for the wrong combinations at least one of the pairs will usually be off. Computer simulations are used to figure out how often the guess is incorrect and to derive corrections for this and for other

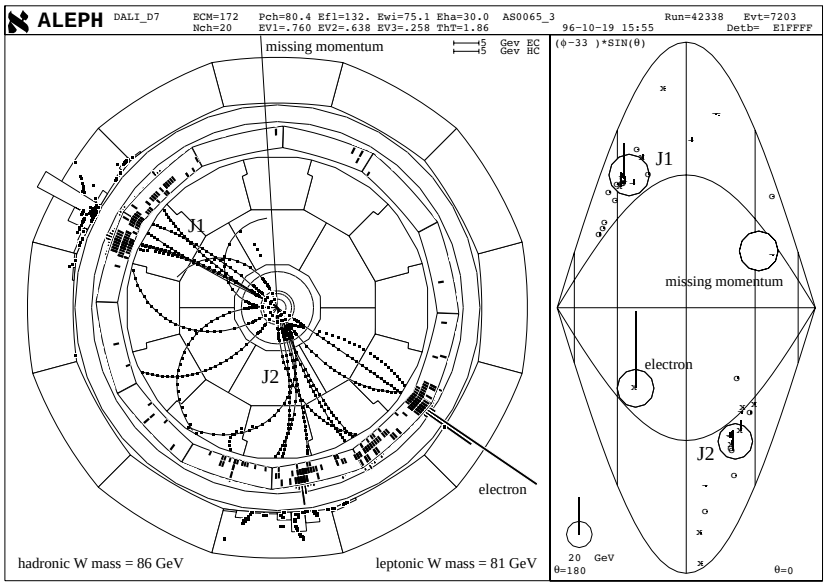

Figure 9.17: An event of the type $e^+e^- \to W^+W^-$ from the ALEPH experiment, where the W^- decays to $e^-\overline{\nu}_e$ and the W^+ decays into hadrons (from [23]).

systematic effects. By the summer of 2000, the measured value of M_W obtained by combining all four LEP experiments [82] was

$$M_W = 80.427 \pm 0.046 \text{ GeV}\,. \tag{9.30}$$

A similar accuracy for M_W has also been achieved by the CDF and D0 experiments at the Tevatron proton–antiproton collider. They find

$$M_W = 80.452 \pm 0.062 \text{ GeV}\,. \tag{9.31}$$

The measurement of M_W provides a test of the Standard Model and not simply a determination of one of its parameters, since by combining equations (9.18) and (9.19) for $\sin\theta_W$ we obtain a relation between the couplings and gauge boson masses, namely,

$$\frac{e^2}{g^2} = 1 - \frac{M_W^2}{M_Z^2}\,. \tag{9.32}$$

In this form the relation does not provide a very sensitive test, since the coupling strength g is not measured to high accuracy. This is because all low energy weak processes such as muon decay depend only on the ratio g^2/M_W^2. This is equivalent to the Fermi constant $G_F = \sqrt{2}g^2/8M_W^2$, which is known to much higher accuracy. In order to provide a more sensitive test, we can rewrite equation (9.32) to give M_W as a function of e (or α), G_F and M_Z. Doing this and including various higher order corrections yields a predicted value for the W mass of

$$M_W = 80.374 \pm 0.034 \text{ GeV}\,. \tag{9.33}$$

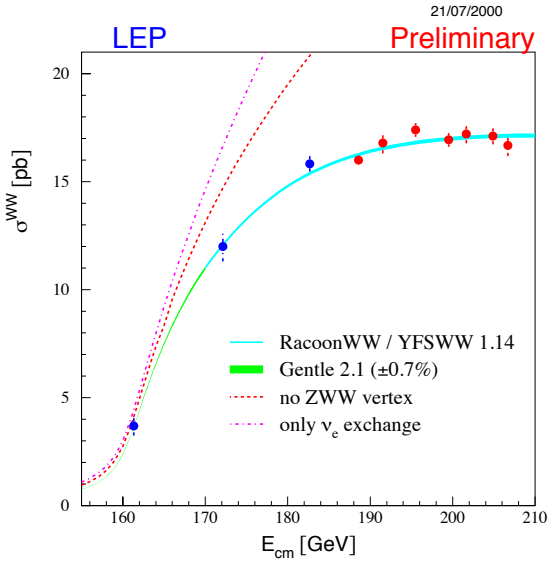

Figure 9.18: The cross section $\sigma(e^+e^- \to W^+W^-)$ measured by the LEP experiments and shown with the Standard Model prediction [82].

This is in good agreement with the values found at LEP II and at the Tevatron, providing an important confirmation of the Standard Model.

Chapter 10

Quantum chromodynamics

In this chapter we take a closer look at the part of the Standard Model that describes the strong interaction, namely, quantum chromodynamics (QCD). This theory is uniquely difficult to test because the fundamental particles of QCD, namely, quarks and gluons, are not observed as free particles. We'll see why the concept of *colour* needed to be introduced, how the theory of QCD is defined, what its phenomenological consequences are, and how these stand in a comparison to experiment.

10.1 Evidence for colour

Ever since it was realized that an atomic nucleus consists of protons and neutrons, it was clear that there must exist a nuclear or 'strong' force, capable of binding them together. Attempts to construct a theory of strong interactions based on the exchange of a massive particle, such as Yukawa's theory of pion exchange, were not very successful. Once electron–proton scattering experiments indicated that nucleons are themselves not elementary particles, the question of strong interactions turned to their constituents, namely, quarks. In the 5 to 10 years following the introduction of the quark model, there emerged evidence that quarks possess an additional property which was called *colour*. Important clues came from the symmetry properties of baryon wave functions, the total hadronic cross section in e^+e^- annihilation, and the π^0 lifetime.

Almost immediately after the quark model was introduced, Greenberg pointed out that it is impossible to construct from it certain baryon wave functions with symmetry properties consistent with the Pauli exclusion principle [83]. The Δ^{++}, for example, is a resonance created in π^+p scattering. It consists of three u quarks, and from the angular distribution observed in the reaction $\pi^+p \to \pi^+p$ it must have spin $J = 3/2$. Furthermore, the Δ^{++} is the lowest mass combination of three u quarks, and any reasonable model of hadrons predicts that the lowest mass state must have orbital angular momentum of zero. This means that the spatial part of the wave function is symmetric upon interchange of any of the two quarks, and to form a $J = 3/2$ state the three quark spins must be aligned parallel, so the spin part of the wave function is symmetric as well.

The rules of quantum mechanics, however, require a system of identical fermions to be described by an antisymmetric wave function, i.e., it must change sign upon interchange of any pair. Greenberg proposed that if the quarks were to possess an additional quantum number,

which later for no fundamental reason was called colour (it certainly has nothing to do with the optical property of colour), then the three u quarks need not be in the same state and the exclusion principle would not be violated. One can show that at least three colours are needed in order to construct an antisymmetric wave function for the Δ^{++}. Other than that, it was not clear from these considerations how many colours there should be or what colour means in any larger context.

The next piece of evidence for colour came from the reaction $e^+e^- \rightarrow$ hadrons. In the quark model, hadronic final states are assumed to result from the reaction $e^+e^- \rightarrow q\overline{q}$, where q represents a quark of any of the possible flavours. The transformation of the quark and antiquark into ordinary hadrons such as pions and kaons was not – and still is not – understood in detail, but could be assumed to occur with unit probability. In this model, therefore, the total cross section for $e^+e^- \rightarrow$ hadrons was simply take to be the equal to the sum of the cross sections to produce a quark–antiquark pair for all of the kinematically accessible flavours, i.e., those with masses $m_q < E_{\rm cm}/2$.

Let's consider this reaction first at centre-of-mass energies significantly less than the mass of the Z, so that to first approximation the amplitude is given by the diagram with an intermediate photon, as shown in Fig. 10.1(a). This is essentially the same diagram as for $e^+e^- \rightarrow \mu^+\mu^-$ in Fig. 10.1(b), the main difference being that the coupling strength for the $q\overline{q}\gamma$ vertex is $\frac{2}{3}e$ for up-type quarks and $\frac{1}{3}e$ for down-type quarks, whereas it is e for the $\mu^+\mu^-\gamma$ vertex. The only other difference in the amplitudes stems from the different masses of the final state particles, but as long as these are significantly smaller than the centre-of-mass energy, they will not have a significant influence on the cross section.

Figure 10.1: Lowest order Feynman diagrams for (a) $e^+e^- \rightarrow q\overline{q}$ and (b) $e^+e^- \rightarrow \mu^+\mu^-$.

Neglecting effects due to the masses of final state particles and using the Feynman diagrams of Fig. 10.1, the total cross sections are found to be

$$\sigma(e^+e^- \rightarrow q\overline{q}) = \frac{4\pi\alpha^2 Q_q^2}{3E_{\rm cm}^2} \,, \tag{10.1}$$

$$\sigma(e^+e^- \rightarrow \mu^+\mu^-) = \frac{4\pi\alpha^2}{3E_{\rm cm}^2} \,, \tag{10.2}$$

where $\alpha = e^2/4\pi$ and Q_q is the quark's charge in units of e, i.e., $\frac{2}{3}$ for u, c and t, and $-\frac{1}{3}$ for d, s and b.

The total hadronic cross section is given by the sum of the cross sections for the kinematically accessible quark flavours. For experiments carried out at the PETRA e^+e^- ring with $E_{\rm cm}$

between 14 and 44 GeV, this meant the five flavours u, d, s, c and b. One usually defines R as the ratio of the cross sections for production of hadrons to that for $\mu^+\mu^-$. Using the cross sections above and including all flavours except top we find

$$\begin{aligned} R &= \frac{\sigma(\mathrm{e^+e^-} \to \text{ hadrons})}{\sigma(\mathrm{e^+e^-} \to \mu^+\mu^-)} \\ &= \sum_{q=u,d,s,c,b} Q_q^2 \;=\; 2 \times \left(\frac{2}{3}\right)^2 \;+\; 3 \times \left(\frac{-1}{3}\right)^2 = \frac{11}{9}\,. \end{aligned} \tag{10.3}$$

Measurements of R, however, indicated a value closer to 4, as seen in Fig. 10.2. Again we are rescued by the concept of colour. Suppose that a quark can come in one of N_c possible colour states, and that an antiquark can carry one of the corresponding 'anticolours'. Furthermore suppose that colour is conserved when the virtual photon decays into the $q\overline{q}$ pair, so that we can get, e.g., red-antired, blue-antiblue, etc., but not red-antiblue. The prediction for R then becomes

$$R = N_\mathrm{c} \sum_q Q_q^2\,. \tag{10.4}$$

The best agreement with the data is found for $N_\mathrm{c} = 3$, for which the prediction is $R = 11/3 \approx 3.7$. We will return later and show how QCD even explains why the measured value of R is slightly larger than this.

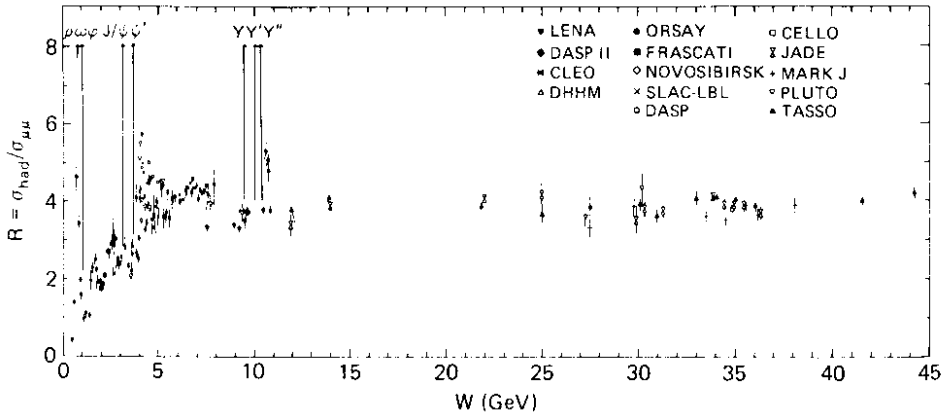

Figure 10.2: Measurements of R, the ratio of $\sigma(\mathrm{e^+e^-} \to \text{ hadrons})$ to $\sigma(\mathrm{e^+e^-} \to \mu^+\mu^-)$ as a function of the centre-of-mass energy (from [3]).

Additional evidence for the assignment $N_\mathrm{c} = 3$ comes from the decay rate of the neutral pion. Here one finds that the π^0 decay rate is proportional to N_c^2, and for $N_\mathrm{c} = 3$ the prediction is $\Gamma(\pi^0 \to \gamma\gamma) = 7.6$ eV [67]. The measured decay rate is $\Gamma(\pi^0 \to \gamma\gamma) = 7.7 \pm 0.6$ eV [7], in good agreement with $N_\mathrm{c} = 3$ and not in agreement with any other integer value.

10.2 The structure of QCD

Around 1972 there emerged a theory of quarks that incorporated the concept of colour. It was based on a local gauge symmetry similar to (but in some important ways different from) the GWS theory of electroweak interactions. A quark q of any flavour was assumed to come in one of three possible colour states, which can be called red, blue and green. The state vector for a quark q can therefore be written

$$\psi_q = \begin{pmatrix} q_{\rm red} \\ q_{\rm green} \\ q_{\rm blue} \end{pmatrix} . \tag{10.5}$$

One then requires that the Lagrangian density describing the quarks be invariant under a certain local gauge symmetry, just as we did with the electroweak theory. The possible symmetries are in fact quite limited, and the one that turns out to agree with experiment is called SU(3), which stands for 'special unitary' in three-dimensions. This means that one allows for a space- and time-dependent transformation of the different colour components given by multiplication of the vector (10.5) by a 3×3 unitary matrix with determinant of unity. Since this transformation acts on the 'colour space' of the quark states, the theory is called Quantum Chromodynamics or QCD. This is done in such a way that the colour plays the role of a charge, but unlike the electric charge of a particle, which is characterized by a single number, the colour charge of a quark is specified by a position in a three-dimensional colour space.

As in the case of the GWS theory, requiring a local gauge symmetry implies the existence of additional gauge bosons, in this case, the gluon. One finds that gluons are characterized by a colour and anticolour, e.g. 'red–antigreen', and that there are eight possible states. Naively one might have expected nine possible colour–anticolour states given three colours, but one of these combinations effectively doesn't count, since it is found to have a wave function such that its coupling to other particles is identically zero. This is called a *colour singlet* state; it is effectively colour neutral.

As in the electroweak theory, the possible vertices involving the quarks and gluons are uniquely predicted and are characterized by a certain coupling strength called $g_{\rm s}$, analogous to the couplings e and g. In analogy with the fine structure constant $\alpha = e^2/4\pi$, one defines the 'strong coupling constant' $\alpha_{\rm s}$ by

$$\alpha_{\rm s} = \frac{g_{\rm s}^2}{4\pi} . \tag{10.6}$$

The possible vertices involving quarks and gluons are qqg, ggg and $gggg$, as shown in Fig. 10.3. The coupling strength for the qqg and ggg vertices is given by $g_{\rm s}$, and for the $gggg$ vertex it is $g_{\rm s}^2$.

In contrast to the electroweak theory, there is nothing in the SU(3) gauge symmetry of QCD that distinguishes between right and left, so parity is conserved in interactions between quarks and gluons. Another difference between QCD and the electroweak theory is that gluons are massless, unlike the W and Z. Unlike the photon, the gluon couples to itself, i.e., there exist both ggg and $gggg$ vertices.

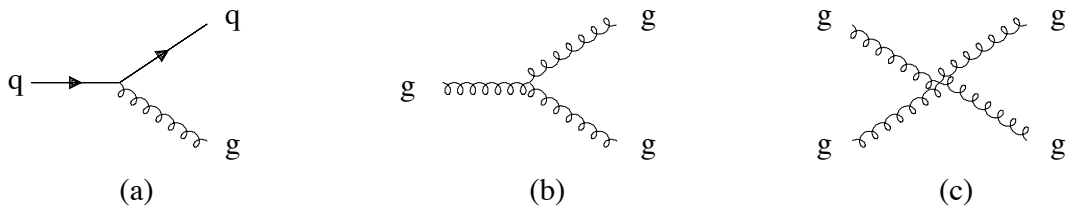

Figure 10.3: Possible couplings between quarks and gluons.

An important property of QCD is that it is 'flavour blind'. That is, the coupling strength of a quark and gluon is the same for all quark flavours. Furthermore, the flavour of a quark never changes upon emission or absorption of a gluon, only its colour does. So although the different flavours of quarks were originally introduced to classify the observed hadron states, the concept of flavour turns out to play essentially no role in QCD, whereas it is of fundamental importance in the weak interaction.

The fundamental particles of QCD are quarks and gluons, but these have never been observed as free particles. Provisionally one must make the additional hypothesis that only colour neutral combinations of quarks and gluons exist as free particles. Using SU(3) as the gauge group for the theory, the basic colour neutral states are $q\overline{q}$ and qqq, i.e., exactly the combinations that correspond to the mesons and baryons of the original quark model. In addition one can form colour neutral combinations of two gluons called *glueballs*, for which there is indeed some indirect experimental evidence. In their original papers introducing the quark model, Gell-Mann and Zweig mentioned the possibility of adding a quark-antiquark pair to a minimal meson or baryon quark configuration to form hadrons with four (tetraquark) or five (pentaquark) quark constituents, which are referred to as exotic hadrons. There is now strong experimental evidence for tetraquark and pentaquark particles [103, 104, 105]. In principle, the fact that one observes only colour neutral states should not be a separate postulate but rather it should be derivable from the Lagrangian of QCD. Someday this may be accomplished but for the present the calculations are too difficult and it has not been demonstrated rigorously.

10.3 The strong coupling constant

An important property of the Standard Model is that the coupling strengths depend on the energy scale of the reaction involved. The precise definition of the energy scale will depend on the process considered, but often it corresponds to the centre-of-mass energy and it is any case proportional to $E_{\rm cm}$. The couplings are said to 'run' with energy. This is seen most dramatically in QCD, where the strong coupling $\alpha_{\rm s}$ is found to decrease for increasing energy scale E as

$$\alpha_{\rm s}(E) = \frac{12\pi}{(33 - 2n_{\rm f})\log(E^2/\Lambda^2)} \,. \tag{10.7}$$

Here $n_{\rm f}$ is the number of quark flavours with masses less than E, and Λ is called the *QCD scale parameter*, which has a value of approximately 200 MeV. From equation (10.7) we can see that if the energy is equal to Λ, then the coupling strength becomes infinite. In fact, (10.7) is itself based on a perturbative expansion in $\alpha_{\rm s}$, which for large $\alpha_{\rm s}$ is no longer valid. The main

message is, however, that for energies on the order of 1 GeV, the strong coupling becomes so large that quarks and gluons become bound into hadrons, i.e. states consisting of three quarks (baryons) or a quark and antiquark (mesons), which are colour neutral. This phenomenon is known as *confinement*. It is not well understood theoretically, since the coupling is too large to allow for reliable predictions using perturbation theory. For energies much larger than Λ, α_s becomes small and perturbation theory can be used. This decrease in the coupling is known as *asymptotic freedom*.

The electromagnetic and weak couplings e and g also depend on the energy scale of the reaction. The weak coupling g decreases slightly and the electric charge e increases with energy. The behaviour of e can be understood qualitatively by considering an electric charge in a vacuum, as shown in Fig. 10.4. If a virtual e^-e^+ pair is created out of the vacuum, this would appear to violate conservation of energy. This is allowed by the uncertainty principle, however, as long as the virtual particles only live for a very short time before recombining. The result is that a certain amount of positive and negative charge is constantly swimming around in the vacuum, and in the presence of the negative point charge in Fig. 10.4, the vacuum becomes polarized. That is, the positrons are attracted towards the charge and electrons are repelled. This has the effect of partially screening some of the original negative charge, just as if it were in a dielectric medium.

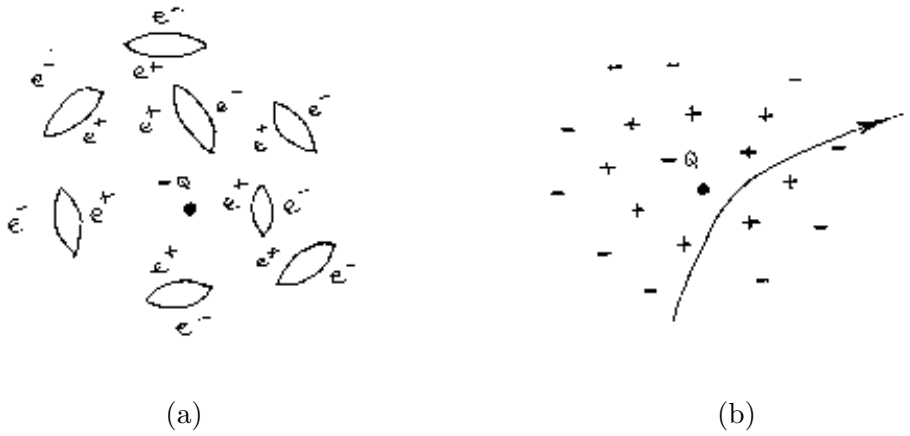

(a) (b)

Figure 10.4: (a) A negative point charge in a vacuum surrounded by virtual e^+e^- pairs. (b) A high energy particle probes the point charge at short distances, penetrating past the screening of the e^+e^- pairs.

If we consider the interaction of another charged particle with our original negative point charge, the effective coupling will be reduced because of the polarization of the vacuum. If, however, the incoming particle has a higher energy, then it will probe the target at a smaller distance scale and the screening effect will be reduced. Hence, the effective electric charge increases for increasing energies.

This type of reasoning leads to the correct qualitative picture, but it does not tell us, for example, why the QCD coupling decreases while the electromagnetic and weak couplings increase. To see this more quantitatively, one must use perturbation theory to compute interaction cross sections. As we have seen, the couplings (e, g, g_s) appear as expansion parameters in a power series. Higher order terms correspond to Feynman diagrams with more virtual particles, and hence more powers of the coupling, as shown in Fig. 10.5. An improved

prediction for the total amplitude is obtained by summing the all diagrams with loops in the boson lines as shown in Fig. 10.5. One can show that the effect of summing this infinite set of loop diagrams is equivalent to replacing the usual constant coupling strengths by effective couplings that depend on the energy scale.

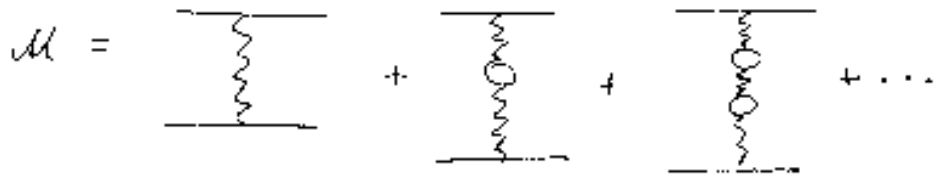

Figure 10.5: Some higher order corrections to a scattering amplitude.

Here the loops correspond to all of the different types of particles which can couple to the boson in question. If the exchanged particle in Fig. 10.5 is a photon, for example, then the loop could be any particle–antiparticle pair with electric charge, such as e^+e^-, $\mu^+\mu^-$, $q\bar{q}$, etc. The contribution of the diagram with the loop depends on the mass of the particle in the loop. To a good approximation, one can say that only particles with masses less than the energy scale of the reaction contribute. This leads to the dependence of α_s on the number of quark flavours n_f with masses less than the energy E, as seen in equation (10.7).

The decrease in the strong coupling for increasing energy is related to the fact that the gluon couples to itself (see Fig. 10.3), whereas the photon does not. That is, an exchanged gluon can have loops with quark–antiquark pairs as shown in Fig. 10.6(a), and also with a gluon pair as in Fig. 10.6(b). It turns out that the gluon loops contribute to the energy dependence with the opposite sign, i.e., they result in the decrease in the coupling for increasing energy.

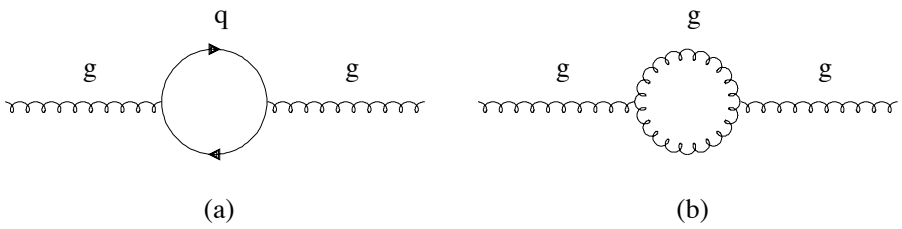

Figure 10.6: Higher order corrections to diagrams with exchanged gluons: (a) a quark–antiquark loop, (b) a gluon loop.

Measurements of α_s from a number of different processes are shown in Fig. 10.7 [84]. We will discuss some of these measurements in Section 10.7. Also shown on the plot is the QCD prediction, which is basically given by equation (10.7), except that higher order improvements have been included. The curve has been fitted to the data by adjusting Λ, which is equivalent to adjusting the value of α_s at a specified energy scale. Here the energy M_Z is used, since a number of important measurements of α_s are carried out using Z decays. One finds $\alpha_s(M_Z) = 0.12$ with an accuracy of 2 to 3 percent.

The fact that the different measured values of α_s all lie reasonably close to the QCD curve (to within the estimated uncertainties) is one of the most encouraging confirmations of the theory. QCD is clearly not verified to the same level of precision as QED or even the electroweak part of

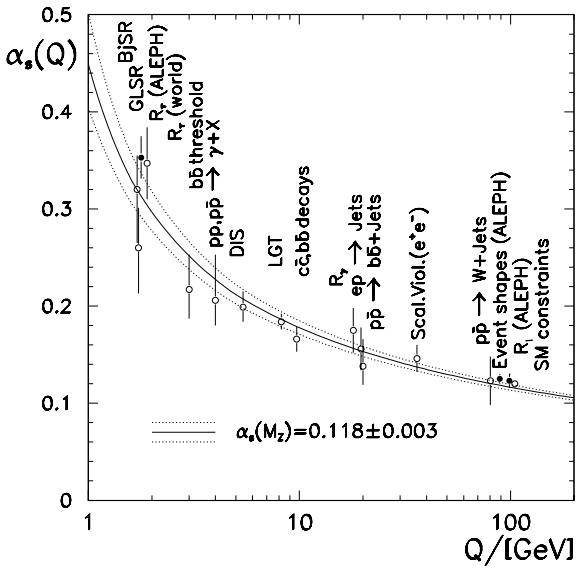

Figure 10.7: Measurements of α_s from different processes shown with the QCD prediction (from [84]).

the Standard Model, but nevertheless several of the measurements on Fig. 10.7 have accuracies at the level of several percent and these all lead to a consistent picture.

10.4 Jets of hadrons

One of the reactions that provides important information about QCD is $e^+e^- \rightarrow$ hadrons. To first approximation this proceeds by e^+e^- annihilation into a virtual photon or Z, which then dissociates into a quark–antiquark pair as in Fig. 10.1(a). In an e^+e^- storage ring where the electron and positron collide head-on, the total momentum of the system is zero and the quark and antiquark come off back-to-back, as shown in Fig. 10.8(a). What we see in the detector, however, are jets of hadrons, which are assumed to follow the directions of the quarks, as in Fig. 10.8(b). We have already seen two-jet events like this from the ALEPH detector at LEP in, e.g., Fig. 4.2.2.

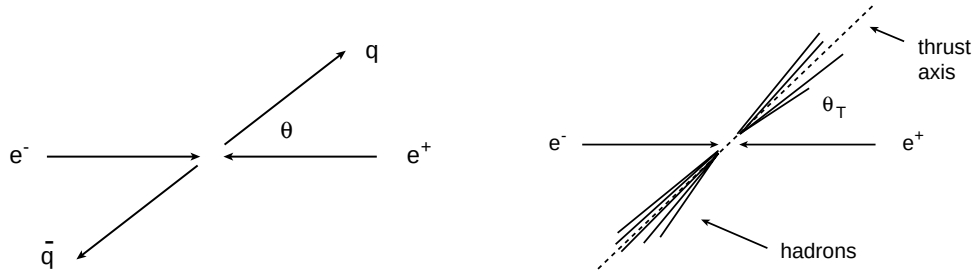

(a) (b)

Figure 10.8: (a) Schematic illustration of the reaction $e^+e^- \rightarrow q\bar{q}$. (b) Jets of hadrons resulting from the quark and antiquark.

Any number of algorithms can be used to determine an axis that approximates the original $q\bar{q}$ direction. Often one takes the axis defined by the unit vector $\mathbf{n}_{\mathrm{T}}$ such that the quantity

$$T = \frac{\sum_i |\mathbf{p}_i \cdot \mathbf{n}_{\mathrm{T}}|}{\sum_i |\mathbf{p}_i|} \tag{10.8}$$

is a maximum. Here $\mathbf{p}_i$ is the momentum vector of the ith particle and the sums extend over all particles in the event. The unit vector that gives the maximum value for T defines the *thrust axis*, which will be at some angle θ_{T} relative to the beam line. It will point more or less along the direction of the two jets. The *thrust* is then defined as the value of T according to (10.8) using this axis. The thrust is close to 1 for an extreme two-jet like configuration, and it approaches 1/2 for an isotropically distributed set of final state particles.

The first thing we can look at with $\mathrm{e^+e^-} \to$ hadrons is the distribution of the angle of the thrust axis relative to the beam line. This should basically follow the predicted angular distribution for the scattering angle θ of the quark relative to the direction of the $\mathrm{e^-}$. In a two-jet event, however, it is difficult to know which jet came from the quark and which came from the antiquark. For a start we don't need to know this, however, and we simply look at the distribution of θ_{T}, which is defined such that $0 \leq \theta_{\mathrm{T}} \leq \pi/2$. If we restrict ourselves to energies where the forwards–backwards asymmetry A_{FB} in equation (9.29) is zero (this is true, e.g., at $E_{\mathrm{cm}} = M_{\mathrm{Z}}$), then the distribution of $\cos\theta_{\mathrm{T}}$ is given by

$$\frac{d\sigma}{d\cos\theta_{\mathrm{T}}} \propto 1 + \cos^2\theta_{\mathrm{T}} \; . \tag{10.9}$$

If we had modelled quarks as spin-zero rather than spin-$\frac{1}{2}$ particles, the prediction (10.9) would be proportional to $\sin^2\theta_{\mathrm{T}}$.

Figure 10.9 shows the distribution $d\sigma/d\cos\theta_{\mathrm{T}}$ from $\mathrm{e^+e^-} \to$ hadrons measured by the ALEPH detector at $E_{\mathrm{cm}} = M_{\mathrm{Z}}$ [84]. The two dotted curves show the predictions of the spin-zero and spin-$\frac{1}{2}$ hypotheses. The solid histograms are modified to include a number of additional effects, the most important of which comes from the fact that the detector does not cover the entire solid angle surrounding the interaction point. Because of this it is possible to measure the thrust axis accurately only if the jets have a certain minimum angle relative to the beam line. For the ALEPH detector this means $\cos\theta_{\mathrm{T}}$ less than around 0.8 ($\theta_{\mathrm{T}} > 36°$). Regardless of this technicality, the plot confirms clearly that jets follow the direction of spin-$\frac{1}{2}$ quarks.

10.5 Hadronization and the string model

The transformation of quarks and gluons into colour-neutral hadrons is called *hadronization*. In principle this should be describable by a theory of strong interactions such as QCD, but owing to calculational difficulties this is not possible at present. In place of rigorous calculations there have been developed a number of QCD-inspired phenomenological models which in fact provide a good description of jet properties.

We can understand roughly why the reaction $\mathrm{e^+e^-} \to$ hadrons usually results in two-jet events by considering the force between a quark and antiquark that we found from consideration of $c\bar{c}$ or $b\bar{b}$ states. The masses of these states could be described by assuming a potential of the form

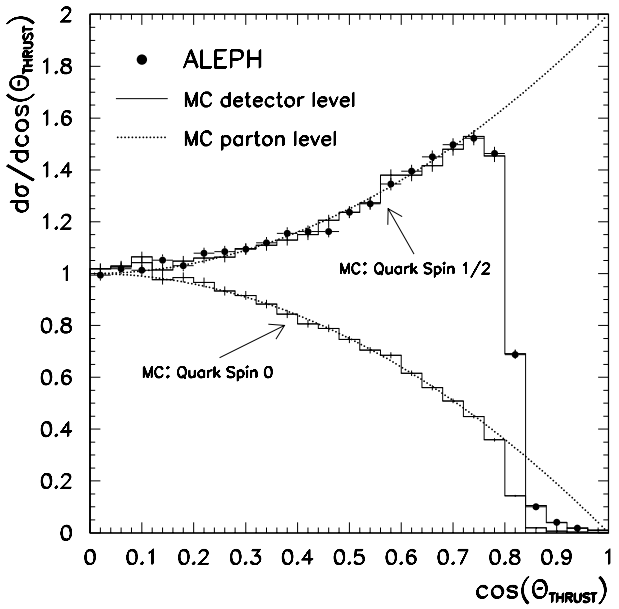

Figure 10.9: The distribution of $\cos\theta_{\rm T}$ for $e^+e^- \to$ hadrons at $E_{\rm cm} = M_{\rm Z}$ measured by the ALEPH experiment [84].

$$V_{\rm QCD}(r) = -\frac{4}{3}\frac{\alpha_{\rm s}}{r} + kr \;, \tag{10.10}$$

with the string tension k being around 1 GeV/fm. The force between a $q\overline{q}$ pair is given by

$$F = -\frac{\partial V_{\rm QCD}}{\partial r} = -\frac{4}{3}\frac{\alpha_{\rm s}}{r^2} - k \;, \tag{10.11}$$

so that at long distances the force does not die off to zero but rather approaches a constant, $-k$. This is in contrast to the attractive force between, say, an e^+e^- pair, which dies off as $1/r^2$ and for which the field lines fan out as in Fig. 10.10(a). It is more similar to the classical situation of a parallel-plate capacitor, where the electric field lines are parallel and thus the attractive force is independent of the separation. The 'chromoelectric' field lines between a $q\overline{q}$ pair are thus also parallel and can be modelled as being confined to a narrow *flux tube* or *string* with transverse size around 1 fm, as shown in Fig. 10.10(b). The string tension, i.e., the attractive force, can be interpreted as the energy per unit length in the flux tube, i.e., around 1 GeV/fm.

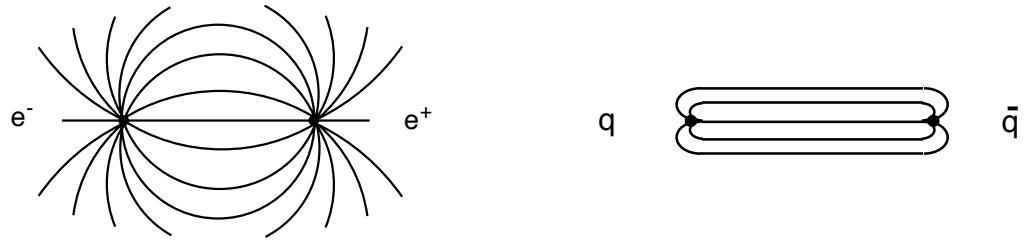

(a) (b)

Figure 10.10: The field lines between (a) an e^+e^- pair and (b) a $q\overline{q}$ pair.

The process of hadron formation in electron–positron annihilation can thus be modelled as shown in Fig. 10.11. The quark and antiquark are produced with high kinetic energies and are receding away from each other. As they separate, they are slowed down by the attractive force and their kinetic energy goes into the energy of the flux tube or string. The string can break by production of a second $q\overline{q}$ pair in its middle, resulting in two shorter and thus lower mass strings. This continues until what is left are small pieces of string which correspond to the mesons that make up the jets. The mesons from the ends of the original string have on average the highest momenta and those formed near the middle are almost at rest in the original string's rest frame.

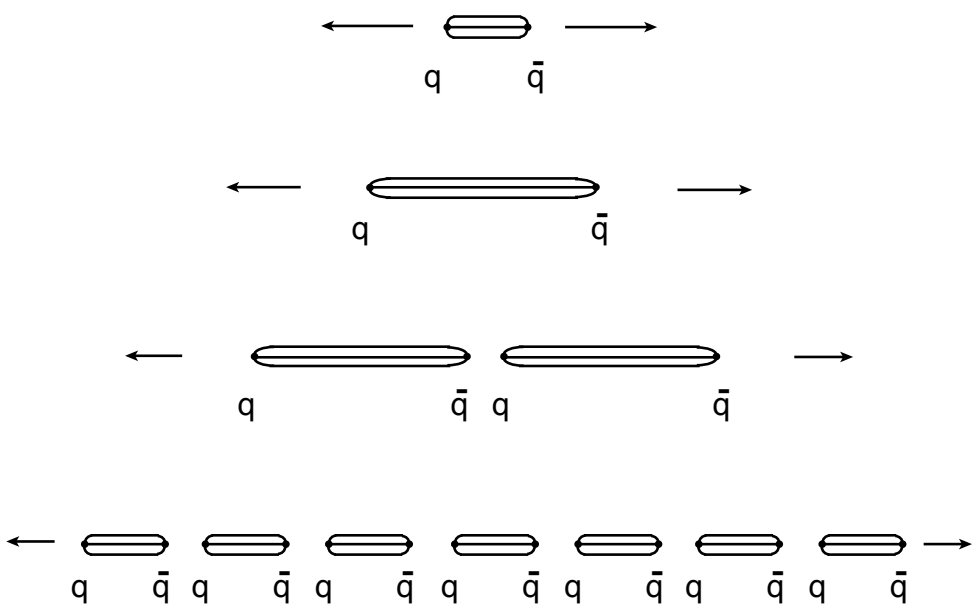

Figure 10.11: Hadron formation in the string model.

This picture of hadron formation is called the *string model*, an important example of which has been developed by Bo Andersson and others at the University of Lund [85]. The model has been implemented as a computer simulation program called *JETSET* (later reincarnated as *PYTHIA*). These and other simulation programs have proven to be invaluable tools in studying processes involving jets of hadrons.

10.6 Gluon emission and event-shape variables

Since the reaction $e^+e^- \to$ hadrons begins to first approximation by $e^+e^- \to q\overline{q}$, it should be possible for the quark or antiquark to emit a gluon at a sufficiently large angle that it will produce a third jet. Such events were first observed at the PETRA e^+e^- ring in the late 1970s. Studies of these events provided the experimental discovery of the gluon, although of course neither free gluons nor free quarks have ever been observed. The three-jet structure becomes increasingly clear at higher energy accelerators such as LEP. An example from the ALEPH experiment at $E_{\rm cm} = 91.2$ GeV is shown in Fig. 10.12.

At the level of quarks and gluons, three-jet events are described to first approximation by the reaction $e^+e^- \to q\overline{q}g$. At leading order in the strong coupling, the amplitude is given by the

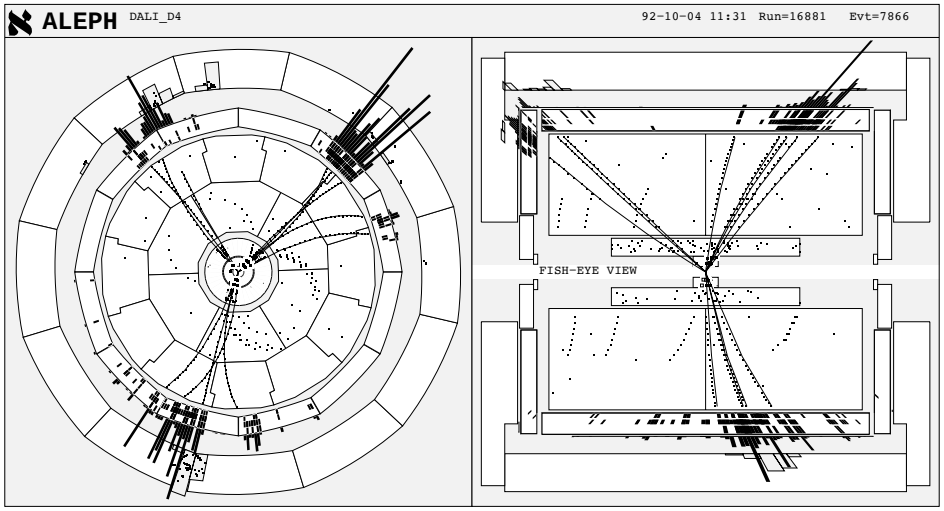

Figure 10.12: A three-jet event produced in e^+e^- collisions at $E_{cm} = 91.2$ GeV (from [23]).

two Feynman diagrams shown in Fig. 10.13. The ratio of the $q\bar{q}g$ cross section to that for $q\bar{q}$ is thus proportional to α_s. We can therefore determine α_s by measuring the ratio of the number of three- to two-jet events. In practice this is done by defining *event-shape variables* such as thrust that characterize the jet structure of an event. The QCD predictions for the distributions of these variables depends on α_s, and one fits the prediction to the measurement by adjusting α_s to achieve the best level of agreement.

Figure 10.13: Leading order Feynman diagrams for $e^+e^- \to q\bar{q}g$ where the gluon is emitted in (a) from the quark and in (b) from the antiquark.

The predicted distribution of an event-shape variable is found by computing the amplitudes for multiparton events such as $q\bar{q}g$. The square of the amplitude gives the probability to produce this final state, which depends on the energies and angles of the quarks and gluons. This can be converted into the probability to find an event with a certain value of, say, the thrust, as defined by equation (10.8). Here it is important that the conversion of partons (quarks and gluons) into hadrons does not change the thrust of the event very much. For a number of event-shape variables like thrust one can show that this should hold, at least at sufficiently high centre-of-mass energies.

The distribution of a variable equivalent to thrust, namely, $L = -\ln(1 - T)$, is shown in Fig. 10.14. The measurements from the ALEPH experiment [86] are shown as points, and the 'uncorrected' curve shows the prediction based on perturbative QCD for a final state consisting

of quarks and gluons. The shaded band represents the prediction after corrections to account for hadronization. The form of the QCD prediction depends on the parameter α_s. If it were zero (or very small) then there would be no gluon emission and we would only see two-jet events near $T = 1$, i.e., at large values of $-\ln(1-T)$. A larger value of α_s increases the likelihood of gluon emission and hence the probability of low-thrust events.

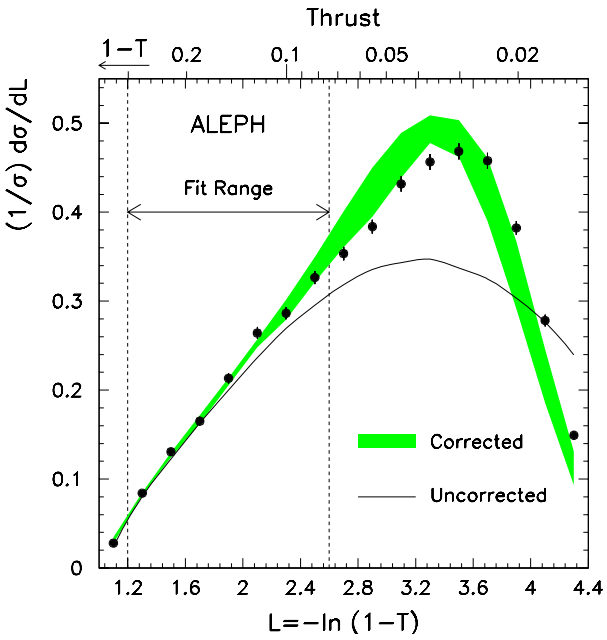

Figure 10.14: The distribution of the event-shape variable $-\ln(1-T)$, where T is the thrust. The QCD prediction (shaded band) has been fitted to the measured distribution (data points) by adjusting the value of α_s [86].

In Fig. 10.14, the value of α_s has been fitted to achieve the best agreement between the points and the curve in the indicated range. This gives $\alpha_s = 0.126 \pm 0.007$. Here the dominant uncertainty does not stem from the measurement accuracy but rather from the calculational difficulties in deriving the QCD curve. That is, the fitted thrust distribution is not the exact QCD prediction but is our best approximation based on an incomplete perturbation series and other corrections to account for hadronization. These uncertainties are reflected by the width of the band in Fig. 10.14. The thrust range for the determination of α_s has been restricted so that their impact is as small as possible.

The same procedure can be carried out using other variables sensitive to gluon emission, collectively called *event-shape variables*. One finds $\alpha_s(M_Z) \approx 0.12$ plus or minus around 3%, although the magnitude of the theoretical uncertainty is a subject of some controversy. These are represented as the data point labelled 'Event shapes (ALEPH)' in the plot of α_s versus energy shown in Fig. 10.7.

In addition to providing a measurement of α_s, distributions of event-shape variables provide an important test of QCD. This is because the QCD prediction contains in principle only a single free parameter, α_s, and we have many measured data points. In practice, however, there are additional parameters related to the modelling of the hadronization and there are uncertainties due to the incomplete perturbation series used to predict the distribution. At least for certain well-defined regions of the variables, however, these uncertainties are at the level of several percent or less, and to this degree of accuracy the QCD predictions are well confirmed.

10.7 Measuring α_s using $\sigma(e^+e^- \to \text{hadrons})$

An additional way to determine α_s is to measure its influence on the total cross section for the reaction $e^+e^- \to$ hadrons. In Section 10.1 we took this to be same as the sum of the cross sections $\sigma(e^+e^- \to q\bar{q})$ for all kinematically accessible quark flavours. If, however, the final state is $q\bar{q}g$, then this will also lead to a hadronic event. The total cross section to produce hadrons is thus the sum of the cross sections for all of the possible final states consisting of quarks and gluons. (Remember that for different final states, one adds probabilities, i.e., cross sections, and not amplitudes.)

We can therefore express the total cross section as a perturbation series in α_s, for which the zeroth order term is given by the cross section for $e^+e^- \to q\bar{q}$. The correction to this at order α_s will include the cross section for $q\bar{q}g$, which we obtain by squaring the sum of the amplitudes in Fig. 10.13.

In addition, there will be corrections to amplitude for $e^+e^- \to q\bar{q}$ from the diagrams with virtual gluons as shown in Fig. 10.15. The total amplitude for $e^+e^- \to q\bar{q}$ is given by the sum of those with and without virtual gluons. The square of this amplitude will contain a term independent of α_s corresponding to the square of the diagram without virtual gluons. There will also be interference terms from the product of this diagram with those containing a virtual gluon, and these terms will be proportional to α_s.

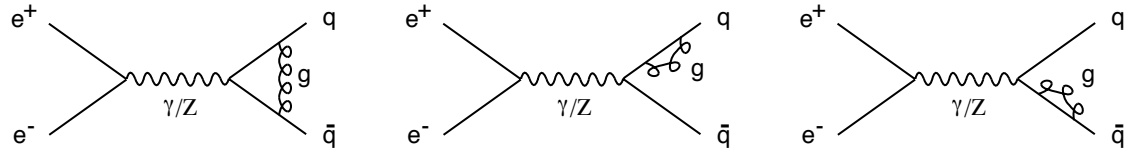

Figure 10.15: Higher order corrections to $e^+e^- \to q\bar{q}$ from virtual gluons.

The correction to the total hadronic cross section to first order in α_s thus consists of the $q\bar{q}g$ amplitude squared plus the correction to the amplitude for $q\bar{q}$ from the interference terms of order α_s. To obtain the total cross section, one must integrate over all possible momenta of the quarks and gluons involved. It turns out that in doing this, the cross section for $q\bar{q}g$ diverges; the QCD prediction to first order in perturbation theory for $q\bar{q}g$ is infinite. The infinities stem from configurations where the gluon's energy goes to zero (called an infrared divergence) and where the gluon and quark momenta are parallel (called a collinear divergence). This is not a problem with QCD; it is a deficiency of perturbation theory, which after all is only a mathematical approximation technique.

In computing the corrections to $\sigma(e^+e^- \to q\bar{q})$ also to order α_s, the Feynman rules also call for an integration over the possible momenta that can be carried by the virtual gluons. These integrals also diverge, but to negative infinity. By what seems like a minor miracle, the divergences in the cross sections for $\sigma(e^+e^- \to q\bar{q}g)$ and $\sigma(e^+e^- \to q\bar{q})$ almost cancel, leaving a small finite correction proportional to α_s. One finds

$$\sigma(e^+e^- \to q\bar{q}) + \sigma(e^+e^- \to q\bar{q}g) = \sigma_0 \left(1 + \frac{\alpha_s}{\pi}\right) , \tag{10.12}$$

where σ_0 is the cross section without QCD corrections given by equation (10.1). In fact, one can show that a similar miracle occurs at each order of perturbation theory. Negative infinities from virtual corrections cancel positive infinities from infrared and collinear gluons. What remain are finite corrections calculable at each order in perturbation theory.

Since there are no gluon corrections to the reaction $e^+e^- \to \mu^+\mu^-$, we can express the correction to the hadronic cross section as an equivalent correction to the quantity R, defined as the ratio of the hadronic to $\mu^+\mu^-$ cross sections. At each order in α_s the corrections become more difficult to compute. For R, the calculation has been carried out to order α_s^3,

$$R = R_0 \left[1 + \frac{\alpha_s}{\pi} + 1.411 \left(\frac{\alpha_s}{\pi} \right)^2 - 12.8 \left(\frac{\alpha_s}{\pi} \right)^3 + \ldots \right] , \tag{10.13}$$

where R_0 is the prediction without QCD corrections, i.e., to order α_s^0 [87].

This now explains why the value of R measured at $E_{cm} \approx 35$ GeV at PETRA was not 11/3 as we predicted in Section 10.1, but rather somewhat higher. Figure 10.7 shows that α_s at this energy is around 0.15. According to equation (10.13) this will increase the prediction for R from 11/3 to 3.85, which in reasonably good agreement with the measured values in Fig. 10.2. In fact, measurements of quantities closely related to R measured by the LEP experiments at E_{cm} close to M_Z allow for an accurate determination of α_s, yielding [7]

$$\alpha_s(M_Z) = 0.1200 \pm 0.0028 . \tag{10.14}$$

The fact that the total hadronic cross section, event-shape variables as well as a number of other processes all give consistent values of α_s is a convincing confirmation of QCD.

Chapter 11

The Higgs mechanism

Local gauge symmetry has been the guiding principle in constructing the Standard Model. If we add to the Lagrangian density the usual terms that describe particle masses, however, we find that the gauge symmetry is broken. In this chapter we take a look at how this problem is circumvented by the *Higgs mechanism*, how its predictions stand in comparison with experiment, and the recent results from the LHC showing the discovery of a new particle compatible with the Higgs boson.

11.1 The Higgs field

In Chapter 9 we argued that the weak interactions could be described by the exchange of an intermediate vector boson (IVB) and that the IVB must be massive in order to explain the very low rates for weak decays. Furthermore we know that most of the fermions observed in Nature are massive (all of them, in fact, if neutrinos also have a mass).

There is a well defined prescription in quantum field theory for describing massive particles. One writes a certain term corresponding to the mass of each particle in the Lagrangian density, and in order for the theory as a whole to be invariant under a transformation, the mass terms as well must be invariant. One can show that the usual mass terms for gauge bosons do not obey the local gauge symmetry required in the Standard Model. Furthermore, for the $\mathrm{SU(2)_L}$ gauge symmetry of the Standard Model, the terms describing fermion masses are not gauge invariant either. So the entire idea of using gauge invariance as a guiding principle for the theory is cast into doubt. In the 1960s, Peter Higgs and others showed that by a suitable modification of the theory, one can have gauge symmetry even with massive particles [71]. In order to understand how this works we need to say a few more words about how particles are described in quantum field theory.

A good analogy for a *quantum field* is a lattice of atoms occupying all space. They are coupled by means of interatomic forces and the system of atoms behaves like a set of coupled quantum mechanical oscillators. Instead of describing the coordinates of each individual oscillator, we can transform to a set of *normal coordinates*, each of which will describe a mode of vibration of the system at a given frequency. One of these modes of vibration, for example, will describe a plane wave of a certain frequency and wavelength propagating in some direction through the lattice. Such a mode of vibration will carry a certain energy and momentum. In quantum field

theory, such a wave or excitation of the lattice corresponds to a particle. This is in fact how *phonons* are described in a crystal lattice. They are quantized collective vibrations in a lattice that carry energy and momentum.

For the quantum field that describes, say, the electron, one must dispense with the 'atoms' in the analogy and allow the lattice spacing to go to zero. All of the electrons in the universe are simply an enormously complicated excitation of a single electron field. Similarly there is a field for every particle type. Furthermore the fields interact, and an excitation in one can be converted into excitations in others. This is how reactions are described in which particles are created and destroyed.

For the usual fields of the Standard Model, the state of lowest energy is the one in which there are no particles present. In the language of quantum field theory one says that the *vacuum expectation value* of the field is zero. In the Higgs mechanism, one adds to the Lagrangian of the theory a term corresponding to the Higgs field. This field is different from the others in that its vacuum expectation value is nonzero. That is, the field has in a particular sense a nonzero value in the state of lowest energy. This part of the field that remains even in the state of lowest energy is what then interacts with all other particles and imparts to them a mass. Furthermore, it must be possible to have excitations of the Higgs field itself, and these correspond to a spin-0 Higgs particle called H.

11.2 The Higgs mechanism and Margaret Thatcher

In 1993, UK Science Minister Waldegrave challenged the particle physics community to answer the question 'What is the Higgs boson, and why do we want to find it?' in one page or less. Among the winners was the following entry from David Miller [88]:

> Imagine a cocktail party of political party workers who are uniformly distributed across the floor, all talking to their nearest neighbours. The ex-Prime Minister enters and crosses the room. All of the workers in her neighbourhood are strongly attracted to her and cluster round her. As she moves she attracts the people she comes close to, while the ones she has left return to their even spacing. Because of the knot of people always clustered around her she acquires a greater mass than normal, that is, she has more momentum for the same speed of movement across the room. Once moving she is harder to stop, and once stopped she is harder to get moving again because the clustering process has to be restarted. In three dimensions, and with the complications of relativity, this is the Higgs mechanism. In order to give particles mass, a background field is invented which becomes locally distorted whenever a particle moves through it. The distortion – the clustering of the field around the particle – generates the particle's mass. The idea comes directly from the Physics of Solids. Instead of a field spread throughout all space a solid contains a lattice of positively charged crystal atoms. When an electron moves through the lattice the atoms are attracted to it, causing the electron's effective mass to be as much as 40 times bigger than the mass of a free electron. The postulated Higgs field in the vacuum is a sort of hypothetical lattice which fills our Universe. We need it because otherwise we cannot explain why the Z and W particles which carry

the Weak Interactions are so heavy while the photon which carries Electromagnetic forces is massless.

Now consider a rumour passing through our room full of uniformly spread political workers. Those near the door hear of it first and cluster together to get the details, then they turn and move closer to their next neighbours who want to know about it too. A wave of clustering passes through the room. It may spread out to all the corners, or it may form a compact bunch which carries the news along a line of workers from the door to some dignitary at the other side of the room. Since the information is carried by clusters of people, and since it was clustering which gave extra mass to the ex-Prime Minister, then the rumour-carrying clusters also have mass. The Higgs boson is predicted to be just such a clustering in the Higgs field. We will find it much easier to believe that the field exists, and that the mechanism for giving other particles mass is true, if we actually see the Higgs particle itself. Again, there are analogies in the Physics of Solids. A crystal lattice can carry waves of clustering without needing an electron to move and attract the atoms. These waves can behave as if they are particles. They are called phonons, and they too are bosons. There could be a Higgs mechanism, and a Higgs field throughout our Universe, without there being a Higgs boson. The next generation of colliders will sort this out.

11.3 The theoretical need for the Higgs

One might wonder why people seem to be so certain that the Higgs, or something like it, must exist. After all, we could always write down the Standard Model for massless particles, which determines the gauge bosons that must exist and how they interact. Then we could simply add the mass terms after the fact, and the resulting model, although no longer gauge invariant, would be in good agreement with essentially all experimental observations.

There are at least two reasons why this is not an attractive option. First, the resulting theory would not be renormalizable, and so we would run into problems in computing higher order corrections in perturbation theory. In addition, without the Higgs, the Standard Model's predictions for certain high energy processes run into internal contradictions much in the way that Fermi's theory of weak interactions didn't make sense without the intermediate vector boson.

Consider, for example, the reaction $W^+W^- \to W^+W^-$, which without the Higgs boson would be described by the Feynman diagrams shown in Fig. 11.1. If we use only these diagrams to predict the cross section, then we find that it exceeds the unitarity limit at an energy of around 1.5 TeV. If, however, the Higgs boson exists, then we have the additional amplitudes shown in Fig. 11.2. By including these, one can show that the unitarity limit is not exceeded, as long as the Higgs mass is less than around 1 TeV.

It is possible in principle to study the reaction $W^+W^- \to W^+W^-$ in very high energy proton–proton collisions, where the Ws are emitted by the quarks of the colliding protons. The energy of Large Hadron Collider at CERN is such that these studies will be near the limit of feasibility. Regardless of whether we ever study $W^+W^- \to W^+W^-$ experimentally, it is clear that the Standard Model cannot be complete without something to keep all cross sections below the unitarity limit.

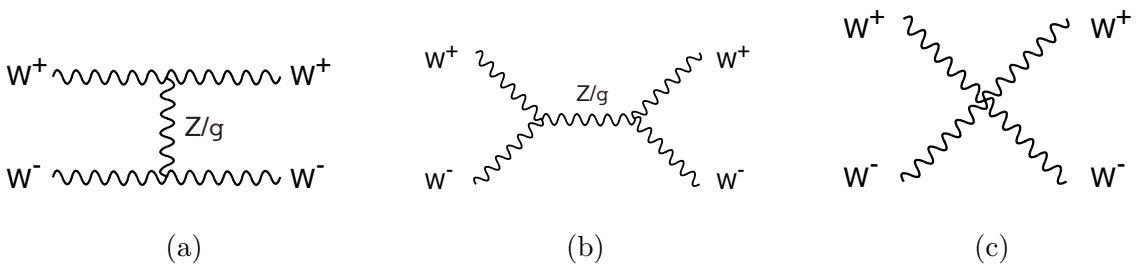

Figure 11.1: Feynman diagrams for $W^+W^- \to W^+W^-$ involving only the gauge bosons W, Z or γ.

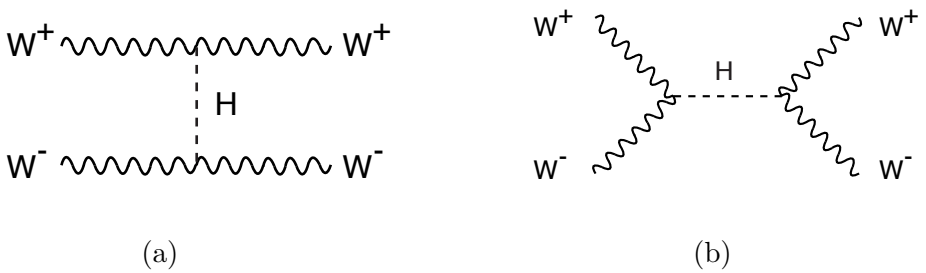

Figure 11.2: Feynman diagrams for $W^+W^- \to W^+W^-$ involving an intermediate Higgs boson.

11.4 Properties of the Higgs boson

In the simplest version of the Higgs mechanism, there should exist a spin-0 Higgs particle denoted as H. It is electrically neutral and has lepton and baryon number of zero. It couples to all massive particles according to the vertex shown in Fig. 11.3. For a particle X, the coupling strength is proportional to the mass m_X. Note that this means there is no direct coupling between the Higgs particle and the photon or gluon. The mass of the Higgs boson itself is not predicted.

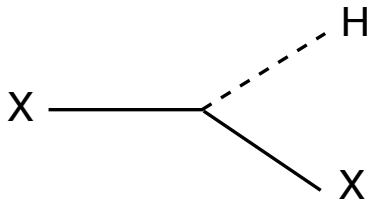

Figure 11.3: The coupling of a particle X to the Higgs boson H. The coupling strength is proportional to the mass m_X.

The scenario with a single neutral Higgs boson is not, however, the only possibility. There are many versions of the Higgs mechanism that can provide the required gauge symmetry. One of the often considered alternatives includes, for example, three neutral and two charged Higgs bosons. In this sense the 'Higgs sector' of the Standard Model is one of its least well understood aspects. For now we will consider only the case where there is a single neutral Higgs boson; this is often called the 'Minimal Standard Model' or MSM.

Before the results from the summer 2012, experimental searches for the Higgs boson had excluded its existence for masses up to around 114 GeV. In the summer of 2000, experiments

at LEP found interesting hints that could indicate the presence of a Higgs boson with a mass of 115 GeV. Unfortunately, the LEP programme was terminated before enough data could be accumulated to confirm or rule out this tentative signal. We will discuss this possible discovery more in Section 11.6.

The fact that the coupling strength is proportional to the mass of the particle with which the Higgs boson interacts means that, apart from some minor exceptions noted below, the Higgs will decay with the highest probability into the particle–antiparticle pair with the highest mass that is kinematically possible. If, for example, the Higgs mass was 115 GeV, as the observations from LEP were suggesting, then it could not decay into real $\mathrm{W}^+\mathrm{W}^-$ or ZZ pairs since these are too massive. These decay modes would be possible if one or both of the Ws or Zs are virtual (typically this is indicated by the notation W^* or Z^*), but then the amplitude is suppressed by the propagator of the off-shell particle. If the mass of the Higgs was 115 GeV, then its most probable decay mode would be into $b\bar{b}$. The ratio of the decay rate of such a Higgs into $b\bar{b}$ to that into $c\bar{c}$ is

$$\frac{\Gamma(\mathrm{H} \to b\bar{b})}{\Gamma(\mathrm{H} \to c\bar{c})} = \left(\frac{m_b}{m_c}\right)^2 \approx \left(\frac{5.0\ \mathrm{GeV}}{1.0\ \mathrm{GeV}}\right)^2 \approx 25\ . \tag{11.1}$$

If the Higgs mass is greater than around 140 GeV, then the most likely decay channel is $\mathrm{H} \to \mathrm{W}^+\mathrm{W}^-$. Until one has $m_\mathrm{H} > 2M_\mathrm{W} \approx 161$ GeV, this of course requires one or both of the Ws to be off-shell. It turns out that $\mathrm{H} \to \mathrm{W}^+\mathrm{W}^-$ remains the dominant decay mode for higher values of m_H, even after the decay into ZZ becomes possible. This is because the rate for $\mathrm{H} \to \mathrm{ZZ}$ loses a factor of two since the ZZ state is made of two identical particles whereas $\mathrm{W}^+\mathrm{W}^-$ is not. The branching ratios of the possible decays of the Higgs are shown in Fig. 11.4 as a function of the Higgs mass.

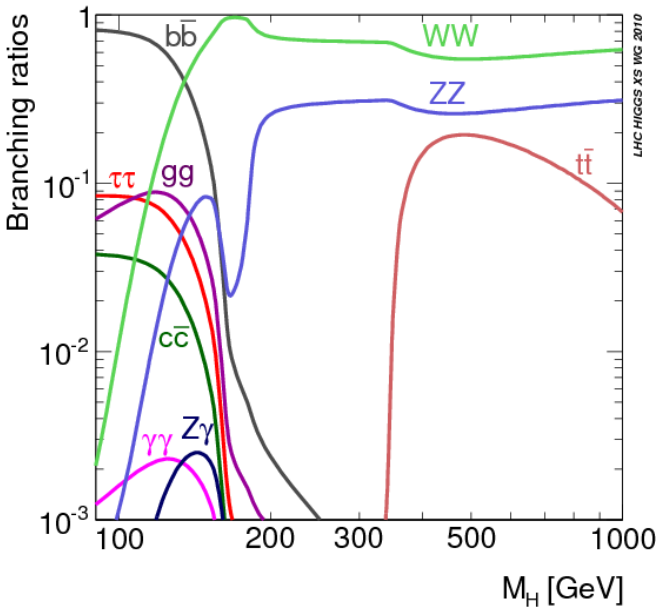

Figure 11.4: Branching ratios of the standard model Higgs decays as a function of the Higgs mass.

11.5 Relating gauge boson masses and coupling strengths

The Higgs mechanism makes an important prediction which has already been confirmed experimentally. The Higgs mechanism relates the masses of the W and Z bosons to the coupling strengths e and g. To lowest order the relation is

$$\frac{e^2}{g^2} = 1 - \frac{M_{\rm W}^2}{M_{\rm Z}^2} \, . \tag{11.2}$$

This equation can be rewritten to predict the W mass as a function of α, $G_{\rm F}$ and $M_{\rm Z}$, all of which are measured to high precision. As we mentioned in Chapter 9, the predicted value is

$$M_{\rm W} = 80.374 \pm 0.034 \text{ GeV} \, . \tag{11.3}$$

This is in excellent agreement with the best direct measurements of $M_{\rm W}$. The LEP experiments, for example, find

$$M_{\rm W} = 80.427 \pm 0.046 \text{ GeV} \, . \tag{11.4}$$

11.6 Searches for the Higgs boson in e^+e^- collisions

The main amplitude for Higgs boson production in e^+e^- collisions is given by the Feynman diagram in Fig. 11.5. Since the virtual Z radiates a Higgs particle, this process can be called *Higgsstrahlung*. If the centre-of-mass energy is greater than the sum $M_{\rm Z} + m_{\rm H}$, then both the Higgs boson and the final Z can be produced on-shell, resulting in a large cross section.

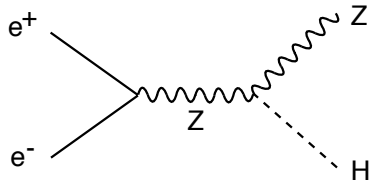

Figure 11.5: Feynman diagram for $e^+e^- \to HZ$.

Physicists at LEP searched for this reaction with energies up to $E_{\rm cm} = 209$ GeV. Since the Z mass is 91 GeV, this means that both the Z and Higgs can be on-shell for $m_{\rm H}$ up to $E_{\rm cm} - M_{\rm Z} = 118$ GeV, in which case both the Z and Higgs would be produced at rest. In fact, in this configuration the cross section is very small, and it grows significantly if $E_{\rm cm}$ is somewhat higher than $M_{\rm Z} + m_{\rm H}$. In the actual data set obtained at LEP at the highest energies, one was sensitive to a Higgs particle with a mass up to around 115 GeV.

For a Higgs particle with a mass in this range, the most likely decay is into $b\bar{b}$. These will result in two jets, each of which will contain a hadron with a b quark, such as B^0, B^+, B_s^+, etc. These particles all have mean lifetimes around 1.5 ps. The B hadron usually inherits a significant fraction of the b quark's energy, which will be around half of 115 GeV. If we consider, for example, B hadrons with an energy of 40 GeV, they will travel on average a distance d before decaying of

$$d = \beta\gamma c\tau_{\rm B} = \frac{\sqrt{E_{\rm B}^2 - m_{\rm B}^2}}{m_{\rm B}} c\tau_{\rm B} = \frac{\sqrt{40^2 - 5.3^2}}{5.3} \text{ GeV } \times 3 \times 10^8 \text{ m/s } \times 1.5 \times 10^{-12} \text{ s } \approx 3.4 \text{ mm .} \tag{11.5}$$

The tracks of the B's decay products will not therefore point back directly to the interaction point and jets containing B hadrons can be identified in this way.

In order to find events of the type $e^+e^- \to HZ$, we should look therefore for two jets from the H, each of which contain a B hadron, and for evidence of a Z. The invariant mass of the two-jet system from the H is $m_{\rm H}$, and similarly the particles from the Z have an invariant mass of $M_{\rm Z}$. The most probable decay mode for the Z is into a quark-antiquark pair, so these events will have four jets of hadrons: two b-jets from the Higgs and two jets (which may or may not contain B hadrons) from the Z. Of course the other decay modes of the Z, e.g., e^+e^-, $\mu^+\mu^-$, etc., are used as well. Note that the technique works even if the Z decays into neutrinos as long as all of the other particles are observed. From energy and momentum conservation the invariant mass of the unseen particles (called the *missing mass*) can be determined. If this is equal to $M_{\rm Z}$ then this almost certainly resulted from a Z decay into $\nu\overline{\nu}$.

Since we do not know *a priori* what the mass of the Higgs boson is, we cannot include it in our selection criteria for candidate events. We can measure the invariant mass of the two jets with B hadrons, however, and enter the value into a histogram. If our data sample includes Higgs events, then we should see a peak in the histogram at $m_{\rm H}$.

From the data sample collected by the ALEPH experiment at energies up to 209 GeV, one obtained the invariant mass distribution for Higgs candidates (i.e., the pair of jets with B hadrons) shown in Fig. 11.6. The data are shown as points and the solid histogram indicates the expected background from processes other than Higgs boson production. The most important background is from the reaction $e^+e^- \to ZZ$, where one of the Zs decays into $b\overline{b}$ and is thus mistaken for a Higgs. This results in the broad peak around $M_{\rm Z}$.

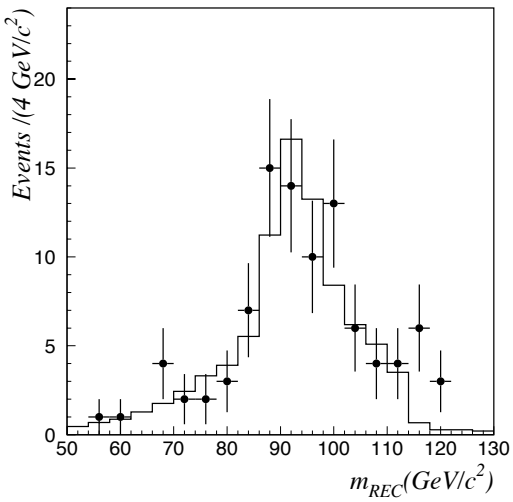

Figure 11.6: The distribution of the reconstructed mass of Higgs boson candidates. The data are shown as points and the solid histogram indicates the expected background from processes other than Higgs boson production [90].

On the right-hand flank of the broad peak, however, there is a significant excess of events at a mass of around 115 GeV. The statistical significance of the excess is equivalent to a three-standard deviation fluctuation of a Gaussian distributed variable, for which the probability is

around 10^{-3}. This does not mean we are 99.9% certain that we have found the Higgs. Rather, we can say that if there is no Higgs boson, then the probability of seeing data as 'Higgs-like' as that which we found is one in a thousand.

A candidate event found by the ALEPH experiment is shown in Fig. 11.7. The two jets with displaced vertices (could) come from the decay of the Higgs; the other two come from a Z. The final statistical significance of the Higgs signal is equivalent to a two standard deviation effect, which is not sufficient to claim a discovery [91].

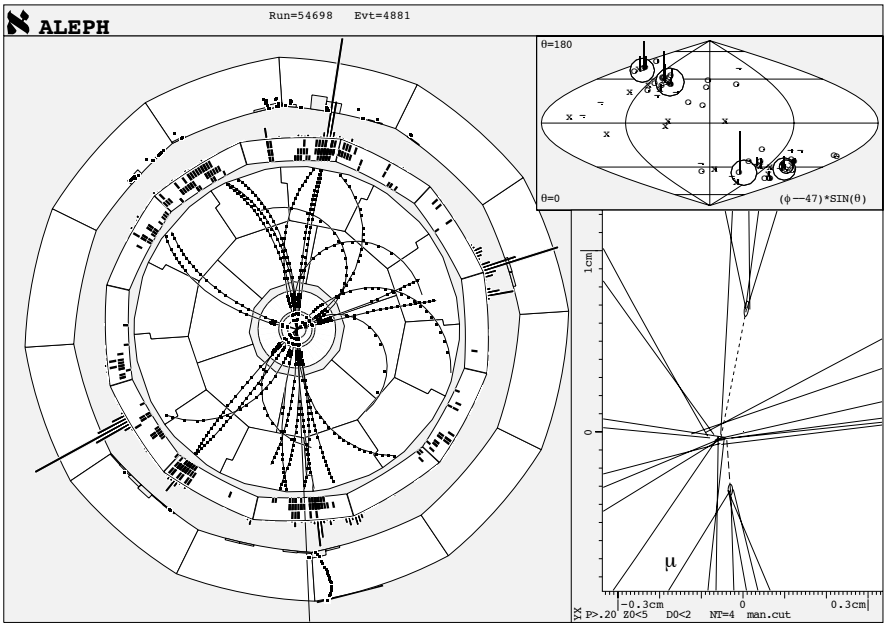

Figure 11.7: A candidate event for the reaction $e^+e^- \to HZ$ recorded by the ALEPH experiment [23].

Fermilab fought a tough battle compared to the LHC for discovering the Higgs, since the energy and luminosity of their $p\overline{p}$ collider did not allow for an easy discovery. We now focus on the recent results from the LHC.

11.7 Searching for the Higgs in proton–proton collisions

The Large Hadron Collider (LHC) is a proton–proton collider housed in the 27 km tunnel that was used by LEP. The design centre-of-mass energy of the LHC is 14 TeV and it has been taking data since September 2009. The two data sets that were used for the Higgs discovery (and other LHC results) were the data taken in 2011 at a centre-of-mass of 7 TeV with an integrated luminosity of about 5 fb^{-1} and the data taken in 2012 at a centre-of-mass of 8 TeV and with a final integrated luminosity of about 20 fb^{-1}. The data set containing the 7 and 8 TeV data is called 'Run 1'. The LHC underwent a long shutdown in 2013/14 and resumed taking data at 13 TeV in the Spring of 2015. The 13 TeV data set of the LHC is called 'Run 2' and is due to finish data-taking in December 2018, with an estimated integrated luminosity of 150 fb^{-1}.

At all those centre-of-mass energies, the dominant Higgs production mechanism is through the collision of two gluons, which come from the colliding protons as shown in Fig. 11.8. The gluon is a massless particle, so it does not couple directly to the Higgs. It can be produced, however, by means of an intermediate quark loop, as shown in Fig. 11.9. Since the Higgs coupling strength is proportional to the particle's mass, the diagram with the top quark loop makes the largest contribution to the total amplitude. Although the gluon fusion process has the largest cross section, other production mechanism offer experimental handles that are useful in identifying Higgs events.

For example, the next most significant production process (labelled Hqq on the plot) is called Vector Boson Fusion because it comes from two W (or Z) bosons being radiated off a quark from each of the protons and fusing together to produce a Higgs. The initial quarks from the proton remain in the final state and will be close to the beam line, offering a distinctive signature. The next process on the plot (HW) is the Associated Production where a W (or Z) boson is radiating off a Higgs. Finally another process being studied at the LHC is the ttH process where the final state contain a top and anti-top quark in addition to a Higgs boson. This last process has a very small cross section but a very distinctive signature with a lot of objects in the final state.

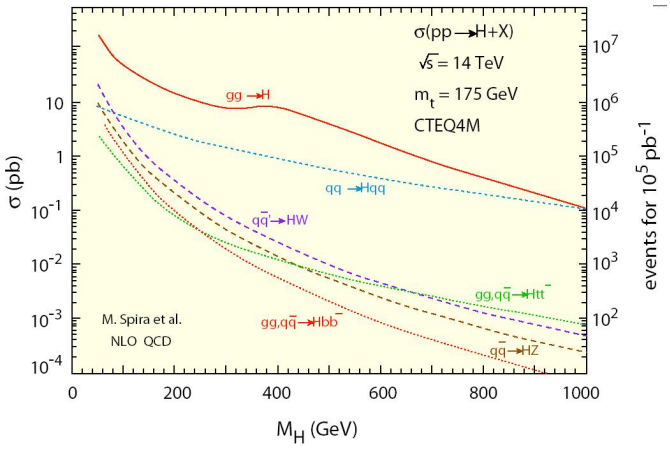

Figure 11.8: Production cross section of the SM Higgs as a function of the Higgs mass.

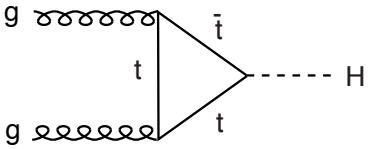

Figure 11.9: Feynman diagram for Higgs boson production by gluon-gluon fusion.

Two general purpose detectors are taking data at the LHC, called CMS (Compact Muon Solenoid) and ATLAS (A Toroidal LHC ApparatuS). A cut-away view of the ATLAS detector is shown in Fig. 11.10; note the people at the bottom for scale [93].

Both ATLAS and CMS were designed to be able to find the Higgs for any mass up to a sizable fraction of 1 TeV.

Since the mass of the Higgs was unknown, teams of particle physicists within ATLAS and CMS designed analyses to look for the Higgs boson at all its possible mass values. For example, if

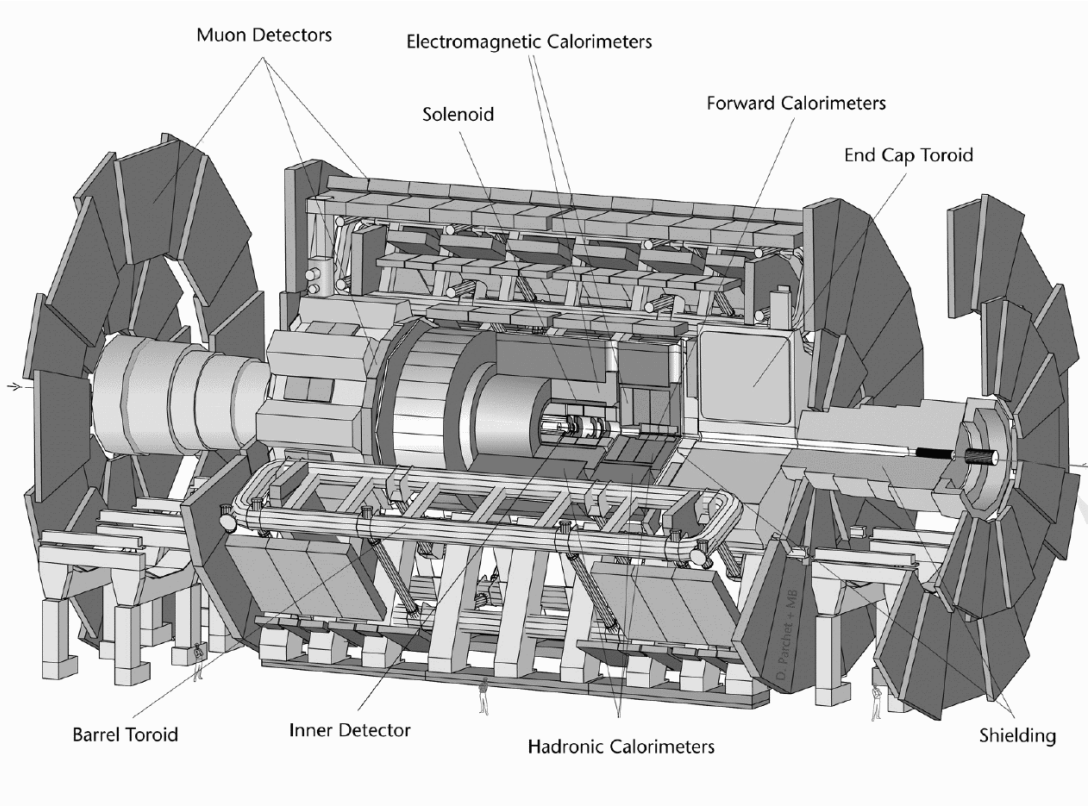

Figure 11.10: The ATLAS detector [93].

the Higgs mass is greater than $2M_{\mathrm{Z}}$, then the decay $\mathrm{H} \to \mathrm{ZZ}$ has a high probability. This can also happen even for lower Higgs masses, but then one of the Zs has to be off-shell, which suppresses the cross section. Nevertheless, for m_{H} greater than around 130 GeV, the decay mode $\mathrm{H} \to \mathrm{ZZ}$ will allow the easiest discovery of the Higgs. If one of the Zs decays into quark–antiquark, then this will result in a pair of jets. These will be almost impossible to disentangle from the large number of other jets that are produced in pp collisions, mainly through radiation of gluons. If, however, the Zs decay into either $\mathrm{e}^+\mathrm{e}^-$ or $\mu^+\mu^-$, they will be much easier to find, since electrons leave characteristic showers in an electromagnetic calorimeter and muons are highly penetrating. The invariant mass of each lepton pair is equal to the Z mass and the combined invariant mass of the four-lepton system is equal to the Higgs mass. A Feynman diagram for such a decay is shown in Fig. 11.11.

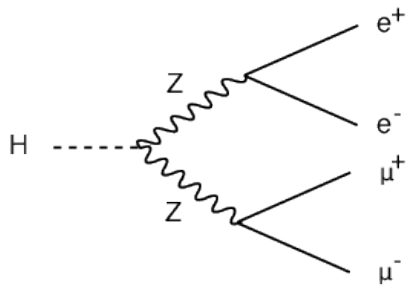

Figure 11.11: Feynman diagram for the decay $\mathrm{H} \to \mathrm{ZZ}$ with $\mathrm{Z} \to \mathrm{e}^+\mathrm{e}^-$ and $\mathrm{Z} \to \mu^+\mu^-$.

If, however, the mass of the Higgs boson is less than around 130 GeV, the most frequent

decay will be into $b\bar{b}$, which will result in two jets, each of which will contain a B hadron. In principle, this could be found by searching for such jets and measuring the invariant mass of the jet–jet pairs. In practice, however, a tremendous number of jets are produced in proton–proton collisions and the Higgs signal from $\mathrm{H} \to b\bar{b}$ would be obscured by this background.

Such a low-mass Higgs can (and has!), however, be found at the LHC by using its decay into two photons. Since the photon is massless, the Higgs does not couple to it directly. The decay $\mathrm{H} \to \gamma\gamma$ is possible, however, by means of an intermediate particle loop as shown in Fig. 11.12. As the coupling strength is proportional to the particle's mass, the largest contributions come from the top quark (Fig. 11.12(a)) and from the W boson (Fig. 11.12(b)). For a Higgs mass in the range between 100 and 150 GeV, the branching ratio for $\mathrm{H} \to \gamma\gamma$ is only around 0.2%. Nevertheless, these events can be distinguished relatively easily from background processes.

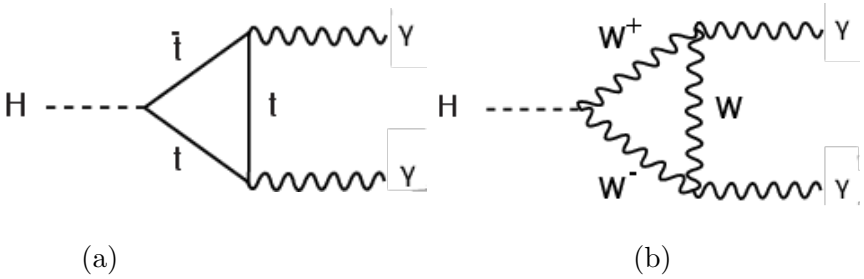

(a) (b)

Figure 11.12: Feynman diagrams for the decay $\mathrm{H} \to \gamma\gamma$ involving (a) a top quark loop and (b) a W boson loop.

For the lower mass range where $\mathrm{H} \to \gamma\gamma$ must be used, the detectors need good electromagnetic calorimeters in order to find the photon–photon system and to measure its invariant mass. For a Higgs mass high enough to allow $\mathrm{H} \to \mathrm{ZZ}$, the detectors need to reconstruct Z decays into $\mathrm{e}^+\mathrm{e}^-$ or $\mu^+\mu^-$ pairs. Figure 11.13, for example, shows a simulated Higgs decay into ZZ, where one Z decays to $\mathrm{e}^+\mathrm{e}^-$ and the other to $\mu^+\mu^-$. The electrons are identified by the characteristic electromagnetic showers left in the calorimeter, while the muons penetrate through the detector's calorimeters and leave signals in the muon chambers.

Just as an example, suppose the Higgs mass had been 300 GeV. In order to predict the cross section for Higgs boson production, we need to know the cross section for the collision of two partons to result in a Higgs, e.g., $\sigma(gg \to \mathrm{H})$, and we also need to know how many partons of the various types (q, $\overline{q}$, g) there are inside the proton and what fraction of the proton's momentum they carry. The parton-level cross sections can be computed using the full set of Feynman rules for the Standard Model. The numbers of partons inside the proton are given by the parton density functions discussed in Chapter 7. These cannot be computed using perturbation theory and in practice they must be measured in deep inelastic lepton–proton scattering.

Using these ingredients with $m_{\mathrm{H}} = 300$ GeV and $E_{\mathrm{cm}} = 14$ TeV, a complete calculation for the Higgs boson production cross section gives $\sigma(\mathrm{pp} \to \mathrm{H}+\mathrm{X}) = 9$ pb [94]. The peak luminosity of the LHC is about $\mathcal{L} = 10^{34}$ cm^{-2}s^{-1}, and in a nominal year one can expect about 10^7 seconds of running time. The expected number of Higgs bosons produced per year is therefore

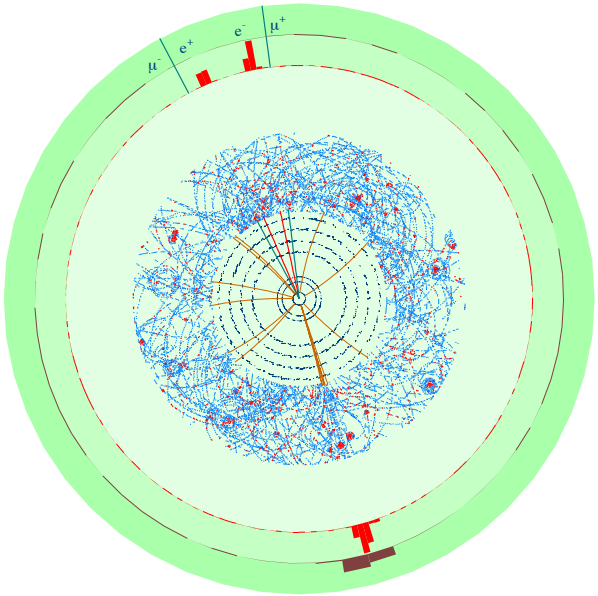

Figure 11.13: Simulated event of $H \to ZZ$ with one Z decaying to electrons and the other to muons. Note the large number of low energy particles coming from the proton interactions. (from [93]).

$$\begin{aligned} N(\mathrm{pp} \to \mathrm{H} + \mathrm{X}) &= \sigma \int \mathcal{L}\, dt \\ &= 9 \text{ pb } \times 10^{34}\ \mathrm{cm}^{-2}\mathrm{s}^{-1} \times 10^{7}\mathrm{s} \times \frac{10^{-36}\ \mathrm{cm}^2}{1 \text{ pb}} \\ &= 9 \times 10^{5}\ . \end{aligned} \tag{11.6}$$

This is not the end of the story, however, since the only Higgs events that can be found easily by the LHC detectors are those where the Higgs decays to ZZ and both Zs decay into either e^+e^- or $\mu^+\mu^-$. For a Higgs mass of 300 GeV, the branching ratio for $H \to ZZ$ is 0.3. The branching ratios for $Z \to e^+e^-$ and $Z \to \mu^+\mu^-$ are each 3.37%, so the fraction of Z decays with either of these two modes is 6.74%, and the fraction of times that both Zs decay in this way is given by the product, $(0.0674)^2 = 0.0045$ or 0.45%. So only $0.3 \times 0.0045 \approx 0.14\%$ of the Higgs bosons produced will decay in such a way that they can be reconstructed easily. On top of this one must take into account that the electron and muon identification of the detectors is not perfect and they cover most but not all of the 4π of solid angle around the interaction point. The *efficiency* ε for events of this type, i.e., the fraction of the events that can be found, is around 70%. So the expected number of signal events actually observed would be

$$\begin{aligned} N(\text{H found}) &= N(\text{H produced})\,\mathcal{B}(\text{H} \to \text{ZZ})\,\mathcal{B}(\text{Z} \to \text{e}^+\text{e}^- \text{ or } \mu^+\mu^-)^2\,\varepsilon \\ &= 9 \times 10^5 \times 0.3 \times 0.0674^2 \times 0.7 \\ &\approx 900\,. \end{aligned} \tag{11.7}$$

On top of this there will be background events, for example, when a quark in one proton collides with an antiquark in the other (which must come from a virtual quark–antiquark pair), and these produce two Zs. Of course, there is no reason for the invariant mass of such a ZZ pair to be clustered around the Higgs mass, and by looking at the distribution of the total invariant mass of the e^+e^- and $\mu^+\mu^-$ pairs, one should see a peak at the Higgs mass from the signal events.

These 900 signal events must be sifted out of a background of inelastic pp collisions that are almost 10^{13} times greater in number. At $E_{\text{cm}} = 14$ TeV the cross section for an inelastic pp collision is about 70 mb, so at a luminosity of 10^{34} $\text{cm}^{-2}\text{s}^{-1}$, the number of events per unit time is 7×10^8 per second, or almost 1 GHz. So in the same 10^7 s of running, there will be 7×10^{15} inelastic pp events. Most of these collisions produce hadrons with relatively low transverse momenta or $p_\perp$, i.e., the component of momentum relative to the beam line. It is only because the muons and electrons from the Z decays stand out – first, by having higher transverse momenta and second, by leaving characteristic signals different from those of hadrons – that the Higgs events can be separated from the background. The problem of finding the Higgs at the LHC is often compared to finding a needle in a haystack.

The very high luminosity of 10^{34} $\text{cm}^{-2}\text{s}^{-1}$, which is necessary in order to produce a significant number of Higgs events in a reasonable time, poses experimental problems that have not been encountered before. The high luminosity means that there will be on average almost two dozen events every time the proton–proton bunches collide. Notice in Fig. 11.13 the large number of lower energy particles in the event. These come mostly from proton–proton collisions other than the one that produced the Higgs but which occurred during the same bunch crossing. At the LHC, bunches of protons collide every 25 ns, so the number of collisions per crossing is $0.7\ \text{ns}^{-1} \times 25\ \text{ns} \approx 17.5$. In fact, about 20% of the 'RF buckets', i.e., regions of the accelerating structure that can contain proton bunches, will be empty. Therefore in those crossings where protons actually collide there will be an average of 22 inelastic collisions.

It's interesting to contrast the enormous event rates at the LHC with the situation at LEP. At LEP I with $E_{\text{cm}} = M_{\text{Z}}$, for example, the cross section for, say, $\text{e}^+\text{e}^- \to$ hadrons was 30 nb, and the luminosity was on the order of 10^{31} $\text{cm}^{-2}\text{s}^{-1}$. The hadronic event rate was therefore

$$30\ \text{nb}\ \times 10^{31}\ \text{cm}^{-2}\text{s}^{-1} \times \frac{10^{-33}\ \text{cm}^2}{\text{nb}} = 0.3\ \text{s}^{-1}$$

or about 1 event every 3 seconds, more than 2 billion times less than the hadronic event rate at the LHC. Furthermore the mean time between bunch crossings at LEP was 22 μs, so the mean number of collisions per bunch crossing was $0.3\ \text{s}^{-1} \times 22 \times 10^{-6}\ \text{s} = 6.6 \times 10^{-6}$. So the problem of multiple interactions in a single bunch crossing was completely negligible at LEP, but it is a large effect at the LHC.

11.8 Summer 2012: the Higgs discovery

On July 4^{th} 2012, CERN held two seminars, the first given by Joe Incandela, the CMS spokesperson and the second given by Fabiola Gianotti the ATLAS spokesperson, followed by a press conference (the CERN web site media page has videos of the day's events). The reason for the world event was the announcement that each collaboration had observed, beyond statistical doubt, the observation of a new particle around the mass of 125 GeV, consistent with the standard model Higgs boson. Each collaboration had kept their results secret until then, and so the seminars were followed by all of the particle physicists that day and represented for many of them the most exciting day of their professional career, from PhD students to senior researchers. The Higgs discovery was displayed on the front page of most of the world's newspapers on the next day.

Owing to the mass of the Higgs boson, the signatures that contributed most to the statistical significance were the Higgs decaying to two photons (shown in Fig. 11.14) and the Higgs decaying to a pair of Z with each Z decaying to electrons or muons (shown in Fig. 11.15), described in the previous section. Each analyses were quite sophisticated despite the simplicity of the signature. The reason for this is that the standard in particle physics for claiming the discovery of a new phenomenon is that the evidence has to reach "5 sigma". This means that if the Higgs boson did not exist, the probability of observing a result as Higgs-like or more so is less than one in a million (the equivalent of getting twenty heads in a row in the coin toss). One way to reach this statistical significance it to just wait until the amount of data accumulated reached this level. In addition one can also achieve this level of sensitivity by, for example, combining information from several channels or by changing the selection criteria in different kinematic regions of the signature to take into account that the background might be reduced in those regions, instead of keeping the selection criteria the same.

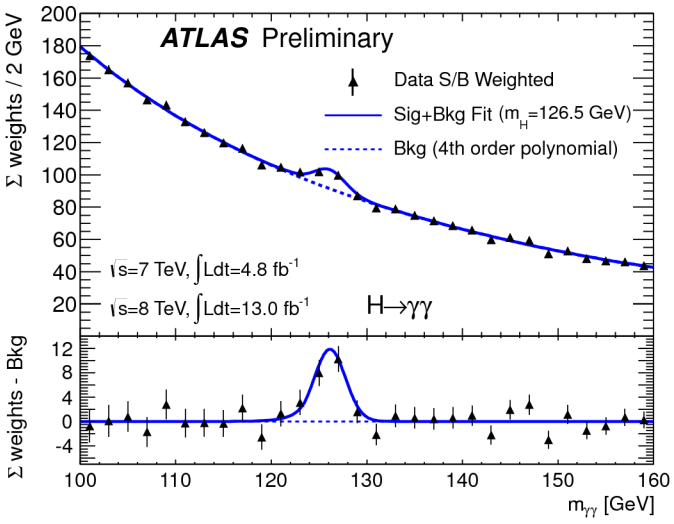

Figure 11.14: ATLAS results for the Higgs decaying to two photons as a function of the invariant mass of the two photons (from [93]).

11.9 Properties of the new Higgs-like particle

Once the discovery of the new particle was established beyond statistical doubt, the next phase was to establish whether the new particle was the long sought-after SM Higgs or some other

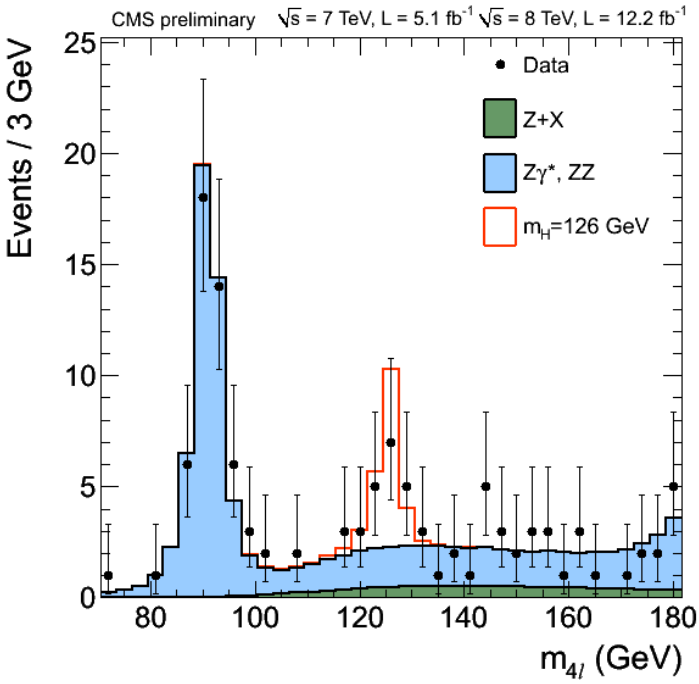

Figure 11.15: CMS results for the Higgs decaying to two Z bosons with each Z boson decaying to either electrons or muons as a function of the invariant mass of the four leptons (from [97]).

particle, or a Higgs within another model than the SM. Measuring the Higgs cross section in all of its possible decays is the first step in identifying its precise nature. Fig. 11.16 shows the current production strengths of the Higgs boson as measured by ATLAS (compared to the SM production).

An interesting Higgs signature is where the Higgs decay to two tau leptons. This is an important channel as it is the first evidence that the new particle decays into leptons, as predicted by the SM. Figs. 11.17 and 11.18 show the coupling measurements to various massive particles from Run 1 and Run 2 respectively. Note that the coupling increases with the mass of the particle and how more precision in these measurements (from the increased Run 2 data set compared to Run 1) is a stringent test of the SM predictions.

Another property of the Higgs that was also measured has been its spin and CP parity (J^P), since the SM predicts a 0^+ Higgs boson. Already the spin-1 hypothesis was strongly disfavoured since it is not possible for an on-shell spin-1 particle to decay directly into two photons. The way to be sensitive to the spin and CP parity quantum numbers is to look at the distribution of various angles between the particles in the final states. For example, Fig. 11.19 shows the expected angular distribution calculated using the two photon channel for two different spin hypotheses. The results from the ATLAS spin analysis are that the $J^P = 0^-,1^+,1^-,2^+$ hypotheses are excluded at a "confidence level" of more than 97.8%.

Much work remains to be done in the Higgs sector: its couplings to various particles need to be measured, for example to the top quark, since it has the largest mass of all the particles. In addition the SM predicts that the Higgs could couple to itself, leading to vertices involving more than one Higgs boson. Measuring those Higgs self-couplings would be a strong test of the SM. Due to the harsh nature of the LHC, coming from the fact that it is a hadron collider, many physicists believe that the best environment for making precise Higgs measurement would be a future linear collider, which would be a Higgs factory.

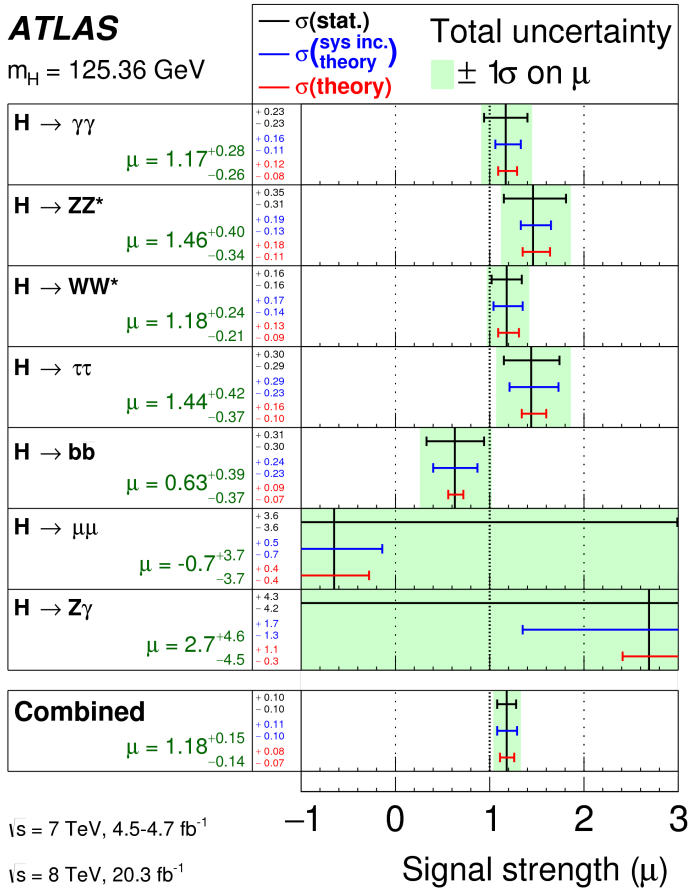

Figure 11.16: Higgs signal strength compared to the SM expectation for various decay channels from ATLAS [98].

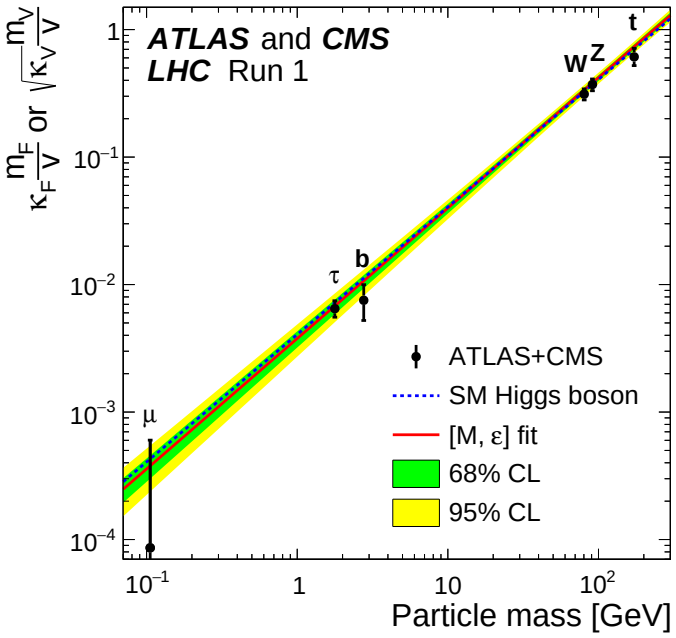

Figure 11.17: Higgs coupling as a function of particle mass [101].

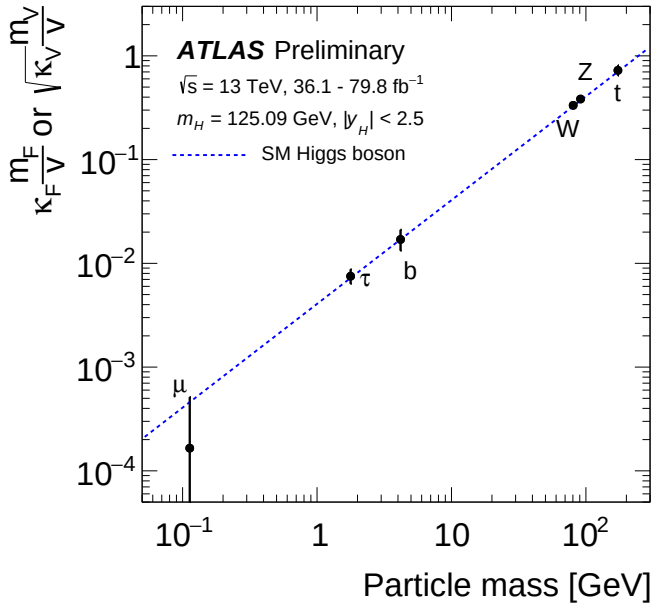

Figure 11.18: Higgs coupling as a function of particle mass from Run 2 of ATLAS [102].

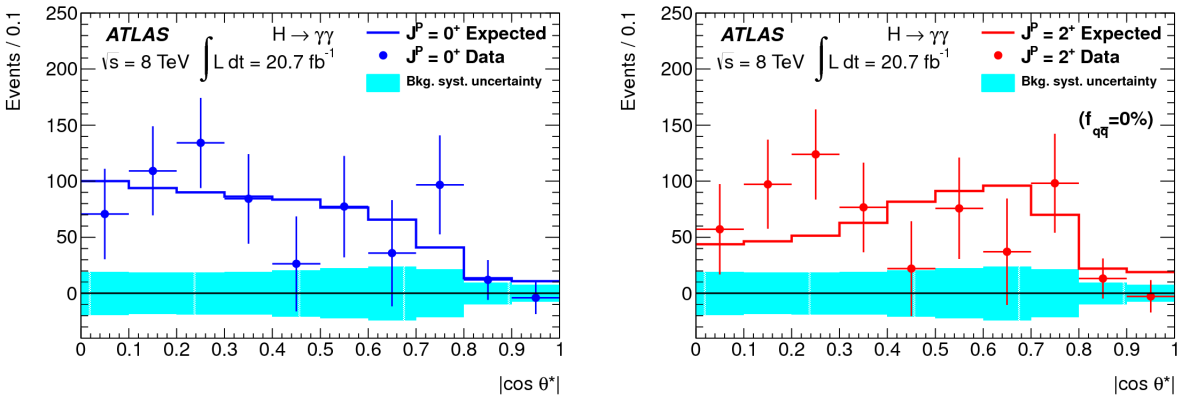

(a) (b)

Figure 11.19: Angular distributions using the decay H $\to \gamma\gamma$ comparing (a) $J^P = 0^+$ and (b) $J^P = 2^+$ using ATLAS data [99].

Chapter 12

Beyond the Standard Model

Having just seen the Higgs mechanism, which is the final ingredient of the Standard Model, in this chapter we take a look at how the Standard Model can be regarded as an effective theory that can be embedded within a more general framework. One specific model of physics beyond the Standard Model is looked at, that of Supersymmetry.

12.1 The Standard Model

In previous chapters, we studied some of the necessary ingredients for formulating the Standard Model of particle physics. As shown in Fig. 12.1 the Standard Model uses the quantum field theory framework and makes explicit use of the local gauge principle, which is necessary in order for the theory to be renormalizable. It also includes the Higgs mechanism in order to preserve the gauge invariance while giving mass to particles. As such it is then not a fundamental theory but rather a model construction used to explain the experimental data. It is rather surprising that such a construction managed to sustain the level of experimental tests that were devised to test its validity.

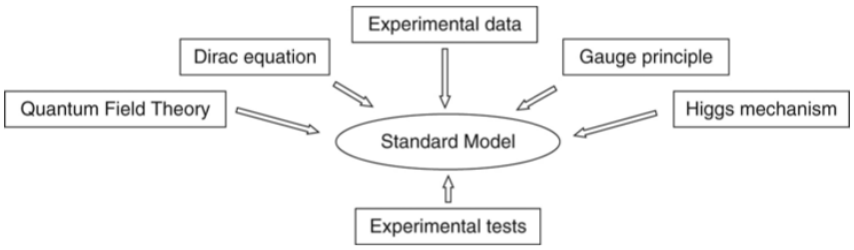

Figure 12.1: Ingredients of the Standard Model [2].

In the Standard Model there are 25 parameters that need to be put by hand and hence that need to be measured experimentally. Those are: the 12 fermion masses (6 quarks and 6 leptons); the three coupling constants e, g and g_s; two parameters that involve the Higgs boson: its vacuum expectation value and its mass; eight parameters coming from the CKM (λ, A, ρ, η) and the neutrino matrices (θ_{12}, θ_{13}, θ_{23}, δ).

If one looks at the masses of the fermions (see Fig. 12.2), we notice that generally speaking there seems to be a very rough pattern, namely that the masses of the fermions are similar for members of a given generation, and that the masses increase as we go from the first to the third generation (the neutrinos don't follow this pattern as much). Also the fact that the three coupling constants are of about the same order of magnitude indicates that there might be an underlying theory, where the Standard Model would be its representation at low energy. We commonly refer to this underlying theory as a Grand Unified Theory or GUT.

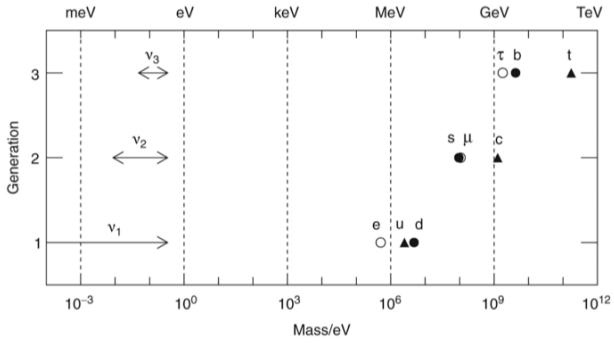

Figure 12.2: Rough pattern to the fermion masses [2].

12.2 Limitations of the Standard Model

One example where the Standard Model is manifestly not the final theory of particle physics has to do with the theoretical calculations of the Higgs boson mass. According to quantum field theory, quantum loop corrections need to be included in the computation of the Higgs boson mass. A representation of such quantum loops are shown in Fig. 12.3. If we were to assume that the Standard Model is valid up to the Planck scale (at which point one needs to take into account quantum gravity, which the Standard Model doesn't describe) then those quantum corrections would make the Higgs mass very much larger than the 125 GeV value that we have recently observed (and which was hinted at by various indirect measurements of the consistency of the Standard Model). It is possible to obtain the observed lower value only if one assumes very careful cancellations coming from all the quantum loop corrections. We call this procedure "fine-tuning" and because we do not like such accidental coincidences, we have named this problem within the Standard Model the "Hierarchy Problem". There are other issues with the Standard Model that go beyond the scope of this course.

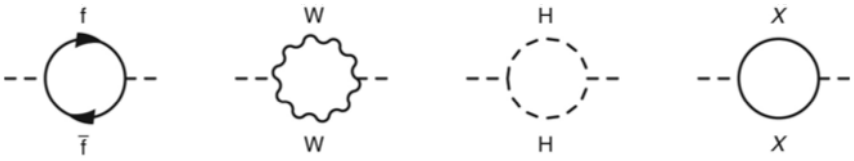

Figure 12.3: Quantum loop contributions to the Higgs mass [2].

12.3 Extensions of the Standard Model

There are several possible theoretical models that attempt to fix the limitations of the Standard Model, while maintaining all of the experimental measurements. The most popular one among theorists is called Supersymmetry and this is described very briefly in the next section. Another model extensively studied at the LHC is that of large extra dimensions. These extra dimensions are called large to contrast them from the infinitesimal extra dimensions that are necessary in the mathematical formulation of string/brane theory.

In large extra dimensions models, all of the particles and interactions live on the "bulk" of the universe (which is our usual dimensions and universe), while gravity live on a brane in addition to the bulk. The graviton, the messenger particle of gravity, would be the connection between the brane and the bulk. This gives a natural explanation to the apparent weakness of the gravitational interaction: it is weak to us since we only live on the bulk. A way of conceptualizing these extra dimensions is to think of an acrobat on a tight rope: this acrobat can only move in one direction: forward and backward, but an ant on this tight rope can move in two dimensions: forward and backward, but also around the rope since the ant is so small.

12.3.1 Supersymmetry

As the name suggests, Supersymmetry (SUSY) introduces a new symmetry: for every Standard Model fermion there is a boson super-partner of the same mass and for every Standard Model boson there is a fermion super-partner of the same mass. This extra symmetry neatly solves the Hierarchy Problem discussed above since for every loop contribution coming from a Standard Model particle there will be an identical loop contribution that will come from the super-partner and it will have opposite sign to the Standard Model particle loop because one is a fermion and the other is a boson contribution. Other theoretical motivations for SUSY are that it appears to unify all three interactions at high energy, as represented in Fig. 12.4. Finally another powerful motivation is that SUSY provides a natural dark matter particle.

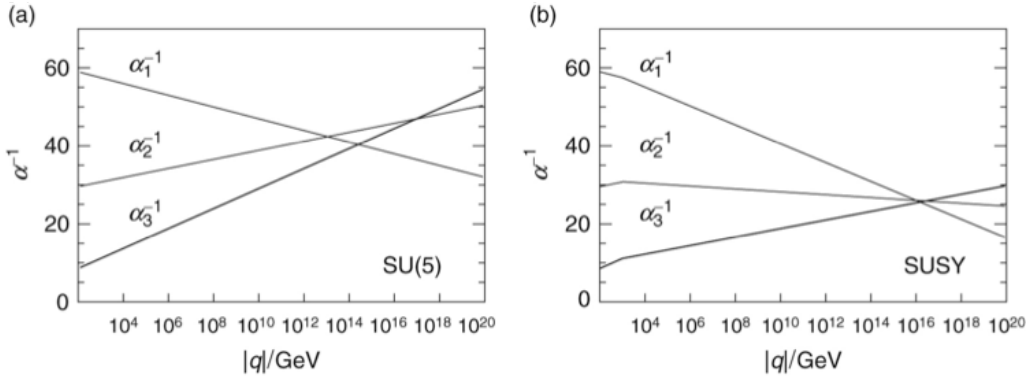

Figure 12.4: On the left is a generic SU(5) GUT extension of the Standard Model which doesn't manage to unify the couplings while on the right this is a supersymmetric extension of a SU(5) theory which appear to unify the coupling constants [2].

The super-partner of a fermion is a spin-0 scalar called a sfermion (for example a squark or a slepton), the super-partner of a spin-1 gauge boson is a spin 1/2 gaugino and the super-partner

of a spin-0 Higgs is a spin-1/2 Higgsino. Supersymmetric particles are typically indicated with a tilde as shown in Fig. 12.5.

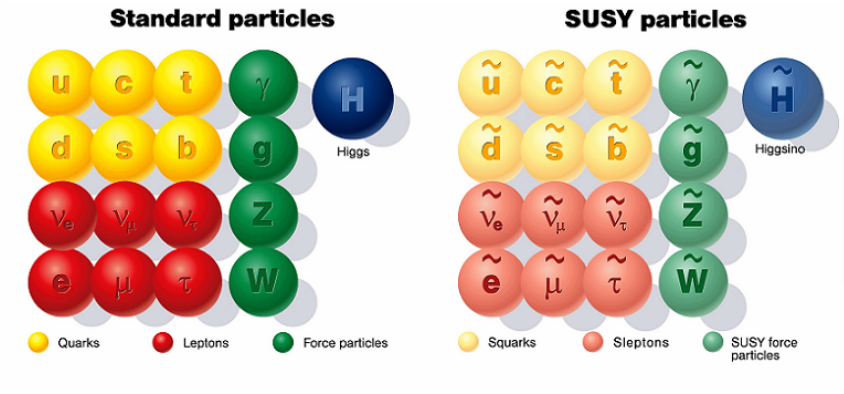

Figure 12.5: Representation of Standard Model particles and their super-partners within SUSY.

In discussing the Higgs mechanism we mentioned that the Higgs field is a doublet and that out of these four degrees of freedom only one remains after the breaking of the electroweak symmetry, and that remaining degree of freedom is the Higgs boson. In SUSY the Higgs field is a two Higgs field doublet which then contains eight degrees of freedom. After electroweak symmetry breaking, five remain corresponding to five Higgs bosons: two charged ones ($H^{\pm}$), two neutral ones that have quantum numbers $J^P = 0^+$ (a light one h^0 and a heavy one H^0) and finally a neutral one with $J^P = 0^-$ (A^0).

Recall that in the Standard Model, the massless gauge bosons B, and W_1, W_2, W_3 mix to give the massive W^+, W^-, Z and the photon. In SUSY the neutral Higgsinos and gauginos mix to give four neutralinos (that are neutral), and the two charged Higgsinos and gauginos mix to give two charginos (that are charged). In the Standard Model we have baryon number and lepton number conservation[1] while in SUSY those can be violated which has the pesky consequence that the proton would decay in 10 milliseconds clearly violating the stability of atoms! Experimentally the proton lifetime is inferred to be longer than 1.6×10^{33} years. In order to protect against this shortcoming, a new quantum number is introduced within SUSY which is called R-parity

$$R = (-1)^{3(B-L)+2S}, \tag{12.1}$$

where B and L are the baryon and lepton numbers while S is the spin of the particle. It follows that R-parity of Standard Model particles is $+1$, while R-parity of SUSY particles is -1. There are a few experimental consequences to R-parity conservation: in collisions, particles will be produced in pairs (a sparticle will always be accompanied by an anti-sparticle), also the lightest SUSY particle (the neutralino) must be stable, this would make a good dark matter candidate, in agreement with current cosmological measurements. In a detector this neutralino would not leave any signal, so one could infer its presence from missing transverse momentum, similarly to what is done for a neutrino going through the detector.

[1]Strictly speaking the Standard Model predicts some non-conservation of Baryon and Lepton number, these non-perturbative processes are called sphalerons.

If the symmetry introduced by SUSY is exact than the masses of the sparticles would be the same as the masses of their particles partners. Obviously this is not the case since we would have detected all of the sparticles by now, this means that SUSY is a broken symmetry. On the other hand, the breaking of SUSY can't be too big, as this would prevent the exquisite cancellation of the loop corrections we mentioned above. There are many models that have been developed to represent a broken SUSY and each of those have on the order of 100 free parameters. There are various theory arguments that favour a mass scale of the sparticles to be at the TeV level, accessible at the LHC. Due to the fact that SUSY is a broken symmetry, this implies that it can't be the final theory at very high energy, it will be, similarly to the Standard Model, a lower energy representation of this hypothetical high-energy final theory. Finally, it is sometimes mentioned that there is a connection between SUSY and the best current mathematical representation of quantum gravity (namely string or brane or M-theory), that connection is that if SUSY were to be true, then its unification with quantum gravity would be feasible, but if SUSY is not true, then that does not imply per say that string theory is wrong, so testing for SUSY is not a test of string theory.

During Run 1 of the LHC (the data collected at 7 and 8 TeV centre-of-mass in 2011 and 2012) as well as Run 2 (data collected at 13 TeV from 2015 to 2018) no hints of SUSY have been detected whatsoever and very stringent limits for masses of the sparticles have been obtained [100]. Some physicists have commented that particle physics is in crisis from not having discovered anything inconsistent with the Standard Model so far. This state of affairs puts into doubt the very concept of naturalness for example. Others believe that it is still too early to draw such firm conclusions and the future runs of the LHC (extending all the way to the mid-2030's) will provide a vast amount of data allowing to test many of the proposed theories.

Bibliography

[1] B.R. Martin and G. Shaw, *Particle Physics*, 2nd edition, Wiley, 1997.

[2] M. Thomson *Modern Particle Physics*, Cambridge University Press, Cambridge (2013)

[3] I.S. Hughes, *Elementary Particles*, 3rd edition, Cambridge University Press, 1996.

[4] D.H. Perkins, *Introduction to High Energy Physics*, 3rd edition, Addison-Wesley, 1987.

[5] R.N. Cahn and G. Goldhaber, *The Experimental Foundations of Particle Physics*, Cambridge, 1989.

[6] Web site of the CMS experiment, `cmsinfo.cern.ch`.

[7] C. Patrignani et al. (Particle Data Group), *The Review of Particle Physics*, Chin. Phys. C, 40, 100001 (2016).

[8] Steven Weinberg, *Dreams of a Final Theory*, Vintage Books, 1994.

[9] Brian Greene, *The Elegant Universe*, Vintage, 1999.

[10] `map.gsfc.nasa.gov`

[11] Web site of the Stanford Linear Accelerator Center, `www.slac.stanford.edu`.

[12] Web site of the Fermi National Accelerator Laboratory, `www.fnal.gov`.

[13] Web site of the European Organisation for Nuclear Research (CERN), `www.cern.ch`.

[14] K. Kleinknecht, *Detectors for Particle Radiation*, 2nd edition, Cambridge, 1999.

[15] Claus Grupen, *Particle Detectors*, Cambridge, 1996.

[16] W.R. Leo, *Techniques for Nuclear and Particle Physics Experiments*, 2nd edition, Springer, New York, 1994.

[17] H.A. Bethe, Annalen der Physik **5** (1930) 325; Zeitschrift für Physik **76** (1932) 263.

[18] F. Bloch, Zeitschrift für Physik **81** (1933) 363.

[19] Lawrence Berkeley National Laboratory Image Library, `imglib.lbl.gov/ImgLib`.

[20] G. Charpak, *Electronic Imaging of Ionizing Radiation with Limited Avalanches in Gases*, 1992 Nobel Lecture, CERN-PPE/93-25 (1993).

[21] A.H. Walenta *et al.*, NIM **92** (1971) 373.

[22] D. Nygren, Phys. Scripta **23** (1981) 584.

[23] Web site of the ALEPH collaboration, `alephwww.cern.ch`, and the ALEPH public pages, `alephwww.cern.ch/Public.html`.

[24] H. Aihara *et al.*, Phys. Rev. Lett. **61** (1988) 1263.

[25] P.A.M. Dirac, Proceedings of the Royal Society **A126** (1920–30) 360; **A133** (1931) 60.

[26] C.D. Anderson, Physical Review **43** (1933) 491.

[27] Seth H. Neddermeyer and Carl D. Anderson, Physical Review **51** (1937) 884.

[28] Seth H. Neddermeyer and Carl D. Anderson, Reviews of Modern Physics **11** (1939) 191; Physical Review **54** (1938) 88.

[29] The Pauli Archive (CERN), `library.cern.ch/archives/paulimain.html`.

[30] E. Fermi, Nuovo Cimento **11** (1934) 1; Zeitschrift für Physik **88** (1934) 161.

[31] F. Reines and C.L. Cowan, Jr., Phys. Rev. **113** (1959) 273.

[32] G. Danby *et al.*, Phys. Rev. Lett. **9** (1962) 36.

[33] The DONUT experiment, Fermilab seminar, 21 July 2000, `f872.fnal.gov`; K. Kodama, et.al., *Observation of tau neutrino interactions*, Physics Letters B **504** (2001) 218.

[34] Y. Fukuda *et al.*, (The Super-Kamiokande Collaboration), Phys. Rev. Lett. **81** (1998) 1562.

[35] M.L. Perl *et al.*, Phys. Rev. Lett. **35** (1975) 1489.

[36] M. Conversi, E. Pancini and O. Piccioni, Phys. Rev. **71** (1947) 209.

[37] D.H. Perkins, Nature **159** (1947) 126.

[38] C.M.G. Lattes, G.P.S. Ochialini and C.F. Powell, Nature **160** (1947) 453.

[39] C.F. Powell, P.H. Fowler and D.H. Perkins, *The study of elementary particles by the photographic method*, Pergamon, New York, 1959.

[40] R. Bjorklund, W.E. Crandall, B.J. Moyer and H.F. York, Phys. Rev. **77** (1950) 213.

[41] G.D. Rochester and C.C. Butler, Nature **160** (1947) 855.

[42] R. Armenteros *et al.*, Phil. Mag. **43** (1952) 597.

[43] E.W. Cowan, Phys. Rev. **94** (1954) 161.

[44] V.E. Barnes *et al.*, Phys. Rev. Lett. **12** (1964) 204.

[45] D. Buskulic *et al.* (ALEPH Collaboration), Z. Phys. C **69** (1996) 379.

[46] R.W. McAllister and R. Hofstadter, Phys. Rev. **102** (1956) 851.

[47] Web site of the H1 experiment, `www-h1.desy.de`.

[48] John F. Martin, *Report from the ZEUS Collaboration at HERA*, in Peris Drell and David Rubin (eds.), *Proceedings of the XVI International Symposium on Lepton and Photon Interactions*, AIP, New York, 1994.

[49] J. Friedman and H. Kendall, *Deep Inelastic Electron Scattering*, Ann. Rev. Nucl. Sci. **22** (1972) 203.

[50] N. Cabibbo, Phys. Rev. Lett. **10** (1963) 531.

[51] S.L. Glashow, J. Iliopoulos and L. Maiani, Phys. Rev. D **2** (1970) 1285.

[52] M.K. Gaillard and B.W. Lee, Phys. Rev. D **10** (1974) 897.

[53] L. Hoddeson, L Brown, M. Riordan and M. Dresden (eds.), *The Rise of the Standard Model*, Cambridge University Press, 1997.

[54] J. Aubert *et al.*, Phys. Rev. Lett. **33** (1974) 1402.

[55] J.E. Augustin *et al.*, Phys. Rev. Lett. **33** (1974) 1406.

[56] G.S. Abrams *et al.*, Phys. Rev. Lett. **33** (1974) 1953.

[57] G. Goldhaber *et al.*, Phys. Rev. Lett. **37** (1976) 255; I. Peruzzi *et al.*, Phys. Rev. Lett. **37** (1976) 569.

[58] R. Barate *et al.* (ALEPH Collaboration) European Physical Journal C **16** (2000) 597.

[59] S.W. Herb *et al.*, Phys. Rev. Lett. **39** (1977) 252.

[60] C. Berger *et al.*, Phys. Lett. **76B** (1978) 243.

[61] C.W. Darden *et al.*, Phys. Lett. **76B** (1977) 246; *ibid.* **78B** (1978) 364.

[62] Website of the Cornell Laboratory of Nuclear Studies, `www.lns.cornell.edu`.

[63] L. Wolfenstein, Phys. Rev. Let. **51** (1983) 1945.

[64] M. Kobayashi and T. Maskawa, Prog. Theor. Phys. **49** (1973) 652.

[65] F. Abe *et al.*, Phys. Rev. Lett. **74** (1995) 2626.

[66] Tony M. Liss and Paul L. Tipton, *The Discovery of the Top Quark*, Scientific American, September, 1997.

[67] R.K. Ellis, W.J. Stirling and B.R. Webber, *QCD and Collider Physics*, Cambridge University Press, 1996.

[68] C.N. Yang and R.L. Mills, Phys. Rev. **96** (1954) 191.

[69] C.S. Wu *et al.*, Phys. Rev. **105** (1957) 1413.

[70] T.D. Lee and C.N. Yang, Phys. Rev. **104** (1956) 254.

[71] P.W. Higgs, Phys. Rev. Lett. **13** (1964) 508.

[72] S.L. Glashow, Nucl. Phys. **22** (1961) 579.

[73] S. Weinberg, Phys. Rev. Lett. **19** (1967) 1264.

[74] A. Salam, *Elementary Particle Theory*, N. Svartholm (ed.), Almqvist, Stockholm (1968) 367.

[75] G. 't Hooft, Nucl. Phys. B **33** (1971) 173.

[76] F.J. Hasert *et al.*, Phys. Lett. **46B** (1973) 138.

[77] G. Arnison *et al.* (UA1 Collaboration), Phys. Lett. **122B** (1983) 103.

[78] G. Arnison *et al.* (UA1 Collaboration), Phys. Lett. **126B** (1983) 398.

[79] The LEP and SLD experiments, *A Combination of Preliminary Electroweak Measurements and Constraints on the Standard Model*, CERN EP/2000-016 (2000).

[80] D. Buskulic *et al.* (ALEPH Collaboration), Zeitschrift für Physik C **59** (1993) 215.

[81] R.Barate *et al.* (ALEPH collaboration), Phys. Lett. B **453** (1999) 107.

[82] The LEP Electroweak Working Group, *lepewwg.web.cern.ch/LEPEWWG*, results presented at the International Conference on High Energy Physics, Osaka, Japan, July 27 - August 2, 2000.

[83] O.W. Greenberg, Phys. Rev Lett. **13** (1964) 585.

[84] R. Barate *et al.* (ALEPH Collaboration), Physics Reports **294** (1998) 1.

[85] B. Andersson, G. Gustafson, G. Ingelman and T. Sjöstrand, Phys. Rep. **97** (1983) 31.

[86] D. Decamp *et al.* (ALEPH Collaboration), Phys. Lett. B **284** (1992) 163.

[87] S.G. Gorishny, A. Kataev and S.A. Larin, Phys. Lett. **B259** (1991) 114; L.R. Surguladze and M.A. Samuel, Phys. Rev. Lett. **66** (1991) 560.

[88] David Miller, *A quasi-political Explanation of the Higgs Boson for Mr Waldegrave*, `www.hep.ucl.ac.uk/~djm/higgsa.html` (1993).

[89] G. Cowan, *Statistical Data Analysis*, Oxford University Press, Oxford (1998).

[90] R. Barate *et al.* (ALEPH Collaboration), *Observation of an Excess in the Search for the Standard Model Higgs Boson at ALEPH*, Phys. Lett. **B495** (2000) 1-17.

[91] The ALEPH, DELPHI, L3 and OPAL Collaborations, *Search for the Standard Model Higgs Boson at LEP*, LHWG Note/2002-01, contributed paper for ICHEP'02, Amsterdam (2002).

[92] Web site of the Superconducting Supercollider, `www.hep.net/ssc`.

[93] Web site of the ATLAS collaboration, `atlas.ch`.

[94] Z. Kunszt, S. Moretti and W.J. Stirling, Z. Phys. C **74** (1997) 479.

[95] Heinrich Hertz, *Über die Beziehungen zwischen Licht und Elektrizität*, Alfred Kröner Verlag, Stuttgart, 1905.

[96] H. Georgi and S.L. Glashow, *Unity of All Elementary Particle Forces*, Phys. Rev. Lett. **32** (1974) 438.

[97] Web site of the CMS collaboration, `cms.web.cern.ch`.

[98] ATLAS Higgs summary plots,

`https://atlas.web.cern.ch/Atlas/GROUPS/PHYSICS/CombinedSummaryPlots/HIGGS/`

[99] ATLAS Collaboration, *Evidence for the spin-0 nature of the Higgs boson using ATLAS data* Phys. Lett. **B 726** (2013) 120-144.

[100] ATLAS SUSY results,

`https://twiki.cern.ch/twiki/bin/view/AtlasPublic/SupersymmetryPublicResults`

[101] ATLAS and CMS Collaborations, *Measurements of the Higgs boson production and decay rates and constraints on its couplings from a combined ATLAS and CMS analysis of the LHC pp collision data at* $\sqrt{s} = 7$ *and 8 TeV* JHEP **08** (2016) 045.

[102] ATLAS Collaboration, *Combined measurements of Higgs boson production and decay using up to 80 fb-1 of proton proton collision data at 13 TeV collected with the ATLAS experiment.*, ATLAS-CONF-2018-031, July 2018.

[103] LHCb Collaboration, *Observation of the resonant character of the* $Z(4430)^-$ *state*, Phys. Rev. Lett. 112, 222002 (2014)

[104] LHCb Collaboration, *Observation of structure in the* J/ψ *pair mass spectrum*, arXiv:2006.16957v1

[105] LHCb Collaboration, *Observation of* $J/\psi p$ *resonances consistent with pentaquark states in* $\Lambda_b^0 \to J/\psi K^- p$ *decays*, Phys. Rev. Lett. 115, 072001 (2015)